The need for a community-wide determination of the fundamental constants

John Martens

Submitted to the graduate degree program in Physics and Astronomy and the graduate faculty of the University of Kansas in partial fulfillment of the requirements for the degree of Doctor of Philosophy

---

John P. Ralston (Chair)

Carey K. Johnson

Ian Lewis

Douglas W. McKay

Daniel Tapia Takaki

Dated defended: 23 July 2021

The dissertation committee for **John Martens**

certifies that this is the approved version of the following dissertation:

The need for a community-wide determination of the fundamental constants

_____

Chair: John P. Ralston

Date Approved: 17 December 2021

Abstract

Tests of fundamental theory are sensitive to the values of the fundamental (physical) constants. These values are determined by a global fit to experimental data and depend on the data, theory, and theory uncertainties that enter the fit. Tests of fundamental theory are thus sensitive, to a greater or lesser extent, to procedural decisions. We label the set of choices that comprise a given global fit procedure as a *scheme*. No single, best scheme exists. For example, a scheme optimized to give values for the fundamental constants with the smallest possible uncertainties might omit anomalous data, while a scheme optimized to test fundamental theory might include anomalous data. Historically, values for the fundamental constants have been determined by the National Institute of Science and Technology (NIST) by an elaborate fit to world data— i.e. by reference to a single scheme. The result is that the scheme dependence of the fundamental constants has effectively been removed from phenomenological consideration. Unfortunately the precision of modern experiments is such that the scheme dependence of tests of fundamental theory (occurring through the scheme dependence of the fundamental constants) can no longer be safely ignored. We argue that any test of fundamental theory should be evaluated using values for the fundamental constants determined via a scheme that includes all data and theory relevant to that test. The alternative— namely, evaluating a given test of fundamental theory using fundamental constants determined via a scheme omitting relevant data or relevant theory or both— has potentially serious consequences for the phenomenology that are difficult to predict from pure thought

alone. We find that an omission of relevant data from the NIST determination of the fundamental constants is responsible for the proton size puzzle, with the puzzle disappearing under a scheme that includes all relevant data. We also find that schemes omitting a relevant theory alternative generally lead to falsely-restrictive exclusion limits— a result that has implications for many proposed solutions to the muon $g-2$ anomaly. We have created an online interface called `CONSTANT FINDER` (`www.www.constantfinder.org/home.jsp`) to enable the community-wide investigation of the scheme dependence of the fundamental constants. With `CONSTANT FINDER`, anyone interested can adjust experimental and theoretical values and uncertainties, and pose theory alternatives within several global data-fitting frameworks.

Acknowledgments

I'm enormously grateful for the many people who have supported me throughout my time in graduate school. I'd like to single out a number of them for special thanks. Thank you:

- to my advisor John Ralston, for your friendship and guidance and for dragging me along on this and so many other projects; my life is the richer for it
- to Daniel Tapia Takaki and Jerry Manweiler, for your many years of mentorship, support, and kindness
- to my dissertation committee members, for your time and help as I finish up
- to the members of the KU theory group, past and present, for countless helpful conversations and, day in and day out, a very pleasant work environment
- to the KU Physics and Astronomy Department staff, and in particular, to Kim Hubbel, Teri Leahy, Kristin Rennells, and Joel Sauerwein, for kindness and support well in excess of any job description
- to my wife Jessie, for your love and support and infinite patience

Contents

List of Figures

List of Tables

Chapter 1

Introduction

1 A problem hidden in plainsight

The values of the constants appearing in precision QED theory are determined upstream of the theory itself by a U.S.-government-funded, least-squares fit to experimental data. Theorists and experimentalists then feed the values of these constants into tests of fundamental theory. The effect is: the determination of the values of these constants falls outside the scope of precision QED theory as it is conventionally practiced by theorists. We will refer to these constants (for now loosely and later more precisely) as the fundamental constants.

On its face, the situation described does not seem especially objectionable. Having standardized values for the fundamental constants, apart from being convenient, seems to provide a common baseline on which to conduct tests of fundamental theory. However, this common baseline has a problem related to a lack of self-consistency, which can be seen as follows.

Tests of fundamental theory depend on the values of the fundamental constants. The values of the fundamental constants depend on the least squares fit procedure used to determine them. Hence changing the fit procedure— e.g., by changing the data or theory included in the fit— in general changes the result of any test of

fundamental theory occurring downstream of the fit. No single fit procedure is appropriate for all circumstances. As an example, if we wanted to test a particular new physics scenario by comparing theory to experiment and to do it in a truly self-consistent way, we would need to evaluate the relevant theory using fundamental constants determined by a least squares fit that included the effects of the new physics scenario. The ideal, then, is not a common baseline but a self-consistent baseline. To ensure self-consistency, any test of fundamental theory should be conducted using fundamental constants determined by a least squares fit that confronts all relevant theory and all relevant experiments.

The importance of self-consistency in tests of fundamental theory is the central topic of this dissertation. We use the muon experimental anomalies— the proton size puzzle and the muon $(g-2)$ anomaly— throughout for illustration. In Ch. 7, for example, the proton size puzzle is shown to be a consequence of a determination of the fundamental constants lacking self-consistency. However the need for self-consistency is not confined to the muon experimental anomalies. In principle, all tests of fundamental theory should be evaluated using fundamental constants determined on a self-consistent basis, but historically such an aim has been impractical due to the computational overhead of refitting the constants. We created a website called `CONSTANT FINDER` as a means of lowering the barrier to refitting the constants. With `CONSTANT FINDER`, users can fit the fundamental constants on a self-consistent basis according to their own assumptions, often in a matter of minutes. The exploratory analyses of Ch. 7 can all be carried out using `CONSTANT FINDER` and give a general sense of how the site is intended to be used.

The remainder of this chapter gives a more detailed introduction to the material above. A description of subsequent chapters is postponed to the end of this chapter.

2 The fundamental constants of the Rydberg sector

The Standard Model Lagrangian has 26 free parameters, one free parameter for every term not predicted by a symmetry. There are 20 quark and lepton masses and mixing angles,[1] three gauge coupling constants, two parameters of the Higgs sector, and the speed of light. The strong CP violating parameter θ_{QCD}, observationally consistent with zero, if counted, would make 27 free parameters.

In precision QED, of these 26 free parameters, only the electric charge e, the electron mass m_e, the muon mass m_μ, and the speed of light c are relevant. These parameters appear variously in the theory expressions of precision QED in the combinations m_e/h, m_e/m_μ, $\alpha = e^2/2\epsilon_0 hc$, and $R_\infty = \alpha^2 h/2m_e c$. α is the fine-structure constant, R_∞ is the Rydberg constant, ϵ_0 is the vacuum permittivity, and h is Planck's constant.

Several remarks are in order at this point.

- The speed of light c is fixed at 299 792 458 m/s due to the SI definition of the meter as the distance travelled by light in a vacuum in $1/299\,792\,458$ seconds.

- The vacuum permittivity $\epsilon_0 = 1/\mu_0 c^2$ is also fixed at a reference value due to the SI definition of the ampere, which fixes the vacuum permeability μ_0 at a reference value.

- m_e/h is a physical observable with dimensions of frequency. m_e and h are not separately observable. Their individual values must be determined, one way or another, from the value of m_e/h. The closely-related Compton wavelength of the electron λ_e $(= h/m_e c)$ sets the fundamental scale of QED. [2]

- The value of m_e/m_μ is fixed at a reference value in the analyses of Ch. 7. The decision is discussed in Appendix A, and subject to the caveat that future

[1] including neutrino masses and mixing angles

[2] An electron confined to within a radius of $\lambda_e/2$ will have an uncertainty in its momentum large enough that pair creation becomes possible. Pair creation requires QED for its proper description.

decrements in various experimental uncertainties, particularly in the measurement of muon $g-2$, may necessitate treating m_e/m_μ as a free parameter.

Precision QED also has an additional four free parameters that arise within the phenomenology. They are the proton mass and charge radius, m_p and r_p, and the deuteron mass and charge radius, m_d and r_d. r_p and r_d are defined in Sec. 5.4 and parameterize quantities about which the theory is ignorant. Their interpretations as charge radii come from physical arguments. Values of m_p [12] and m_d [13] are determined via Penning trap experiments and are functionally independent of the other free parameters under discussion. Consequently m_p and m_d are fixed at reference values in the analyses of Ch. 7.

Hereafter the collection of free parameters (α, R_∞, λ_e, r_p, r_d) is referred to as the fundamental physical constants of the Rydberg sector, or simply *the fundamental constants*. The fundamental constants, as free parameters, must be determined by fitting precision QED theory to experimental data. In that sense, precision QED theory is not predictive, while precision QED theory plus five experiments is.

The relationships between the fundamental constants are superintended by a diverse set of experiments.

- Muonic hydrogen (muonic deuterium) spectroscopy experiments constrain the values of r_p (r_d).
- Electronic hydrogen (electronic deuterium) spectroscopy experiments constrain the values of r_p and R_∞ (r_d and R_∞).[3]
- Electron and muon anomalous moments experiments constrain the value of α.
- Atomic interferometry experiments constrain the value of λ_e.

Figure 1.1 gives a schematic representation of these dependencies.

Tensions exist where the experiments overlap. The value of r_p determined from electronic hydrogen spectroscopy differs by $4-7\sigma$ [5] from the value of r_p determined

[3] Atomic spectroscopy experiments depend on the value of α but do not heavily constrain it.

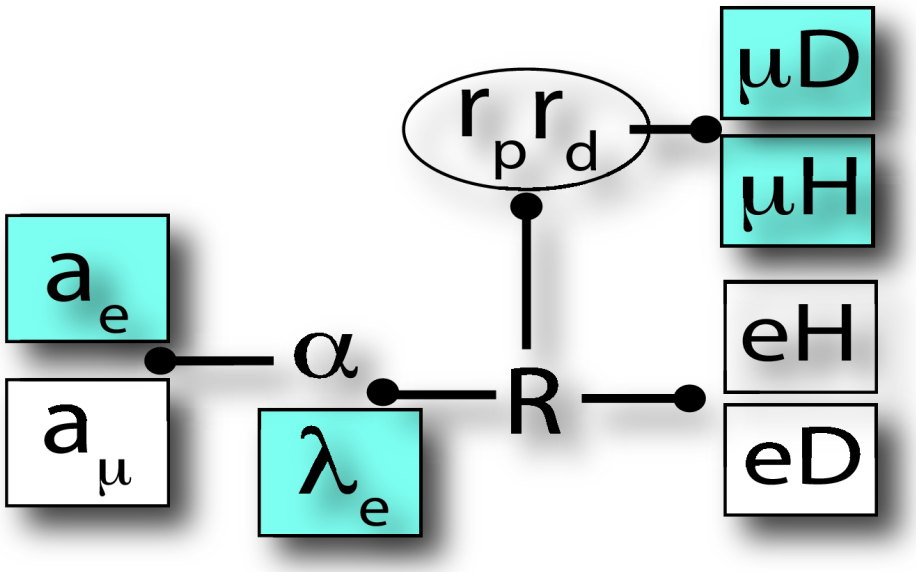

Figure 1.1: Schematic of the dependencies between experimental data and the fundamental physical constants of the Rydberg sector.

from muonic hydrogen spectroscopy, a discrepancy referred to as the proton size puzzle. The value of α determined from the measurement of the electron anomalous moment, when plugged into the muon anomalous moment's theory, gives a $3-4\sigma$ discrepancy [2] between the theoretical and experimental values of the muon anomalous moment, a discrepancy referred to as the muon $g-2$ anomaly. The value of α determined from the definition of $\lambda_e = \alpha^2/2R_\infty$, with λ_e fixed by atomic interferometry experiments and R_∞ fixed by electronic hydrogen and deuterium spectroscopy experiments, differs by 2.4σ from the value of α determined from the electron anomalous moment [3].

These tensions are not dispositive of an inconsistency in QED theory or the existence of new physics beyond the Standard Model, though both eventualities are possible. What they do demonstrate conclusively is the need for a global, viz. self-consistent, determination of the fundamental constants. Piecemeal determinations are inappropriate in the current era of high-precision experiments, and have led to

the piecemeal inconsistencies above.

Ironically these piecemeal inconsistencies have entered the literature stream as a consequence of a putatively global determination of the fundamental constants.

3 The CODATA adjustments

The Committee on Data for Science and Technology (CODATA) was established in 1966 as an interdisciplinary committee of the International Council for Scientific Unions. The task group on fundamental constants was created in 1969 to provide a self-consistent set of recommended values for the fundamental physical constants, including those of the Rydberg sector. CODATA has since periodically published [14, 15, 16, 17, 18, 19, 5, 20] recommended values for the fundamental constants, most recently in 2016.

The CODATA recommended values for the fundamental constants are determined via an elaborate least-squares fit that assumes QED (and weak) theory is *exact*. The 2010 CODATA adjustment (C10)[4] [5] states: "our main purpose here is not to test physical theory critically but to obtain 'best' values of the fundamental constants." Standardization is the aim, specifically, standardized values for the fundamental constants with the smallest possible error bars. When a discrepant experimental datum would degrade the precision of one or more of the fundamental constants, CODATA has historically omitted the discrepant datum from the fit. To limit the size of the error bars on R_∞, the 2010 and 2014 CODATA adjustments omitted muonic charge radius data. Similarly, to limit the size of the error bars on α, the 2006, 2010, and 2014 CODATA adjustments omitted the measurement [2] of the muon anomalous magnetic moment.[5]

Savely Karshenboim, a theorist and member of the CODATA fundamental con-

[4]The 2010 CODATA adjustment used the most precise data available on December 31, 2010 and was published in 2012.

[5]Muonic charge radius data was not available prior to the 2010 adjustment. The muon anomalous magnetic moment measurement was not available prior to the 2006 adjustment.

stants task group, notes [21],"The SI system has been created for legal use and trade rather than for scientific applications. We [physicists] do not care about actual SI definitions because we do not consider seriously the legal side of SI." Physicists wanting to test fundamental QED theory, however, no longer have the luxury of neglecting the legal side of SI. In the current era of high-precision experiments, tests of fundamental QED theory are sensitive to the "legal" procedures used to determine the fundamental constants and their uncertainties.

Consider Adjustment 3 of Table XXXVII of C10, which furnishes the C10 recommended values for the fundamental constants. Adjustment 3 has 149 input data and 82 adjustable constants. Table XVIII of C10 lists the 50 principal input data that go into the determination of the C10 recommended value for the Rydberg constant. Of these 50 input data, 25 are experimental data. The other 25 are initial values for additive corrections to theoretical frequency predictions. The additive corrections parameterize systematic uncertainties associated with the theory.[6] These 50 input data determine 28 adjustable constants: r_p, r_d, R_∞, and 25 additive corrections. (A recommended value for α is determined in a separate sector of the Adjustment 3 fit.) The reason fitting 28 adjusted constants to 25 experimental data does not result in a perfect fit is discussed in Sec. 1.

The C10 recommended values are self-consistent *given the inputs to Adjustment 3*. The Adjustment 3 inputs include electronic hydrogen spectroscopy data but omit muonic hydrogen spectroscopy data and include the electron anomalous magnetic moment measurement but omit the muon anomalous magnetic moment measurement. Adjustment 3 is thus a *piecemeal* fit. The C10 recommended value for r_p is the value of r_p determined from electronic hydrogen. A separate value for r_p can be determined from muonic hydrogen. Likewise, the recommended value for α is the value of α determined from the electron anomalous moment. A separate value for

[6]The additive corrections are nominally associated with theoretical uncertainties but ultimately cannot be disambiguated from possible systematic experimental uncertainties added to the experimental frequency measurements.

α can be determined from the muon anomalous moment.

The C14 recommended values for r_p and α, which go into the current definition of the muon experimental anomalies, were determined on the basis of only three of the boxed sectors of Fig. 1.1: eH, eD, and a_e. One can ask whether the muon anomalies would persist if r_p and α were determined via a global fit procedure that included all the boxed sectors of Fig. 1.1.

Also not clear is whether the muon experimental anomalies are even related to muons. Consider first the proton size puzzle. r_p appears at leading order in the perturbation theory for the muonic hydrogen energy levels and at next-to-next-to leading order in the perturbation theory for the electronic hydrogen energy levels (see Sec. 6.1). Consequently the value of r_p determined from electronic hydrogen data is less precise than the value determined from muonic hydrogen data, and also enormously more sensitive to small effects from higher-order corrections and possible new physics. This line of argument suggests, with appropriate hedging on all sides, the proton size puzzle may have its origins in the electronic hydrogen sector.

The muon $g-2$ anomaly can be similarly deconstructed. The most precise measurement of the electron anomalous magnetic moment is due to Gabrielse [22]. Matching this measurement to the 10th-order (in e) perturbative calculation of Kinoshita [23] yields a determination of α that is a full order of magnitude better than the second-most precise determination of α available to C14, which is due to Bouchendira [24].[7] The C14 determination of α, which includes the measurements of Refs. [22] and [24], is nevertheless dominated by the more precise Ref. [22] datum. The result is: the C14 determination of α effectively fits one parameter to one data point and does not meaningfully test QED theory. If, as happened in 2007 [25], an error or errors were found in the electron anomalous moment calculation of Kinoshita, the value of α would be shifted in the next CODATA adjustment, possibly dramatically, if the error were large enough. The correction of the 2007

[7] A recent determination of α by Parker [3], using an atomic interferometry technique similar to that of Bouchendira, has precision comparable to the Gabrielse determination. See Sec. 1.

error, for instance, shifted α by 6.5σ [5]. Thus, though perhaps not likely, an undiscovered error relating to the theoretical or experimental value of the electron anomalous magnetic moment could be responsible for the muon $g-2$ anomaly. The time-evolution of the CODATA recommmended values for α is shown in Fig. 1.2.

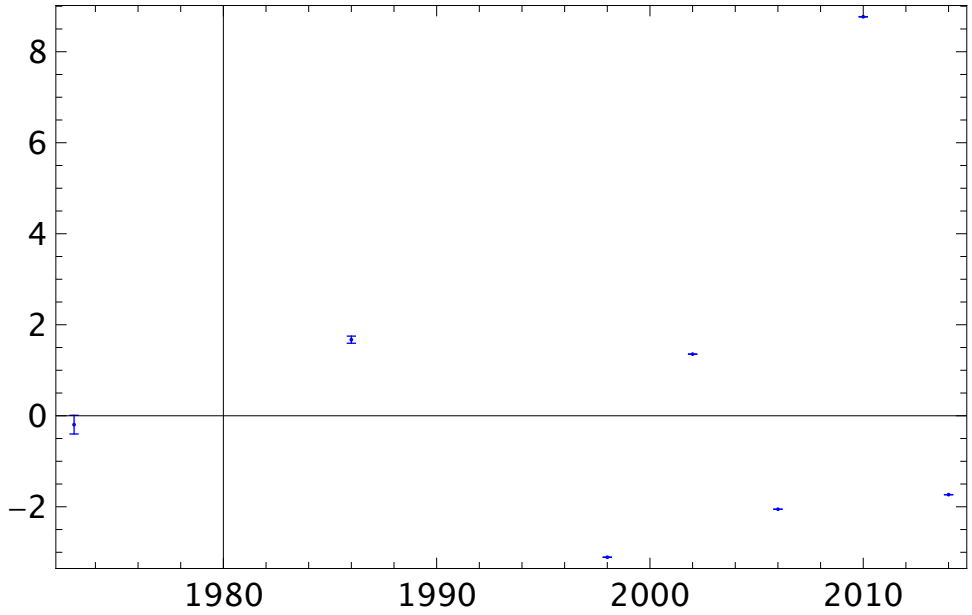

Figure 1.2: Time-dependence of determinations of the fine-structure constant [1]. For each jth determination in the year shown, the y-axis shows the subsequent difference $(\alpha_{j+1} - \alpha_j)/\bar{\Delta}\alpha_j$, where the reported uncertainties are σ_j, with the average $\bar{\Delta}a_j = (\sigma_{\alpha j} + \sigma_{\alpha j+1})/2$. Error bars are $10^3\bar{\Delta}\alpha_j$.

We maintain a global approach to fitting the fundamental constants, compassing all relevant data and all relevant theory, is necessary in any of the following circumstances: 1) when determining how robust a precision QED experimental anomaly is; 2) when attempting to isolate the cause of an anomaly; or 3) when proposing a solution to an anomaly that involves a modification of existing theory.

This last point is important and largely ignored in the literature, whether out of practicality or carelessness. Take the muon $g-2$ anomaly as an example. Adding a new particle that, for simplicity, couples only to muons gives a contribution Δa_μ to the muon anomalous magnetic moment via the QED vertex correction diagram, with the photon in the loop replaced by the new particle; see Fig. 6.1. The temptation

is to tune the mass and coupling of the new particle to account for the discrepancy between a_μ(experiment) and a_μ(theory) and be done.[8] The issue is the value of α used to determine the value of a_μ(theory) was determined without accounting for the effects of the new particle. Accounting for the effects of the new particle will in general shift the value of α, and self-consistency requires (re-)determining α *with the new physics included in the fit.* Testing QED entails testing alternatives to QED, and testing alternatives to QED *self-consistently* entails performing bespoke global fits to world data that include the proposed theory alternative in the fit.

We reiterate: CODATA serves a vital need in providing values for the fundamental constants for legal use and trade. However that need is at odds with the equally vital need to test QED theory. A separate program is needed to test QED theory. The Particle Data Group (PDG) publishes values for the fundamental constants in an annual review, which is year in and year out the top-cited reference in high-energy physics. The PDG has a manifestly scientific (rather than legal) bent. For example a recent annual review [26] cites 22 limits on the photon mass from 22 sources spanning 40 years. However culling globally self-consistent values for the fundamental constants, which include the effects of any relevant theory alternatives, from the PDG reviews is not possible.

The situation is problematic. Phenomenologists currently assess a theory alternative, putatively solving one or the other of the muon experimental anomalies, on the basis of values of r_p and α coming out of an inconsistent, piecemeal fit procedure that omits both muon experimental data and the effects of the theory alternative. In other words, electron, muon, and beyond-Standard-Model theory are being assessed using values for the fundamental constants determined from electron data and Standard Model theory alone. We have created a website called `CONSTANT FINDER` (`www.www.constantfinder.org/home.jsp`) to remedy the situation. `CONSTANT FINDER` enables users to fit the fundamental constants according

[8] Any exclusion limits relevant to the proposed new particle should also be considered.

to their own assumptions. Users have control over all aspects of the fit via an intuitive interface, including the method of fitting, the input data, the experimental and theoretical uncertainties, and any theory alternatives. The site makes self-consistent likelihood-ratio tests between the Standard Model and an arbitrary theory alternative possible. `CONSTANT FINDER` is discussed in Ch. 7.

4 Scheme dependence

We put a name to the dependence of the fundamental constants on the experiments and theory used to define them, namely, *scheme dependence*.[9] To belabor the point, a given fit to the fundamental constants can be optimized for the purpose of standardization or for the purpose of testing the underlying theory. It can include this datum and omit that datum or include that datum and omit this datum. It can countentance this new-physics scenario or that new-physics scenario or no new-physics scenario at all, and on and on. The fitted values of the fundamental constants depend sensitively— pathologically, sometimes— on the procedural conventions used to make the fit. We emphasize: a scheme is appropriate or inappropriate according to context. To specify the scheme for a fit is to specify the Bayesian priors for that fit.

A well-defined scheme specifies the following:

- the method of fitting,
- the input data,
- the underlying theory, and
- values for experimental and theoretical uncertainties.

There is no consistent convention in the literature for how to report, and how much to report about, the scheme dependence of a fit. We suggest a minimum standard is

[9]Scheme dependence as defined here is distinct from the scheme dependence of quantum field theory, associated with renormalizing ultraviolet divergences.

that the fit be reproducible by an interested reader, which is wholly different from reporting how a fitted parameter gets 'renormalized' under a change of scheme.

Notably: CODATA does report some information on the scheme dependence of its fits. Table XIX of C14 lists the values of r_p and R_∞ determined on the basis of different sets of input data. For example Adjustment 3 omits muonic hydrogen, finding $r_p = 0.8751(61)$ fm, while Adjustment 11, otherwise identical to Adjustment 3, includes muonic hydrogen, finding $r_p = 0.84100(39)$ fm. C14 reports a comparatively low probability of chi-squared for Adjustment 11, with the adjustment yielding 72.8 units of chi-squared for 55 degrees of freedom, corresponding to a probability of 0.0054 by Wilks' Theorem. The corresponding Birge ratio[10] of 1.15, reported in C14 without errors, is indicative of underfitting. Adjustment 11 suggests the muonic hydrogen data is inconsistent with the electronic hydrogen data.

However the Table XIX adjustments, taken together, account for only part of the total scheme dependence implicit in the C14 fit procedure, the part relating to the selection of data, and even that part not in full. We substantively reproduced Adjustment 11 in Ch. 7 and arrived at a starkly different conclusion, finding the proton size puzzle can be solved by a global fit, like Adjustment 11, that includes all relevant data. One scheme, Adjustment 3, creates the puzzle. Another scheme, Adjustment 11, affirms it. And a third scheme, which is a reasonable facsimile of Adjustment 11, solves it. Where is the truth? Is it behind door number one? door number three? Whatever the case, the discrepancy defining the proton size puzzle is not robust against the choice of scheme. The lack of robustness of the proton size puzzle is discussed in Ch. 7.

`CONSTANT FINDER` was created out of a recognition of the need for phenomenologists to be able to raise and address questions like these. This point is separate from the point— also central to our program— that self-consistent Rydberg-sector phenomenology *requires* re-fitting the fundamental constants subject to any proposed

[10]The Birge ratio $R_B = \sqrt{\chi^2/\nu}$, where $\nu :=$ degrees of freedom.

theory alternatives.

Our analyses, which can be reproduced using `CONSTANT FINDER`, have led to a variety of interesting results.

- The proton size puzzle is an artifact of a piecemeal determination of the fundamental constants. A global fit to all relevant data solves the proton size puzzle.

- The same global fit that solves the proton size puzzle also shifts the best-fit value for the Rydberg constant by 4.6σ relative to the C14 recommended value.

- The new-physics parameter values that solve the muon $g-2$ anomaly differ depending on whether the fundamental constants are fixed at CODATA reference values or allowed to float to best-fit values along with the new-physics parameters.

- The recent Parker, et al. [3] determination of the fine-structure constant complicates the analysis. Absent the Parker result, the muon $g-2$ anomaly and the proton size puzzle can be solved simultaneously with a $10-50\ MeV$ boson, without sacrificing lepton universality and while evading current exclusion limits.

- The complications brought about by the Parker result can be overcome. However, the solutions are conditioned on essentially speculative (though well-motivated) assumptions.

The dissertation is organized as follows. Chapter 2 describes the global fit procedure. Chs. 3-6 describe the theory relevant to the global fits, while Chs. 7 and 8 provide global fit results and a `CONSTANT FINDER` user guide, respectively. Ch. 9 contains concluding remarks and functions as a kind of prospectus for the fundamental constants program outlined in this dissertation.

Chapter 2

Global fits to the fundamental constants

1 The method of fitting

`CONSTANT FINDER` determines values for the fundamental constants on the basis of scheme-dependent maximum likelihood fits. Users specify a scheme of their choice, including the type of fit to be made, and `CONSTANT FINDER` makes the fit: see Ch. 7. The fit-types available to users are: chi-squared, chi-squared with pull, chi-squared marginalized over nuisance parameters, and chi-squared with correlations. We derive equations for each of these fit-types below, starting from first principles— although with no attempt at rigor. The goal here, as with `CONSTANT FINDER` generally, is transparency.

1.1 Chi-squared

The frequentist notion of probability is defined with respect to an ensemble of identically-prepared experiments measuring an observable $x \in \mathrm{X}$, where X is a random variable defining the space spanned by x. The ensemble, on normaliza-

tion[1], defines a probability density function (pdf) $f(x)$, with $f(x)$ the single-event probability of observing x.

$f(x|\theta)$ defines a family of pdf's parametric in θ, representing *(probability) models*, where θ is a list of model parameters containing parameters of interest, a, and nuisance parameters, b. Parameters of interest are free parameters of the physical theory— which we identify throughout with the fundamental constants. Nuisance parameters are related to systematic uncertainties. The two model parameter types are discussed in more detail below. $f(x|\theta)$ can be interpreted as the single-event probablity of observing x given fixed values of model parameters θ. The shift from consideration of a pdf $f(x)$ to a pdf $f(x|\theta)$, conditioned on θ, forces a Bayesian perspective on us since the model parameters θ lack a frequentist interpretation.

We extend the single-event probability $f(x|\theta)$ to capture the probability of a dataset D consisting of a set of measurements $\{x_j\}$, $j = 1...n$

$$F(D|\theta) = \prod_j^n f(x_j|\theta). \tag{2.1}$$

We can turn the discussion of probability models on its ear and consider $F(D^*|\theta)$ for fixed $D = D^*$, such that F becomes an explicit function of model parameters θ. $F(D^*|\theta) \equiv \mathcal{L}(\theta)$ defines a likelihood function[2], and $log\mathcal{L}(\theta)$ defines a log-likelihood function.

For datasets containing multiple observables— height and weight, for instance— Eq. 2.1 can be generalized to

$$\mathcal{L}(\theta) = \prod_k \prod_j^{n_k} f(x_{kj}|\theta), \tag{2.2}$$

where x_{kj} denotes the result of the jth measurement of observable k.

For datasets in which each data point corresponds to a distinct observable k, the

[1] $\int_X f(x)dx = 1$

[2] $\mathcal{L}(\theta)$ is not a pdf since $\int d\theta\, \mathcal{L}(\theta) \neq 1$.

likelihood function (Eq. 2.2) takes the simplified form

$$\mathcal{L}(\theta) = \prod_k f(x_k|\theta). \tag{2.3}$$

For concreteness, let us limit the discussion of Eq. 2.3 to the observables $x_k \to x_k^{exp}$ of Table 2.1. Inspection of Table 2.1 shows the x_k^{exp} have symmetric uncertainties σ_k^{exp}, where σ_k^{exp} is conventionally interpreted[3] as defining a one-sigma confidence interval— that is, if x_k^{exp} were measured many, many times, 68% of the values of x_k^{exp} would be within σ_k of the true value μ_k of observable x_k. Accordingly, the distribution of x_k^{exp} can be approximated by a Gaussian

$$f(x_k^{exp}) = exp[-\frac{(x_k^{exp} - \mu_k)^2}{2(\sigma_k^{exp})^2}]. \tag{2.4}$$

The Gaussian normalization has been suppressed here and elsewhere. Equation 2.4 could also have been obtained by application of the Central Limit Theorem. Let x_k^{exp} be the sample average of a large number of measurements n of observable x_k, and let σ_k be the uncertainty in a single measurement of x_k, where σ_k is related to σ_k^{exp} as $\sigma_k/\sqrt{n}$.[4] Then, by the Central Limit Theorem, $\sqrt{n}(x_k^{exp} - \mu_k)$ converges in distribution to $N(0, \sigma_k)$ as $n \to \infty$. We make the statement, relevant for Sec. 2.2, that each x_k^{exp} of Table 2.1 is consistent with a sample average taken over a large number of observations n.

To take $f(x_k^{exp})$ into $f(x_k^{exp}|\theta)$, we can, by fiat, replace μ_k with a model for x_k parameterized in terms of θ, which we denote $x_k^{th}(\theta)$. The replacement $\mu_k \to x_k^{th}(\theta)$ amounts to a hypothesis that the data point x_k^{exp} was drawn from a Gaussian distribution centered at $x_k^{th}(\theta)$. Hypothesis tests, discussed in Sec. 2.4, are a natural

[3]The 'uncertainty' σ_k refers to the combined standard uncertainty of the measurement x_k^{exp}, representing the combined uncertainty due to random and systematic effects. The uncertainty due to random effects is captured by the estimated standard deviation from x_k^{exp}. The uncertainty due to systematic effects is the combined uncertainty due to corrections for systematic effects. NIST has codified a set of best practices relating to standard uncertainties: see [18].

[4]neglecting any uncertainties due to systematic effects

extension of this procedure. A hypothesis test determines the relative truth of two competing hypotheses or, more precisely, the relative likelihood of the data given two competing models.[5]

With the considerations above in mind, we rewrite Eq. 2.3 as

$$\mathcal{L}(\theta) = \prod_k exp[-\frac{(x_k^{exp} - x_k^{th}(\theta))^2}{2(\sigma_k^{exp})^2}] \tag{2.5}$$

for k running over the Table 2.1 data.

Equation 2.5 is frequently recast as a chi-squared function

$$\chi^2(\theta) \equiv -2log\mathcal{L}(\theta) = \sum_k \frac{(x_k^{exp} - x_k^{th}(\theta))^2}{(\sigma_k^{exp})^2}. \tag{2.6}$$

When Eq. 2.5 applies, minimizing chi-squared is equivalent to maximizing the likelihood.

1.2 Chi-squared with pull

Maximizing the likelihood function can be interpreted one of two ways: as finding the values for the model parameters that maximize the probability of the data given the model; or as finding the values for the model parameters that maximize the probability of the model given the data. The latter perspective is the more natural one in view of our aim: we want best values for the fundamental constants given the data. This perspective implicitly makes use of Bayes' Theorem

$$P(\theta|x) = \frac{P(x|\theta)P(\theta)}{P(x)} \qquad \text{(Bayes' Thm.)}, \tag{2.7}$$

where $P(\theta|x)$ is the posterior probability, $P(x|\theta)$ is the likelihood function, $P(\theta)$ is the prior probability, and $P(x)$ is the evidence, which functions as an overall normalization.

[5]Bayes' Theorem provides a means of determining the relative likelihood of two competing models *given the data*. See Sec. 1.2.

Interpreting the likelihood function of Eq. 2.2 as the likelihood of the model given the data is equivalent to inserting the likelihood function into Eq. 2.7 with a uniform prior ($P(\theta) = 1$). We can generalize Eq. 2.2 to allow for non-uniform priors

$$\mathcal{L}(\theta = a, b) = \prod_k f(x_k|a, b)\eta(b). \tag{2.8}$$

Despite the misleading label $\mathcal{L}$, $\mathcal{L}(a, b)$ can be interpreted only as a posterior probability. The prior $\eta(b)$ quantifies the degree of belief in the model. The values of the nuisance parameters b are pegged to systematic uncertainties associated with x_k. If the systematic uncertainties are systematic *experimental* uncertainties, Eq. 2.8 has a frequentist, in addition to the more obvious Bayesian, interpretation since $\eta(b)$ can be defined in a frequentist way— which is to say, on the basis of relative freqencies determined from an ensemble of experiments. However if the systematic uncertainties are *theoretical* uncertainties, Eq. 2.8 is expressly and exclusively Bayesian since $\eta(b)$ has no possible frequentist definition.

The chi-squared function defined from Eq. 2.8 is

$$\chi^2(a, b) = -2log\mathcal{L}(a, b) = \sum_k \frac{(x_k^{exp} - x_k^{th}(a) - b_k)^2}{(\sigma_k^{exp})^2} + \frac{b_k^2}{\Delta_k^2}, \tag{2.9}$$

which is referred to as *chi-squared with pull*. Equation 2.9 restricts the form of $\eta(b)$ such that $\eta(b) = exp[-\frac{b_k^2}{2\Delta_k^2}]$, up to an overall normalization. Δ_k represents an estimate of the theoretical or systematic experimental uncertainty of x_k, and the b_k are assumed to be Gaussian-distributed with mean zero and variance Δ_k^2.

Equation 2.9 explains how a fit containing more fitted parameters than data points could result in something other than a trivial fit. A fit to Eq. 2.9 is trivial when the number of parameters of interest a exceeds the number of data points and non-trivial otherwise, irrespective of the number of nuisance parameters in the fit. The exception to this rule is for $\Delta_k \to \infty$, in which case nuisance parameter b_k should be counted as a parameter of interest.

1.3 Chi-squared marginalized over nuisance parameters

Marginalization of Eq. 2.9 over the nuisance parameters takes chi-squared into a particularly simple form

$$\chi^2(a) = \int db\, \chi^2(a,b) = \sum_k \frac{(x_k^{exp} - x_k^{th}(a))^2}{(\sigma_k^{exp})^2 + \Delta_k^2}, \tag{2.10}$$

in which the experimental and theoretical uncertainties for a given datum are added in quadrature. Equation 2.10 is due to Cousins and Highland [27] and often referred to as a *Bayesian-averaged* model.

1.4 Chi-squared with correlations

Equations 2.6-2.10 do not account for correlations between the data points x_k^{exp}.[6] Chi-squared, including the effects of correlations between data points, is given by

$$\chi^2(a) = (x_k^{exp} - x_k^{th}(a)) C^{-1}_{kk'} (x_{k'}^{exp} - x_{k'}^{th}(a)), \tag{2.11}$$

where repeated indices are summed over. The matrix C^{-1} is the inverse covariance matrix, which is related to the correlation matrix c as

$$C^{-1}_{kk'} = \frac{c_{kk'}}{\sigma_k^{exp} \cdot \sigma_{k'}^{exp}}. \tag{2.12}$$

$c_{kk'}$ represents the correlation between data points x_k^{exp} and $x_{k'}^{exp}$. Equation 2.11 reduces to Eq. 2.6 when C^{-1} is diagonal. The definitions of Eqs. 2.9 and 2.10 can be similarly extended to include the effects of non-trivial correlations. The default correlations used by `CONSTANT FINDER` *when fit-type "chi-squared with correlations" is selected* are given in Table $XVII$ of C14.

[6] Data points of the same k but differing j are in principle uncorrelated, having ostensibly been pulled at random from the same underlying distribution.

2 The global fit procedure

With the fit-types defined as above, the task remaining is to estimate the model parameters θ. We denote estimates of model parameters with a circumflex ($\hat{\theta}$) to distinguish them from the true values of the model parameters, written without a circumflex. An estimate of a model parameter— also called an *estimator*— has properties of bias, variance, consistency, and robustness, with the properties of bias and variance closely linked. We discuss these properties below in the context of estimators and then maximum likelihood estimators (since the estimators θ appearing in the chi-squared functions of Sec. 1.1 are maximum likelihood estimators). Again, transparency is the goal.

2.1 Properties of estimators

Bias and variance

The bias of an estimator is defined as the difference between the expected value of the estimator $\hat{\theta}_j$ and the true value of the parameter θ_j

$$B(\hat{\theta}_j) = E[\hat{\theta}_j] - \theta_j, \tag{2.13}$$

where the expected value $E[\hat{\theta}_j] = \int dx\, \hat{\theta}_j(x) f(x)$. Non-zero bias, when it exists, results from the simplifying assumptions of the model.

The variance of an estimator measures the spread of the estimates from one data sample to another

$$var(\hat{\theta}_j) = E[(\hat{\theta}_j - E[\hat{\theta}_j])^2] = E[\hat{\theta}_j^2] - E[\hat{\theta}_j]^2. \tag{2.14}$$

Bias relates to the accuracy of an estimate; variance, to its precision. In principle, we want to minimize both bias and variance. However there is a well-known tradeoff between the two, which can be seen from the mean squared error between θ_j and

$\hat{\theta}_j$:

$$mse(\hat{\theta}_j) = E[(\theta_j - \hat{\theta}_j)^2] = B(\hat{\theta}_j)^2 + var(\hat{\theta}_j). \tag{2.15}$$

The first equality is a definition, while the second equality hides half a page of algebra. For fixed $mse(\hat{\theta}_j)$, the second equality makes the bias-variance tradeoff apparent. For an unbiased estimator, Eq. 2.15 reduces to $mse(\hat{\theta}_j) = var(\hat{\theta}_j)$.

The Cramer-Rao bound places a bound on the minimum variance of an unbiased estimator. An unbiased estimator is not guaranteed to achieve the Cramer-Rao bound. However, when it does, it is called *efficient*. Efficient estimators are always unbiased.

We derive the Cramer-Rao bound below for a one-dimensional ('scalar') estimator θ and then generalize it to multi-dimensional θ.

The derivation is as follows. An unbiased estimator has

$$E[\hat{\theta}(x) - \theta] = \int dx\, (\hat{\theta}(x) - \theta) f(x|\theta) = 0, \tag{2.16}$$

with $f(x|\theta)$ a likelihood function.

Differentiating Eq. 2.16 with respect to θ gives

$$\begin{aligned} 0 = \frac{\partial}{\partial\theta} \int (\hat{\theta}(x) - \theta) f(x|\theta)\, dx &= \int dx\, (\hat{\theta}(x) - \theta) \frac{\partial f(x|\theta)}{\partial\theta}\, dx - \int f(x|\theta)\, dx \\ &= \int (\hat{\theta}(x) - \theta) f(x|\theta) \frac{\partial \log f(x|\theta)}{\partial\theta}\, dx - 1, \end{aligned} \tag{2.17}$$

where on the second line we have used $\frac{\partial \log f(x|\theta)}{\partial\theta} = \frac{1}{f(x|\theta)} \frac{\partial f(x|\theta)}{\partial\theta}$ and $\int dx\, f(x) = 1$.

Applying the Cauchy-Schwarz inequality[7] to Eq. 2.17 finds

$$\begin{aligned} 1 &= \{ \int dx\, [(\hat{\theta}(x) - \theta)\sqrt{f(x|\theta)}] \cdot [\sqrt{f(x|\theta)} \frac{\partial \log f(x|\theta)}{\partial \theta}] \}^2 \\ &\leq [\int dx\, (\hat{\theta}(x) - \theta)^2 f(x|\theta)] \cdot [\int dx\, f(x|\theta) (\frac{\partial \log f(x|\theta)}{\partial \theta})^2] \\ &\equiv var(\hat{\theta}) \cdot I(\theta), \end{aligned} \tag{2.18}$$

where on the third line we have defined the quantity $I(\theta) \equiv E[(\partial \log f(x|\theta)/\partial\theta)^2] = -E[\partial^2 \log f(x|\theta)/\partial\theta^2]$, known as the *Fisher information*, and used the fact that for an unbiased estimator $mse(\hat{\theta}) = var(\hat{\theta})$.

Equation 2.18 gives the Cramer-Rao bound for an unbiased scalar estimator

$$var(\hat{\theta}) \geq I(\theta)^{-1}. \tag{2.19}$$

The generalization of the Cramer-Rao bound to a multi-dimensional collection of unbiased estimators is

$$cov(\hat{\theta}_i, \hat{\theta}_j) \geq I_{ij}(\theta)^{-1}. \tag{2.20}$$

The single-number variance of Eq. 2.19 has been replaced in Eq. 2.20 by a covariance matrix. Likewise $I(\theta)^{-1}$ has been updated to a square matrix of the same dimension as θ. Equation 2.20 implies the diagonal element $I(\theta)^{-1}_{jj}$ defines the minimum variance of estimator $\hat{\theta}_j$.

The elements of the Fisher information matrix are

$$I_{ij}(\theta) = -E[\frac{\partial^2 \log f(x|\theta)}{\partial\theta_i \partial\theta_j}] \rightarrow I_{ij}(\theta) \approx \frac{1}{2} \frac{\partial^2}{\partial\theta_i \partial\theta_j} \chi^2(\theta). \tag{2.21}$$

To the right of the arrow, we have substituted $-\frac{1}{2}\chi^2(\theta)$ for $\log f(x|\theta)$, pursuant to Eq. 2.6, and removed the expected value, which is in general difficult to compute.

[7] The Cauchy-Schwarz inequality in probability theory is

$$var(X) \cdot var(Y) \geq [cov(X, Y)]^2$$

for random variables X and Y. Insertion of $X = \hat{\theta}(x) - \theta$ and $Y = \partial \log f(x|\theta)/\partial\theta$, with $[cov(X,Y)]^2 = [E[(X - \mu) \cdot (Y - \nu)]]^2 = [E[X \cdot Y]]^2 = 1$, into the expression above gives Eq. 2.18.

Equations 2.20 and 2.21 can be combined to obtain minimum uncertainty estimates for unbiased parameters of interest a :

- Compute the elements of the Fisher information matrix, $I_{ij} \equiv \frac{1}{2}\frac{\partial^2}{\partial a_i \partial a_j}\chi^2(\theta = (a,b))$;
- Evaluate I at the best-fit values for $\theta = (a,b)$;
- Invert I;
- Compute the uncertainty of a_j, $u(a_j) \equiv \sqrt{I^{-1}_{jj}}$.

Consistency

A consistent estimator converges to its true value as the number of data points n goes to infinity— that is, a consistent estimator is unbiased in the limit $n \to \infty$. When a consistent estimator achieves the Cramer-Rao bound in the limit $n \to \infty$, it is called *asymptotically* efficient.

Robustness

As the name suggests, robustness refers to the robustness of an estimator against outliers in the data. The median of a dataset, for example, is considered robust while the mean is not. Quantitative measures of robustness vary: see [28]. Operationally, estimators should also be robust against deviations from the assumptions entering the fit.

2.2 Properties of maximum likelihood estimators

For a given likelihood function (Eq. 2.2), the maximum likelihood occurs at the model parameter values that give the data the largest probability. By applying Bayes' Theorem, we can reinterpret the maximum likelihood as occurring at the model parameter values that give the model the largest probability given the data— assuming a uniform prior. Equation 2.8 extends Eq. 2.2 to general priors and as

such can be interpreted *only* as the likelihood of the model given the data. The model parameter values that maximize the likelihood are referred to as maximum likelihood estimates, while the model parameters themselves are maximum likelihood estimators.[8]

Maximum likelihood estimators (MLE's) are consistent and asymptotically efficient. For finite n, the bias of an MLE is zero up to order $1/\sqrt{n}$.[9] For large enough n, MLE's are effectively unbiased with uncertainties well-approximated by the Fisher information matrix.

Bias and variance, revisited

The reference dataset for `CONSTANT FINDER`, which is shown in Table 2.1, contains 21 experimental data x_k^{exp} corresponding to 21 distinct observables x_k. In the language of MLE's, Table 2.1 consists of $n = 1$ measurement of each of 21 distinct observables. Large values of n are nowhere to be found. However each x_k^{exp} is consistent with—wholly independent of any experimental reality— a sample average over a large number of measurements n of observable x_k. See the discussion below Eq. 2.3. Therefore maximum likelihood fits to Table 2.1 data should be reliable, provided the maximum likelihood estimators (viz. the fundamental constants) are consistently defined across all 21 terms of chi-squared.

The procedural decision to fit the 21 experimental data of Table 2.1 via a maximum likelihood fit was initially made in order to reproduce the least-squares adjustments of CODATA. From a purely Bayesian perspective, the procedure represents a set of prior assumptions and needs no justification.

The procedure is:

[8] The estimates obtained from Eq. 2.8 are technically *maximum a posteriori* (MAP) estimates, not maximum likelihood (ML) estimates. The important distinctions between ML estimates and MAP estimates have already been made in the text. Further distinctions are largely semantic.

[9] With a second-order bias correction, the bias of an MLE is zero up to order $1/n$. The second-order bias of a scalar MLE can be obtained by expanding $\mathcal{L}'(\hat{\theta}) = 0$ to second-order in $(\hat{\theta} - \theta)$:

$$\mathcal{L}'(\theta) + (\hat{\theta} - \theta)\mathcal{L}''(\theta) + 1/2(\hat{\theta} - \theta)^2\mathcal{L}'''(\theta) = 0.$$

- Minimize a chi-squared function to obtain best-fit values for the fundamental constants;
- Then compute the inverse Fisher information matrix to obtain uncertainties for the fundamental constants.

Robustness, revisited

As discussed in Sec. 2.1, estimators should be robust against deviations from the assumptions entering the fit. One of the assumptions of primary concern to us in the context of the fits of Ch. 7, is that the errors between x_k^{exp} and $x_k^{th}(\theta)$ are normally distributed with mean zero, else the mapping $-2log\mathcal{L} \rightarrow \chi^2$ is inappropriate.

For instance, theoretical uncertainties not accounted for in the Ch. 7 fits, of comparable size to or larger than the corresponding experimental uncertainties, could lead to estimators lacking robustness. The $1S2S$ transition in electronic hydrogen, which has an experimental uncertainty of 10 Hz with a theoretical uncertainty of order 10^3 times larger, is an extreme example of mismatched theoretical and experimental uncertainties leading to estimators lacking robustness. The effect of the $1S2S$ transition on fits to the fundamental constants is discussed in App. B. Adding nuisance parameters to the fit is an obvious workaround, and the one employed by CODATA. We opt against adding nuisance parameters to the Ch. 7 fits for reasons discussed in Sec. 3 and simply exclude the $1S2S$ from the Ch. 7 fits.

2.3 Chi-squared minimization with FindMinimum

`CONSTANT FINDER` uses the Mathematica function FindMinimum to minimize the chi-squared functions of Sec. 1.1. FindMinimum defaults to the Levenberg-Marquardt method when the function to be minimized is a sum of squares:

$$S(\vec{\theta}) = \sum_j (y_j - f_j(\vec{\theta}))^2. \tag{2.22}$$

Here $\vec{\theta}$ can be regarded as consisting of the fundamental constants plus any nuisance parameters.

The Levenberg-Marquardt method is as follows.

- An initial guess is made for $\vec{\theta}$. `CONSTANT FINDER` fixes the initial values for the fundamental constants at C14 reference values and the initial values for nuisance parameters at zero.
- A step $\vec{\delta}$ is determined according to the Levenberg-Marquardt method such that $\vec{\theta} \to \vec{\theta} + \vec{\delta}$.
- $\vec{\theta}$ is updated until $|\vec{\delta}|$ falls below a predefined threshold.

The minimum value of $S(\vec{\theta})$ obtained in this way is a local minimum and thus sensitive to the initial guess for $\vec{\theta}$. False minima however are not a concern when fitting the fundamental constants provided the initial guess assigned to the fundamental constants is not unreasonable— within a handful of sigma, say, of the C14 reference values.

In the procedure above the steps $\vec{\delta}$ are determined by iteratively computing

$$\frac{\partial S(\vec{\theta} + \vec{\delta})}{\partial \vec{\delta}} = 0, \tag{2.23}$$

where $f_j(\vec{\theta} + \vec{\delta})$ is approximated within $\vec{S}(\vec{\theta} + \vec{\delta})$ as $f_j(\vec{\theta}) + \frac{\partial f_j(\vec{\theta})}{\partial \vec{\theta}} \cdot \vec{\delta} \equiv f_j(\vec{\theta}) + \vec{J}_j \cdot \vec{\delta}$. Upon differentiation, Eq. 2.23 becomes

$$(J^T J)\vec{\delta} = J^T(\vec{y} - \vec{f}(\vec{\theta})), \tag{2.24}$$

where J is a matrix whose ith row corresponds to $\vec{J}_i$. Likewise $\vec{y}$ and $\vec{f}(\vec{\theta})$ are column vectors whose ith rows correspond to y_i and $f_i(\vec{\theta})$, respectively. Equation 2.24 can be solved for $\vec{\delta}$. However the Levenberg-Marquardt method adds a so-called

damping term to Eq. 2.24

$$(J^T J + \lambda I)\vec{\delta} = J^T(\vec{y} - \vec{f}(\vec{\theta})). \tag{2.25}$$

where I is the identity and λ is a non-negative damping factor. The value of the damping factor is adjusted at each step to control the rate of convergence of the fit. When λ is large, $\vec{\delta}$ is roughly in the direction of the gradient and the step-wise decrease in $S(\vec{\theta})$ is also large.

Anecdotally, FindMinimum performs as well as MINUIT [29] and in one case, unrelated to fitting the fundamental constants, outperformed it, when MINUIT got hung up on a local minimum.

2.4 Hypothesis tests

The viability of a given alternative is formulated in terms of a hypothesis test, where one scheme, $Scheme-1$, is compared to a second scheme, $Scheme-2$. $Scheme-1$ represents the null hypothesis, which for our purposes is the Standard Model. $Scheme-2$ represents the Standard Model plus a theory alternative. The statment that an alternative is viable is equivalent to the statement— which we will make more precise— that the data are incompatible with the null.

We start with the notion of a test statistic t which maps a dataset $\mathcal{D}$ into the real line. We want a test statistic that allows us to reject $Scheme-1$ (i.e. the null) if the probability of $Scheme-1$ to produce data at least as extreme as the data in $\mathcal{D}$ is too low, where "too low" is defined by reference to a parameter α, called the size of the test. The size of the test corresponds to the probability that the null is rejected when the null is true. This type of error is referred to as Type-I error. Type-II error refers to the probability β that the null is accepted when the alternative hypothesis (i.e. $Scheme-2$) is true. The parameter $1-\beta$ is called the power of the test. Formally, the goal is to define the test statistic t in such a way that it maximizes $1-\beta$ for fixed α. For two simple hypotheses— that is, models

without any free parameters— the likelihood ratio does exactly this: it maximizes $1-\beta$ for fixed α. The likelihood ratio is encoded as

$$t = \frac{\mathcal{L}(\mathcal{D}|Scheme-2)}{\mathcal{L}(\mathcal{D}|Scheme-1)} \tag{2.26}$$

and compared to a parameter $k(\alpha)$ defining the boundary of the acceptance region, where $k(\alpha)$ depends on the size of the test. For $t < k(\alpha)$ ($t > k(\alpha)$), we accept (reject) the null. The result, which is due to Neyman and Pearson, is called the Neyman-Pearson lemma [30].

The Neyman-Peason lemma however cannot be extended to models with multiple free parameters. In that case, the likelihood ratio statistic is no longer guaranteed to maximize $1-\beta$ for fixed α. For models with multiple free parameters, the workaround is to work with the distribution of the test statistic t. The general procedure is as follows.

We define a log-likelihood ratio $\tilde{t}$

$$\tilde{t} = -2ln(\frac{\mathcal{L}(\mathcal{D}|\hat{\mu}^{Scheme-1})}{\mathcal{L}(\mathcal{D}|\hat{\mu}^{Scheme-2})}), \tag{2.27}$$

where $\tilde{t}$ updates the test statistic t of Eq. 2.26 and $\hat{\mu}^{Scheme-2}$ contains the maximum-likelihood (ML) estimators of $\hat{\mu}^{Scheme-1}$ plus additional ML estimators parameterizing the alternative to the null. We maximize $\tilde{t}$ using the Mathematica function FindMinimum (see Sec. 2.3) and denote the maximum value of $\tilde{t}$ as $\tilde{t}_0$ and the corresponding ML estimates as $(\hat{\mu}^{Scheme-1})^*$ and $(\hat{\mu}^{Scheme-2})^*$.[10] For $-2ln\mathcal{L}(\mathcal{D}|\hat{\mu}) \to \chi^2$ of Eq. 2.6, $\tilde{t}$ corresponds to the difference in chi-squared between $Scheme-2$ and $Scheme-1$.

According to Wilks' Theorem, under broad conditions, as the sample size (i.e. the number of datasets $\mathcal{D}$) approaches infinity, the distribution of $\tilde{t}$ converges to a chi-squared distribution with $N-M$ degrees of freedom, where $N-M$ is the

[10] The maximum-likelihood estimators common to $\hat{\mu}^{Scheme-1}$ and $\hat{\mu}^{Scheme-2}$ take the same value in $(\hat{\mu}^{Scheme-1})^*$ as in $(\hat{\mu}^{Scheme-2})^*$.

difference in dimensionality between the ML estimators of $Scheme-2$ and $Scheme-1$.

Wilks' Theorem allows us to compute a so-called p-value, where

$$\begin{aligned} p &= \int_{\tilde{t}_0}^{\infty} f(\tilde{t}|(\hat{\mu}^{Scheme-1})^*, (\hat{\mu}^{Scheme-2})^*) d\tilde{t} \\ &= \int_{\tilde{t}_0}^{\infty} \chi^2_{N-M}(\tilde{t}|(\hat{\mu}^{Scheme-1})^*, (\hat{\mu}^{Scheme-2})^*) d\tilde{t}. \end{aligned} \tag{2.28}$$

p defines the probability of drawing a test statistic $\tilde{t}$ larger than $\tilde{t}_0$ from the distribution $f(\tilde{t}|(\hat{\mu}^{Scheme-1})^*, (\hat{\mu}^{Scheme-2})^*)$. p can thus be compared to the size of the test α. For $p < \alpha$, we reject the null $(Scheme - 1)$ in favor of the alternative $(Scheme - 2)$. The conventional, 5σ threshold for discovery corresponds to $\alpha = 2.87 \times 10^{-7}$. ($p < 2.87 \times 10^{-7}$ corresponds to a *very* low Type-I-error probability.) Discovery is a charged term and frankly misleading if applied to the results of the Ch. 7 analyses.

We speak instead of a given alternative being favored over the null at the level of 2σ (5σ) if $p < 0.05$ $(p < 2.87 \times 10^{-7})$. 2σ (i.e. 95%) confidence intervals are a natural extension of this kind of language. For example, take $\hat{\mu}^{Scheme-1}$ to be the set of fundamental constants and $\hat{\mu}^{Scheme-2}$ to be the set of fundamental constants plus two additional parameters $\hat{\xi}_1$ and $\hat{\xi}_2$ used to parameterize scheme two. $\hat{\xi}_1$ and $\hat{\xi}_2$ could be the mass and coupling of a new particle, e.g. Then, we can define by brute force a region in $(\hat{\xi}_1, \hat{\xi}_2)$-space where $p(\hat{\xi}_1, \hat{\xi}_2|(\hat{\mu}^{Scheme-1})^*) < 0.05$, which corresponds to a 2σ confidence interval. Here $((\hat{\mu}^{Scheme-1})^*, \xi_1^*, \xi_2^*)$ are the values of $(\hat{\mu}^{Scheme-1}, \hat{\xi}_1, \hat{\xi}_2)$ that maximize $\tilde{t}$, and p is an explicit function of $\hat{\xi}_1$ and $\hat{\xi}_2$. Nuisance parameters do not present an additional complication. They can be optimized along with$(\hat{\mu}^{Scheme-1}, \hat{\xi}_1, \hat{\xi}_2)$ and lumped in with $(\hat{\mu}^{Scheme-1})^*$ as conditions on p.

3 A reference scheme

The hypothesis testing described above requires a well-specified null hypothesis. As a practical matter, the null is encoded in the analyses of Ch. 7 via a *reference scheme* that is, one, consistent with Standard Model theory, two, includes all relevant data, and, three, is as simple as possible but no simpler. Details are below.

The data used in the reference scheme are shown in Table 2.1 and populate the boxes of Fig. 1.1. The Table 2.1 data, referred to in subsequent chapters as the 'reference set', can be divided into sectors: a spectroscopy sector, a moments sector, and a Compton sector, where the spectroscopy sector can be further subdivided with respect to measurements of eH, eD, μH, and μD transition frequencies and the moments sector with respect to measurements of the electron and muon anomalous moments. Table 2.1 includes the muonic data omitted from the "final adjustment" (Adjustment 3) of C14, which furnishes the current CODATA reference values for the fundamental constants.

The muonic data are: a_μ, the measured value of the muon anomalous magnetic moment; $\Delta E_{LS}(\mu H)$, a measurement of the Lamb shift in muonic hydrogen; and $\Delta E_{LS}(\mu D)$, a measurement of the the Lamb shift in muonic deuterium. The measured value of a_μ was included in the final adjustment of C14. However the theory expression for a_μ was not, because of "concerns about the theory".[11]

Notable omissions from Table 2.1 are the $1S2S$ transition in electronic hydrogen, spectroscopic transitions involving $n = 3$ states, determinations of the fine-structure constant from quantum Hall experiments, determinations of the proton charge radius from electron scattering experiments, and results from muonic helium spectroscopy experiments. The decisions to omit these data are discussed below. The measurement of h/m_{Cs}, due to Parker, et al. [3], is also not included in Table 2.1. However

[11] The concerns relate to the $> 3\sigma$ discrepancy between the experimental and theoretical values of a_μ and disagreement between calculations of $a_\mu^{LO,VP}(had)$ and $a_\mu^{\ell\times\ell}(had)$, where $a_\mu^{LO,VP}(had)$ and $a_\mu^{\ell\times\ell}(had)$ are, respectively, the leading hadronic vacuum polarization and the hadronic light-by-light contributions to a_μ.

its effects on the global fit are explored extensively in Ch. 7.[12] The Parker, et al. experiment is discussed in Sec. 1.

- *The $1S2S$ transition in electronic hydrogen.* Including the $1S2S$ transition in the global fit generates untenable results. Adjustments can be made to the global fit to correct the underlying issue (which is related to a mismatch between experimental and theoretical uncertainties), but once those adjustments are made, there is little to be gained by including the $1S2S$ in the fit. Omitting the $1S2S$ from the reference scheme is a simpler alternative, and our preference. The $1S2S$ is discussed in Appendix B.

- *Transitions involving $n = 3$ states.* Table 4 of Ref. [31] contains theory predictions for 56 electronic hydrogen energy levels. Of the 56 predictions, eleven disagree with experiment at the 2σ level. Ten of those are associated with $n = 3$ or $n = 6$ energy levels. The $n = 3$ and $n = 6$ levels are determined from transition frequency measurements involving $n = 3$ states due to Zhao, et al. [32]. Ref. [31] makes a convincing circumstantial case the Zhao measurements have an uncorrected systematic shift, a conclusion which our own analyses support. Consequently we omit them from the reference scheme.

- *Determinations of the fine-structure constant from quantum Hall experiments.* The determinations of the fine-structure constant from quantum Hall experiments [20] have relative precision $\gtrsim 2\times10^{-8}$, which is not competitive with the relative precision of the determinations of Refs. [22] and [3] ($\lesssim few \times 10^{-10}$).

- *Proton charge radius determinations from electron scattering experiments.* The determinations of the proton charge radius from electron scattering (relative precision $\sim 10^{-2}$) have precision comparable to the proton charge radius determinations from electronic hydrogen spectroscopy (relative precision $\lesssim 10^{-2}$).

[12] The Parker measurement yields a prediction for the value of the fine-structure constant with comparable precision to the most-precise prediction for α, coming out of the measurement of the electron anomalous moment by Gabrielse, et al. The Parker prediction for α differs from the Gabrielse prediction by 2.4σ.

However the charge radius determinations from electron scattering data are sensitive to procedure. According to Ref. [33], variations in procedure can yield charge radius values anywhere from 0.84 to 0.89 fm. A recent preliminary determination of the proton charge radius from electron scattering, due to the PRad collaboration at Jefferson Lab [34], has relative precision comparable to the charge radius measurements from muonic hydrogen spectroscopy. The PRad result is still sensitive to the procedural-dependence noted by Ref. [33], but that sensitivity is largely blunted by the high precision of the experiment. A second electron scattering experiment, due to the A1 collaboration, is underway at MAMI in Mainz [35]. The $A1$ experiment should yield a value for the proton charge radius competitive with those from muonic hydrogen spectroscopy. Additionally, the MUSE (MUon proton Scattering Experiment) collaboration at Paul Scherrer Institute is, as the name of the collaboration suggests, conducting a muon scattering experiment (μ^- on p and μ^+ on $\bar{p}$) [36].

- *Muonic helium spectroscopy measurements.* The CREMA collaboration has successfully measured the $2S2P$ Lamb shift in muonic helium-3 and -4 [37]. However the theory for muonic helium-3 and -4 is still somewhat unsettled. The CREMA collaboration in a final report summary to CORDIS writes, "As the theory is being actively developed, the numbers have become a moving target, but the results seem to be stabilizing now." Ref. [38] gives a review of muonic helium-3 theory; Ref. [39], of muonic-helium-4 theory.

The experimental uncertainties for the Table 2.1 data, which are shown in the third column of the Table, are taken as given in the literature. The theory we choose for our reference scheme is nominally the Standard Model. The spectroscopic theory is defined in C14. The theory for the electron and muon anomalous moments is defined in [23] and [40], respectively. The moments theory is reviewed in Ch. 3; the spectroscopic theory, in Ch. 4.

Experimental datum [units]	Experimental value	σ_{expt}
$\nu_H(2S1/2 - 8S1/2)$ [Hz]	$7.70649350012000 \times 10^{14}$	8600
$\nu_H(2S1/2 - 8D3/2)$ [Hz]	$7.70649504450000 \times 10^{14}$	8300
$\nu_H(2S1/2 - 8D5/2)$ [Hz]	$7.70649561584200 \times 10^{14}$	6400
$\nu_H(2S1/2 - 12D3/2)$ [Hz]	$7.99191710472700 \times 10^{14}$	9400
$\nu_H(2S1/2 - 12D5/2)$ [Hz]	$7.99191727403700 \times 10^{14}$	7000
$\nu_H(2P1/2 - 2S1/2)$ [Hz]	$1.05784500000000 \times 10^{9}$	9000
$\nu_H(2S1/2 - 2P3/2)$ [Hz]	9911200000	12000
$\nu_H(2P1/2 - 2S1/2)$ [Hz]	1057862000	20000
$\nu_D(2S1/2 - 8S1/2)$ [Hz]	$7.708590412457 \times 10^{14}$	6900
$\nu_D(2S1/2 - 8D3/2)$ [Hz]	$7.708591957018 \times 10^{14}$	6300
$\nu_D(2S1/2 - 8D5/2)$ [Hz]	$7.708592528495 \times 10^{14}$	5900
$\nu_D(2S1/2 - 12D3/2)$ [Hz]	$7.99409168038 \times 10^{14}$	8600
$\nu_D(2S1/2 - 12D5/2)$ [Hz]	$7.994091849668 \times 10^{14}$	6800
$\nu_D(2P1/2 - 2S1/2)$ [Hz]	1059280000	60000
$\nu_D(2S1/2 - 2P3/2)$ [Hz]	9912610000	300000
$\nu_D(2P1/2 - 2S1/2)$ [Hz]	1059280000	60000
a_e	0.00115965218072	2.8×10^{-13}
a_μ	0.00116592089	6.3×10^{-10}
$\Delta E_{LS}(\mu H)$ [meV]	202.3706	0.0023
$\Delta E_{LS}(\mu D)$ [meV]	202.8785	20.0034
λ_e [m]$/10^{-12}$	2.4263102367	1.1×10^{-9}

Table 2.1: Experimental data used in the reference scheme defined in the text. Data is from Refs. [6, 7, 8, 9, 2, 10, 11, 20].

The reference scheme is almost completely specified. All that remains is to specify a fit-type. We choose a chi-squared function without correlations or nuisance parameters (Eq. 2.6). The choice has the benefit of allowing us to monitor outputs of the global fit in relation to inputs, and very few drawbacks. For the data and theory of the reference scheme, including correlations in the global fit has a negligible effect. Likewise, adding nuisance parameters to the fit does not substantively change the fit results.[13]

[13]Adding nuisance parameters to the global fit would have been necessary had we included the $1S2S$ in the reference scheme.

Chapter 3

The moments sector

As discussed in Ch. 2, the global fit of Eq. 2.6 is divided notionally into various sectors: a moments sector, which includes measurements of the electron and muon anomalous moments; a spectroscopy sector, which includes measurements of transition frequencies in hydrogenlike atoms; and a Compton sector, which includes measurements of the Compton wavelength of the electron.

The theory relevant to these sectors is reviewed in Chs. 3-6: the moments sector in this chapter, the spectroscopy sector in Ch. 4, the Compton sector in Ch. 5, and new physics contributions to the moments and spectroscopy sectors in Ch. 6. The emphasis throughout is on developing an intuition and an appropriately global framework for the theory entering the Ch. 7 analysis. Leading and next-to-leading results are emphasized. Higher-order results are discussed in the context of theoretical uncertainties, and to give an accounting of the current state of the art. Important experiments are also described and discussed.

1 The magnetic moment and orbital and spin angular momentum

The magnetic moment is well-defined in classical electrodynamics. Consider the vector potential $\vec{A}$ at $\vec{x}$ due to a current distribution spread over a region in 3-space defined pointwise by a set of coordinates $\{\vec{x}'\}$:

$$\vec{A}(\vec{x}) = \frac{\mu_0}{4\pi} \int d\vec{x}' \frac{\vec{J}(\vec{x}')}{|\vec{x} - \vec{x}'|}, \tag{3.1}$$

where $\vec{J}(\vec{x}')$ denotes the current at $\vec{x}'$ and μ_0 is the permeability of free space.[1]

Expanding $1/|\vec{x} - \vec{x}'|$ in powers of $|\vec{x}'|$ in the limit $|\vec{x}| >> |\vec{x}'|$ finds

$$\vec{A}(\vec{x}) = \frac{\mu_0}{4\pi} \int d\vec{x}' \vec{J}(\vec{x}')[\frac{1}{|\vec{x}|} + \frac{\vec{x} \cdot \vec{x}'}{|\vec{x}|^3} + ...]. \tag{3.2}$$

With the help of a vector calculus integral identity, the first term— the monopole term— integrates to zero, while the second term— the dipole term, which we denote $\vec{A}^{dip}$— gives

$$\begin{aligned} \vec{A}^{dip} = \frac{\mu_0}{4\pi} \frac{1}{|\vec{x}|^3} [-\frac{1}{2} \vec{x} \times \int d\vec{x}' (\vec{x}' \times \vec{J}(\vec{x}'))] \\ \equiv \frac{\mu_0}{4\pi} \frac{\vec{m} \times \vec{x}}{|\vec{x}|^3}. \end{aligned} \tag{3.3}$$

Here $\vec{m}$ is the magnetic (dipole) moment, equal to $\frac{1}{2} \int d\vec{x}' (\vec{x}' \times \vec{J}(\vec{x}'))$.

For a current distribution arising from a distribution of charged particles of mass M, charge e, and velocity $\vec{v}_i$, $\vec{m}$ becomes

$$\vec{m} = \frac{1}{2} \sum_i \vec{x}_i \times \vec{v}_i = \frac{e}{2M} \sum_i \vec{L}_i \equiv \frac{e}{2M} \vec{L}, \tag{3.4}$$

where $\vec{L} = \sum_i \vec{L}_i$ is the total orbital angular momentum.

[1] Equation 3.1 is derived in Jackson [41]. The derivation, in outline, is as follows. $\vec{\nabla} \cdot \vec{B} = 0$ implies $\vec{B} = \vec{\nabla} \times \vec{A}$. An expression for $\vec{B}$— $\vec{B} = \frac{\mu_0}{4\pi} \vec{\nabla} \times \int d\vec{x}' \frac{\vec{J}(\vec{x}')}{|\vec{x} - \vec{x}'|}$— can be obtained by consideration of the magnetic induction $d\vec{B}$ due to a current element $Id\vec{\ell}$. Equation 3.1 follows immediately.

An expression for the intrinsic spin magnetic dipole moment can be obtained by replacing $\vec{L}$ with $g\vec{S}$, where $\vec{S}$ corresponds to the intrinsic spin angular momentum and a constant factor g has been inserted in anticipation of future developments.

Both the intinsic spin and orbital magnetic moments appear in the non-relativistic Dirac Hamiltonian $H^{D,NR}$ in the presence of a magnetic field:

$$H^{D,NR} = \frac{\vec{p}^2}{2M} + \frac{e}{2M}\vec{B}\cdot(\vec{L} + g\vec{S}), \tag{3.5}$$

where $\vec{S} = \vec{\sigma}/2$. The meaning of g is apparent in Eq. 3.5. g specifies the coupling strength of $\vec{B}\cdot\vec{S}$ relative to the coupling strength of $\vec{B}\cdot\vec{L}$. A derivation of Eq. 3.5 starting from Eq. 4.3 can be found in Ref. [42].[2] We will return to Eq. 3.5 shortly.

Let us first develop some intuition surrounding the *intrinsic spin* magnetic moment of an electron. We start by writing down the (relativistic) Dirac Hamiltonian for a free electron: $H^D = \vec{\alpha}\cdot\vec{p} + \beta M$, where $\alpha_k = \gamma_0\gamma_k$ and $\beta = \gamma_0$. According to the Heisenberg picture, the equation of motion for the kth component of the electron's position operator $\vec{x}$ is

$$\begin{aligned} \dot{x}_k &= i[H, x_k] \\ &= i[\beta M, x_k] + i[\alpha_j p_j, x_k] \\ &= \alpha_k. \end{aligned} \tag{3.6}$$

Similarly,

$$\dot{\alpha}_k = i[H, \alpha_k] = 2i(p_k - \alpha_k H). \tag{3.7}$$

Integrating the right-hand side of Eq. 3.7 twice with respect to time finds

$$x_k(t) = x_k(0) + p_k H^{-1} t + \frac{i}{2}H^{-1}(\alpha_k(0) - p_k H^{-1})\cdot(e^{-2iHt} - 1). \tag{3.8}$$

Equation 3.8 was obtained assuming p_k and H are time-independent and $\alpha_k(t) =$

[2] The derivation stops short of deriving the term $\sim \vec{B}\cdot\vec{L}$ in Eq. 3.5. That term can be shown to fall out of the term $(\vec{p} + e\vec{A})^2/2M$ of Hitoshi Eq. 50. In particular, in Coulomb gauge ($\vec{\nabla}\cdot\vec{A} = 0$), $(\vec{p} + e\vec{A})^2/2M$ contains a term $e\vec{p}\cdot\vec{A}/M$. For a homogeneous magnetic field in the $\hat{z}$-direction, $\vec{A}$ can be written as $B/2(\hat{z}\times\hat{r})$. Algebra then finds $e\vec{p}\cdot\vec{A}/M = eB\hat{z}\cdot\vec{L}/2M \to e\vec{B}\cdot\vec{L}/2M$.

$e^{iHt}\alpha_k(0)e^{-iHt}$. The important term in Eq. 3.8 for our purposes is the third term, which oscillates with amplitude $\sim \frac{1}{2}H^{-1}\alpha_k(0) \sim \frac{1}{2M} \sim \frac{\lambda_e}{2}$. (We have taken $\alpha_k(0) = c = 1$ for simplicity.) The oscillatory motion is called *zitterbewegung* or 'jitter motion'. The cartoon is of a point electron creating Compton-wavelength-sized current loops as it moves through free space. The parallel with the orbital magnetic moment we derived from classical arguments is obvious. (Note: no forces are acting on the electron. The electron's jitter motion is due to its intrinsic spin, which— at the risk of being too didactic— bears no relation to a spinning beach ball.)

Zitterbewegung is not a classical phenomenon. The electron's jitter motion disappears upon taking the expectation value of x_k between Schrodinger wave functions. The angular frequency of the jitter also has a deep quantum origin. The electron's energy has characteristic angular frequency H, while the jitter has characteristic angular frequency $2H$. A 2π oscillation associated with the electron's energy thus corresponds to a 4π oscillation associated with the electron's jitter. Here we get a glimpse of the physical manifestation of the 4π-periodicity of $SU(2)$. (Note: the spin-1/2 of the electron is responsible for zitterbewegung and not the other way around.)

2 The g-factor and the electron anomalous magnetic moment

Let us finally make the leap into quantum field theory. The Dirac equation in the presence of an electromagnetic field is $(i\not{D} - m)\psi = 0$, where $\not{D} = \gamma_\mu(\partial_\mu + ieA_\mu)$. Multiplying on the left by $(i\not{D} + m)$ finds

$$(\not{D}^2 + m^2)\psi = 0, \tag{3.9}$$

where $\not{D}^2 = D_\mu^2 + F_{\mu\nu}\sigma_{\mu\nu}$ and $\sigma_{\mu\nu} = \frac{i}{2}[\gamma_\mu, \gamma_\nu]$.

Equation 3.9 can be rearranged to yield

$$\frac{(H-eA_0)^2}{2M}\psi = \frac{1}{2M}[(\vec{p}-e\vec{A})^2 + \frac{e}{2}F_{\mu\nu}\sigma_{\mu\nu} + m^2]\psi, \tag{3.10}$$

where $Re[F_{\mu\nu}\sigma_{\mu\nu}] = iF_{ij}[\gamma_i, \gamma_j]$, which reduces to $-2\vec{B}\cdot\sigma = -4\vec{B}\cdot\vec{S}$ in the Weyl basis.

Then, $Re[\frac{e}{4M}F_{\mu\nu}\sigma_{\mu\nu}] = -\frac{e}{M}\vec{B}\cdot\vec{S}$ of Eq. 3.10 can be compared directly to $\frac{ge}{2M}\vec{B}\cdot\vec{S}$ of Eq. 3.5. The Dirac equation thus predicts $g = 2$. As a sidenote, Eq. 3.9 resembles the Klein-Gordon equation for a scalar ϕ, plus a term $\sim F_{\mu\nu}\sigma_{\mu\nu}$, which is proportional to the intrinsic spin magnetic moment of the electron. Here we see once again: the electron's intrinsic spin magnetic moment is a spin-1/2 phenomenon.

If additional terms in the Hamiltonian $\sim F_{\mu\nu}\sigma_{\mu\nu}$ exist, they will necessarily correct the value of g. Loop corrections in perturbation theory provide such terms. These terms can be organized as an expansion in $\Box/M^2$ and lumped into a form factor that gets updated at each order in perturbation theory. That is, the loops take

$$g = 2 \rightarrow g = 2 + 2F_2(\Box/M^2), \tag{3.11}$$

where F_2 is the Pauli form factor.

Let us see how g gets updated more explicitly. The most general possible parity- and gauge-invariant Lorentz structure for the three-point vertex diagram shown in Fig. 3.1 is

$$\Gamma_\mu = F_1(p^2/M^2)\gamma_\mu + F_2(p^2/M^2)\frac{i\sigma_{\mu\nu}}{2M}p_\nu, \tag{3.12}$$

where $p^\mu = q_2^\mu - q_1^\mu$ is the four-momentum of the (off-shell) photon in Fig. 3.1 and F_1 and F_2 are the Dirac and Pauli form factors.

The matrix element for Fig. 3.1 is

$$\begin{aligned} i\mathcal{M} &= i\mathcal{M}_\mu\epsilon_\mu^*; \\ \mathcal{M}_\mu &= ie\bar{u}(q_2)\Gamma_\mu u(q_1). \end{aligned} \tag{3.13}$$

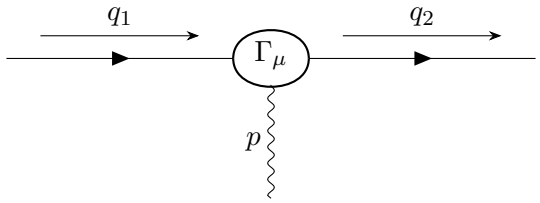

Figure 3.1: Three-point vertex diagram, where Γ_μ (Eq. 3.12) represents the most general possible Lorentz structure.

Application of the Gordon identity[3] to Eq. 3.13 finds

$$i\mathcal{M} = [ie\bar{u}(q_2)(q_1^\mu + q_2^\mu)F_1 u(q_1) + ie\bar{u}(q_2)\frac{i\sigma^{\mu\nu}}{2M}p_\nu(F_1+F_2)u(q_1)]\epsilon_\mu^*. \tag{3.14}$$

With the replacement $\epsilon_\mu^* \to A_\mu$, the second term of Eq. 3.14 becomes

$$\begin{aligned} & ie\bar{u}(q_2)\frac{i\sigma_{\mu\nu}}{2M}p_\nu A_\mu(F_1+F_2)u(q_1) \\ &= -ie\bar{u}(q_2)\frac{\sigma_{\mu\nu}}{4M}2\partial_\nu A_\mu(F_1+F_2)u(q_1) \\ &= \frac{ie}{4M}\bar{u}(q_2)\sigma_{\mu\nu}F_{\mu\nu}(F_1+F_2)u(q_1), \end{aligned} \tag{3.15}$$

where the third line uses $2\partial_\mu A_\nu = F_{\mu\nu} + (\partial_\mu A_\nu + \partial_\nu A_\mu)$ and the anti-symmetry of $\sigma_{\mu\nu}$.

The second term of Eq. 3.14 can be used to determine g. As discussed above, $Re[\frac{e}{4M}F_{\mu\nu}\sigma_{\mu\nu}] = -\frac{e}{M}\vec{B}\cdot\vec{S}$ implies $g = 2$. Likewise, Eqs. 3.14-3.15 allow us to read off $g = 2(F_1+F_2)$. The form factors F_1 and F_2 in the expression for g are evaluated at $p^2 = 0$ by convention. F_1 renormalizes the electric charge by modifying the coupling $e\bar{\psi}\gamma_\mu\psi A_\mu$, with $F_1(0) = 1$ to all orders in perturbation theory. Thus we are left with $g = 2 + 2F_2(0)$, in agreement with Eq. 3.11

At leading order, the Fig. 3.1 amplitude reduces to

$$\begin{aligned} i\mathcal{M} &= ie\bar{u}(q_2)\gamma_\mu u(q_1) \\ &= ie\bar{u}(q_2)[(F_1=1)\cdot\gamma_\mu + (F_2=0)\cdot\frac{i\sigma_{\mu\nu}}{2M}p_\nu]u(q_1). \end{aligned} \tag{3.16}$$

[3] $\bar{u}(q_2)\gamma^\mu u(q_1) = \bar{u}(q_2)(q_1^\mu + q_2^\mu)u(q_1) + \bar{u}(q_2)\frac{i\sigma^{\mu\nu}}{2M}p_\nu u(q_1)$

$F_2 = 0$ implies $g = 2$. The first correction to $g = 2$ occurs at next-to-leading order and shifts g by $\frac{\alpha}{2\pi}$. The next-to-leading-order calculation is substantively carried out in Sec. 1 and amounts to calculating the part of the vertex-correction diagram of Fig. 3.2 proportional to F_2.

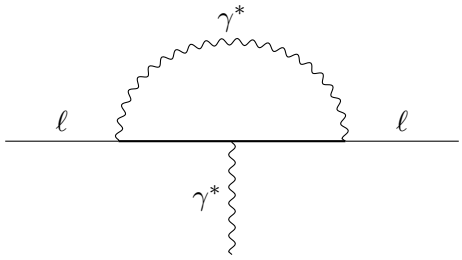

Figure 3.2: Leading contribution to the electron and muon anomalous magnetic moments.

At leading order, the electron interacts directly with the magnetic field. At next-to-leading order, the electron emits a virtual photon and then, off its mass shell, interacts with the magnetic field before reabsorbing the virtual photon.

3 Calculation of the electron anomalous magnetic moment beyond NLO

For many years, Kinoshita, et al. [23] have had and extended on the most complete calculation of the electron anomalous moment, $a_e = (g-2)/2$. The calculation now includes diagrams through 10th order in e. We sketch the basic details of the calculation. The calculation splits $a_e(theory)$ into three parts:

$$a_e(theory) = a_e(QED) + a_e(hadron) + a_e(weak). \tag{3.17}$$

The three parts are defined and discussed below.

α is a free parameter of $a_e(theory)$. Setting α equal to its CODATA recommended value finds

$$a_e(theory) = 1159652182.032(13)(12)(720) \times 10^{-12}, \tag{3.18}$$

where $a_e(QED)$ is of order 10^{-3}, while $a_e(hadron)$ and $a_e(weak)$ are of order 10^{-12}. The third uncertainty in $a_e(theory)$, which is the dominant source of uncertainty, is due to the uncertainty in the value of α. The first and second uncertainties are due to the uncertainties in $a_e(QED)$ and $a_e(hadron)$, respectively. The uncertainty in $a_e(weak)$ is negligible.

$a_e(QED)$ represents the total QED contribution to $a_e(theory)$, where

$$a_e(QED) = A_1 + A_2(m_e/m_\mu) + A_2(m_e/m_\tau) + A_3(m_e/m_\mu, m_e/m_\tau) \tag{3.19}$$

and $A_n = \sum_i (\frac{\alpha}{\pi})^i A_n^{(2i)}$.

The measurement of a_e, due to Gabrielse, et al. [22], which is discussed below, has 0.24 ppt precision. For $a_e(theory)$ to have comparable precision, A_1 must be calculated through $\mathcal{O}[(\frac{\alpha}{\pi})^5]$ since $(\frac{\alpha}{\pi})^5 \sim 0.07 \times 10^{-12}$. The mass dependences of A_2 and A_3 enter through lepton loops.[4] A_2 and A_3 have been calculated [23] through $\mathcal{O}[(\frac{\alpha}{\pi})^4]$ and are tiny compared to A_1 due to the smallness of m_e/m_μ and m_e/m_τ:

$$a_e(QED; mass - dependent) = 2.7475719(13) \times 10^{-12} << \frac{\alpha}{2\pi}. \tag{3.20}$$

$a_e(hadron)$ receives contributions from leading, next-to-leading, and next-to-next-to-leading hadron vacuum polarization (HVP) diagrams, as well as a hadronic light-by-light scattering diagram. The leading HVP diagram is shown in Fig. 3.3. The total contribution due to hadronic interactions is $a_e(hadron) = 1.6927(120) \times 10^{-12}$, with the uncertainty dominated by the leading HVP diagram.

$a_e(weak)$ includes the leading and next-to-leading electroweak contributions to a_e. The leading diagrams are shown in Fig. 3.4. The total contribution due to electroweak interactions is $a_e(weak) = 0.03053(23) \times 10^{-12}$.

[4] Mass *ratios* appear in the expressions for A_2 and A_3 in place of masses for the simple reason a_e is dimensionless.

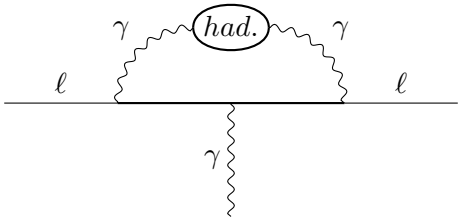

Figure 3.3: Leading hadronic vacuum polarization contribution to the electron and muon anomalous magnetic moments.

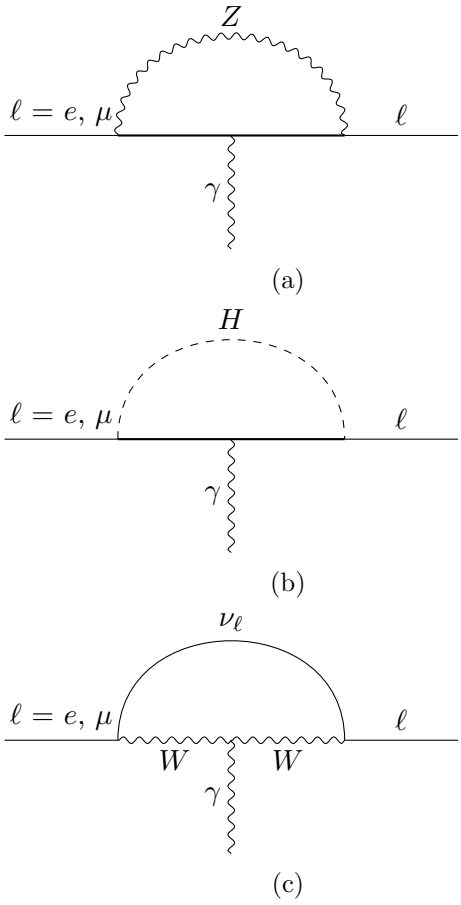

Figure 3.4: Leading electroweak contributions to a_e and a_μ.

4 Measurement of the electron anomalous magnetic moment

The most precise measurement of the electron anomalous magnetic moment a_e is due to Gabrielse, et al. [22]. The experiments, which continue pioneering work by

Dehmelt [43], use Penning traps to isolate a single electron in an electromagnetic cage. A magnetic field in the $\hat{z}$ direction confined the electron to a circular orbit in the $x-y$ plane, while a quadrupole electric field confined the electron in the $\hat{z}$ direction.

The experiments use a radio frequency field to induce particular transitions between the energy levels of the trapped electron. The induced transitions enable measurement of the electron's cyclotron frequency ω_c and a so-called anomaly frequency $\omega_a = \omega_s - \omega_c$, where ω_s is the spin precession frequency of the electron. The electron anomalous magnetic moment a_e is simply the ratio of ω_a to ω_c :

$$\omega_s = \frac{g}{2}\frac{e|\vec{B}|}{m_e}, \quad \omega_c = \frac{e|\vec{B}|}{m_e} \qquad \rightarrow \qquad \frac{\omega_s - \omega_c}{\omega_c} = \frac{g-2}{2} \equiv a_e. \tag{3.21}$$

The expression for ω_c can be obtained by balancing the centripetal and Lorentz forces on an electron in a homogeneous magnetic field. The expression for ω_s can be obtained by solving the Schrodinger equation

$$i\dot{\psi} = H\psi \;\rightarrow\; i\begin{bmatrix}\dot{c}_+ \\ \dot{c}_-\end{bmatrix} = -\frac{ge}{4m_e}B_z\sigma_z\begin{bmatrix}c_+ \\ c_-\end{bmatrix} \tag{3.22}$$

for $c_\pm$ and computing $< S_x >$ and $< S_y >$, where $< S_x >$ and $< S_y >$ can be seen to precess with frequency $\omega_s = \frac{g}{2}\frac{e|\vec{B}|}{m_e}$.

The result of the measurement is

$$a_e(exp) = 1159652180.73(28) \times 10^{-12}. \tag{3.23}$$

Equating $a_e(exp)$ with $a_e(theory)$ of Kinoshita [23], which is an explicit function of the fine-structure constant α, furnishes a value for α^{-1}, namely,

$$\alpha^{-1} = 137.035999084(33)(39). \tag{3.24}$$

The first (second) number in parentheses gives the experimental (theoretical) uncertainty. The value of Eq. 3.24 can be compared to

$$\alpha^{-1} = 137.035999046(27), \tag{3.25}$$

which is the determination of Parker, et al. [3], based on an atomic interferometry experiment discussed in Sec. 1. The two predictions, which only *together* comprise a test of QED, differ by 2.4σ.

4.1 Measurement of the electron anomalous magnetic moment: experimental details

The experimental details of the Gabrielse result are relevant to our program, for reasons that will become clear. We review the experimental details here.

Magnetron motion

We start from the beginning, with an electron in a Penning trap subject to a homogeneous magnetic field and a quadrupole electric field. The classical equations of motion for the electron are

$$\begin{aligned} \ddot{x} - \frac{1}{2}\omega_z^2 x + \omega_c y = 0; \\ \ddot{y} - \frac{1}{2}\omega_z^2 y - \omega_c x = 0; \\ \ddot{z} + \frac{1}{2}\omega_z^2 z = 0. \end{aligned} \tag{3.26}$$

With the substitution $\xi = x + iy$, the first two lines of Eq. 3.26 can be combined into a single equation:

$$\ddot{\xi} - i\omega_c \dot{\xi} - \frac{1}{2}\omega_z^2 \xi = 0, \tag{3.27}$$

which reduces to

$$\omega(\omega - \omega_c) = \frac{1}{2}\omega_z^2 \tag{3.28}$$

for $\xi = e^{i\omega t}$. Solutions to Eq. 3.28 are, by inspection, $\omega = \omega_c'$ and $\omega = \omega_c - \omega_c'$, where ω_c' is the cyclotron frequency after accounting for the effects of the quadrupole electric field and $\omega_c - \omega_c' = \omega_m$ is the frequency of the magnetron motion of the electron.

The electron's motion— neglecting the smearing effects of thermal noise— consists of fast cyclotron motion about a guiding center that is simultaneously precessing in a circular orbit in the $x - y$ plane at magnetron frequency ω_m and oscillating in the $\hat{z}$ direction at axial frequency ω_z. The frequencies are well-separated and ordered such that $\omega_c >> \omega_z >> \omega_m$. However the classical equations of motion are insufficient by themselves; $a_e \neq 0$ is after all a purely quantum effect.

The Schrodinger equation for the trapped electron is

$$[\frac{\pi^2}{2m_e} + U + \frac{1}{2}\omega_c\sigma_z]\psi = E_S\psi, \tag{3.29}$$

where $\vec{\pi} = \vec{p} + e\vec{A}$ is the electron's (kinetic) momentum, U is the electrostatic potential energy associated with the electron having axial frequency ω_z, and E_S is an energy eigenvalue:

$$E_S = m_s\omega_c + (n + 1/2)\omega_c' + (k + 1/2)\omega_z - (q + 1/2)\omega_m, \tag{3.30}$$

where $m_s = \pm 1/2$ and $n, k, q = 0, 1, 2....$ Wave function ψ of Eq. 3.29 is the result of projecting state $|nm_skq>$ onto a basis.

Spin and relativistic effects

The precision of the Gabrielse measurement requires consideration of relativistic effects, which are not captured in Eqs. 3.29-3.30.

The energy eigenvalue associated with the Dirac Hamiltonian for an electron

moving in a plane perpendicular to a magnetic field $\vec{B} = B_z\hat{z}$ is

$$E_D = m_s\omega_a + \sqrt{m_e^2 + 2m_e(n + m_s + 1/2)\omega_c}. \tag{3.31}$$

ω_c falls under the square root, while ω_a does not. Hence the relativistic effects inherent in the Dirac Hamiltonian shift ω_c (and ω_s) but not ω_a.

For non-vanishing axial motion, $E_D \to E'_D$ takes the form

$$E_D \to E'_D = \sqrt{[m_s\omega_a + \sqrt{m_e^2 + 2m_e(n + m_s + 1/2)\omega_c}]^2 + \pi_z^2}. \tag{3.32}$$

ω_a is now under a square root and so receives a relativistic correction. The square roots of Eq. 3.32 have the effect of coupling the modes of the electron's motion, with relativistic effects cropping up in every mode.

Equation 3.32 can be expanded as

$$\begin{aligned} E'_D - m_e \approx{}& (n + m_s + 1/2)\omega_c - (n + m_s + 1/2)^2\omega_c^2/2m_e + \pi_z^2/2m_e \\ & - \pi_z^4/8m_e^3 - (n + m_s + 1/2)\pi_z^2/2m_e^2 + m_s\omega_a - m_s\omega_z\pi_z^2/2m_e, \end{aligned} \tag{3.33}$$

where terms through order (kinetic energy)$^2/m_e$ have been kept. The terms can be interpreted as follows. The second term of Eq. 3.32 gives the first-order relativistic shift in ω_c due to the electron's spin and cyclotron motions. The fourth term gives the first-order relativistic shift in the axial kinetic energy, while the fifth and seventh terms couple ω_c and ω_a to π_z.

The relativistic contributions to E'_D (Eq. 3.33) can be added to E_S (Eq. 3.30) to obtain a relativistic expression for the energy E_P of an electron subject to trap conditions. (Note: E_S contains terms proportional to ω_m and ω_z arising as a consequence of the quadrupole electric field. However E_P neglects the *relativistic* effects of the quadrupole electric field.) Formally, this addition is carried out through the Pauli approximation. The Pauli approximation reduces the 4×4 Dirac Hamiltonian for an electron in a homogeneous magnetic field and quadrupole electric field—

which is analytically intractable— to an exactly solvable 2×2 'Pauli' Hamiltonian. Regardless of methodology,

$$\begin{aligned} E_P - m_e &= E_S + < E'_{D,rel} > \\ &= (n + m_s + 1/2)\omega_c - (n + m_s + 1/2)^2\omega_c^2/2m_e + (k + 1/2)\omega_z \\ &- 3/16(k + 1/2)^2\omega_z^2/m_e - (n + m_s + 1/2)\omega_c(k + 1/2)\omega_z/2m_e \\ &+ m_s\omega_a - m_s\omega_a(k + 1/2)\omega_z/2m_e - (q + 1/2)\omega_m. \end{aligned} \tag{3.34}$$

Equation 3.34 can be used to compute transition frequencies. In the limit $k\omega_z$, $q\omega_m \to 0$,

$$\begin{aligned} E(n + 1, m_s) - E(n, m_s) &= \omega_c - (n + m_s + 1)\omega_c^2/m_e; \\ E(n, 1/2) - E(n + 1, -1/2) &= \omega_a. \end{aligned} \tag{3.35}$$

Then,

$$\begin{aligned} \frac{E(n, 1/2) - E(n + 1, -1/2)}{E(n + 1, 1/2) - E(n, 1/2)} &= \frac{\omega_a}{\omega_c - (n + 3/2)\omega_c^2/m_e} \\ &\approx a_e + (n + 3/2)\frac{a_e\omega_c}{m_e}. \end{aligned} \tag{3.36}$$

Equation 3.36 is the one used by Gabrielse, et al. in Ref. [22] to determine a_e.

Unaccounted-for relativistic effects

We suggest the limits $k\omega_z$, $q\omega_m \to 0$ that led to Eq. 3.36 were hasty, with the result that relativistic corrections of roughly the same order of magnitude as $u(a_e)$ were omitted from the Gabrielse determination of a_e.

The argument is as follows. According to the equipartition theorem, at thermal equilibrium the electron's energy should be distributed evenly between its modes, such that $n\omega_c \approx k\omega_z \approx q\omega_m$. For $\omega_c/2\pi = 149.0\ GHz$ and $\omega_z = 199.9\ MHz$ [44], we expect $k \sim \frac{\omega_c}{\omega_z}n \sim 10^3 n$. Recomputing Eq. 3.36 for non-zero k, while retaining

the limit $q\omega_m \to 0$ for simplicity, finds

$$\begin{aligned}\frac{E(0,1/2,k_n+\Delta k_n)-E(1,-1/2,k_n)}{E(1,1/2,k_d+\Delta k_d)-E(0,1/2,k_d)} \\ = a_e + \frac{3a_e\omega_c}{m} + \frac{\omega_z}{2\omega_c}(\Delta k_n - a_e\Delta k_d) \\ + \frac{\omega_z}{4m}(\Delta k_n + 2a_e(k_d-k_n) - a_e(\Delta k_n + 2\Delta k_d) + a_e^2\Delta k_d),\end{aligned} \tag{3.37}$$

where the term $a_e\omega_z/2m(k_d-k_n)$ in Eq. 3.37 is of size $\sim 7\times10^{-13}$ for $(k_d-k_n)=10^2$, which is slightly larger than the total experimental uncertainty of 2.8×10^{-13}.

In Sec. 4 we explore the effects of adding such a correction to $a_e(exp)$. Taken with a positive (negative) sign, the correction decreases (increases) the tension between Eqs. 3.24 and 3.25, with important consequences for the disposition of the muon $(g-2)$ anomaly.

5 Theory of the muon anomalous magnetic moment

The leading non-zero contribution to the muon anomalous moment is the same as the leading non-zero contribution to the electron anomalous moment, which is clear from the fact that $a_e^{LO} = \frac{\alpha}{2\pi}$ is independent of the mass of the electron. The discussion above, about the Dirac Hamiltonian and so on, applies to electons and muons alike. The differences between a_e and a_μ emerge only at higher-orders in perturbation theory.

As with a_e, the most complete calculation of a_μ is due to Kinoshita, et al. [40]. The calculation is organized in the same way as the calculation of a_e, with

$$a_\mu(theory) = a_\mu(QED) + a_\mu(hadron) + a_\mu(weak). \tag{3.38}$$

$a_\mu(theory)$ differs from $a_\mu(exp)$ by $\sim 2.1{-}3.9\sigma$, with the size of the discrepancy— larger or smaller— determined by the value assigned to $a_\mu(hadron)$, which has a theoretical uncertainty of the same magnitude as the total experimental uncertainty

(see Sec. 5.2).

A judicious choice of $a_\mu(hadron)$ cannot resolve the discrepancy. The discrepancy, referred to as the muon $g-2$ anomaly, is presumed to be a consequence of an experimental error or new physics. A new measurement of $a_\mu(exp)$ is underway at Fermilab [45]. $a_\mu(exp)$ is discussed in Sec. 6. The new physics, if it exists, is expected to scale like m_μ^2/Λ^2 for $\Lambda >> m_\mu$, with Λ the scale of the new physics. Under the assumption of lepton universality, the new physics contribution to a_e would be $(m_\mu/m_e)^2 \sim 40,000$-times smaller, and negligible.[5] Possible new physics contributions are discussed in Sec. 1.

Similar to $a_e(QED)$,

$$a_\mu(QED) = A_1 + A_2(\frac{m_\mu}{m_e}) + A_2(\frac{m_\mu}{m_\tau}) + A_3(\frac{m_\mu}{m_e}, \frac{m_\mu}{m_\tau}), \tag{3.39}$$

where $A_n = \sum_i (\frac{\alpha}{\pi})^i A_n^{2i}$.

The leading contribution to A_1 is the leading contribution to a_μ, namely, $\frac{\alpha}{2\pi}$. The leading contributions to the mass-dependent terms $A_2(\frac{m_\mu}{m_e})$ and $A_2(\frac{m_\mu}{m_\tau})$ are due to photon vacuum polarization insertions in the leading vertex correction loop and are discussed below.

5.1 Mass-dependent contributions to $a_\mu(QED)$

The photon propagator is perturbatively corrected by vacuum polarization insertions. The insertions take the general form of one-particle irreducible (1PI) bubbles. A 1PI bubble, by definition, cannot be cut into two pieces by cutting one of the bubble's internal lines.

Each insertion of a 1PI bubble into the photon propagator corresponds to the insertion of a polarization tensor $\Pi_{\mu\nu} = (q^2 g_{\mu\nu} - q_\mu q_\nu)\Pi(q^2)$. The factor of $(q^2 g_{\mu\nu} -$

[5] In the analyses of Ch. 7, $m_e << m_\mu \sim \Lambda$. The fact m_μ and Λ are of the same magnitude complicates the scaling of the new physics contribution to a_μ. Thus, in the context of the analyses of Ch. 7, the factor of 40,000 is merely indicative of the relative suppression of the new physics contribution to a_e. It should not be taken literally.

$q_\mu q_\nu$) in $\Pi_{\mu\nu}$, constructed from the available tensors— where q_μ is the four-momentum of the incoming photon— ensures $\Pi_{\mu\nu}$ satisifies the Ward identity (i.e., $q_\mu \Pi_{\mu\nu} = 0$).

The photon propagator at nth order contains n insertions of $\Pi_{\mu\nu}$. Summing the vacuum polarization contributions to the photon propagator to all orders— often referred to as 'summing the bubbles'— gives the full photon propagator. The result of the all-orders calculation is a shift in the photon propagator:

$$\frac{-ig_{\mu\nu}}{q^2} \rightarrow \frac{-ig_{\mu\nu}}{q^2(1-\Pi(q^2))}. \tag{3.40}$$

Gauge terms proportional to $q_\mu q_\nu$, which give zero when contracted with an external current, have been omitted from Eq. 3.40. The factor of $\frac{1}{1-\Pi(q^2)}$ to the right of the arrow is the net result of summing the bubbles and is responsible for renormalizing the electric charge.

The full photon propagator retains the pole at $q^2 = 0$, and the photon remains massless. $\Pi(q^2)$ must be regular at $q^2 = 0$ since (according to the conventional textbook argument) a pole at $q^2 = 0$ would require a massless single-particle intermediate state, not describable by a 1PI bubble.

The analyticity of $\Pi(q^2)$ implies the following dispersion relation holds

$$\frac{\hat{\Pi}(q^2)}{q^2} \equiv \frac{\Pi(q^2) - \Pi(0)}{q^2} = \frac{1}{\pi} \int \frac{ds}{s} Im\hat{\Pi}(s) \frac{1}{s - q^2}, \tag{3.41}$$

where $\hat{\Pi}(q^2) \equiv \Pi(q^2) - \Pi(0)$ and $Im\Pi(0) = 0$. The left-hand side of Eq. 3.41 is obtained by contracting $\mathcal{I} = \int ds \Pi(s) \frac{1}{s(s-q^2)}$ around the poles at $s = 0$ and $s = q^2$, while the right-hand side is obtained by evaluating $\mathcal{I}$ around a closed circular contour, pinched along the $Re[s] > 0$ axis to avoid the branch cut in $\Pi(s)$.

At lowest order, $\hat{\Pi}(s) \rightarrow \hat{\Pi}_2(s)$ corresponds to the insertion of a fermion loop in the photon propagator. We take the fermion loop to be an electron loop for the time being. The branch cut in $\Pi_2(s)$ is then associated with the threshold for producing an e^+e^- pair.

The right-hand side of Eq. 3.41 contains a factor of $1/(s-q^2)$, which is the propagator for a photon of mass-squared q^2. Accordingly, the contribution to a_μ due to the insertion of an electron loop in the leading vertex correction loop is

$$a_\mu(e\,\text{loop}) = \frac{1}{\pi}\int_{4m_e^2}\frac{ds}{s}\,Im\hat{\Pi}_2(s)\,a_\mu^V(s), \tag{3.42}$$

where $a_\mu^V(s)$ is the contribution to a_μ due to the leading vertex correction loop, with a massive vector particle in place of the massless photon. See Fig. 6.1. An expression for $a_\mu^V(s)$ (Eq. 6.6) is derived in Sec. 1. The expression takes the form of $\frac{\alpha}{\pi}$ times a kernel $K(s)$.

An expression for $Im\hat{\Pi}_2(s)$ for $s > 4m_e^2$ can be obtained by computing the electron loop. The calculation is done, for example, in Chapter 7.5 of Peskin and Schroeder [46]. The result is

$$Im\hat{\Pi}_2(s) = -\alpha/3\cdot\sqrt{1-4m_2^2/s}\cdot(1+2m_e^2/s). \tag{3.43}$$

Then,

$$a_\mu(e\,\text{loop}) = -(\frac{\alpha m_\mu}{3\pi})^2\int_{4m_e^2}\frac{ds}{s^2}\cdot\sqrt{1-4m_2^2/s}\cdot(1+2m_e^2/s)\cdot\hat{K}(s), \tag{3.44}$$

where $\hat{K}(s) = \frac{3s}{m_\mu^2}K(s)$ is slowly varying over the integration region.

The leading contribution to $A_2(m_\mu/m_e)$ is

$$A_2^{(4)}(m_\mu/m_e) = a_\mu(e\,\text{loop})/(\frac{\alpha}{\pi})^2, \tag{3.45}$$

where the superscript on the left-hand side denotes the 4th-order in e. The expression for $A_2^{(4)}(m_\mu/m_\tau)$, the vacuum polarization contribution due to a τ loop, is identical to Eq. 3.45, except with $m_e \to m_\tau$. $A_2^{(4)}(m_\mu/m_e)$ is dominated by a term $\sim ln(m_\mu/m_e)$, while $A_2^{(4)}(m_\mu/m_\tau)$ is dominated by a term $\sim (m_\mu/m_\tau)^2$.

The muon-loop vacuum polarization contribution to a_μ follows from Eq. 3.45,

as well— this time, with $m_e \to m_\mu$. The result however is mass-*independent* and is included in $A_1^{(4)}$.

Contributions to $A_3(m_\mu/m_e,\, m_\mu/m_\tau)$ start at three-loops (6th order in e). The leading contribution is due to the vertex-correction diagram with two lepton-loop insertions, one an electron loop and the other a τ loop.

5.2 Hadronic vacuum polarization contribution to a_μ

The leading hadronic vacuum polarization to a_μ replaces $\hat{\Pi}_2(q^2)$ in Eq. 3.42 with a hadronic contribution $\hat{\Pi}_{had}$. However the hadronic contribution to the vacuum polarization— which at leading order entails the insertion of a quark loop into the leading vertex correction diagram— cannot be computed perturbatively due to the breakdown of pQCD at low energies. The difficulty of defining quark masses is a related complication.

The workaround is to apply the optical theorem to $Im\hat{\Pi}_{had}(q^2)$, which has

$$Im\hat{\Pi}_{had}(q^2) = \frac{s}{4\pi\alpha}\sigma_{tot}(e^+e^- \to hadrons), \tag{3.46}$$

where $\sigma_{tot}(e^+e^- \to hadrons)$ can be determined from experiment [47]. At low energies, the cross section is dominated by $\sigma_{tot}(e^+e^- \to \pi^+\pi^-) \sim (1 - \frac{4m_\pi^2}{s})^{3/2} \cdot |F_\pi(s)|^2$. $F_\pi(s)$ is the electromagnetic form factor of the pion, and $\sigma_{tot}(e^+e^- \to \pi^+\pi^-)$ goes like $(\sqrt{1 - \frac{4m_\pi^2}{s}})^3$ rather than $\sqrt{1 - \frac{4m_\pi^2}{s}}$ due to spin suppression at the $\gamma\pi^+\pi^-$ vertex.

The convention is to split the leading hadronic vacuum polarization contibution $a_\mu^{(4)}(HVP)$ into two parts

$$a_\mu^{(4)}(HVP) = (\frac{\alpha m_\mu}{3\pi})^2[\int_{m_{\pi^0}^2}^{E_0^2} ds \frac{R_{had}^{exp}\hat{K}(s)}{s^2} + \int_{E_0^2}^{\infty} ds \frac{R_{had}^{pQCD}\hat{K}(s)}{s^2}], \tag{3.47}$$

where $R = \sigma_{tot}(e^+e^- \to hadrons) \cdot (3s/4\pi\alpha^2)$ and the superscripts on R refer to the way in which $\sigma_{tot}(e^+e^- \to hadrons)$ is determined.

The theoretical value for $a_\mu^{(4)}(HVP)$ is $6931(33)(7) \times 10^{-11}$. The first number in parentheses is due to the uncertainty in R_{had}^{exp}; the second number, to the uncertainty in R_{had}^{pQCD}. For comparison, the total experimental uncertainty of a_μ is $\sqrt{54^2\ (stat.) + 33^2\ (syst.)} \times 10^{-11} \approx 63 \times 10^{-11}$.

5.3 Electroweak contribution to a_μ

The leading electroweak contributions to a_μ are shown in Fig. 3.4. The corresponding contributions to a_e are much smaller due to the smaller mass of the electron.

The total electroweak contibution to a_μ, up to two-loop order, is

$$a_\mu(weak) = 153.6(1.0) \times 10^{-11}. \tag{3.48}$$

6 Measurement of the muon anomalous magnetic moment

The muon anomalous magnetic moment a_μ was measured by the E821 experiment at Brookhaven [2]. The experiment measured the anomaly frequency ω_a of muons trapped in a storage ring and the magnitude of the trapping magnetic field $B = |\vec{B}|$. The experimental values for ω_a and B were then fed into the equation $\omega_a = a_\mu \frac{eB}{em_\mu}$ (cf. Eq. 3.21), and a value for a_μ was extracted, where:

$$a_\mu(exp) = 11659208.0(5.4)(3.3) \times 10^{-10}. \tag{3.49}$$

The numbers in parentheses represent statistical and systematic uncertainties, respectively. $a_\mu(exp)$ differs from $a_\mu(theory)$ by $2 - 4\sigma$. The discrepancy is discussed in Sec. 5.

The measurement of ω_a proceeded as follows. $2.4\,GeV$ protons from a proton storage ring were directed onto a fixed target, producing pions, which subsequently decayed into muons and neutrinos. The muons, with spin vectors nominally pointing

in the direction of their momentum due to the details of the pion decay[6], were then injected into a storage ring, where they were confined radially by a homogeneous magnetic field and axially by a quadrupole electric field. Once injected into the storage ring, the muons traversed a circular orbit at cyclotron frequency ω_c for the duration of their lifetime, their spin vectors precessing at frequency $\omega_s \neq \omega_c$.

The expression for the anomaly frequency $\omega_a = \omega_s - \omega_c$ of the trapped muons is derived and discussed in App. H, and shown below:

$$\vec{\omega}_a = \frac{e}{m_\mu}(a_\mu \vec{B} - (a_\mu - \frac{1}{\gamma^2 - 1})\vec{v} \times \vec{E}). \tag{3.50}$$

$\gamma = 1/\sqrt{1 - v^2/c^2}$ is a Lorentz factor. The experiment was run at the 'magic' γ of 29.3, ensuring that the second term of Eq. 3.50 was small and $\vec{\omega}_a$ reduced to $a_\mu \frac{e\vec{B}}{m_\mu}$.

After repeatedly orbiting the storage ring, the muons decayed[7] via $\mu^+ \rightarrow e^+ \nu_e \bar{\nu}_\mu$,[8] with the direction of positron emission strongly correlated with the direction of the muon spin vector. The details of the correlation are specified by the muon decay rate

$$d\Gamma(\mu^+ \rightarrow e^+ \nu_e \bar{\nu}_\mu) = N(E_e)(1 + \frac{1 - 2x_e}{3 - 2x_e} cos\theta) d\Omega, \tag{3.51}$$

where $cos\theta$ defines the angle between the direction of the positron in the muon rest frame and the direction of the muon spin vector, $N(E_e)$ is an overall normalization which is an explicit function of positron energy E_e, and $x_e = 2E_e/m_\mu$, with $m_\mu/2$ representing the maximum positron energy.

[6] π^- is a pseudoscalar, $\bar{u}\gamma_5 d$. The matrix element for the decay $\pi^- \rightarrow \mu^- \bar{\nu}_\mu$, which proceeds via the weak interaction, contains a factor of $(1 - \gamma_5)$. The factor of $(1 - \gamma_5)$ projects out only chirally left-handed (right-handed) particle (anti-particle) states. Consequently $\bar{\nu}_\mu$ is in a right-handed chiral state, which, due to the near masslessness of $\bar{\nu}_\mu$, is also a right-handed *helicity* state. By spin conservation at the effective interaction vertex, the μ^- is also in a right-handed helicity state, with its spin vector in the direction of its three-momentum. Note: the μ^- must be in a left-handed *chiral* state due to the factor of $(1 - \gamma_5)$ in the matrix element. The decay $\pi^- \rightarrow \mu^- \bar{\nu}_\mu$ is helicity suppressed and only possible because of the finite mass of the muon.

[7] The average muon lifetime was $64.435 \mu s$ in the laboratory frame and $2.19711 \mu s$ in the muon rest frame.

[8] The decay $\mu^- \rightarrow e^- \bar{\nu}_e \nu_\mu$ was also considered, but separately. The E821 experiment obtained two values for $a_\mu(exp)$, one from μ^+ decays and the other from μ^- decays. The two values for $a_\mu(exp)$ were then combined, subject to the assumption of CPT symmetry, to give the value for $a_\mu(exp)$ of Eq. 3.49.

The decay positrons were detected by a calorimeter, with the expected number of decay positrons with energy greater than E[9] at time t after the muons were injected into the storage ring given by

$$N(t) = N_0(t)exp(-t/\gamma\tau_{rest})(1 + A(E)sin(\omega_a t + \phi(E))), \tag{3.52}$$

where τ_{rest} is the muon lifetime in the muon rest frame and ϕ is a positron-energy-dependent phase. Equation 3.52 corresponds to exponential decay modulated by the anomaly frequency ω_a. The experimental data (see Fig. 5.1) was fitted to Eq. 3.52, with the fit yielding an experimental value for ω_a.

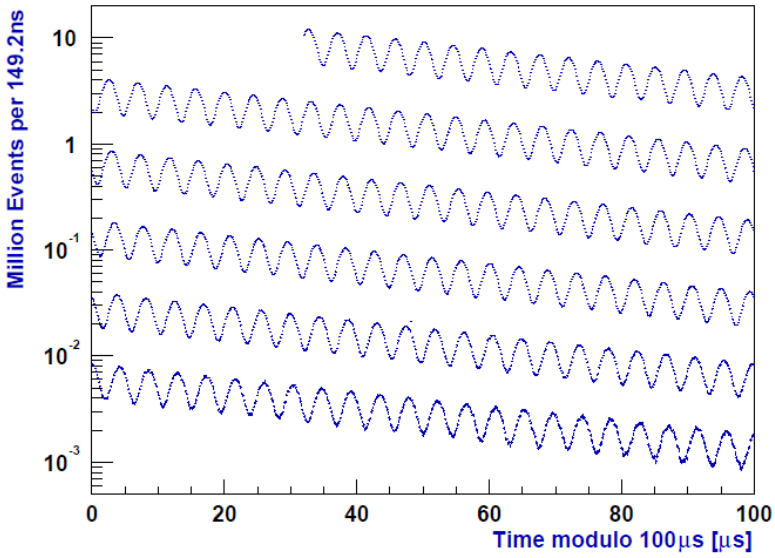

Figure 3.5: Number of muon decays N versus time as measured by the E821 experiment at Brookhaven National Lab. The data of the figure was used to determine a value for the muon anomaly frequency ω_a. See discussion in text. The figure is reprinted from [2].

The magnitude of the trapping magnetic field B was determined separately from ω_a. The Larmor spin precession frequency ω_p of a proton in water was measured and related to B via the expression $\omega_p = (1 + a_p)\frac{eB}{2m_p}$.

[9]The criterion $E_e > E$ selected preferentially for positrons emitted in the forward direction.

The final step in obtaining a value for a_μ was algebra:

$$\omega_a = a_\mu \frac{eB}{m_\mu} \quad \rightarrow \quad a_\mu = \frac{2m_\mu \mu_p}{e}\frac{\omega_a}{\omega_p} = (1+a_\mu)\frac{\mu_p}{\mu_\mu}\frac{\omega_a}{\omega_p} \quad \rightarrow \quad a_\mu = \frac{R}{\lambda - R}, \quad (3.53)$$

where $\mu_\mu = (1+a_\mu)\frac{e}{2m_\mu}$, $\mu_p = (1+a_p)\frac{e}{2m_p}$, $\lambda = \frac{\mu_\mu}{\mu_p}$, and $R = \omega_a/\omega_p$. The experimental value for λ came from spectroscopy measurements of ground-state muonium performed at LAMPF at Los Alamos [48]. The gymnastics of Eq. 3.53 were done to minimize the effect of the uncertainty of m_μ on the total uncertainty of a_μ.

A new measurement of a_μ, using the same muon storage ring as the E821 experiment, is underway at Fermilab [45]. The experiment (E989) is expected to improve on the precision of the E821 experiment by a factor of three, with the improvement coming from upgrades to "outdated or underperforming components from E821".

Chapter 4

The spectroscopy sector

The spectroscopy data of the reference dataset (Table 2.1) consist of transition frequencies from electronic hydrogen (ep), muonic hydrogen (μp), electronic deuterium (ed), and muonic deuterium (μd) experiments. The bound states ep, μp, ed, μd are called *hydrogenlike*, having in common a single, bound lepton and a nuclear charge $Z = 1$.

The theory for electronic hydrogen has a history going back more than a century, which has led to perturbative expressions for the electronic hydrogen energy levels, organized in small parameters $Z\alpha$, α/π, and m_e/m_p. The theory for the other hydrogenlike bound states is identical, up to appropriate mass substitutions and the following qualifications:

- Replacement of the spin-1/2, strongly-bound proton with the spin-1, weakly-bound deuteron requires modification of nuclear structure and hyperfine corrections to the energy levels.

- Replacement of the electron with the 200-times heavier muon dramatically changes the weight with which certain diagrams, particularly those involving closed electron loops, contribute to the energy levels.

Schrodinger theory predicts that hydrogenlike states with the same principal

quantum number n but different total angular momentum j and orbital angular momentum ℓ will have the same energy, E_n. Dirac theory lifts the degeneracy with respect to j while keeping the degeneracy with respect to ℓ intact.[1] Lifting the degeneracy with respect to j splits the lines of the Schrodinger spectrum, and the Dirac spectrum is said to acquire a *fine structure*: $E_n \to E_{nj}$. The degeneracy of the Dirac spectrum with respect to ℓ is lifted by radiative, recoil, nuclear structure, and hyperfine splitting corrections to Dirac theory. The resulting spectrum is said to acquire a *hyperfine structure*: $E_{nj} \to E_{nj\ell}$.

The hyperfine structure was first observed by Lamb and Retherford [49] in 1947, who measured a non-zero value for the $2S_{1/2}-2P_{1/2}$ transition frequency in electronic hydrogen, in contradiction of Dirac theory.[2] The $2S_{1/2} - 2P_{1/2}$ energy difference in electronic hydrogen became known as the Lamb shift. Over time the Lamb shift has acquired a broader meaning and now refers, except in historical contexts, to any energy difference between hydrogenlike bound-states not captured by Dirac theory.

The spectroscopic theory of hydrogenlike atoms is discussed below, starting with Schrodinger theory and extending to the modern formalism. Bound-state physics is a rich subject, both broad and deep. References have been provided in those places where depth or breadth is perceived to be especially lacking. Complete formulas can be found in Ref. [20], which allow for computation of theoretical values for arbitrary hydrogenlike bound-state transition frequencies.

[1] $\vec{J} = \vec{L} + \vec{S}$ commutes with the Dirac Hamiltonian. $\vec{L}$ and $\vec{S}$ do not.

[2] Twenty years prior to Lamb and Retherford's measurement, Uehling predicted $\nu_{2S_{1/2}-2P_{1/2}} \sim -30MHz$ on the basis of a vacuum polarization calculation. Lamb and Retherford however found $\nu_{2S_{1/2}-2P_{1/2}} \sim 1000MHz$. The discrepancy (sign and magnitude!) was subsequently explained by Bethe via a calculation of the leading self-energy correction to the electronic hydrogen energy levels.

1 Schrodinger theory

The energy levels for a hydrogenlike atom, obtained by solving the Schrodinger equation for a lepton (e or μ) in a Coulomb potential, are

$$E_n = -\frac{\alpha^2 mc^2}{2n^2}, \tag{4.1}$$

which has units of energy, eV. m is the mass of the lepton. The levels are anharmonic (i.e. not equally spaced) due to the n^{-2}-dependence of Eq. 4.1. Equation 4.1 is derived in Appendix D using group theoretic arguments relating to the $SO(4)$ symmetry of the Schrodinger equation. n^2 in this context represents the dimension of the irreducible representations of $SO(4)$ (see App. D). The spherical symmetry in the problem ($V = V(r)$) implies only rotational invariance under $SO(3)$. The additional symmetry is dynamical in origin and partially broken in the Dirac equation: see Sec 2.1.

The binding energy of a hydrogenlike atom is

$$\alpha^2 mc^2/2 = hc\dot{R_\infty}(m/m_e) = 13.6(m/m_e)\ [eV],$$

where the first equality defines the Rydberg constant, $R_\infty = \alpha^2 m_e c/2h\ [m^{-1}]$. The muon in muonic hydrogen is accordingly $(m_\mu/m_e) \sim 200$ times more deeply bound than the electron in electronic hydrogen. Background thermal fluctuations enter at the level of $10^{-4} \cdot T\ [eV]$ for background temperature $T\ [K]$. Sub-Kelvin background temperatures are consequently the norm in modern precision spectroscopy experiments.

In units of freqency, Eq. 4.1 becomes

$$\nu_n = -\frac{\alpha^2 mc^2/h}{2n^2} = -\frac{R_\infty c}{n^2}\ [s^{-1}]. \tag{4.2}$$

The full, modern theory for hydrogenlike bound-states perturbatively corrects Schrodinger theory. The perturbative expansion of the energy levels for the full theory starts at order $\alpha^2 mc^2/2h = R_\infty c$, with the higher-order terms all containing a factor of $R_\infty c$, which allows the energy levels for the full theory to be written in the (now-conventional) factorized form $\nu_{n\ell j} = R_\infty c \cdot \hat{\nu}_{n\ell j}$, where $\hat{\nu}_{n\ell j}$ is an explicit function of α and the nuclear charge radius r_N ($N = p$ or d). The dependence of $\hat{\nu}_{n\ell j}$ on α is due to radiative corrections to the energy levels; the dependence on r_N, to finite nuclear-size corrections.

The relevant energy scales are well-separated

$$m(Z\alpha)^2 << mZ\alpha << m << M,$$

with M the mass of the nucleus. $mZ\alpha$ gives the scale of the lepton momentum[3] and can also be identified with the inverse Bohr radius of the hydrogenlike atom a_0^{-1}.

2 Dirac theory

2.1 The Dirac equation

Typical derivations of the Dirac Hamiltonian take a "square root" of the Klein-Gordon equation. The result is a Hamiltonian with first-order derivatives in time and space and Lorentz-covariant equations of motion ($H\psi = i\partial_t \psi$), known collectively as the Dirac equation. The Dirac algebra follows from self-consistency arguments.

The Dirac eigenvalue equation is

$$\begin{aligned} i\gamma^0 \cdot [\vec{\gamma} \cdot \vec{\nabla} + m + ie\not{A}]u_N &= E_N u_N(\vec{x}), \\ i\gamma^0 \cdot [\vec{\gamma} \cdot \vec{\nabla} + m + ie\not{A}]v_N &= -E_N v_N(\vec{x}), \end{aligned} \tag{4.3}$$

where u_N (v_N) is a four-component particle (antiparticle) Dirac wave function for

[3] $< n|\vec{p}^2|n > = (mZ\alpha/n)^2$ for stationary states $|n>$.

continuum-state or bound-state N.[4] Negative-energy solutions are evident on the right-hand side of the second line.

The ansatz

$$u_N = \frac{1}{\sqrt{2}} \begin{pmatrix} f_N + ig_N \\ f_N - ig_N \end{pmatrix}, \quad v_N = \frac{1}{\sqrt{2}} \begin{pmatrix} g_N - if_N \\ g_N + if_N \end{pmatrix}, \tag{4.4}$$

preserves normalization conditions arising from the orthogonality of Dirac wave functions of different energy.[5] f_N and g_N are by inspection two-component wave functions. Under this ansatz and for an electrostatic external field with $\vec{A} = 0$, Eq. 4.3[6] reduces to

$$\begin{aligned} (\vec{\sigma} \cdot \vec{\nabla}) f_N &= (E_N + eA^0 + m) g_N, \\ (\vec{\sigma} \cdot \vec{\nabla}) g_N &= -(E_N + eA^0 - m) f_N. \end{aligned} \tag{4.5}$$

2.2 The non-relativistic limit of the Dirac equation

The non-relativistic limit of Eq. 4.5 is instructive. For a bound-state $E_N + m \approx 2m >> |eA^0|$. Insertion of this approximation into Eq. 4.5 immediately implies the following:

- $g_N \approx (\vec{\sigma} \cdot \vec{\nabla}/2m) f_N \sim (mZ\alpha/2m) f_N << f_N$ for lepton momentum of the order of the inverse Bohr radius of the atom.

- $(E_N - m) f_N \approx [-eA^0 - \vec{\nabla}^2/2m] f_N$, which is the Schrodinger equation. Since spin and orbital degrees of freedom are not coupled in the equation, f_N can be decomposed into the simple product $f_N = \chi_N \cdot \psi_N$, where χ_N is a constant,

[4] $u_N(\vec{x}) =< 0|\psi(\vec{x})|N >$, where $\psi(\vec{x})$ is the electron or muon field, $|0>$ is the vacuum, and $|N>$ is one of a complete set of orthonormal state vectors.

[5] The orthogonality of Dirac wave functions of different energy can be shown as follows:

$$0 = \int d^3x \; \vec{\nabla}(u_N^\dagger i\gamma^0 \vec{\gamma} u_M) = \int d^3x \; u_N^\dagger (\gamma^0 i\vec{\nabla} \cdot \vec{\gamma} - \vec{\gamma} \cdot i\vec{\nabla}\gamma^0) u_M) = (E_M - E_N^*) \int d^3x \; u_N^\dagger u_M,$$

where Eq. 4.3 has been applied to obtain the third equality. Hence $\int d^3x \; u_N^\dagger u_M = 0$ for $M \neq N$. More generally, $\int d^3x \; u_N^\dagger u_M \sim \delta_{NM}$, up to a normalization. Likewise, $\int d^3x \; v_N^\dagger v_M \sim \delta_{NM}$.

[6] in the Weyl basis

two-component spinor and ψ_N is a one-component Schrodinger wave function. Index N labels the quantum numbers n, ℓ, j of the bound-state.

- $u_N \approx \frac{1}{\sqrt{2}} \begin{pmatrix} 1 + i(\vec{\sigma} \cdot \vec{\nabla})/2m \\ 1 - i(\vec{\sigma} \cdot \vec{\nabla})/2m \end{pmatrix} f_n$. Non-relativistic approximations for $\bar{u}_M u_N$, $\bar{u}_M \gamma^0 u_N$, etc. can be calculated from this expression for u_N and will be used in Sec. 4.1 to compute expectation values of operators contributing to the Lamb shift.

2.3 The Dirac spectrum

Solving Eq. 4.5 for E_N— in the presence of a Coulomb potential, $eA_0 = Z\alpha/r$— solves the Dirac spectrum for a hydrogenlike bound-state. A solution requires parameterizing f_N and g_N, which is done in textbooks by now-standard physical arguments; see App. E The solution is

$$E_N \to E_{nj} = m[1 + (\frac{Z\alpha}{n - j - 1/2 + \sqrt{(\kappa(j+1/2))^2 - (Z\alpha)^2}})^2]^{-1/2}, \tag{4.6}$$

where $\kappa = \pm 1$ is a quantum number related to parity as $\eta_N = (-1)^\ell = (-1)^{j-1/2\cdot\kappa}$. η_N is the intrinsic parity of state vector $|N>=|nj>$. The Dirac spectrum is by inspection degenerate with respect to ℓ and κ. The degeneracy with respect to ℓ is due to the $SO(3)$ symmetry of the Dirac equation, while the degeneracy with respect to κ is due to its parity symmetry and can be regarded, as with the $SO(3)$ symmetry, as a residue of the $SO(4)$ symmetry of the Schrodinger equation.[7]

For hydrogenlike atoms, E_{nj} can be expanded in powers of $Z\alpha = \alpha << 1$

$$E_{nj} = m[1 - \frac{1}{2}(\frac{Z\alpha}{n})^2 + \frac{Z\alpha}{n}^4 (\frac{3}{8} - \frac{n}{2j+1}) + ...]. \tag{4.7}$$

The second term is the binding energy from non-relativistic Schrodinger theory. The

[7] Since $\ell^{max} = j - 1/2$, $\eta = (-1)^{\ell^{max}}$ implies κ must be positive, and the symmetry of the Dirac equation under κ disappears.

third term is the first relativistic correction to the Schrodinger-theory binding energy. Equation 4.7 can be improved trivially by replacing the lepton mass coefficient m with the reduced mass of the bound-state μ where appropriate

$$E_{nj} = m - \mu[\frac{1}{2}(\frac{Z\alpha}{n})^2 - \frac{Z\alpha}{n}^4(\frac{3}{8} - \frac{n}{2j+1}) + ...]. \tag{4.8}$$

The relativistic corrections are ordered in powers of $(Z\alpha)^2$, which is a consequence of the relativistic energy being ordered in powers of $p^2/m^2 \sim (mZ\alpha)^2/m^2 = (Z\alpha)^2$:

$$E = \sqrt{p^2 + m^2} = m[1 + \frac{1}{2}\frac{p^2}{m^2} - \frac{1}{8}(\frac{p^2}{m^2})^2 + ...]. \tag{4.9}$$

Corrections to the energy relating to the spin-1/2 of the lepton only modify the coefficients of $(Z\alpha)^{2n}$ in the expansion, which can be seen, at least superficially, by comparing Eq. 4.9 to Eq. 4.7.

2.4 The exact mass dependence of the Dirac spectrum

Equation 4.8 is ultimately a stopgap. The exact mass-dependence at order $(Z\alpha)^4$ and beyond requires careful consideration of the relativistic two-body problem, with a lepton of mass m and a nucleus of mass M. The non-relativistic Hamiltonian for the two-particle system in the center-of-mass frame is

$$H = \frac{\vec{p}^2}{2m} + \frac{\vec{p}^2}{2M} - \frac{Z\alpha}{r}. \tag{4.10}$$

First-order relativistic corrections to the nonrelativistic energy are of order $v^2/c^2 \sim (Z\alpha)^2$ and appear at order $(Z\alpha)^4$ of the expansion in $Z\alpha$. These corrections can be obtained from the sum of the relativistic free-particle Hamiltonians for m and M and the relativistic one-photon exchange. Additional exchange photons bring in at least one additional factor of $Z\alpha$, pushing diagrams with two or more exchange photons to order $(Z\alpha)^5$ and higher. The first-order relativistic corrections to Eq.

4.10 make up what is called the Breit potential. The Breit potential, due to Gregory Breit, is discussed and partially derived in App. F. Ultimately it corrects Eq. 4.7 by terms depending on the mass M of the nucleus such that

$$E_{nj\ell} = m + M - \mu\frac{1}{2}(\frac{Z\alpha}{n})^2 + \mu\frac{Z\alpha}{n}^4(\frac{3}{8} - \frac{n}{2j+1} + \frac{\mu}{4n(m+M)}) \\ + \frac{(Z\alpha)^4\mu^3}{2n^3M^2}(\frac{1}{j+1/2} - \frac{1}{\ell+1/2})(1-\delta_{\ell 0}), \tag{4.11}$$

where μ is the reduced mass. The fourth term breaks the degeneracy of the Dirac spectrum with respect to ℓ and gives a non-zero contribution to the Lamb shift. The contribution is small compared to the total Lamb shift due to the suppression induced by the factor of $(\mu/M)^2$. The part of the fourth term proportional to $\delta_{\ell 0}$ is called the Darwin-Foldy term and is non-zero only for spin-1/2 nuclei. As a consequence, Eq. 4.11 contributes to the Lamb shift in hydrogen but not deuterium.[8]

The dominant contributions to the Lamb shift for any hydrogenlike bound-state come from one-loop radiative corrections, which require quantum field theory— more particularly, bound-state quantum field theory— for their complete description.

3 Bound-state quantum field theory

The existence of a hydrogenlike bound-state— consisting of a lepton of mass m bound to a $Z = 1$ nucleus of mass $M >> m$— implies the existence of a pole at $E = M + m - 13.6(m/m_e)\ eV$. However no single diagram contains such a pole. Instead the pole is a divergence arising from the sum of all diagrams at center-of-mass energies near $M + m$. The divergence is associated with the breakdown of the perturbation theory, occurring when the nucleus and lepton momenta are $\lesssim mZ\alpha \sim$ [size of atom]$^{-1}$.

Hydrogenlike bound-states are held together by the Coulomb interaction between

[8] The deuteron has spin-1.

lepton and nucleus. We follow Weinberg [50] and introduce the Coulomb interaction at the level of the Lagrangian by replacing the vector potential A_μ in the Lagrangian with $A_\mu + \mathcal{A}_\mu$, where $\mathcal{A}_\mu(x)$ is an external vector potential due to an infinite-mass point source identified with the nucleus. This replacement— of $A_\mu + \mathcal{A}_\mu$ for A_μ or, equivalently, the nucleus for an external field— and the formalism that follows it, is known as the *external field approximation*.

The external field modifies the propagator S of the lepton field such that $S \to S_\mathcal{A}$, where

$$\begin{aligned} -iS_\mathcal{A}(x,y) = -iS(x-y) + (-i)^2 \int d^4z_1 S(x-z_1) e\gamma^\mu \mathcal{A}_\mu(z_1) S(z_1-y) \\ + (-i^3) \int d^4z_1 \int d^4z_2 S(x-z_1) e\gamma^\mu \mathcal{A}_\mu(z_1) S(z_1-z_2) e\gamma^\nu \mathcal{A}_\nu(z_2) S(z_2-y) ... \, . \end{aligned} \tag{4.12}$$

The terms of Eq. 4.12 correspond to Feynman diagrams with a variable number of insertions of the external field in the lepton line. The photons attached to the lepton line are attached to the nucleus line in all possible orders. Only in the non-relativistic limit do the uncrossed "ladder" diagrams dominate the sum.

$S_\mathcal{A}$ can alternatively be written as a time-ordered two-point correlation function

$$-iS_\mathcal{A} = < 0|T\psi(x)\bar{\psi}(y)|0 >_\mathcal{A}, \tag{4.13}$$

where $|0>_\mathcal{A}$ represents the vacuum for the free-field Hamiltonian plus interactions with the external field. For $x^0 > y^0$ and after the insertion of a complete set of states, Eq. 4.13 becomes

$$\begin{aligned} -iS_\mathcal{A} &= < 0|\psi(x)|0 >< 0|\bar{\psi}(y)|0 >_\mathcal{A} + \sum_N < 0|\psi(x)|N >< N|\bar{\psi}(y)|0 >_\mathcal{A} \\ &= \sum_N < 0|\psi(x)|N >< N|\bar{\psi}(y)|0 >_\mathcal{A} \, . \end{aligned} \tag{4.14}$$

As before, the sum over N runs over bound states and continuum states. We ignore the continuum states in what follows. On the second line the vacuum expectation

value of the field $\psi(x)$ is taken to be zero. By construction $\psi(x)$ annihilates a positive-energy lepton for $x^0 > y^0$ and creates a negative-energy antilepton for $x^0 < y^0$. Hence for $x^0 > y^0$, $< 0|\psi(x)|N >= u_N$ and $< N|\bar{\psi}(x)|0 >= \bar{u}_N$. (We ignore the antilepton wave functions which are irrelevant to the phenomenology.) With these substitutions for u_N and $\bar{u}_N$, Eq. 4.14 becomes $-iS_{\mathcal{A}} = \sum_N u_N(x)\bar{u}_N(y)$.

The vacuum for the full Hamiltonian H is related to $|0>_{\mathcal{A}}$ as[9]

$$|\Omega >= lim_{t\to\infty(1-i\epsilon)} \frac{e^{-iHt}}{< \Omega|0 >_{\mathcal{A}}}|0 >_{\mathcal{A}} . \tag{4.15}$$

Replacing $|0>_{\mathcal{A}} \equiv |0>$ in $S_{\mathcal{A}}$ with the full interacting vacuum $|\Omega>$ and again taking $x^0 > y^0$ finds

$$\begin{aligned} -iS_{\mathcal{A}} \to -iS'_{\mathcal{A}} &=< \Omega|\psi(x)\bar{\psi}(y)|\Omega > \\ &= \lim_{t\to\infty(1-i\epsilon)} \frac{1}{|< \Omega|0 >|^2} \\ &\times \sum_N < 0|e^{iHt}\psi(x)|N >< N|\bar{\psi}(y)e^{-iHt}|0 > \\ &= \sum_N e^{-iE'_N(x^0-y^0)} U_N(x)\bar{U}_N(y), \end{aligned} \tag{4.16}$$

where $U_N = u_N/ < \Omega|0 >$. Equation 4.16 can be Fourier transformed to give $S'_{\mathcal{A}}$ as a function of energy E

$$S'_{\mathcal{A}}(\vec{x},\vec{y};E) = \int_\infty^\infty dx^0 e^{iE(x^0-y^0)} S'_{\mathcal{A}}(x,y) = \sum_N \frac{U_N(\vec{x})\bar{U}_N(\vec{y})}{E'_N - E - i\epsilon}. \tag{4.17}$$

$S'_{\mathcal{A}}$ has poles at bound-state energies E'_N. $S_{\mathcal{A}}$, likewise, has poles at bound-state energies E_N. The free[10] and interacting quantities under consideration are related

[9]This relation can be established by time-evolving $|0>$ by the full Hamiltonian H:

$$e^{-iHt}|0 >= \sum_N e^{-iE_N t}|N >< N|0 >= e^{-iE_0 t}|\Omega >< \Omega|0 > + \sum_{N\neq 0} e^{-iE_N t}|N >< N|0 > .$$

Since $E_N > E_0$, in the limit $t \to \infty(1 - i\epsilon)$, the sum over $N \neq 0$ vanishes. What remains can be solved for $|\Omega >$ to obtain Eq. 4.15, which takes $E_0 =< \Omega|H|\Omega >$ to be zero. $< \Omega|0 >$ must be non-zero. Otherwise H would in no way consitute a small perturbation of the free Hamiltonian.

[10]Here, the free quantities under consideration are free up to the interaction of the external field.

by trivial ansatz by $S'_{\mathcal{A}} = S_{\mathcal{A}} + \delta S_{\mathcal{A}}$, $E'_N = E_N + \delta E_N$, and $U_N = u_N + \delta u_N$, where $\delta S_{\mathcal{A}}$, δE_N, and δu_N are defined order-by-order in perturbation theory.

With these identifications, Eq. 4.16 becomes

$$\begin{aligned} S'_{\mathcal{A}}(\vec{x}, \vec{y}; E) &= \sum_N \frac{(u_N + \delta u_N)(\bar{u}_N + \delta \bar{u}_N)}{E_N + \delta E_N - E - i\epsilon} \\ &= S_{\mathcal{A}} ... - \sum_N \frac{u_N \bar{u}_N}{(E_N - E)^2} \delta E_N. \end{aligned} \tag{4.18}$$

The last term on the second line is the only term containing a factor of δE_N. Solving for δE_N (i.e. the shift in the pole energy associated with swapping $S_{\mathcal{A}}$ for $S'_{\mathcal{A}}$) is then a matter of identifying the term in $\delta S_{\mathcal{A}} \sim u_N \bar{u}_N / (E_N - E)^2$.

The lowest-order radiative corrections to $S_{\mathcal{A}}$ can be accounted for perturbatively by summing all one-loop diagrams with one incoming and one outgoing lepton (denoted $\Sigma_{\mathcal{A}}$) between external-field-dressed lepton propagators

$$\delta S_{\mathcal{A}} = \int d^4 z \int d^4 w S_{\mathcal{A}}(x, z) \Sigma_{\mathcal{A}}(z, w) S_{\mathcal{A}}(w, y). \tag{4.19}$$

The diagrams associated with $\Sigma_{\mathcal{A}}$ are shown in Fig. 4.1 and consist of tadpole and self-energy diagrams plus counterterms, which reduce, respectively, to vacuum polarization and vertex-correction diagrams for a single insertion of the external field.

With appropriate substitutions for $S_{\mathcal{A}}$ and a transformation to energy variables, Eq. 4.19 becomes

$$\delta S_{\mathcal{A}} = \sum_{N,M} \frac{u_N(\vec{x}) \bar{u}_M(\vec{y})}{(E_N - E)(E_M - E)} \int d^3 z \int d^3 w \;\; \bar{u}_N(\vec{z}) \tilde{\Sigma}_{\mathcal{A}}(\vec{z}, \vec{w}) u_M(\vec{w}), \tag{4.20}$$

where $\tilde{\Sigma}_{\mathcal{A}}$ is $\Sigma_{\mathcal{A}}$ recast in terms of energy. Comparing Eq. 4.20 to Eq. 4.18 finds

$$\delta E_N = \int d^3 z \int d^3 w \;\; \bar{u}_N(\vec{z}) \tilde{\Sigma}_{\mathcal{A}}(\vec{z}, \vec{w}; E_N) u_N(\vec{w}), \tag{4.21}$$

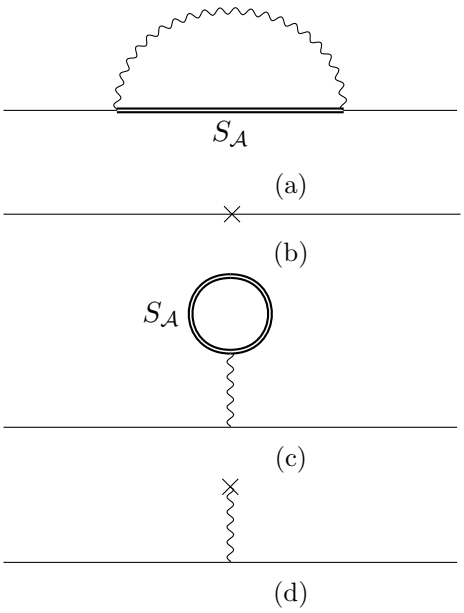

Figure 4.1: Diagrams for the one-loop radiative corrections to the hydrogenlike bound-state energy levels, and their counterterms. Double fermion lines correspond to $S_{\mathcal{A}}$ (Eq. 4.14), the fermion propagator in the presence of external field $\mathcal{A}$. Diagram (a) gives the dominant contribution to the Lamb shift for electron hydrogen. Diagram (c) gives the dominant contribution to the Lamb shift for muonic hydrogen.

or, equivalently,

$$\delta E_N = -\int d^3p' \int d^3p \;\; \bar{u}_N(\vec{p}')\tilde{\Sigma}_{\mathcal{A}}(\vec{p}', \vec{p}; E_N)u_N(\vec{p}). \tag{4.22}$$

Equations 4.21 and 4.22 give the lowest-order radiative corrections to the energy pole of bound-state N. The equations are very general and can be used to compute the leading radiative corrections to the energy— which are also the leading contributions to the Lamb shift— for all hydrogenlike bound-states. δE_N is complex for unstable bound-states, with its real part corresponding to the energy shift and its imaginary part corresponding to $-\Gamma/2$, where Γ is the bound-state decay rate. For muonic hydrogen, for example, Γ is given by the muon decay rate. For positronium, Γ must be determined from the various e^+e^- annihilation channels.

The matrix elements contributing to δE_N at any order of perturbation theory are— out of practicality and with minimal loss of precision— typically evaluated

using the non-relativistic approximation for u_N developed in Sec. 2.2:

$$u_N \approx \frac{1}{\sqrt{2}} \begin{pmatrix} 1 + i(\vec{\sigma} \cdot \vec{\nabla})/2m \\ 1 - i(\vec{\sigma} \cdot \vec{\nabla})/2m \end{pmatrix} f_N. \tag{4.23}$$

f_N again is composed of the product of a one-component, Schrodinger-Coulomb wave function and a constant, two-component, free-particle Dirac spinor. The terms $\sim i(\vec{\sigma}\cdot\vec{\nabla})/2m$ can often be neglected in Eq. 4.23. Higher-order terms can be included in Eq. 4.23 as well, if the calculation warrants.

4 Leading contributions to the Lamb shift

The leading radiative corrections come from the one-loop tadpole and self-energy diagrams. The self-energy diagram (Fig. 4.1(a)) contains a naive infrared divergence that is cut off by the virtuality of the lepton, which is of the order of the binding energy. The diagram is typically evaluated by splitting the integral over the virtual photon energy into a high-energy region and a low-energy region. In the low-energy region the lepton can be treated non-relativistically, while the effects of the external field must be treated to all orders. In the high-energy region the lepton must be treated relativistically, while the effects of the external field can be treated to lowest-order. We take a slightly different tack, again following Weinberg [50], and split the photon propagator into nominally high- and low-energy parts

$$\frac{1}{k^2} = [\frac{1}{k^2 + \mu^2}] + [\frac{1}{k^2} - \frac{1}{k^2 + \mu^2}]. \tag{4.24}$$

The propagator $\frac{1}{k^2+\mu^2}$ corresponds to a fictitious photon with mass taken to be in the range $mZ\alpha^2$ (binding energy) $<<$ μ $<<$ $mZ\alpha$ (electron momentum). The first term of Eq. 4.24 is the high-energy part; the second, the low-energy part.

The tadpole diagram (Fig. 4.1(c)) is not infrared divergent and requires no special care. Its contribution to the energy will be considered alongside the high-

energy part of the self-energy correction.

4.1 The high-energy part of the one-loop energy shift

Because $m(Z\alpha)^2 << \mu$, the high-energy part of the self-energy correction needs to be computed only to first-order in the external field:

$$\tilde{\Sigma}_{\mathcal{A}}(\vec{p}', \vec{p}; E_N) \to \tilde{\Sigma}_{\mathcal{A}(1)}(\vec{p}', \vec{p}; E_N) = -ie\mathcal{A}_\mu(\vec{p}' - \vec{p})\Gamma_1^\mu(\vec{p}', E_N, \vec{p}, E_N), \tag{4.25}$$

where Γ_1^μ is determined by expanding the factors of $S_{\mathcal{A}}$ in Eq. 4.22 and keeping only terms linear in $\mathcal{A}_\mu$. The factors of $S_{\mathcal{A}}$ are all contained in $\tilde{\Sigma}_{\mathcal{A}}$, which is evident by inspection of diagrams (a) and (c) of Fig. 4.1. Under the restriction of Eq. 4.25, diagrams (a) and (c) contain exactly one insertion of the external field and reduce to vertex-correction and vacuum polarization diagrams, respectively. Both diagrams contribute to Γ_1^μ. Equation 4.22 becomes

$$[\delta E_N]_{high-E} = -\int d^3p' \int d^3p \;\; \bar{u}_N(\vec{p}')\Gamma_1^\mu(\vec{p}', E_N, \vec{p}, E_N)u_N(\vec{p})\mathcal{A}_\mu(\vec{p}' - \vec{p}). \tag{4.26}$$

At tree-level $\Gamma_1^\mu \to \gamma_\mu$, suggesting the identification

$$\bar{u}_N[\gamma^\mu + \Gamma_1^\mu]u_n = \bar{u}_N[\gamma^\mu F_1(q^2) + \frac{i}{2}[\gamma^\mu, \gamma^\nu]q_\nu F_2(q^2)]u_N, \tag{4.27}$$

where the right-hand side gives the most general vertex structure allowed by parity, gauge, and Lorentz invariance, with F_1 and F_2 the well-known Dirac and Pauli form factors. F_1 and F_2 are defined order-by-order in perturbation theory and understood here to be truncated at one-loop level, to match the vertex structure on the left-hand side. By Eq. 4.27,

$$\Gamma_1^\mu = \gamma^\mu(F_1(q^2) - 1) + \frac{i}{2}[\gamma^\mu, \gamma^\nu]q_\nu F_2(q^2).$$

The one-loop contributions to F_1 and F_2 are computed in nearly every introductory quantum field theory text. Making use of these results reduces the problem of computing $[\delta E_N]_{high-E}$ to a sum of problems already solved. The results, to one-loop level, are

$$\begin{aligned} F_1(q^2) = 1 + \frac{e^2}{24\pi^2}(\frac{q^2}{m^2})[\ln(\frac{\mu^2}{m^2}) + \frac{2}{5} + \frac{3}{4}]; \\ F_2(q^2) = \frac{e^2}{16\pi}. \end{aligned} \tag{4.28}$$

The term $\sim 2/5$ in F_1 is from the vacuum polarization diagram. The remaining terms in F_1, and the lone term in F_2, are contributed by the vertex-correction diagram.

The calculation of $[\delta E_N]_{high-E}$ is straightforward, if tedious. The prescription is:

- Fourier transform Eq. 4.26 into position space;
- Take $\mathcal{A}_\mu \to \mathcal{A}_0$ ($\vec{\mathcal{A}} = 0$) inside Eq. 4.26, which sends $eF_{\mu\nu}(\vec{x}) \to \vec{\nabla}[eA_0(\vec{x})]$;
- Set $e\vec{\nabla}^2\mathcal{A}^0(\vec{x}) = -Ze^2\delta^3(\vec{x})$;
- Use the non-relativistic approximations for $\bar{u}_M u_N$, $\bar{u}_M\gamma^0 u_N$, etc. alluded to in Sec. 2.2.

The result is

$$\begin{aligned} [\delta E_N]_{F_1} &= \frac{Ze^4}{12\pi^2m^2}[\ln(\frac{m}{\mu}) - \frac{1}{5} - \frac{3}{8}] \cdot |f_N(0)|^2; \\ [\delta E_N]_{F_2} &= \frac{Ze^4}{32\pi^2m^2} \cdot |f_N(0)|^2 + \frac{ie^2}{16\pi^2m^2}\int d^3x f_N^\dagger(\vec{x})\vec{\sigma} \cdot [\vec{\nabla}(e\mathcal{A}_0(\vec{x})) \times \vec{\nabla} f_N(\vec{x})]; \\ [\delta E_N]_{high-E} &= [\delta E_N]_{F_1} + [\delta E_N]_{F_2}. \end{aligned} \tag{4.29}$$

The index N labels the bound-state, with $N = (n,\, \ell,\, j)$ and $f_{n\ell j}(\vec{x})$ a non-relativistic Schrodinger-Coulomb wave function. The first term of $[\delta E_N]_{F_2}$ cancels against the third term of $[\delta E_N]_{F_1}$. Since $[\delta E_N]_{F_1} \sim |f_N(0)|^2$ is non-zero only at the origin, $[\delta E_N]_{F_1}$ contributes only to states with $\ell = 0$, which are the only states with support

at the origin. The second term of $[\delta E_N]_{F_2}$ by contrast contributes only to states with $\ell \neq 0$, which can be seen from the fact $< \vec{\sigma} \cdot \vec{\nabla}(e\mathcal{A}^0(\vec{x}) \times \vec{p}) >_{NN} = -Ze < (\vec{\sigma} \cdot \vec{L})/r^3 >_{NN}$.

$[\delta E_N]_{high-E}$ is dominated by the factor of $\ln(m/\mu)$ in the first term of $[\delta E_N]_{F_1}$. Treating μ as a cutoff and setting it equal to the binding energy $m(Z\alpha)^2$— the approximate scale at which the naive infrared divergence of the self-energy loop is cut off— while ignoring the subdominant contributions of Eq. 4.29, predicts a Lamb shift for electronic hydrogen $E_{2S_{1/2}-2P_{1/2}} \approx$ 1300 MHz. 1300 MHz is about 30% larger than the experimental value. The actual cutoff is determined by the low-energy part of δE_N. To cancel the μ-dependence of Eq. 4.29, the low-energy part is required to give a term $\sim \ln(\mu/\Lambda)$, with Λ a cutoff energy, fixed by the low-energy calculation. It turns out Λ is considerably larger than $m(Z\alpha)^2$, which shifts the predicted value for the Lamb shift down by $\sim 30\%$. The low-energy part of the energy shift is discussed in the next subsection.

4.2 The low-energy part of the one-loop energy shift

The contribution to the energy shift from the infrared-finite vacuum polarization diagram was considered in the previous section and does not need to be considered here. The only diagram relevant to the calculation of the low-energy part of the energy shift is the self-energy diagram, which can be calculated from Eq. 4.21:

$$[\delta E_N]_{low-E} = \int d^3z \int d^3w \;\; \bar{u}_N(\vec{z}) \cdot [\tilde{\Sigma}_{\mathcal{A}}(\vec{z}, \vec{w}; E_N)]_{low-E} \cdot u_N(\vec{w}), \tag{4.30}$$

where

$$\begin{aligned}[\tilde{\Sigma}_{\mathcal{A}}(\vec{z}, \vec{w}; E_N)]_{low-E} = \int dz^0 e^{iE_N(z^0-w^0)} \cdot \{ie^2\gamma^\rho S_{\mathcal{A}}(z,w)\gamma_\rho D(z-w;\mu) \\ + \delta m(\mu)\delta^4(z-w) - (Z_2(\mu)-1)(\gamma^\mu(\partial_\mu + ie\mathcal{A}_\mu) + m)\}.\end{aligned} \tag{4.31}$$

The three terms inside the curly brackets of Eq. 4.31 are obtained by application of the Feynman rules to the diagrams of Fig. 4.1(a)-(b) and apply equally to the high-energy calculation, with the understanding that the form and interpretation of $D(z-w;\mu)$ and $S_{\mathcal{A}}$ differ between the low- and high-energy regimes. In the low-energy (high-energy) regime, $D(z-w;\mu)$ is taken to be the low-energy (high-energy) part of the photon propagator in position space. The counterterms $\delta m(\mu)$ and $Z_2(\mu)$ are calculated in a given regime using the relevant form of $D(z-w;\mu)$. The $Z_2(\mu)$-dependence however disappears from Eq. 4.31, because the third term in curly brackets acting on $u_N(\vec{w})$ gives zero by the Dirac equation. $S_{\mathcal{A}}$, in the high-energy calculation, was approximated by the second term of Eq. 4.12, containing only one insertion of the external field. The low-energy calculation however must account for photon momenta smaller than the binding energy and requires keeping the terms of Eq. 4.12 to all orders in the external field. For calculational convenience, $S_{\mathcal{A}}$ is replaced in Eq. 4.31 not by Eq. 4.12 but by the functionally equivalent Eq. 4.14, rewritten here in energy variables

$$-iS_{\mathcal{A}}(\vec{x},\vec{y};E)=\sum_N \frac{u_N(\vec{x})\bar{u}_N(\vec{y})}{E_N-E-i\epsilon}. \tag{4.32}$$

All the pieces needed to calculate $[\delta E_N]_{low-E}$ are present in Eqs. 4.30-4.32. The calculation is done in detail in Ref. [50] and involves more tricks than physical insights. The result is

$$[\delta E_N]_{low-E}=\frac{e^2}{6\pi^2}\sum_M (E_M-E_N)|\vec{v}_{MN}|^2[\ln(\frac{\mu}{2|E_M-E_N|})+\frac{5}{6}+i\pi\theta(E_N-E_M)]. \tag{4.33}$$

E_N and E_M are, respectively, the energies of the initial-state and intermediate-state leptons in the self-energy diagram, with the sum over M running over possible intermediate-state lepton energies. As expected, the infrared divergence of the logarithm is cut off by the virtuality of the lepton and regulated within the calculation

by subtraction of the δm counterterm.[11] $\vec{v}_{MN}$ is the expectation value of the velocity operator $i\vec{\nabla}/m$ evaluated between Schrodinger-Coulomb wave functions $f_M^\dagger$ and f_N. The imaginary part of $[\delta E_N]_{low-E}$ parameterizes the possibility lepton state N decays to lepton state M, allowed only if $E_N > E_M$. Only the real part of Eq. 4.33 is relevant to calculation of the Lamb shift. The imaginary part— as with the imaginary part of $[\delta E_N]_{high-E}$— contributes to the decay rate Γ, given by the imaginary part of the total energy shift.

4.3 The total one-loop energy shift

It remains to relate Eq. 4.33 to the high-energy part of the energy shift (Eq. 4.29). The relation $(E_M - E_N)\vec{v}_{NM} = [\vec{v}, H]_{NM}$, which may be easily verified, with H the Schrodinger-Coulomb Hamiltonian, leads to

$$\begin{aligned}\sum_M (E_M - E_N)|v_{MN}|^2 &= \frac{1}{2}\sum_M ([v^i, H]_{NM} \cdot v^i_{MN} + v^i_{NM} \cdot [H, v^i]_{MN}) \\ &= -\frac{1}{2m^2}[p^i, [p^i, H]]_{NN}.\end{aligned} \tag{4.34}$$

$-e\mathcal{A}^0(\vec{x})$ is the only term in the non-relativistic Hamiltonian that does not commute with $\vec{p}$.[12] Equation 4.34 becomes

$$\begin{aligned}\sum_M (E_M - E_N)|v_{MN}|^2 &= -\frac{e}{2m^2}(\vec{\nabla}^2\mathcal{A}^0(\vec{x}))_{NN} \\ &= \frac{Ze^2}{2m^2}|f_N(0)|^2,\end{aligned} \tag{4.35}$$

where $\vec{\nabla}^2\mathcal{A}^0(\vec{x}) = -Ze\delta^3(\vec{x})$. Equation 4.35 allows $[\delta E_N]_{high-E}$ (Eq. 4.29) to be added directly to $[\delta E_N]_{low-E}$ (Eq. 4.33) to obtain a μ-independent total energy

[11] as in the textbook calculation of the electron self-energy in the absence of an external field

[12] perhaps most easily seen by 'quantizing' the Poisson bracket $\{p^i, H\}$

shift, with the result

$$[\delta E_N]_{total} = \frac{e^2}{6\pi}\sum_M (E_M - E_N)|v_{MN}|^2[\ln(\frac{m}{2|E_N - E_M|}) + \frac{5}{6} - \frac{1}{5}] \\ - \frac{e^2}{16\pi^2 m^2}(\sigma\cdot\vec{\nabla}(e\mathcal{A}^0(\vec{x}))\times\vec{p})_{NN}. \tag{4.36}$$

The M-dependence of the logarithm in Eq. 4.33 necessitates writing Eq. 4.29 in terms of $\sum_M (E_M - E_N)|v_{MN}|^2$ rather than writing Eq. 4.33 in terms of $(\vec{\nabla}^2\mathcal{A}^0(\vec{x}))_{NN}$.

Equation 4.36 conceals a lot of information. Its perturbative structure, lost in the details of the calculation, can be teased out of each of the terms of $[\delta E_N]_{total}$:

$$\text{[first term]} \sim e^2\cdot\frac{Ze^2}{m^2}\cdot|f_N|^2 \sim \alpha\cdot\frac{\alpha}{m^2}\cdot(\frac{\alpha\cdot m}{n})^3 \sim \frac{R_\infty}{n^3}\cdot(Z\alpha)^2\cdot\alpha; \\ \text{[second term]} \sim \frac{e^2}{m^2}\cdot\vec{\nabla}(eA^0)\cdot|f_N|^2 \sim \frac{\alpha}{m^2}\cdot\alpha\cdot(\frac{\alpha\cdot m}{n})^3 \sim \frac{R_\infty}{n^3}\cdot(Z\alpha)^2\cdot\alpha. \tag{4.37}$$

Both terms have the same perturbative structure— an important consistency check— and contain five powers of α: two (implicit in R_∞) from Schrodinger theory, two from the first-order relativistic correction, and one from the first-order radiative corrections.

The first term of Eq. 4.36 is the energy shift due to the F_1 contributions of the naively-infrared-divergent self-energy calculation (first two terms in brackets) and the infrared-finite vacuum polarization calculation (third term in brackets). The second term is the energy shift due to the infrared-finite F_2 contribution of the self-energy calculation. The ℓ-dependence of Eq. 4.36 is considered below, as a step on the way to computing the (first-order radiative contribution to the) Lamb shift.

a. $\ell = 0$:

The second term of Eq. 4.36 is non-zero only for $\ell \neq 0$, as discussed in part **b** below. Consequently the total energy shift for states with $\ell = 0$ is given by the first term

of Eq. 4.36:

$$[\delta E_N]_{total} \cdot \delta_{\ell 0} \approx \frac{e^2}{6\pi} \sum_M (E_M - E_N)|v_{MN}|^2 [\ln(\frac{m}{2\Delta E_N}) + \frac{19}{30}]. \tag{4.38}$$

$|E_M - E_N|$ has been replaced inside the logarithm by the mean excitation energy ΔE_N. This replacement allows for the replacement of $\sum_M (E_M - E_N)|v_{MN}|^2$ in Eq. 4.38 with the expression on the second line of Eq. 4.35 and finds

$$[\delta E_N]_{total} \cdot \delta_{\ell 0} \approx \frac{4\alpha(Z\alpha)^4 m}{3\pi n^3} [\ln(\frac{m}{2\Delta E_N}) + \frac{19}{30}]. \tag{4.39}$$

b. $\ell \neq 0$:

The second term of Eq. 4.36 can be rewritten as

$$\begin{aligned} &- \frac{e^2}{16\pi^2 m^2} [-Ze(\frac{1}{r^3}\vec{\sigma} \cdot \vec{L})_{NN}] \\ &\quad = -\frac{e^2}{16\pi^2 m^2} [-Ze \int \frac{d^3r}{r^3} f_N^\dagger \{\vec{J}^2 - \vec{L}^2 - \vec{S}^2\} f_N] \\ &\quad = \frac{\alpha(Z\alpha)^4 m}{2\pi n^3} [\frac{j(j+1) - \ell(\ell+1) - s(s+1)}{\ell(\ell+1)(2\ell+1)}](1 - \delta_{\ell 0}), \end{aligned} \tag{4.40}$$

where on the second line $(\vec{L} \cdot \vec{\sigma})\, f_N = (2\vec{L} \cdot \vec{S})\, f_N = (\vec{J}^2 - \vec{L}^2 - \vec{S}^2)\, f_N = (j(j+1) - \ell(\ell+1) - s(s+1))\, f_N$, which is zero for $\ell = 0$.[13]

The first term of Eq. 4.36 vanishes for states with $\ell \neq 0$ according to Eq. 4.38. Equation 4.38 however averages over the M-dependence of $\ln|E_M - E_N|$ of Eq. 4.36 so that

$$\sum_M (E_M - E_N)|v_{MN}|^2 \ln|E_M - E_N| \rightarrow \ln\Delta E_N \sum_M (E_M - E_N)|v_{MN}|^2.$$

Postponing the averaging over M allows the first term of Eq. 4.36 to be rewritten

[13] For a spin-1/2 nucleus, $s(s+1) = 3/4$.

suggestively as

$$\frac{e^2}{6\pi}\sum_M (E_M - E_N)|v_{MN}|^2 \cdot [\ln(\frac{R_\infty}{|E_N - E_M|}) + (\text{terms independent of M})] \\ \rightarrow \frac{e^2}{6\pi}\sum_M (E_M - E_N)|v_{MN}|^2 \cdot \ln(\frac{R_\infty}{|E_N - E_M|}). \tag{4.41}$$

The terms independent of M do not contribute to the energy shift for states with $\ell \neq 0$. An expression identical to the expression on the second line of Eq. 4.41 can be pulled out of the energy shift for $\ell = 0$ states (see Eq. 4.38). The two expressions encode contributions to the energy shift due to the physical infrared cutoff. Analogy with Eq. 4.38 suggests Eq. 4.41 contributes to the energy shift for $\ell \neq 0$ states as

$$[\delta E_N]_{IR}(1 - \delta_{\ell 0}) = \frac{4\alpha(Z\alpha)^4 m}{3\pi n^3}\ln(\frac{R_\infty}{\Delta E_N}), \tag{4.42}$$

which careful calculation confirms. The factor of R_∞ inside the logarithm is chosen by convention and is the scale at which the infrared divergence would naively be expected to be cut off. The state-dependent quantities $\ln(\Delta E_N/R_\infty)$ must be calculated numerically and are called Bethe logarithms, often denoted $\ln k_0(n, \ell)$. The ultimate significance of the factor of R_∞ is to define the units in which ΔE_N is computed.

The total energy shift for states with $\ell \neq 0$, from Eqs. 4.40 and 4.42, is

$$[\delta E_N]_{total}(1 - \delta_{\ell 0}) = \frac{\alpha(Z\alpha)^4 m}{\pi n^3}[-\frac{4}{3}\ln(\frac{\Delta E_N}{R_\infty}) + \frac{1}{2}(\frac{j(j+1) - \ell(\ell+1) - s(s+1)}{\ell(\ell+1)(2\ell+1)})]. \tag{4.43}$$

For illustration, we compute the $2S_{1/2} - 2P_{1/2}$ Lamb shift in electronic hydrogen, determined from Eqs. 4.39 and 4.43:

$$[\delta E]_{2S_{1/2}} - [\delta E]_{2P_{1/2}} = 1039.31 - (-12.88) = 1052.19\,\text{MHz}, \tag{4.44}$$

which may be compared to the experimental value of 1057.845(9) MHz. Equation

4.44 is conventionally given the following qualitative gloss.

- The vacuum polarization diagram contributes to the Lamb shift in electronic hydrogen with a negative sign, because the virtual-pair creation associated with the vacuum polarization correction increases the strength of the electron's binding.

- The self-energy diagram contributes to the Lamb shift in electronic hydrogen with a positive sign, because the finite spread of the electron associated with the self-energy correction decreases the strength of the electron's binding.

- The overwhelming majority of the Lamb shift in electronic hydrogen is contributed by the first-order radiative corrections of Fig. 4.1.

- The three points above are general features of the Lamb shift for any hydrogenlike bound-state.

- The self-energy contribution dominates the Lamb shift in electronic hydrogen, evidenced by the fact $[\delta E]_{2S_{1/2}} - [\delta E]_{2P_{1/2}} > 0$. This is however not a general feature of hydrogenlike bound-states. Notably: the vacuum polarization contribution dominates the Lamb shift in muonic hydrogen, a consequence of m_μ being a factor of 200 larger than m_e. See Section 6.1.

Section 6 compares the electronic and muonic Lamb shifts. Section 7 discusses the Lamb shift in deuterium.

5 The full Lamb shift, including *all* effects

5.1 Organization of the contributions to the Lamb shift

Dirac theory treats the nucleus as an infinite-mass point source. Modeling the effects of a *physical* nucleus— chiefly, the effects of its finite mass and size, its nuclear polarizability, and its spin— corrects the Dirac spectrum and further breaks the

degeneracy with respect to ℓ, broken already by the leading radiative corrections and the Darwin-Foldy term. The finite-mass corrections are referred to as recoil corrections. The finite-size and polarizability corrections are referred to as nuclear-structure corrections. The subset of nuclear-spin corrections accounting for the relative orientation of the lepton and nucleus spins are referred to as hyperfine-splitting corrections. We postpone discussion of the hyperfine splitting corrections until Sec. 5.7.

The perturbation theory is rather intricate, with expansions in $(Z\alpha)$ (relativistic corrections), (α/π) (radiative corrections), and (m/M) (recoil corrections) to keep straight. Experimental precision ultimately determines where the perturbative expansions are truncated. Convergence of the various perturbative series is seldom discussed but potentially problematic: see Sec 9.

Equation 4.11 suggests all contributions to the Lamb shift contain a common factor $m(Z\alpha)^4 \sim R_\infty \cdot (Z\alpha)^2$, which turns out to be the case. The leading radiative corrections are of order $m(Z\alpha)^4(\alpha/\pi)$, the leading recoil correction is of order $m(Z\alpha)^4(m/M)$, and the leading nuclear-size correction is of order $m(Z\alpha)^4 < r^2 >$, where $< r^2 >$ is the rms charge radius of the nucleus.

The radiative corrections are calculated at fixed order in the relativistic expansion of Eq. 4.7 since, at fixed order in the relativistic expansion, all radiative corrections, $\sim (\alpha/\pi)^\ell$, are assumed to originate from the same distances.[14] The higher-order radiative corrections follow the same template as the first-order corrections calculated above and are conventionally split into an F_1 contribution and an F_2 contribution, with the F_1 contribution further split into a vacuum polarization contribution and a self-energy contribution. Hadronic vacuum polarization contributions and electroweak contributions are considered separately.

Recoil corrections $\sim (Z\alpha)^j \cdot (m/M)^k \cdot m$, organized as a sum over k for fixed j, are split off from radiative-recoil corrections $\sim (Z\alpha)^j \cdot (m/M)^k \cdot (\alpha/\pi)^\ell \cdot m$. The

[14] For high Z atoms, the relativistic corrections are calculated at fixed order in the radiative expansion.

recoil and radiative-recoil corrections account for the essentially two-body nature of hydrogenlike bound-states and give corrections to the energy levels beyond those given by the trick— equivalent to treating the bound-state as a one-body problem— of replacing the lepton mass m with the reduced mass m_r.

Nuclear size and radiative nuclear size corrections are organized in the same way as the recoil and radiative recoil corrections, with corrections $\sim (Z\alpha)^j \cdot m$ and $\sim (Z\alpha)^j \cdot (\alpha/\pi)^\ell \cdot m$, respectively, for $j \geq 4$ and $\ell \geq 1$. Radiative nuclear size corrections are especially important in muonic hydrogen where nuclear size effects give a comparatively large contribution to the energy levels (Sec. 6.3). The recoil and nuclear size corrections vanish in the respective limits of infinite nuclear mass and infinitesimal nuclear size.

Care must be taken at every step of the calculation to avoid double-counting. For instance, the Sachs electric form factor $G_E(Q^2) = F_1(Q^2) - Q^2/4M^2 \cdot F_2(Q^2)$ corrects the Coulomb potential for the finite-size of the nucleus (Sec. 5.4), where $q^2 = -Q^2$ is the mass-squared of the virtual photon probing the nucleus. For $Q^2 << m^2$, $G_E(Q^2) \approx G_E(0) + G'_E(0) \cdot Q^2$. The part of the correction proportional to $G_E(0) = 1$ corresponds to a point-like nucleus and is already implicitly taken into account by the radiative corrections. The part proportional to $G'_E(0)$ receives contributions from $F'_1(0)$ and $F_2(0)$, with $F_2(0)$ the anomalous moment of the nucleus. The $F_2(0)$ contribution is conventionally split off from the $F'_1(0)$ contribution, to separate the effects of the anomalous moment of the nucleus from what are more properly considered 'finite-size' effects. Under this convention, the leading nuclear-size correction, naively proportional to $G_E(Q^2)$, is instead taken to be proportional to $F_1(Q^2) - 1$.

5.2 Higher-order radiative corrections

Equation 4.36 gives the total energy shift due to the leading radiative corrections to the energy (Fig. 4.1). The corrections are of order $\alpha(Z\alpha)^4$. The first term of Eq.

4.36 is obtained from the next-to-leading contributions to F_1;[15] the second term, from the next-to-leading contribution to F_2.

Similarly, the corrections of order $\alpha^n(Z\alpha)^4$ $(n \geq 1)$ are obtained from the N^nLO contributions to F_1 and F_2. Here N^nLO refers to the nth-order beyond the (trivial) leading order contributions to F_1 and F_2.

The corrections of order $\alpha^n(Z\alpha)^5$ have the added complication of being induced by diagrams with two exchange photons, while corrections of order $\alpha^n(Z\alpha)^6$ have at least three exchange photons.

5.3 Recoil corrections

Radiative corrections are calculated using the external field approximation, in which the nucleus is taken to be infinitely heavy. Recoil (and radiative-recoil) corrections account for the finite mass M of the nucleus and the "truly relativistic two-body nature of the bound-state problem".

The Breit potential— which is the name given to the first-order relativistic corrections to the non-relativistic two-particle Hamiltonian of Eq. 4.10— generates all corrections to the energy levels of order $(Z\alpha)^4$. These corrections are shown in Eq. 4.11. The mass-dependence of Eq. 4.11 is exact. The nth-order relativistic corrections $(n > 1)$ generate additional corrections of order $(Z\alpha)^{2(n+1)}$.[16] However the recoil corrections that emerge from these nth-order relativistic corrections are not complete.

As a case in point, the leading nontrivial recoil correction appears at order $(Z\alpha)^5(m/M)$ and is therefore not a part of the Breit spectrum. The correction is instead generated, in the high-energy regime, by two-photon exchange diagrams. The origin of the correction is discussed in App. G. The Breit spectrum also misses recoil corrections of order $\geq (Z\alpha)^6$, some of which are relevant to the phenomenology.

[15] The next-to-leading contributions to F_1 include contributions from the one-loop self-energy and vacuum polarization diagrams.

[16] Recall that $E = \sqrt{p^2 + m^2} = m[1+1/2(p^2/m^2)-1/8(p^2/m^2)^2+...]$ and $p^2/m^2 \sim m(Z\alpha)^2/m^2 \sim (Z\alpha)^2$.

5.4 Nuclear structure corrections

Finite size corrections

The elastic scattering amplitude for a virtual photon incident on a proton is

$$i\mathcal{M} = -ie\bar{U}(P', S')[F_1(q^2)\gamma_\mu + F_2(q^2)\frac{i\sigma_{\mu\nu}}{2m_P}q_\nu]U(P, S)\cdot\epsilon_\mu. \tag{4.45}$$

m_P is the mass of the proton, P (S), P' (S'), are the four-momenta (spin) of the incoming proton and outgoing proton, and $q = P' - P$ is the four-momentum of the virtual photon. As before (Eq. 3.14), the quantity in brackets represents the most general possible parity-invariant and gauge-invariant Lorentz structure for the three-point vertex in QED.

Equation 4.45 can be written more compactly as

$$i\mathcal{M} = -ie < P'|J_\mu|P > \cdot\epsilon_\mu, \tag{4.46}$$

where J_μ is the current to which the virtual photon couples. In the Breit frame (discussed below), the longitudinal polarization vector $\epsilon^L_\mu = (q_3, 0, 0, q_0)/\sqrt{-q^2}$ reduces to $(1, 0, 0, 0)$. Hence,

$$< P'|J_\mu|P > \cdot\epsilon^L_\mu =< P'|J_0|P > \equiv < J_0 > . \tag{4.47}$$

$< J_0 >$ is a Lorentz-invariant object *resembling* the (Fourier transform of) the proton's electric charge density. We are interested principally in how the Coulomb potential is modified as a consequence of this 'proton charge density'— or equivalently, how the Coulomb potential is modified as a consequence of the finite size of the proton.

From Eq. 4.45

$$< J_0 >= \bar{U}(P')[(F_1(q^2) + F_2(q^2))\gamma_0 - F_2(q^2)\frac{E_P}{m_P}]U(P). \tag{4.48}$$

With the textbook identities $\bar{U}(P')\gamma_0 U(P) = 2m_P$ and $\bar{U}(P')U(P) = 2E_P$, Eq. 4.48 becomes

$$\begin{aligned} < J_0 >&= 2m_P[F_1(q^2) - \frac{\vec{P}^2}{m_P^2}F_2(q^2)] \\ &= 2m_P[F_1(q^2) + \frac{q^2}{4m_P^2}F_2(q^2)] \\ &\equiv 2m_P G_E(q^2). \end{aligned} \tag{4.49}$$

The second equality uses the relations $\vec{P} = -\vec{P}'$ and $E_P = E_{P'}$, which hold in the Breit frame. The third equality uses the definition of the Sachs electric form factor $G_E(q^2) = F_1(q^2) + \frac{q^2}{4m_P^2}F_2(q^2)$.

For the Coulomb potential, Eq. 4.48 reduces to

$$< J_0 >= \bar{U}(P')\gamma_0 U(P) = 2m_P. \tag{4.50}$$

Comparing Eqs. 4.49 and 4.50, we see the Coulomb potential receives a correction due to the finite size of the proton, where

$$V = \frac{e^2}{q^2} \quad \rightarrow \quad V = \frac{e^2}{q^2} \cdot G_E(q^2). \tag{4.51}$$

For q^2 suitably small, the modified Coulomb potential can be approximated as

$$V \approx \frac{e^2}{q^2} \cdot [G_E(0) + q^2 \cdot \frac{dG_E(q^2)}{dq^2}|_{q^2=0}, \tag{4.52}$$

where $G_E(0) = F_1(0) = 1$. The shift in the Coulomb potential due to the finite size of the proton is then

$$\delta V = 4\pi\alpha \cdot \frac{dG_E(q^2)}{dq^2}|_{q^2=0}. \tag{4.53}$$

The convention in the literature is to interpret G_E in the Breit frame as the Fourier transform of the proton's electric charge density:

$$G_E(q^2 \rightarrow -\vec{q}^2) = \int d^3\vec{r} e^{i\vec{q}\cdot\vec{r}} \rho(|\vec{r}|). \tag{4.54}$$

The argument of G_E connotes a shift to the Breit frame. (q^2 equals $-\vec{q}^2$ in the Breit frame.) The issue with Eq. 4.54 is that the actual scattering event, of photon on proton, is dynamical: the photon probe disturbs the proton target. In the Breit frame $q_0 = 0$ and $\vec{P} = -\vec{P}'$ so that the proton in and out states are similarly Lorentz contracted.[17] Referring the scattering event to the Breit frame effectively— but not totally— deconvolves recoil effects (due to the probe) from internal structure effects (which exist in the proton independent of the scattering). Equation 4.54 is thus valid up to effects induced by the photon probe on the proton target. With this understanding, we return to Eq. 4.54.

For small $\vec{q}^2$,

$$\begin{aligned} G_E(-\vec{q}^2) &= \int d^3\vec{r}\,[1 - i\vec{q}\cdot\vec{r} - \frac{1}{2}(\vec{q}\cdot\vec{r})^2 + ...]\,\rho(r) \\ &\approx 1 - \frac{1}{2}\vec{q}^2 \int d\Omega\, d^3r\; r^2\rho(r) cos\theta \\ &= 1 - \frac{2\pi}{3}\vec{q}^2 \int d^3r\; r^2\rho(r) \\ &= 1 - \frac{1}{6}\vec{q}^2 \int d^3\vec{r}\; r^2\rho(r) \equiv 1 - \frac{1}{6}\vec{q}^2 < r^2 >, \end{aligned} \tag{4.55}$$

where $r = |\vec{r}|$ and $< r^2 >= \int d^3\vec{r}\; r^2\rho(r)$ is the proton charge radius squared.

From Eq. 4.55,

$$\frac{dG_E(0)}{d\vec{q}^2} = -\frac{1}{6} < r^2 > . \tag{4.56}$$

The left- and right-hand sides of Eq. 4.56 transform as three-vectors squared. We can promote $dG_E(0)/d\vec{q}^2$ to a Lorentz scalar simply by replacing $\vec{q}^2$ with $-q^2$. (Recall that $q^2 = -\vec{q}^2$ in the Breit frame.) The Lorentz-invariant quantity $6\frac{dG_E(0)}{dq^2}$ can then be interpreted in the Breit frame as the proton charge radius squared. The convention in the literature however is to attach the label r_p^2 to $6\frac{dG_E(0)}{dq^2}$, regardless of the choice of frame.

[17] The Breit frame conditions $q_0 = 0$ and $\vec{P} = -\vec{P}'$ imply that, in the Breit frame, the proton scatters off the photon as if the photon were a brick wall. The Breit frame is thus sometimes called the 'brick wall' frame.

Plugging $\frac{dG_E(0)}{dq^2} = \frac{1}{6} r_p^2$ into Eq. 4.57 and Fourier transforming finds

$$\delta V \approx \frac{2\pi}{3}\,\alpha\, r_p^2\, \delta(\vec{r}). \tag{4.57}$$

Due to the delta function, the leading finite-size correction $\Delta E =< \psi|\delta V|\psi >= \frac{2\pi}{3}\,\alpha\, r_p^2\, |\psi(0)|^2 > 0$ contributes only to S-states. ΔE is positive, because the finite size correction smears out the proton's electric charge. The electron is thus bound less tightly to the smeared-out proton than it would be to a pointlike proton.

The next-order nuclear-size correction $\sim (Z\alpha)^5$ comes from two-photon-exchange diagrams (Fig. 4.2) with one and two insertions of $(F_1(q^2) - 1)\gamma_\mu$. (An insertion of the form $F_1(q^2)\gamma_\mu + F_2(q^2)\frac{i\sigma_{\mu\nu}}{2m_P} q_\nu$ includes contributions from both the pointlike nucleus and the anomalous moment of the nucleus. Those contributions are (sensibly) conventionally included with the radiative corrections.)

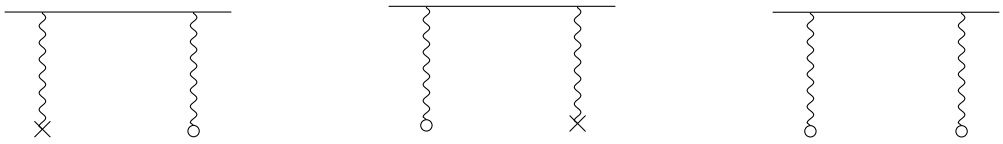

Figure 4.2: Next-to-leading nuclear size correction with one insertion and two insertions of $(F_1(q^2) - 1)$. An empty dot indicates an insertion of $(F_1(q^2) - 1)$.

In the external field approximation, the loop integrals associated with the two-photon-exchange diagrams reduce to $\int_0^\infty \frac{dq}{q^4}(F_1(q^2)-1)$ (one insertion) and $\int_0^\infty \frac{dq}{q^4}(F_1(q^2)-1)^2$ (two insertions). The total $\mathcal{O}((Z\alpha)^5)$ nuclear size correction is

$$\Delta E = -\frac{m(Z\alpha)^5}{3n^3} m_r^3 < r^3 >, \tag{4.58}$$

where $< r^3 >$ is the third Zemach moment:

$$< r^3 >= \int d^3r_1 d^3r_2 \rho(r_1)\rho(r_2)|\vec{r}_1 + \vec{r}_2|^3. \tag{4.59}$$

For electronic hydrogen, Eq. 4.58 gives a correction $\Delta E(1S) \approx 40\ Hz$.

Nuclear polarizability corrections

The leading nuclear polarizability corrections appear at order $(Z\alpha)^5$— the same order as the second-order contributions to the nuclear-size correction. The nuclear polarizability corrections account for the effects of inelastic intermediate nuclear states. The leading diagrams have two exchange photons; see Fig. 4.3.

Figure 4.3: Leading nuclear polarizability corrections.

The diagrams of Fig. 4.3 contribute corrections of the form

$$\Delta E \sim -|\psi(0)|^2 \cdot \alpha \int \frac{d^4k}{(2\pi)^4} \frac{D_{im} D_{jn}}{k^4} \frac{tr[\gamma_i(1+\gamma_0)m - \hat{k}]}{k^2 - 2mk_0} M_{mn}. \tag{4.60}$$

The loop generating the integral of Eq. 4.60 consists of the two exchange photons ($\frac{D_{im}D_{jn}}{k^4}$), the lepton propagator ($\frac{tr[\gamma_i(1+\gamma_0)m-\hat{k}]}{k^2-2mk_0}$), and the photon-nucleus inelastic forward Compton amplitude (M_{mn}). The factor of α comes from the two photon insertions in the lepton line, while the factor of $|\psi(0)|^2$ indicates Eq. 4.60 contributes only to S-states. A factor of $Z^2\alpha$ is hidden in M_{mn}.

ΔE is negative for typical parameterizations of M_{mn}. The lepton in the bound state polarizes the nucleus. The attraction of the lepton to the induced nuclear dipole increases the binding energy (decreasing the energy). For electronic hydrogen, $\Delta E(nS) \sim -100/n^3\ Hz$.

5.5 Hadronic corrections

The leading hadronic vacuum polarization (HVP) diagram is shown in Fig. 4.4. The diagram gives a correction of order $\alpha(Z\alpha)^4$— the same order as the leading electron and muon vacuum polarization diagrams. The HVP insertion of Fig. 4.4

modifies the Coulomb potential according to Eq. 3.40, with

$$V = -\frac{e^2}{\vec{q}^2} \quad \rightarrow \quad V = -\frac{e^2}{\vec{q}^2(1 - \Pi(-\vec{q}^2))}. \tag{4.61}$$

For $|\vec{q}|^2 << m^2$, the right-hand side of Eq. 4.61 can be approximated as

$$V = -\frac{e^2}{\vec{q}^2}(1 + \vec{q}^2 \cdot \Pi'(0)), \tag{4.62}$$

where $\Pi'(0) = d\Pi(-\vec{q}^2)/d\vec{q}^2|_{\vec{q}^2=0}$.

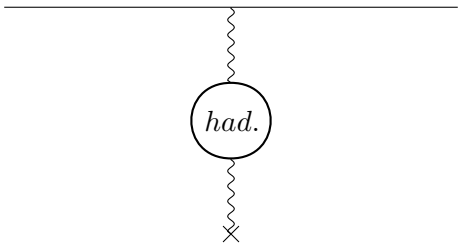

Figure 4.4: Leading hadronic vacuum polarization correction.

The correction to the Coulomb potential due to Equation 4.62 is thus

$$\delta V = -4\pi\alpha\Pi'(0)\delta(\vec{r}). \tag{4.63}$$

The corresponding correction to the energy levels is

$$\Delta E = < \psi|\delta V|\psi > = -4\pi\alpha\Pi'(0)|\psi(0)|^2. \tag{4.64}$$

A numerical value for $\Pi'(0)$ can be obtained through Eqs. 3.41 and 3.46. The sign of ΔE is negative for the reasons discussed in Sec. 4.3.

5.6 Electroweak corrections

The leading contribution to the energy levels due to the weak interaction is given by the diagram of Fig. 4.5. The diagram generates a correction

$$\Delta E \approx -7.7 \times 10^{-13} \frac{\alpha (Z\alpha)^3 m_r}{\pi n^3} \delta_{\ell 0}, \tag{4.65}$$

which is negligible for phenomenological purposes.

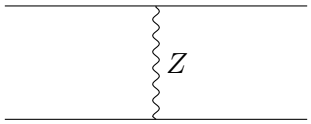

Figure 4.5: Leading electroweak correction.

5.7 Hyperfine splitting corrections

The hyperfine splitting (hfs) corrections account for the relative orientation of the lepton and nucleus spin vectors. The hfs corrections are responsible for the splitting of the $1S_{1/2}$ state into $1S_{1/2}^{F=0}$ and $1S_{1/2}^{F=1}$ states. We will discuss the splitting in detail below, beginning with a qualitative picture. The $1S_{1/2}^{F=0} - 1S_{1/2}^{F=1}$ transition holds a similar standing in the hfs literature as the $2S_{1/2} - 2P_{1/2}$ transition does in the Lamb shift literature.

A system with a spin-1/2 lepton bound to a spin-1/2 nucleus can be a represented as a linear combination of four basis states: a spin singlet state $((\uparrow\downarrow - \downarrow\uparrow)/\sqrt{2})$ corresponding to $F = 0$ and three spin triplet states $(\uparrow\uparrow,\ (\uparrow\downarrow + \downarrow\uparrow)/\sqrt{2},\ \downarrow\downarrow)$ corresponding to $F = 1$. The spin singlet state has spin-0. Its lepton and nucleus spin vectors are nominally anti-aligned, while its lepton and nucleus *currents* are nominally aligned.[18] The spin triplet states have spin-1, with lepton and nucleus spin vectors (currents) nominally aligned (anti-aligned).

By the rule that parallel currents attract each other and anti-parallel currents

[18] Here, $current := charge \times spin - vector$.

repel each other, we then expect the spin singlet state ($F = 0$) to have lower energy than the spin triplet states ($F = 1$).

The leading hfs correction is due to the interaction of the magnetic moment of the nucleus $\vec{\mu}_N$ with the magnetic field generated by the lepton magnetic moment. The interaction Hamiltonian is given by

$$\Delta H = -\vec{\mu}_N \cdot \vec{B}, \tag{4.66}$$

where $\vec{B}$ can be obtained from $\vec{A}_{dip}$ of Eq. 3.3.

A naive calculation of $\vec{B} = \vec{\nabla} \times \vec{A}_{dip}$ finds

$$\vec{B} = -\frac{\mu_0}{4\pi r^3}[\vec{\mu}_\ell - 3\frac{(\vec{r} \cdot \vec{\mu}_\ell)}{r^2}\vec{r} - \frac{e}{m}\vec{L}]. \tag{4.67}$$

$\vec{B}$ of Eq. 4.67 however is not the $\vec{B}$ of Eq. 4.66. The $\vec{B}$ of Eq. 4.66 receives an additional contribution

$$\delta\vec{B} = \frac{2}{3}\mu_0 \vec{m}\delta(\vec{r}), \tag{4.68}$$

which is due to Fermi. Here $\vec{m}$ is the magnetic (dipole) moment of the lepton. Equation 4.68 can be derived by integrating $\int_{r<R} d^3r(\vec{\nabla}\times\vec{A}_{dip})$ under the assumption that the lepton current is isolated to a ball of radius R.

Equations 4.66-4.68 then give

$$\Delta H = \frac{\mu_0}{4\pi}[-\frac{8\pi}{3}\vec{\mu}_\ell \cdot \vec{\mu}_N \delta(\vec{r}) + \frac{1}{r^3}[\vec{\mu}_\ell \cdot \vec{\mu}_N - 3\frac{(\vec{r} \cdot \vec{\mu}_\ell)(\vec{r} \cdot \vec{\mu}_N)}{r^2} - \frac{e}{m}\vec{L} \cdot \vec{\mu}_N]], \tag{4.69}$$

where $\vec{\mu}_\ell = g_\ell \frac{e}{2m}\vec{S}_\ell$ and $\vec{\mu}_N = g_N \frac{e}{2M}\vec{S}_N$. For S-states, only the first term of Eq. 4.69 contributes to the energy. For all other states, only the second term contributes.

The splitting between the $1S_{1/2}^{F=0}$ and $1S_{1/2}^{F=1}$ states is thus

$$E(1S_{1/2}^{F=1}) - E(1S_{1/2}^{F=0}) = -\frac{\mu_0}{4\pi}\frac{8\pi}{3}|\psi(0)|^2[< \vec{\mu}_\ell \cdot \vec{\mu}_N >^{F=1} - < \vec{\mu}_\ell \cdot \vec{\mu}_N >^{F=0}], \tag{4.70}$$

where $< \vec{S}_\ell \cdot \vec{S}_N >= -3/4\hbar^2$ for the spin singlet state ($F = 0$) and $1/4\hbar^2$ for the spin triplet states ($F = 1$).[19] Algebra then finds

$$E(1S_{1/2}^{F=1}) - E(1S_{1/2}^{F=0}) = \frac{8}{3}(1 + a_\ell)(1 + a_N)\frac{m}{M}(Z\alpha)^4(\frac{m_r}{m})^3 mc^2 \equiv (1 + a_\ell)E_F, \tag{4.71}$$

where a_ℓ and a_N are the anomalous moments of the lepton and nucleus, respectively, and the factor E_F is the skeleton that the hfs perturbation theory organizes itself around. Note: $E(1S_{1/2}^{F=1}) - E(1S_{1/2}^{F=0})$ is positive, as expected, and evaluates to zero for $\delta\vec{B} \to 0$.

Higher-order hfs corrections can be systematically introduced in the same way as the higher-order corrections of the Lamb shift, namely, via expansions in α, $Z\alpha$, and (m/M).

- Relativistic corrections are given by the matrix element $\Delta E =< n|\gamma_0\vec{\gamma}\vec{A}|n >$, where $|n >$ are Dirac-Coulomb eigenkets and $\vec{A}$ is the vector potential generated by the magnetic moment of the nucleus.

- The dominant radiative corrections are generated by lepton self-energy corrections at the lepton-photon vertex. These corrections take the form $\Delta E = a_\ell E_F$, as can be seen from Eq. 4.71. Vacuum polarization contributions are negligible for electronic hydrogen and heavily suppressed for muonic hydrogen.

- The leading nuclear structure and recoil effects appear at order $Z\alpha E_F$.

The precision of the hfs measurements in electronic hydrogen is higher than the precision of hfs theory. As a consequence, eH transition frequency measurements are referred to a hyperfine centroid prior to being compared to eH theory. The procedure removes hfs theory corrections from the phenomenology. The eH theory appearing in the reference scheme, for example, contains no hfs corrections.

[19] $\vec{S} = \vec{S}_\ell + \vec{S}_N$ is the total spin. Then, $\vec{S}_\ell \dot{\vec{S}}_N = 1/2(\vec{S}^2 - \vec{S}_\ell^2 - \vec{S}_N^2)$, where $S_{\ell,N} = \sqrt{1/2(1/2+1)}\hbar$ and $S(F+1) = \sqrt{1(1+1)}\hbar$ and $S(F=0) = 0$.

The hyperfine splittings in muonic hydrogen have not yet been measured. μH transition frequencies must be compared directly to a representation of μH theory that includes all hfs corrections down to a given size.

6 eH theory versus μH theory

The three primary differences between electronic hydrogen (eH) theory and muonic hydrogen (μH) theory are a consequence of the muon being about 200 times heavier than the electron. We list the differences below and then discuss each in turn.

- *Electron vacuum polarization corrections.* Radiative corrections generated by electron loops are much larger in μH than in eH.
- *Self-energy corrections.* Self-energy corrections are much larger in eH than in μH.
- *Nuclear size corrections.* The leading nuclear size correction is the second-largest contribution to the Lamb shift in μH but stands as a small effect among (competing) small effects in the Lamb shift in eH.

6.1 Electron vacuum polarization corrections

Following Pachucki [51], we introduce parameters $\beta_\mu = m_e/\mu_\mu\alpha$ and $\beta_e = m_e/\mu_e\alpha$, where μ_μ and μ_e correspond respectively to the reduced mass of μH and eH. β_μ is of order 1, while $\beta_e \sim 1/\alpha$. The parameters β_ℓ ($\ell = e, \mu$), as we will see, are useful for explaining why the electron loop contributions to the muonic Lamb shift are much larger than electron loop contributions to the electronic Lamb shift.

We consider the leading electron-loop contribution to the Lamb shift in eH and μH, corresponding to an electron loop insertion in the tree-level Coulomb exchange diagram. The electron loop insertion modifies the Coulomb potential such that

$$V(-\vec{q}^2) = -\frac{e^2}{\vec{q}^2} \quad \to \quad V(-\vec{q}^2) = -\frac{e^2}{\vec{q}^2(1-\hat{\Pi}_2(-\vec{q}^2))}. \tag{4.72}$$

$\hat{\Pi}_2(-\vec{q}^2) = \Pi_2(-\vec{q}^2) - \Pi_2(0)$ is related to the non-trivial part of the electron-loop polarization tensor, which takes the form $\Pi_2^{\mu\nu} = (q^2 g^{\mu\nu} - q^\mu q^\nu)\Pi_2(q^2)$. Equation 4.72 is motivated in the discussion preceding Eq. 3.40 and given further context throughout Sec. 5.1. The exact form of $\hat{\Pi}_2(-\vec{q}^2)$, obtained by calculating the electron loop, is not important for present purposes.

The modified Coulomb potential in position space is

$$V(\vec{r}) = -\int \frac{d^3q}{(2\pi)^3} e^{i\vec{q}\cdot\vec{r}} \frac{e^2}{\vec{q}^2(1-\hat{\Pi}_2(-\vec{q}^2))}. \tag{4.73}$$

Performing the angular integration finds

$$V(\vec{r}) = \frac{ie^2}{(2\pi)^2 r}\int_0^{+\infty} dq\, q \frac{e^{iqr}}{q^2+\mu^2}[1+\hat{\Pi}_2(-q^2)], \tag{4.74}$$

where $q = |\vec{q}|$, $r = |\vec{r}|$, and a fictitious photon mass μ has been introduced to regulate the integral. The pole at $q = i\mu$ recovers the Coulomb potential in the limit $\mu \to 0$. Additionally, $\hat{\Pi}_2(-q^2)$ has a branch cut starting at $q = 2im_e$, which gives a contribution $\delta V(\vec{r})$ to $V(\vec{r})$:

$$\begin{aligned}
\delta V(\vec{r}) &= \frac{ie^2}{(2\pi)^2 r}\int_2^{+\infty} \frac{dQ}{Q}\, e^{-m_e Q r}\, Disc.\, \hat{\Pi}_2(Q^2) \\
&= \frac{ie^2}{(2\pi)^2 r}\int_2^{+\infty} \frac{dQ}{Q}\, e^{-m_e Q r}\, 2iIm\hat{\Pi}_2(Q^2) \\
&= -\frac{\alpha}{\pi r}\int_4^{+\infty} \frac{dQ^2}{Q^2}\, e^{-m_e Q r}\, Im\hat{\Pi}_2(Q^2),
\end{aligned} \tag{4.75}$$

where $Q = -iq/m_e$.

The first-order contribution of $\delta V(\vec{r})$ to the Lamb shift is

$$E_{eVP}(2P) - E_{eVP}(2S) = \int d^3r \delta V(\vec{r})(\rho_{2P} - \rho_{2S}), \tag{4.76}$$

where $\rho_{2S} = |R_{20}|^2$, $\rho_{2S} = |R_{21}|^2$, and R_{20} and R_{21} are the radial wave functions for the $2S$ and $2P$ states, respectively.

Computing the integral with respect to r finds

$$E_{eVP}(2P) - E_{eVP}(2S) = \mu_\mu (Z\alpha)^2 \frac{1}{\pi} \int_4^\infty \frac{dQ^2}{Q^2} Im\hat{\Pi}_2(Q^2) \frac{(\beta_\ell Q)^2}{2(1+\beta_\ell Q)^4}, \qquad (4.77)$$

where the contribution of $E_{eVP}(2P) - E_{eVP}(2S)$ to the electronic (muonic) Lamb shift replaces β_ℓ with β_e (β_μ).

For $\beta_\ell = \beta_e \sim 1/\alpha$, $E_{eVP}(2P) - E_{eVP}(2S)$ is of order α^5. For $\beta_\ell = \beta_\mu \sim 1$, however, $E_{eVP}(2P) - E_{eVP}(2S)$ is only of order α^3. (Note: $Im\hat{\Pi}_2(Q^2)$ is hiding a factor of α, which comes from the electron loop.) The leading electron loop contribution to the Lamb shift in μH is effectively enhanced by a factor of $1/\alpha^2$ relative to the leading electron loop contribution to the Lamb shift in eH. Equation 4.77 gives by far the largest contribution to the Lamb shift in μH, contributing e.g. 205.006 meV to $E(2P_{1/2}) - E(2S_{1/2}) \approx 202\ meV$ in μH.

The physical picture behind Eq. 4.77 is the following. The Coulomb potential is strongly distorted by vacuum polarization insertions only within a radius of about a Compton wavelength $\sim 1/m_e$ of the nucleus. Muonic hydrogen has a Bohr radius $a_0(\mu H) = \frac{1}{m_\mu \alpha} \approx \frac{1}{200\alpha}\frac{1}{m_e}$ of roughly the same size as the Compton wavelength—meaning, the muon spends a significant proportion of its time in the region in which the Coulomb potential is strongly distorted. By contrast, the Bohr radius of electronic hydrogen $a_0(eH) = \frac{1}{m_e \alpha}$ is much larger than the Coulomb wavelength, so the electron spends comparatively little time in the region of strongly distorted Coulomb potential.

6.2 Self-energy corrections

Self-energy corrections smear out the wavefunctions of the electron in eH and the muon in μH. The self-energy corrections are accommodated within quantum field theory by shifting the Feynman rule for the three-point vertex in QED from $-ie\gamma_\mu$ to $-ie\Gamma_\mu = -ie(F_1(q^2)\gamma_\mu + \frac{i\sigma_{\mu\nu}}{2m} q_\nu F_2(q^2))$, where m is the mass of the electron or muon and q_μ is the four-momentum of the virtual photon mediating the Coulomb

interaction.

For simplicity, we consider an eH or μH atom in a state with $\ell = 0$. Its energy is independent of $F_2(q^2)$; see Eq. 4.38 and the discussion surrounding it. We thus take $-ie\Gamma_\mu = -ieF_1(-\vec{q}^2)\gamma_\mu$. The self-energy corrections modify the Coulomb potential such that

$$V(-\vec{q}^2) = -\frac{e^2}{\vec{q}^2} \quad \rightarrow \quad V(-\vec{q}^2) = -\frac{e^2 F_1(-\vec{q}^2)}{\vec{q}^2}. \tag{4.78}$$

Fourier transforming the modified Coulomb potential on the right-hand side of Eq. 4.78 while expanding $F_1(-\vec{q}^2)$ about $\vec{q}^2 = 0$ finds

$$V(\vec{r}) \approx -\frac{\alpha}{r} - 4\pi\alpha \frac{dF_1(-\vec{q}^2)}{d\vec{q}^2}|_{\vec{q}^2=0}\delta(\vec{r}), \tag{4.79}$$

where the first term is the Coulomb potential and the second term is the modification of the Coulomb potential due to the self-energy corrections. The factor $\frac{dF_1(-\vec{q}^2)}{d\vec{q}^2}$ in the second term is proportional to the charge-radius-squared of the electron in eH or the muon in μH (cf. Eq. 4.57).

The leading self-energy correction to the $\ell = 0$ energy levels in eH (μH) is proportional to m_e (m_μ); see Eq. 4.38. The shift in the Coulomb potential due to the leading self-energy correction is thus proportional to $1/m_e^2$ in eH and $1/m_\mu^2$ in μH. These facts, together with Eq. 4.79, imply

$$\frac{dF_1(-\vec{q}^2)}{d\vec{q}^2}|_{\vec{q}^2=0} \quad \propto \quad < r_\ell^2 > \quad \propto \quad 1/m_\ell^2, \tag{4.80}$$

where $< r_\ell^2 >$ is the charge-radius-squared of lepton ℓ, with ℓ corresponding to the electron in eH or the muon in μH. The upshot of Eq. 4.80 is: the muon's charge in a μH atom is spread over a much smaller volume than the electron's charge in an eH atom. Consequently the leading self-energy correction (Fig. 4.1), which we saw in Sec. 4.3 comprises the bulk of the Lamb shift in electronic hydrogen, comprises only a small part of the Lamb shift in muonic hydrogen.

6.3 Nuclear size corrections

The comparatively small Bohr radius of muonic hydrogen implies the muon in μH is more sensitive to the finite-size of the nucleus than the electron in eH. The leading nuclear size correction (Eq. 4.57), which comprises about 2% of the Lamb shift in μH, comprises only about $(m_e/m_\mu)^2 \cdot 2\% \sim 0.01\%$ of the Lamb shift in eH.

7 Deuterium theory

Deuterium consists of an electron bound to a deuteron, with the deuteron composed of a proton and a neutron. Deuterium thus has $Z = 1$. The primary differences between deuterium theory and hydrogen theory[20] relevant to atomic spectroscopy are the following.

- *The proton in a hydrogen atom is spin-1/2; the deuteron in a deuterium atom is spin-1.*[21] The Darwin-Foldy term (see Eq. 4.11 and subsequent discussion) assumes a spin-1/2 nucleus and does not contribute to the Lamb shift in deuterium.

- *The proton charge radius r_p differs from the deuteron charge radius r_d.* The deuteron charge-radius-squared is conventionally modeled as $r_d^2 = r_p^2 + r_{deut}^2$, where r_{deut}^2 is determined on the basis of the frequency difference between the $1S2S$ transition in electronic deuterium $f_{1S2S,\,eD}$ and the $1S2S$ transition in electronic hydrogen $f_{1S2S,\,eH}$. The frequency difference, commonly referred to as an isotope shift, is measured and compared to theory, and a value for $r_{deut}^2 = r_d^2 - r_p^2$ is extracted. Because r_d is larger than r_p, the nuclear structure corrections (finite size and polarizability) are larger in deuterium than in hydrogen. Within the global fits of Ch. 7, r_d is modeled as $\sqrt{r_p^2 - r_{deut}^2}$.

[20] Hydrogen here refers to eH or μH.

[21] The deuteron in its ground state is in a spin triplet state but an isospin singlet state. The isospin *triplet* is populated by a diproton state, a dineutron state, and an excited deuteron state, all of which are spin singlet states and unstable. Deuterium is, at least empirically, composed of a lepton and a stable, spin-1 nucleus.

Although we could have just as easily defined r_d as a free parameter of the Ch. 7 global fits, independent of r_p. In that case, we would have added the experimental datum for the $1S2S$ isotope shift to the reference set (Table 2.1) to ensure the self-consistency of the fits, viz., to enforce the constraint $r_{deut}^2 = r_d^2 - r_p^2$.

- *The reduced mass of hydrogen differs from the reduced mass of deuterium.*

- *Deuterium spectroscopy is potentially sensitive to new physics that couples to neutrons.* A neutron-nucleus scattering experiment due to Barbieri and Ericson [52] places limits on the size of the coupling of new physics to neutrons: $\frac{g_e g_n}{4\pi} \lesssim 3.4 \times 10^{-11} (\frac{m_X}{MeV})^4$, where m_X is the mass of a scalar boson and g_e (g_n) is the coupling of the new particle to the electron (neutron). The new physics that enters the Ch. 7 global fits is assumed not to couple to neutrons. Alternative assumptions can be investigated using `CONSTANT FINDER`. The new physics entering the global fits is discussed in Ch. 6.

8 The canonical eH spectroscopy experiment: the measurement of the $1S2S$ transition

The measurement of the $1S_{1/2} - 2S_{1/2}$ transition frequency in electronic hydrogen, due to Hansch, et al. [53], has an uncertainty of $10Hz$ (relative precision 4.2×10^{-15}), which is more than two orders of magnitude smaller than the uncertainty of the second-most precisely-measured electronic hydrogen transition frequency (see Table 2.1).

The $1S2S$ measurement proceeded as follows. A 486 nm dye laser was frequency-doubled and introduced into a vacuum chamber where it excited two-photon Doppler-free $1S2S$ transitions in a population of hydrogen atoms prepared in the ground-state. The hydrogen atoms, some fraction of them in the (metastable) $2S$ state, were then conducted a distance of 13 cm into a detection region, where an electric field

nudged the hydrogen atoms in the $2S$ state into the $2P$ state. The hydrogen atoms in the $2P$ state subsequently decayed to the ground state, emitting Lyman-alpha photons which were detected by photomultipliers. The $1S2S$ transition frequency was measured by comparing the frequency of the dye laser at which the number of photomultiplier counts was a maximum to an atomic Cesium clock.

The comparison of the dye laser frequency to the atomic clock involved several steps. First, the frequency of a diode laser was measured using an optical comb, with comb spacing set by the atomic Cesium clock. The second-harmonic of the diode laser was phase locked to the dye laser prior to the measurement, such that the dye laser had a frequency of $7f - 2\Delta f$, while the diode laser had a frequency of $3.5f - \Delta f$. Second, the frequency $4f$ of a doubly frequency-doubled $339\mu m$ He-Ne laser was measured using the optical comb. Third, the dye laser (frequency $7f - 2\Delta f$) and doubly frequency-doubled He-Ne laser (frequency $4f$) were sent through an optical frequency divider located upstream of the optical comb. The output of the optical frequency divider had a frequency of $4f - \Delta f$, which was then measured by the optical comb.

The two-photon $1S2S$ transition frequency corresponds to a frequency of $28f - 8\Delta f$. (Recall that the dye laser, of frequency $7f - 2\Delta f$, was frequency-doubled prior to interacting with the hydrogen.) The $1S2S$ transition frequency was thus reconstructed from the three optical comb frequency measurements and the empirical formula

$$f_{1S2S} = 28f - 8\Delta f = 64(N_2 f_R - f_{c_2}) - 8(N_1 f_R - f_{c_1}), \tag{4.81}$$

where f_R is the comb spacing in units of frequency, N_1 (N_2) is the number of comb spacings between $4f$ and $3.5f - \Delta f$ ($4f - \Delta f$ and $3.5f - \Delta f$), and f_{c_1} (f_{c_2}) is the frequency difference between $4f$ ($4f - \Delta f$) and the nearest tooth on the optical comb.

Equation 4.81 measures the frequency of a particular hyperfine transition of the $1S2S$, namely, the $1S_{1/2}^{F=1} - 2S_{1/2}^{F=1}$. However the final value for the $1S2S$ transition

frequency reported in Ref. [54] and used in the CODATA adjustments corresponds to the hyperfine centroid of the $1S2S$ transition. f_{1S2S} of Eq. 4.81 receives a correction of $f_{hf} = 310712233(13)\,Hz$ [54] to account for the hyperfine splitting of the $1S$ and $2S$ energy levels. The result is

$$f_{1S2S}^{h.f.centroid} = 2466061413187103(46)\,Hz. \tag{4.82}$$

Equation 4.82 was published in the year 2000. The $46\,Hz$ uncertainty of Eq. 4.82 has since shrunk to $10\,Hz$ due to better control of systematic effects.

The $10\,Hz$ uncertainty of the $1S2S$ is an extraordinary achievement. However the theory uncertainty of the $1S2S$ is estimated to be at least $10^4\,Hz$ [55]. An experimental datum with a theory uncertainty (that much) larger than its experimental uncertainty complicates the determination of the fundamental constants. The issue is discussed in Sec. 2.2. Our reference analysis omits the $1S2S$ from the reference set of Table 2.1. The decision to omit the $1S2S$ is discussed in Appendix B. The effects of including the $1S2S$ in the global fit as a function of the value of the theory uncertainty assigned to the $1S2S$ can be evaluated using `CONSTANT FINDER`.

9 The reliability of eH spectroscopy data and theory

A small uncorrected systematic effect, common to all the electronic hydrogen spectroscopy measurements of the reference set (Table 2.1), could explain the proton size puzzle. According to Ref. [56], the systematic effect would only need to be about 10^{-3} times the size of the linewidth. We have no reason, however— apart from the existence of the puzzle itself— to believe such a systematic effect exists.

Regarding the reliability of eH theory: the eH data of the reference set— which reinforce the proton size puzzle; see Line 9 of Table 7.4— have experimental uncertainties at least five times as large as their respective estimated theory uncertainties. To explain the proton size puzzle, any revision to eH theory *consistent with*

the Standard Model would have to be enormously inconsistent with current theory uncertainty estimates. On this basis, we judge eH spectroscopy theory to be reliable (enough).

This judgment should be weighed against the following, however. Consider the two-loop self-energy correction to the eH energy levels.

- *There is significant disagreement about the size of the $B60$ contribution to the two-loop self-energy correction, and the size of the disagreement is (modestly) underreported by CODATA.* The two-loop self-energy correction is organized as

$$\Delta E = m_e(\frac{\alpha}{\pi})^2 \frac{(Z\alpha)^4}{n^3} F(Z\alpha), \tag{4.83}$$

where

$$F(Z\alpha) = B_{40} + (Z\alpha)B_{50} + (Z\alpha)^2[B_{60} + B_{61}L + B_{62}L^2 + B_{63}L^3] + ... \tag{4.84}$$

and $L = ln[(Z\alpha)^{-2}]$.

Jentschura [57] calculated B_{60} for the $1S$ energy level, finding $B_{60}(1S) = -61.6(9.2)$, while Yerokhin [58] calculated $B_{60}(1S) = -127(39)$. The Jentschura value for $B_{60}(1S)$ shifts the $1S$ energy level by $-6.2\,kHz$; the Yerokhin value, by $-12.7\ kHz$. One small higher-order effect is thus responsible for a $6\,kHz$ uncertainty in the $1S$ energy level.

The C14 value for $B_{60}(1S)$ is -81.3(0.3)(19.7). The first number in parentheses represents a state-dependent uncertainty. The second represents a state-independent uncertainty common to all S states. The C14 value for $B_{60}(1S)$ is the average of the Jentschura value for $B_{60}(1S)$ and the result of a second calculation of $B_{60}(1S)$ by Yerokhin [59], which was obtained by extrapolating a numerical calculation of $F(Z\alpha)$ at $Z >> 1$ to $Z = 1$. The magnitude of the second Yerokhin value for $B_{60}(1S)$ ($B_{60}(1S) = -101(15)$) is smaller than the magnitude of the first Yerokhin value, likewise for the uncertainties. The

uncertainties of the $C14$ value for $B_{60}(1S)$ were fixed at half the difference between the Jentschura value for $B_{60}(1S)$ and the second Yerokhin value.

- *The two-loop self-energy correction is not under perturbative control.* Reference [57] specifies values for the $B_{60} - B_{63}$ terms of Eq. 4.83 for the $1S$ energy level:

$$(Z\alpha)^2[B_{60} + B_{61}L + B_{62}L^2 + B_{63}L^3] = (Z\alpha)^2[-61.6 + 476 - 62 + 282]. \quad (4.85)$$

The terms of Eq. 4.85 do not decrease in size. There is every reason to believe the leading log expansion fails. The leading log expansion shows the same pattern for the $2S$ energy level (not shown).

10 The canonical μH spectroscopy experiment: the measurement of the $2S^{F=1}_{1/2} - 2P^{F=2}_{3/2}$ transition

The measurement of the $2S^{F=1}_{1/2} - 2P^{F=1}_{3/2}$ transition in muonic hydrogen was performed by Pohl, et al. at the $\pi E5$ beam-line of the proton accelerator at Paul Scherrer Institute. Muons from a muon beam were stopped in hydrogen gas to form highly excited μH atoms. 99% of the excited μH atoms decayed to the $1S$ state, while the remaining excited μH atoms decayed to the $2S$. A pulsed laser was then brought into contact with the μH atoms, tuned to induce $2S - 2P$ transitions. The μH atoms in the $2P$ state subsequently decayed to the ground state, emitting 1.9-keV X-rays detected using photo-diodes. The $2S^{F=1}_{1/2} - 2P^{F=1}_{3/2}$ transition frequency was determined by tuning the pulsed laser to the frequency that maximized the number of 1.9-keV X-ray counts.

The measured transition frequency was compared to the theory expression for the $2S^{F=1}_{1/2} - 2P^{F=2}_{3/2}$ transition frequency and a value for r_p extracted. The theory expression is

$$E(2S^{F=1}_{1/2} - 2P^{F=2}_{3/2}) = 209.9779(49) - 5.2262r_p^2 + 0.0347r_p^3\, meV, \quad (4.86)$$

with $r_p = \sqrt{< r_p^2 >}\, fm$. The first term of Eq. 4.86 is primarily contributed by the leading electron loop contribution to the muonic Lamb shift (Eq. 4.77). The second term is the total finite-size contribution (Eq. 4.57). The third term is the third Zemach moment (Eq. 4.58). The hyperfine structure corrections included in Eq. 4.86 are reviewed in Martynenko [60]. The various contributions to Eq. 4.86 are collected in Table I of Ref. [61].

The value for the proton charge radius extracted from equating Eq. 4.86 with the value of the measured transition frequency is

$$r_p = 0.84184(67)\, fm, \tag{4.87}$$

which is a few percent smaller than the value from eH spectroscopy reported in $C10$ ($r_p \approx 0.87\, fm$). The discrepancy between these two r_p values was the initial basis for the proton size puzzle. Our paper [62], of the hundreds of papers that followed the announcement of the proton size puzzle, was the first to critically evaluate the $C10$ determination of r_p.

11 The reliability of μH spectroscopy data and theory

The energy levels in muonic hydrogen $\sim m_\mu/n^2$ are well-spaced compared to the energy levels in electronic hydrogen $\sim m_e/n^2$. Morever, the $2S_{1/2}^{F=1} - 2P_{3/2}^{F=2}$ transition in muonic hydrogen has the largest separation of all the $2S - 2P$ muonic hydrogen transitions. As a consequence, the systematic effects accounted for in the Pohl measurement are smaller, as a proportion of signal size, than the systematic effects that must be accounted for in measurements of the Lamb shift in electronic hydrogen.

The μH theory of Eq. 4.86 is likewise reliable on its face. The one-loop electron vacuum polarization contribution and the finite size contribution are the two largest contributions to Eq. 4.86. Uncalculated higher-order terms or calculation mistakes

are unlikely to account for the proton size puzzle. Disagreements about the correct values for the two-photon exchange correction (Sec. 5.4) and the third Zemach moment are responsible for the two largest theory uncertainties. However those theory uncertainties are too small to explain the proton size puzzle. The total theory uncertainty of $E(2S_{1/2}^{F=1} - 2P_{3/2}^{F=2})$ is roughly the same size as the total experimental uncertainty.

Chapter 5

The Compton sector

The Compton wavelength emerges naturally from Schrodinger theory. The Schrodinger equation for an electron in a Coulomb potential is

$$i\hbar\frac{\partial}{\partial t}\psi = (-\hbar^2\frac{\vec{\nabla}^2}{2m_e} - \frac{Ze^2}{4\pi\epsilon_0}\frac{1}{r})\psi, \tag{5.1}$$

which can be rewritten as

$$i\frac{\partial}{c\partial t}\psi = (-\frac{\lambda\!\!\!^{-}}{2}\vec{\nabla}^2 - \frac{\alpha}{r})\psi, \tag{5.2}$$

where $\lambda\!\!\!^{-} \equiv \frac{\hbar}{m_e c}$ and $\alpha \equiv \frac{Ze^2}{4\pi\epsilon_0\hbar c}$. $\lambda = 2\pi\lambda\!\!\!^{-} = \frac{h}{m_e c}$ is the Compton wavelength of the electron, and α is the fine-structure constant. λ and α are free parameters, with α a dimensionless coupling and $\lambda\!\!\!^{-1}$ $[m^{-1}]$, by inspection of Eq. 5.2, effectively a mass.

λ sets the fundamental scale of QED, beyond which QED becomes necessary for the proper description of nature. The standard, handwaving argument is as follows: localizing an electron to within a radius of $\lambda/2$ implies the uncertainty in the electron's energy is large enough to allow for the creation of another particle of the same mass as the electron:

$$\frac{\hbar}{2}\frac{1}{\Delta p} \leq \Delta x \leq \frac{\lambda\!\!\!^{-}}{2} = \frac{1}{2}\frac{\hbar}{m_e c} \quad \rightarrow \quad \Delta p > m_e c \quad \rightarrow \quad \Delta E > m_e c^2. \tag{5.3}$$

λ appears in the Rydberg sector in the definition of the Rydberg constant, tying the Rydberg to the fine-structure constant

$$R_\infty = \frac{\alpha^2}{2\lambda}.$$

Precise values for λ have been determined from atomic interferometry experiments (Sec. 1).

1 The measurement of h/m_{At} $(At = Cs,\ Rb)$

The measurement of a_e by Gabrielse, et al. (Sec. 4) furnishes a prediction for α. However that prediction is not a test of QED. $a_e(exp)$ of Gabrielse is set equal to $a_e(theory;\ \alpha)$ of Kinoshita, and a prediction for α is extracted, testing nothing. To test QED, a second, independent prediction for α— with comparable precision to the Gabrielse prediction— is needed. A series of atomic interferometry experiments have been performed, in part, to fill this void.

At the time of publication of $C14$, the second-most precise determination of α (the determination of Gabrielse being the most-precise) was due to an atomic interferometry experiment by Bouchendira, et al. [24]. The experiment measured the recoil velocity v_r of a Rubidium atom (Rb) after the atom absorbed a photon of momentum $\hbar k$. Here k corresponds to the wave number of the laser stimulating the absorption. A value for h/m_{Rb} was obtained through an expression for the recoil velocity: $v_r = \hbar k/m_{Rb}$, where k is known and v_r is measured. Finally, to pin down a value for α, the definition of the Rydberg constant R_∞ was used:

$$\alpha^2 = \frac{2R_\infty}{c}\frac{m_{Rb}}{m_e}\frac{h}{m_{Rb}}. \tag{5.4}$$

R_∞ is determined to 0.006 ppb precision, while m_{Rb}/m_e is determined to better than 0.1 ppb precision. The value for m_{Rb}/m_e was stitched together from measurements

of the relative masses[1] of the electron and Rubidium, $A_r(e)$ [5] and $A_r(Rb)$[63].

The prediction for α obtained from the Bouchendira measurement and Eq. 5.4 is

$$\alpha^{-1} = 137.035998996(85), \tag{5.5}$$

which has 0.62 *ppb* relative uncertainty, roughly an order of magnitude off the precision of the Gabrielse prediction. The precision of Eq. 5.4 is limited principally by the precision of the measurement of h/m_{Rb} (relative uncertainty 1.2 *ppb*).

Parker, et al. [3] were able to obtain a prediction for α competitive with the Gabrielse prediction using Cesium atoms (Cs). The Parker result was published too late for inclusion in $C14$. The experiment measured h/m_{Cs}, to 0.4*ppb*, finding

$$\alpha^{-1} = 137.035999046(27), \tag{5.6}$$

where α^{-1} was determined on the basis of Eq. 5.4 with Rb replaced everywhere by Cs.

Equation 5.6 can be compared directly to the Gabrielse prediction (Eq. 3.23). The two predictions differ by 2.4σ. A possible explanation for the discrepancy is discussed in Sec. 4, while the Parker experiment is discussed in more detail below.

The Parker, et al. experiment went as follows. Cesium atoms were conducted into an optical trap and accelerated upwards, creating a fountain of Cs atoms. As the Cs atoms fell back to Earth, they were put through an interferometry sequence, which is shown in Fig. 5.1. Counterpropagating laser pulses imparted momentum $2n\hbar k$ ($n = 5$) to the atoms in the fountain, with 50% probability. The atoms in the fountain were thus split into two populations, which we denote $|0>$ and $|n>$. The two populations were split again by a second set of counterpropagating lasers, with $|0> \rightarrow |0>_A + |0>_C$ and $|n> \rightarrow |n>_B + |n>_D$. The populations $|0>_A$ and $|n>_B$ travelled upward; the populations $|0>_C$ and $|n>_D$, downward. The four popu-

[1] Relative masses for Rb and e were determined from measurements of the cyclotron frequency ratios of pairs of ions— C^{6+} and Rb or C^{6+} and e— simultaneously trapped in a Penning trap.

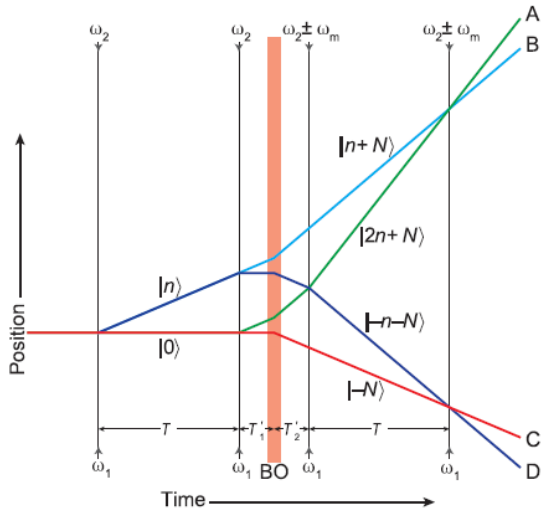

Figure 5.1: Schematic of the atomic interferometry experiment of Parker, et al. [3] used to determine h/m_{Cs}. The experiment is described in the text. The figure is reprinted from [3].

lations were then accelerated via Bloch oscillations[2] which transferred momentum $2N\hbar k$ ($N = 125 - 200$) to the upgoing populations and momentum $-2N\hbar k$ to the downgoing populations. A third and fourth set of laser pulses recombined population $|0>_A$ with population $|n>_B$ and population $|0>_C$ with population $|n>_D$. The phase difference $\Delta\phi_1$ between $|0>_A$ and $|n>_B$ was measured, along with the phase difference $\Delta\phi_2$ between $|0>_C$ and $|n>_D$. To limit systematic effects due to gravity and vibrations, the total phase $\Delta\phi = \Delta\phi_1 - \Delta\phi_2$ was computed. $\Delta\phi$ was then compared to an empirical relation for $\Delta\phi$:

$$\Delta\phi = 16n(n+N)\omega_r T - 2n\omega_m T, \tag{5.7}$$

where T is the time interval between the first and second and third and fourth pulses, ω_r is the photon recoil frequency, equal to $\hbar k^2/2m_{Cs}$, and ω_m is the frequency difference between the first and second pulses. ω_m was tuned so that $\Delta\phi$ equaled

[2] A Bloch oscillation refers to the oscillation of a particle confined to a periodic potential while simultaneously being accelerated by a constant force.

zero, which occurred by inspection of Eq. 5.7 for

$$\omega_m = 8(n+N)\omega_r = 8(n+N)\hbar k^2/2m_{Cs}. \tag{5.8}$$

Since n, N, k, and ω_m were known or measured, a value for h/m_{Cs} could be readily inferred from Eq. 5.8. The result is

$$h/m_{Cs} = 3.0023694721(12) \times 10^{-9} m^s/s. \tag{5.9}$$

Chapter 6

New-physics contributions to the global fit

Incorporating theory alternatives into the global fits of Ch. 7 is an important means of stress-testing Standard Model theory. The theory alternatives can take many guises and need not be particularly well-motivated. Some examples are: replacing the principal quantum number n in the global fit with $n^{1+\delta}$ under a half-baked, MOND-like hypothesis, with δ a free parameter; truncating a given perturbative expansion in the global fit at a given order; doubling all theoretical uncertainties in the global fit; and adding new-physics contributions to the global fit.

Adding new physics to the global fit in general requires theoretical superstructure—relating a term in a Lagrangian to an experimental observable— the other theory alternatives listed above do not. Nevertheless adding new physics to the global fit is straightforward and made easier by the fact any new physics, if it exists, must be weakly-coupled to the Standard Model to evade experimental bounds. As a consequence new physics contributions to the global fit need only be considered at leading order.

The simplest low-energy extensions of the Standard Model hypothesize the existence of a hidden sector which interacts with the Standard Model exclusively through

a so-called portal interaction. A new scalar particle would interact through a scalar portal, a new vector through a vector portal, and so on. We list the most common portal interactions below.

- *Scalar portal*, $\mathcal{L} \supset g\phi\bar{\psi}\psi$.

  ϕ is a scalar field. g gives the coupling of ϕ to Standard Model fermion ψ.[1]

- *Pseudoscalar portal*, $\mathcal{L} \supset \frac{\partial_\mu a}{f_a}\bar{\psi}\gamma_\mu\gamma_5\psi \rightarrow i\frac{m_\psi}{f_a}\, a\bar{\psi}\gamma_5\psi \equiv ig\, a\bar{\psi}\gamma_5\psi$.

  If a is assumed to be an axion, the mass and coupling of a are tightly constrained by astrophysical and cosmological constraints on the axion decay constant f_a and by the details of the strong-CP problem a was introduced to solve. If a is assumed to be merely *axion-like*, which is to say, a generic pseudoscalar, the mass and Standard-Model couplings of a can be treated as free parameters.

- *Neutrino portal*, $\mathcal{L} \supset Y_N LHN$.

  N is a Standard-Model-singlet sterile neutrino, conventionally introduced in connection with the seesaw mechanism [64]. N couples with strength Y_N to Standard Model lepton and Higgs doublets L and H via a Yukawa interaction.

- *Vector portal*, $\mathcal{L} \supset g'\bar{\psi}\gamma_\mu\psi A'_\mu$.

  A'_μ is an electrically neutral vector particle that couples to Standard Model fermion ψ with strength g'. The vector portal interaction is conventionally induced by kinetic mixing between the Standard Model and a hidden sector $U(1)$: see App. I.

In Ch. 7, we explore the effects of these portal interactions (neutrino portal excepted) on Rydberg sector phenomenology. Each portal interaction unambiguously specifies a set of contributions to the global fit, with the mass and Standard Model couplings of the new particle taken as free parameters of the fit. The fit contribu-

[1] A scalar portal interaction coupling ϕ to the Standard Model Higgs is of limited use at low energies but is often introduced at collider energies.

tions for a given portal interaction, particularly at leading order, are very general. A new scalar or vector, for example, adds a Yukawa term to the energy levels of the spectroscopy sector and only for $\ell = 0$ states, while the leading contribution to the spectroscopy sector due to a new pseudoscalar can be neglected altogether. This generality allows us to adopt an essentially bottom-up perspective, in which the analyses of Ch. 7 are carried out with respect to generic new particles with given mass, coupling, and Lorentz structure, rather than in view of specific portal models. We refer to these generic new particles as *no-name bosons*.

The global fits of Ch. 7, which are discussed at length in Ch. 2, test new-physics hypotheses in relation to the null of the Standard Model. If a test indicates a new physics scenario— instantiated by a new particle with given mass, couplings, and Lorentz structure— is a viable alternative to the Standard Model, as determined by $\Delta\chi^2$, a Lagrangian or Lagrangians can always be reverse engineered and a top-down perspective adopted. Having a reason to propose a new-physics scenario *independent of the global fit* is not strictly necessary. The mass and couplings of the new particle favored by the global fit are tantamount to a testable prediction.

Of course, the proton size puzzle and muon $g - 2$ anomaly provide ample reason to introduce new physics into the Rydberg sector, regardless of any global fit. Top-down models, solving the proton size puzzle and/or the muon $g - 2$ anomaly, are everywhere: see Refs. [65, 66, 67, 68, 69, 70, 71, 72]. Top-down models can be parameterized within the global fit as special cases of the bottom-up scalar, pseudoscalar, and vector interactions considered here and in Ch. 7.

A new scalar, pseudoscalar, or vector that couples to Standard Model fermions will in general contribute to the spectroscopy and moments sectors of the global fit.[2] Exactly how is discussed below.

[2]The Compton sector of the global fit consists entirely of the definition for the Rydberg and does not depend on new physics considerations.

1 New-physics contributions to the moments sector

The leading contribution to the electron and muon anomalous magnetic moments due to the interaction of a new scalar, pseudoscalar, or vector X_J ($J = S$, P, V) is shown in Fig. 6.1. Figure 6.1 is identical to the diagram for the leading contributions to a_e and a_μ (Fig. 3.2), except with particle X_J in place of the photon in the loop.

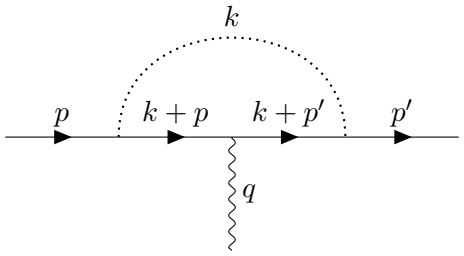

Figure 6.1: The leading contribution to the moments sector of the global fit due to the interaction of a new particle X_J (dotted line) with Standard Model leptons. Subscript J denotes particle X as a scalar S, pseudoscalar P, or vector V.

The calculation proceeds in the same way as textbook calculations of the leading contributions to a_e and a_μ, up to corrections for the Lorentz structure and nonzero mass of X_J. The calculation is sketched below.

The vertex structure of Fig. 6.1 is

$$ie\Gamma^\mu(p,p') = e\cdot g_J^2\int\frac{d^4k}{(2\pi)^4}\frac{1}{k^2-M^2}\{--\}_J\frac{\not{p}'+\not{k}+m}{(p'+k)^2-m^2}\gamma^\mu\frac{\not{p}+\not{k}+m}{(p+k)^2-m^2}\{--\}_J \equiv e\cdot g_J^2\int\frac{d^4k}{(2\pi)^4}\frac{N_J^\mu}{D}, \tag{6.1}$$

where m is the mass of the electron or muon, M is the mass of X_J, and $\{--\}_J = 1$, γ_5, γ_ν for $J = S$, P, V, respectively. The denominator D of Eq. 6.1 is the same for all J.

After the introduction of Feynman parameters and a shift of the loop momentum k, D becomes

$$D^{-1} = \int dxdydz\delta(x+y+z-1)\frac{2}{(\ell-\Delta)^3}, \tag{6.2}$$

where ℓ is the shifted loop momentum, equal to $k + xp + yp'$, and $\Delta = (1-z)^2 m^2 - xyq^2 - M^2 z$.

The calculation of N_J^μ is considerably more involved and entails:

- replacing loop momentum k with shifted loop momentum ℓ;
- making use of the gamma-matrix identities listed in footnote[3] and the Feynman parameter identities listed in footnote [4];
- discarding terms in N^μ linear in ℓ, which integrate to zero;
- discarding terms in N^μ not proportional to $i\sigma^{\mu\nu}q_\nu/2m$, which do not contribute to the lepton anomalous moments (Sec. 2); and
- putting the initial- and final-state leptons on-shell via the Dirac equation and the relations $p^2 = m^2 = p'^2$.

The result is

$$\begin{aligned} N_S^\mu &\supset -im(z^2-1)\sigma^{\mu\nu}q_\nu \equiv \tilde{N}_S(i\sigma^{\mu\nu}q_\nu/2m) \\ N_P^\mu &\supset im(z-1)^2\sigma^{\mu\nu}q_\nu \equiv \tilde{N}_P(i\sigma^{\mu\nu}q_\nu/2m) \\ N_V^\mu &\supset -2imz(1-z)\sigma^{\mu\nu}q_\nu \equiv \tilde{N}_V(i\sigma^{\mu\nu}q_\nu/2m), \end{aligned} \tag{6.3}$$

where $\tilde{N}_J$ is the coefficient of the $(i\sigma^{\mu\nu}q_\nu/2m)$-term in N_J^μ.

Combining Eqs. 6.1-6.3 yields an expression for the contribution to $F_2(q^2)$ due to Fig. 6.1

$$\begin{aligned} iF_2^J(q^2) &= g_J^2 \int dxdydz\delta(x+y+z-1)\tilde{N}_J \int \frac{d^4\ell}{(2\pi)^3}\frac{2}{(\ell^2-\Delta)^3} \\ &= g_J^2 \int dxdydz\delta(x+y+z-1)[\frac{-i}{16\pi^2\Delta}]\tilde{N}_J, \end{aligned} \tag{6.4}$$

In the limit $q^2 \to 0$, Eq. 6.4 can be interpreted as an integral expression for a_ℓ^J,

[3] $\gamma^\nu\gamma_\nu = 4$; $\gamma^\nu \not{a}\gamma_\nu = -2\not{a}$; $\gamma^\nu \not{a}\not{b}\gamma_\nu = 4ab$; $\gamma^\nu \not{a}\not{b}\not{c}\gamma_\nu = -2\not{c}\not{b}\not{a}$; $\{\gamma_\mu, \gamma_5\} = 0$. a_μ, b_μ, and c_μ are arbitrary four-vectors.

[4] $p - xp - yp' = zp' - (1-x)q$; $p' - xp - yp' = zp + (1-y)q$.

the contribution to the lepton anomalous magnetic moment due to Fig. 6.1

$$\begin{aligned} a_\ell^J = F_2^J(0) &= g_J^2 \int dz[\frac{-1}{16\pi^2\Delta}]\tilde{N}_J \int dxdy\delta(x+y+z-1) \\ &= \frac{g_J^2 m^2}{8\pi^2}\int_0^1 dz[\frac{(z^2-1)\delta_{JS}-(z-1)^2\delta_{JP}+2z(1-z)\delta_{JV}}{(1-z)^2m^2-M^2z}](1-z). \end{aligned} \tag{6.5}$$

With $J = V$, $M = 0$, and $g_V^2 = e^2 = 4\pi\alpha$, such that Fig. 6.1 reduces to Fig. 3.2, Eq. 6.5 evaluates to Schwinger's famous result[5]

$$F_2^V(0) = \frac{2m^2 4\pi\alpha}{8\pi^2 m^2}\int dz \frac{z(1-z)}{(1-z)^2}(1-z) = \frac{\alpha}{2\pi},$$

as required.

The integrals of Eq. 6.5 have been carried out in Refs. [73]. The results are

$$a_\ell^J(r) = \frac{g_J^2}{8\pi^2}H_J(r), \tag{6.6}$$

where $r = M^2/m^2$ and

$$H_S(r) = \frac{3-2r}{2} + \frac{r(r-3)}{2}\ln(r) - (r-1)\sqrt{r(r-4)}\ln[\frac{\sqrt{r}+\sqrt{r-4}}{2}],$$

$$H_P(r) = -(-\frac{2r+1}{2} + \frac{r(r-1)}{2}\ln(r) - \frac{r^{3/2}(r-3)}{\sqrt{r-4}}\ln[\frac{\sqrt{r}+\sqrt{r-4}}{2}]),$$

$$H_V(r) = \frac{1-2r}{2} + \frac{r(r-2)}{2}\ln(r) - \frac{r^{1/2}(r^2-4r+2)}{\sqrt{r-4}}\ln[\frac{\sqrt{r}+\sqrt{r-4}}{2}].$$

The expressions for H_J continue cleanly to $r < 4$ and remain positive for $r > 0$, suggesting all three particles X_J are viable candidate solutions to the muon $g-2$ anomaly, which has a_μ(Standard Model theory) $< a_\mu$(experiment). Additionally, $a_\mu^J(r)$ is 2-3 orders of magnitude larger than $a_e^J(r)$ for $J = S$, P, V, which opens the door, at least in principle, to lepton-universal solutions to the muon $g-2$ anomaly.

The expressions for H_J simplify in the limit $M >> m$, as would be the case for

[5] $\frac{\alpha}{2\pi}$ is inscibed on Schwinger's tombstone at Mt. Auburn Cemetery in Cambridge, MA.

an electron interacting with a $\gtrsim 10$ MeV particle X:

$$H_S \approx \frac{\ln(r) - 7/6}{r}$$
$$H_P \approx 1 - \frac{\ln(r) - 11/6)}{r} \tag{6.7}$$
$$H_V \approx \frac{1}{3r}.$$

Equation 6.7 was obtained by expanding $H_J(r)$ at $r = \infty$. For $m \to m_\mu \approx 105$ MeV and $M \sim 10 - 100$ MeV[6], the exact expressions for $H_J(r)$ (Eq. 6.6) should be used.

2 New-physics contributions to the spectroscopy sector

Consider lepton-nucleus scattering, mediated by scalar particle X_S of mass M. Since the lepton of mass m and the nucleus of mass m_N (and $Z = 1$) are distinguishable, we need to consider only the t-channel exchange of Fig. 6.2.

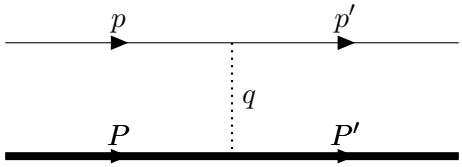

Figure 6.2: The leading contribution to the spectroscopy sector of the global fit due to the interaction of a new particle X_J (dotted line) with Standard Model fermions. Subscript J denotes particle X as a scalar S, pseudoscalar P, or vector V.

The corresponding matrix element is

$$i\mathcal{M} = -ig_N^S g_\ell^S (\bar{u}^{s'}(p')u^s(p)\frac{1}{(p'-p)^2 - M^2}\bar{U}^{r'}(P')U^r(P)), \tag{6.8}$$

where $q^2 = (P' - P)^2 = (p' - p)^2 \to -|\vec{q}|^2$ in the non-relativistic limit and the superscripts s, s', r, and r' denote spin indices. With the textbook definitions $u^s(p) = \sqrt{m}(\xi^s\, \xi^s)^T$ and $\bar{u}^{s'}u^s = 2m\xi^{s'\dagger}\xi^s = 2m\delta^{ss'}$, Eq. 6.8 becomes

$$i\mathcal{M} = \frac{ig_N^S g_\ell^S}{|\vec{q}|^2 + M^2} 2m\delta^{ss'} 2m_N \delta^{rr'}. \tag{6.9}$$

[6]The range $M \sim 10 - 100$ MeV is typical of the values of M used in the analyses of Ch. 7.

Comparison of Eq. 6.9 to the Born approximation for the scattering amplitude in non-relativistic quantum mechanics

$$< p'|iT|p >= -i\tilde{V}(\vec{q})2\pi\delta(E_{p'} - E_p),$$

yields the Yukawa potential in momentum-space

$$V(\vec{q}) = \frac{-g_N^S g_\ell^S}{\vec{q}^2 + M^2}. \tag{6.10}$$

Fourier transformation of Eq. 6.10 gives

$$\begin{aligned} V(r) &= \int \frac{d^3q}{(2\pi)^3} \frac{-g_N^S g_\ell^S}{\vec{q}^2 + M^2} e^{i\vec{q}\vec{x}} \\ &= \frac{-g_N^S g_\ell^S}{4\pi^2} \int_0^\infty dq\, \vec{q}^2 \frac{e^{iqr} - e^{-iqr}}{iqr} \frac{1}{\vec{q}^2 + M^2} = \frac{-g_N^S g_\ell^S}{4\pi^2 ir} \int_{-\infty}^{+\infty} dq\, \frac{q e^{iqr}}{\vec{q}^2 + M^2} \\ &= \frac{-g_N^S g_\ell^S}{4\pi} \frac{e^{-Mr}}{r}, \end{aligned} \tag{6.11}$$

where on the second line $q \equiv |\vec{q}|$.

For vector exchange, $V(r)$ has the opposite sign. The sign difference can be traced to swapping the scalar propagator in Eq. 6.8, which is proportional to i, for a vector propagator, proportional to $-ig_{\mu\nu}$.

- For $sign(g_\ell^S) = \pm sign(g_N^S)$, scalar exchange produces an attractive/repulsive potential.
- For $sign(g_\ell^V) = \pm sign(g_N^V)$, vector exchange produces a repulsive/attractive potential.

The contribution to the hydrogenlike bound-state energy levels due to Fig. 6.2 is given by

$$\begin{aligned} \Delta E_{n\ell} &=< \psi_{n\ell}|V(r)|\psi_{n\ell} > \\ &= \mp 4 \cdot (\frac{m_r \alpha}{n})^3 \cdot \frac{g_N^{S/V} g_\ell^{S/V}}{4\pi M^2} \cdot \delta_{\ell 0}, \end{aligned} \tag{6.12}$$

where m_r is the reduced mass of the hydrogenlike bound-state and the plus (minus) sign corresponds to vector (scalar) exchange.

The leading finite nuclear size contribution to the bound-state energy levels ΔE_{FNS} is proportional to $< r^2 > \cdot \delta_{\ell 0}$. The contribution of Fig. 6.2 to the energy levels will shift the global fit such that $\Delta E_{FNS} \rightarrow \Delta E_{FNS} + \Delta E_{n\ell}$. For a $2S2P$ transition, a positive value of $\Delta E_{n\ell}$ will decrease the fitted value of $< r^2 >$; a negative value will increase it. Because ΔE_{FNS} is much larger in muonic hydrogen than it is in electronic hydrogen (Sec. 6.3), the value of $< r^2 >$ determined by a fit to electronic hydrogen data will be much more sensitive to $\Delta E_{n\ell}$ than the value of $< r^2 >$ determined by a fit to muonic hydrogen data.

Pseudoscalar exchange is heavily suppressed in the non-relativistic limit and contributes only negligibly to the hydrogenlike bound-state energy levels. The justification is as follows.

In the non-relativistic limit,

$$\bar{u}\gamma_5 u \approx \frac{-i}{2m}[\vec{\nabla} f^\dagger \vec{\sigma} f + f^\dagger \vec{\nabla} \cdot \vec{\sigma} f], \tag{6.13}$$

where f is composed of a constant two-component spinor and a one-component Schrodinger wave function and σ_j are 2×2 Pauli matrices. See Sec.2.2.

Equation 6.13 can be rewritten via fast integration by parts as

$$\bar{u}\gamma_5 u \approx \frac{i}{2m}[f^\dagger \vec{\sigma} \cdot \vec{\nabla} f - [\text{surface term}]]. \tag{6.14}$$

With Eq. 6.14, the matrix element corresponding to Fig. 6.2, with particle X_P in the t-channel, is

$$\begin{aligned} i\mathcal{M} &= \frac{ig_\ell^P}{4m}\frac{ig_N^P}{m_N} f_\ell^\dagger \sigma^i q^i f_\ell \frac{i}{q^2 - M^2} f_N^\dagger \sigma^i q^i f_N \\ &= \frac{ig_\ell^P g_N^P}{4m\, m_N} f_\ell^\dagger f_\ell\, f_N^\dagger f_N \frac{(\vec{\sigma}\cdot\vec{q})(\vec{\sigma}\cdot\vec{q})}{\vec{q}^2 + M^2}. \end{aligned} \tag{6.15}$$

The non-relativistic potential can be read directly from Eq. 6.15

$$V(\vec{q}) = \frac{i g_\ell^P g_N^P}{4m\, m_N} \frac{(\vec{\sigma}\cdot\vec{q})(\vec{\sigma}\cdot\vec{q})}{\vec{q}^2 + M^2}. \tag{6.16}$$

$V(\vec{q})$, which becomes a 'derivative interaction' in coordinate space, goes to zero as $|\vec{q}|$ goes to zero. The contribution to the hydrogenlike bound-state energy levels due to Eq. 6.16 is vanishingly small.

Chapter 7

Global fit results

This chapter presents the results of a variety of global fits. The purpose of the chapter is threefold. First, the fit results presented here are relevant to the phenomenology and ultimate disposition of the precision QED experimental anomalies (Sec. 2), namely, the proton size puzzle and muon $g-2$ anomaly. Second, the results can be reproduced using `CONSTANT FINDER` and stand as examples of the ways in which the site can be used. Third, the results show (pointedly) a) the dangers of using one-size-fits-all values of the fundamental constants in tests of fundamental theory and b) the need for a community-wide mechanism like `CONSTANT FINDER` for determining the fundamental constants.

The chapter is organized as follows. The first section (Sec. 1) relates to the validation of the `CONSTANT FINDER` code. The second section (Sec. 2) discusses the results of global fits to Standard Model physics, including a global fit to the reference scheme. The reference scheme serves in this and subsequent sections as a de facto null hypothesis, roughly equivalent to the statement, "the Standard Model is true." See Sec. 3 for details. The third section (Sec. 3) discusses the results of global fits to a theory alternative that adds the effects of a no-name vector boson (Ch. 6) to the Standard Model. The fourth section explores the effects of the Parker datum (Sec. 1) on the global fit results. Finally, the fifth section, which closes the chapter,

alternately replaces the no-name vector boson in the global fit with no-name scalar and psuedoscalar bosons.

1 Validation of the `CONSTANT FINDER` code

The early stages of this project centered on the spectroscopy sector, and the proton size puzzle. The author and his advisor (John P. Ralston) separately typed the spectroscopy sector theory formulas of C10 into Mathematica,with each implementation of the C10 spectroscopy theory requiring about 30,000 keystrokes.

Initial validation was done by fitting data using a basic chi-squared function (Eq. 2.6). The two codes gave the same results to within machine precision. The author's code, with updates based on the results of C14, has been folded into the `CONSTANT FINDER` algorithm.

A second round of validation was also done. The second round of validation involved comparing the results from the two sets of code (hereafter, simply 'our code') to published results. Principally,

- We reproduced the r_p values and error bars of Fig. 8.3.[1] Figure 8.3 is reprinted from Ref. [4]. Its r_p values were determined by solving the system of equations below for r_p and R_∞ :

$$\begin{aligned} f^{exp}_{1S2S} &= f^{th}_{1S2S}(r_p,\, R_\infty); \\ f^{exp}_{J} &= f^{th}_{J}(r_p,\, R_\infty). \end{aligned} \tag{7.1}$$

  Subscript J runs over the fourteen eH spectroscopic transitions of the figure. The error bars in the figure were determined by re-solving Eq. 7.1 for r_p and R_∞, with $f^{exp}_J \to f^{exp}_J + \sigma^{exp}_J$ and $f^{exp}_{1S2S} \to^{exp}_{1S2S}$.[2] Here σ^{exp}_J is the experimental uncertainty of transition J.

[1] The author thanks Thomas Udem for providing code used to check the error bars of Fig. 8.3, as well as for his general helpfulness.

[2] f^{exp}_{1S2S} was held fixed since $100 \cdot \sigma^{exp}_{1S2S} \lesssim \sigma^{exp}_J$ for all J.

- We also reproduced to thirteen-digit accuracy and better the 56 theoretical level frequency values of Table 4 of Ref. [31], which are due to Jentschura [55].[3] The mean difference between the predictions of our code and the Jentschura predictions of Table 4 was 65 Hz, with a standard deviation of 568 Hz. Normalized to the relevant experimental uncertainties, these numbers translate to a mean (normalized) difference squared $\Delta f_{tt}^2 = (1/56)\sum_i (f_i^{theory-1} - f_i^{theory-2})^2/(\sigma_i^{exp})^2$ of 0.003 and a standard deviation of 0.010. The quantity $(f_i^{theory-1} - f_i^{theory-2})^2/(\sigma_i^{exp})^2$ was less than 0.04 for all i.

The theory expressions we typed in for the moments and Compton sectors, as well as for the μH and μD transitions of the reference scheme, were vetted along similar lines. Those expressions required far fewer keystrokes. The moments sector theory of the `CONSTANT FINDER` algorithm was checked against the numbers in Refs. [23] and [40], the Compton sector theory against the numbers in Ref. [20], and the μH and μD theory against the numbers in Refs. [61] and [11], respectively.

[3] A comparison of level frequencies is more demanding than a compartion of transition frequencies since many level contributions cancel in transitions.

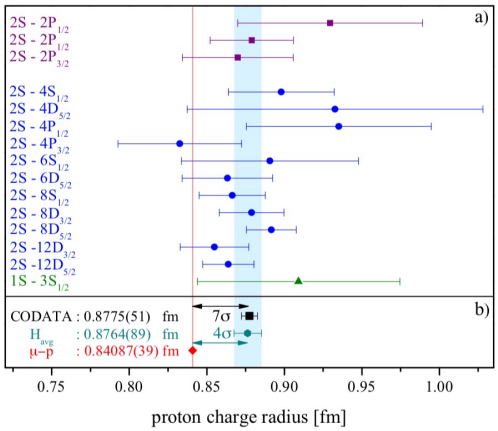

Figure 1. a) The proton charge radius obtained from precision spectroscopy of atomic hydrogen. Either radio frequency measurements of the 2S-2P Lamb shift (violet) or optical transition frequencies (blue from the 2S and green from the 1S state) are used. To extract the two parameters, the Rydberg constant and the proton charge radius, each of these measurements needs to be combined with another independent measurement, which is the 1S-2S transition frequency here. b) The analysis reveals a 4σ discrepancy between the hydrogen mean value (H_{avg}) and the value determined from laser spectroscopy of muonic hydrogen (μ–p). An even larger inconsistency of 7σ is obtained when including proton-electron scattering data. This CODATA analysis also uses deuterium data, that have only limited effect on the proton charge radius, because its nucleus is not a proton. A similar picture is obtained when plotting the corresponding results for the Rydberg constant.

Figure 7.1: Proton charge radius determinations from Ref. [4]. The determinations were used in the validation of the `CONSTANT FINDER` code. See text for details. The figure and its caption are reprinted from Ref. [4].

2 A global fit to the Standard Model

2.1 A global fit to the reference scheme

A quick review of the problem space: The proton size puzzle, the muon $g-2$ anomaly, and the discrepancy between the Parker and Gabrielse determinations of α are each defined on the basis of a piecemeal fit to data. The problem with such piecemeal fits is: the values of r_p and α depend on each other and on all the data of the Rydberg sector. The pattern of dependencies is depicted in Fig. 7.2.[4] This pattern requires, for reasons of self-consistency, that r_p and α be determined globally, rather than on a piecemeal basis. 'Global' values for α and r_p— if we knew them— would redefine the respective magnitudes

[4]Figure 7.2 is identical to Fig. 1.1.

of the three experimental anomalies above. To what extent do these redefinitions change the phenomenology? We would like to know. We have defined a reference scheme (Sec. 3) to be used in the global fit. The reference scheme captures all relevant Standard Model theory and all relevant experiments, with the exception of the atomic interferometry experiment of Parker, et al., whose effects on the global fit are discussed in Secs. 4-5. The goal, as already intimated, is a self-consistent, no-frills assessment of the size of the three experimental anomalies above.

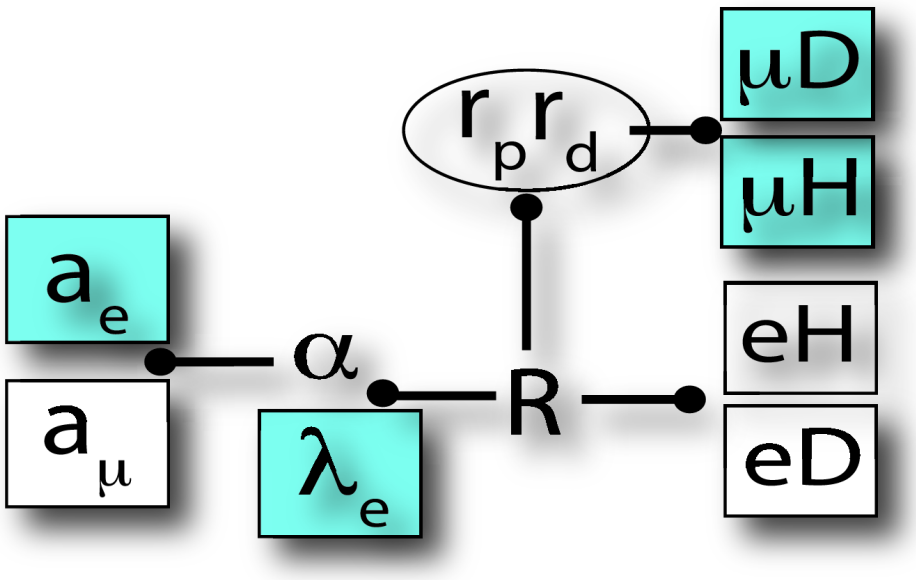

Figure 7.2: Schematic of the dependencies between experimental data and the fundamental physical constants of the Rydberg sector.

The results of the global fit to the reference scheme are discussed below and summarized in Tables 7.1-7.3.

The third column of Table 7.1 shows fitted values for the reference scheme observables, obtained from a global fit to the reference scheme. The corresponding experimental values and experimental uncertainties are shown for comparison in the second and fourth columns, respectively. With the exception of the observables a_μ and $\nu_H(2P1/2 - 2S1/2)$, the fitted and experimental values of Table 7.1 differ

within their respective experimental uncertainties. Of the fitted values for a_μ and $\nu_H(2P1/2 - 2S1/2)$, only the fitted value for a_μ, which differs from experiment by $3.9\sigma_{expt}$, is true cause for concern. (The fitted value for $\nu_H(2P1/2 - 2S1/2)$ differs from experiment by $1.5\sigma_{expt}$.)

The results of Table 7.1 are corroborated in Table 7.2. Table 7.2 gives the sector-wise chi-squared budget for the global fit. Chi-squared in the a_μ sector, with its one experimental datum, is 15.7[5]. Each of the remaining sectors contributes less than one unit of chi-squared per datum.

Hence the only anomaly evident in the global fit to the reference scheme is the muon $g - 2$ anomaly. The muon $g - 2$ anomaly's persistence under the reference scheme can be understood in view of Fig. 7.2. The theory expressions for a_e, a_μ, and the transition frequencies in the eH and eD sectors all depend explicitly on α. However the extreme precision of the Gabrielse measurement of a_e means that the Gabrielse datum overwhelmingly determines the value of α. The effect is: the Gabrielse datum pins down the value of α. That value of α then flows through to the theory expression for a_μ, creating an 'anomalous' residual in the a_μ sector of the fit. The global fit thus effectively reproduces the piecemeal fit procedure that created the muon $g - 2$ anomaly in the first place.

The fitted values of the fundamental constants from the global fit to the reference scheme are shown in Table 7.3. The fitted values for R_∞ and α are given relative to their respective $C14$ reference values (denoted R^*_∞ and α^*). The details of the Table 7.3 results are as follows. The fit to the reference scheme shifts R_∞ relative to its $C14$ value by 4.6σ. The fit also shifts r_p and r_d from their $C14$ values by 2.1σ and $x.x\sigma$, respectively, with r_p and r_d taking values consistent with the smaller radius values that have been predicted from μH and μD experiments.

Interestingly Tables 7.1-7.3 show no evidence of a proton size puzzle. A global fit to the reference scheme resolves the proton size puzzle in favor of the muonic radius

[5] $|a_\mu^{expt} - a_\mu^{th}|/\sigma_{expt} = \sqrt{15.7} = 3.9$

value. The only apparent cost of the solution is a shift in the best-fit value of the Rydberg constant. However, since the only meaningful constraints on the Rydberg constant are present in the fit, the cost of the solution has already been absorbed by the fit.

In view of the proton size puzzle's stature and long standing, the mechanics of the solution to the puzzle offered by the fit to the reference scheme are astonishingly simple. The Gabrielse datum fixes α at a value consistent with the C14 reference value. The μH datum fixes r_p at a 'small' value, $\sim 0.84\ fm$. Then, R_∞, as the only remaining free parameter, floats inside the eH and eD sectors to its best-fit value, 4.6σ away from the C14 reference value. The fit is well-behaved everywhere except in the previously-discussed a_μ sector (see Table 7.2).

The solution is stable even in the eH sector of the fit. Figure 7.3 shows chi-squared in the eH sector as a function of r_p, with R_∞, α, and r_d fixed at the fitted values of Table 7.3. The chi-squared minimum is at a manifestly 'muonic' radius value, $r_p \sim 0.85\,fm$. For reference, the $C14$ recommended value for r_p ($= 0.8775\,fm$), which is a de facto 'electronic' radius value, is to the right of the Fig. 7.3 plot window.

The proton size puzzle can be seen as an artifact of comparing the r_p values determined from two separate piecemeal fit procedures, where one value of r_p is determined from $\chi^2_{\mu H}$ and the other from χ^2_{eH}. When a truly global, self-consistent fit procedure is used— i.e., when r_p and R_∞ are allowed to find their level in the context of a global fit that accounts for all relevant experimental data (see Fig. 7.2)— the proton size puzzle disappears. The only experimental anomaly that remains is the muon $g-2$ anomaly.

Experimental datum	Experimental value	Fitted value	σ_{expt}
$\nu_H(2S1/2-8S1/2)$ [Hz]	$7.70649350012000 \times 10^{14}$	$7.70649350015089 \times 10^{14}$	8600.
$\nu_H(2S1/2-8D3/2)$ [Hz]	$7.70649504450000 \times 10^{14}$	$7.70649504448244 \times 10^{14}$	8300.
$\nu_H(2S1/2-8D5/2)$ [Hz]	$7.70649561584200 \times 10^{14}$	$7.70649561577394 \times 10^{14}$	6400.
$\nu_H(2S1/2-12D3/2)$ [Hz]	$7.99191710472700 \times 10^{14}$	$7.99191710480623 \times 10^{14}$	9400.
$\nu_H(2S1/2-12D5/2)$ [Hz]	$7.99191727403700 \times 10^{14}$	$7.99191727407767 \times 10^{14}$	7000.
$\nu_H(2P1/2-2S1/2)$ [Hz]	$1.05784500000000 \times 10^{9}$	$1.05783220761556 \times 10^{9}$	9000.
$\nu_H(2S1/2-2P3/2)$ [Hz]	9911200000	9911209318	12000.
$\nu_H(2P1/2-2S1/2)$ [Hz]	1057862000	1057832208	20000.
$\nu_D(2S1/2-8S1/2)$ [Hz]	$7.708590412457 \times 10^{14}$	$7.7085904124256 \times 10^{14}$	6900.
$\nu_D(2S1/2-8D3/2)$ [Hz]	$7.708591957018 \times 10^{14}$	$7.70859195700519 \times 10^{14}$	6300.
$\nu_D(2S1/2-8D5/2)$ [Hz]	$7.708592528495 \times 10^{14}$	$7.70859252845263 \times 10^{14}$	5900.
$\nu_D(2S1/2-12D3/2)$ [Hz]	$7.99409168038 \times 10^{14}$	$7.99409168041396 \times 10^{14}$	8600.
$\nu_D(2S1/2-12D5/2)$ [Hz]	$7.994091849668 \times 10^{14}$	$7.9940918497316 \times 10^{14}$	6800.
$\nu_D(2P1/2-2S1/2)$ [Hz]	1059280000	1059220261	60000
$\nu_D(2S1/2-2P3/2)$ [Hz]	9912610000	9912815235	300000
$\nu_D(2P1/2-2S1/2)$ [Hz]	1059280000	1059220261	60000
a_e	0.00115965218072	0.00115965218078	2.8×10^{-13}
a_μ	0.00116592089	0.00116591840	6.3×10^{-10}
$\Delta E_{LS}(\mu H)$ [meV]	202.3706	202.3705	0.0023
$\Delta E_{LS}(\mu D)$ [meV]	202.8785	202.8785	0.0034
λ_e [m]$/10^{-12}$	2.4263102367	2.4263102356	1.1×10^{-9}

Table 7.1: Experimental data compared to calculations by the Constant Finder. Calculated values are based on a Standard Model fit to Table 2.1 data. Fitted constants for the fit appear in Table 7.3.

χ^2	dof	$\chi^2_{\lambda_c}$	$\chi^2_{\mu H}$	$\chi^2_{\mu D}$	$\chi^2_{a_e}$	$\chi^2_{a_\mu}$	χ^2_{eH}	χ^2_{eD}
27.5	17	0.18	0.0012	0.000095	0.042	15.7	7.4	4.3

Table 7.2: Contributions to χ^2 for global fits with different observables omitted. dof stands for the number of degrees of freedom. Standard Model physics is assumed. The a_μ sector, when it appears in the global fits, contains only one experimental observable while contributing 15.7 units of chi-squared. All other sectors across all fits have well-controlled contributions to χ^2.

$(\delta R_\infty/R^*_\infty)/10^{-12}$	$(\delta\alpha/\alpha^*)/10^{-10}$	r_p fm	r_d fm
$-13.4(2.9)$	$-2.2(2.2)$	0.84088(26)	2.12870(13)

Table 7.3: Fitted values of $\delta R_\infty/R^*_\infty$, $\delta\alpha/\alpha^*$, r_p, r_d for a global fit to the reference scheme, where R^*_∞, α^* are reference values. Standard Model physics is assumed, and all relevant data has been included in the fit, with the exception of the Parker datum, which is discussed and accounted for in subsequent sections. There is a 2.1σ discrepancy between the fitted value of r_p and the corresponding C14 reference value.

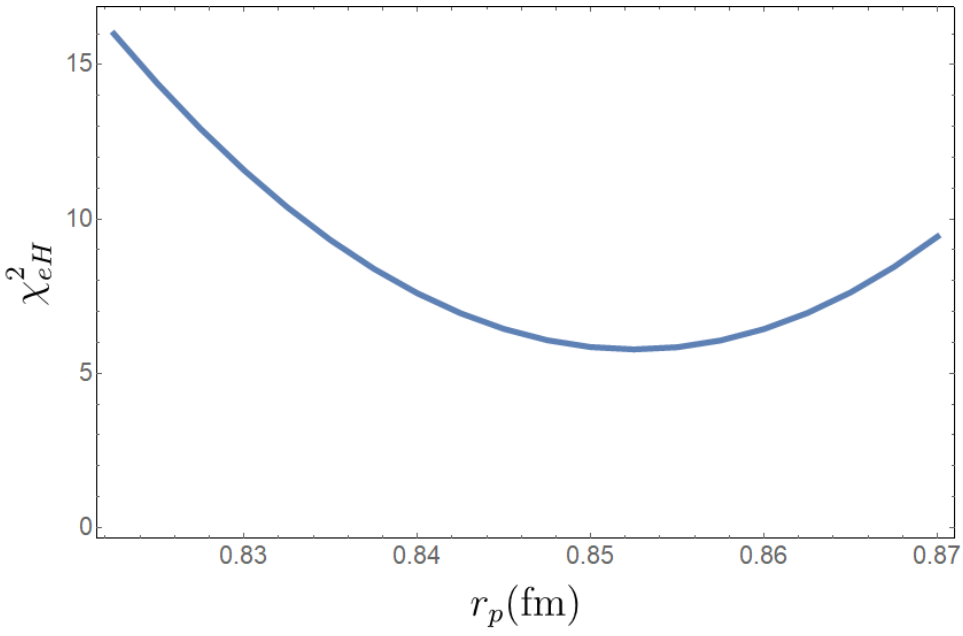

Figure 7.3: χ^2_{eH} versus r_p, with R_∞, α, and r_d fixed at the fitted values of Table 7.3. When the muonic data is included in the analysis, the electronic hydrogen spectroscopy data favors a 'small' proton radius value $\sim .85$ fm.

2.2 Variations on the global fit to the reference scheme

In this section, we systematically omit data from the reference scheme to investigate the effect of those omissions on the global fit. In particular, we would like to know how robust the muon experimental anomalies are under changes to the input data of the global fit. The results of the various fits are compiled in Tables 7.4 and 7.5, and assume Standard Model physics throughout. Tables 7.4 and 7.5 are discussed line by line below.

line	omit	$(\delta R_\infty/R^*_\infty)/10^{-12}$	$(\delta\alpha/\alpha^*)/10^{-10}$	r_p fm	r_d fm
1	*none*	−13.4(2.9)	−2.2(2.2)	0.84088(26)	2.12870(13)
2	λ_c	−13.4(2.9)	−2.7(2.4)	0.84088(26)	2.12870(13)
3	μH	−10.1(3.6)	−2.2(2.2)	0.859(11)	2.12870(13)
4	μD	−14.7(4.4)	−2.2(2.2)	0.84088(26)	2.1265(55)
5	μH, μD	3.4(9.5)	−2.2(2.2)	0.883(19)	2.1433(96)
6	a_e	−13.4(2.9)	−0.068(5.)	0.84088(26)	2.12870(13)
7	a_μ	−13.4(2.9)	−2.2(2.2)	0.84088(26)	2.12870(13)
8	a_e, a_μ	−13.4(2.9)	−0.086(5.)	0.84088(26)	2.12870(13)
9	μH, μD, a_μ	3.4(9.5)	−2.2(2.2)	0.883(19)	2.1433(96)
10	eH	−12.0(3.9)	−2.2(2.2)	0.84087(26)	2.12870(13)
11	eD	−15.2(4.4)	−2.2(2.2)	0.84088(26)	2.12870(13)
12	eH, eD	−500(1100)	−2.7(2.2)	0.84087(26)	2.12870(13)
13	eD, μD	−15.2(4.4)	−2.2(2.2)	0.84088(26)	–

Table 7.4: Fitted values of $\delta R_\infty/R^*_\infty$, $\delta\alpha/\alpha^*$, r_p, r_d for global fits with different observables omitted, where R^*_∞, α^* are reference values. Standard Model physics is assumed. Line 9 omits all muonic observables and gives fitted values consistent with the values of C14. There is a 2.1σ discrepancy between the r_p values of Line 1 and Line 9. The first line, *omit none*, generates Table 7.3.

- The fit given by Line 1 of Tables 7.4 and 7.5 reproduces the fit to the reference scheme of the previous section (Tables 7.2 and 7.3).

- The Line 2 fit omits the electron Compton wavelength λ_c from the fit to the reference scheme. The role of λ_c in the reference scheme fit is to enforce the definition of the Rydberg: $R_\infty := \alpha^2/2\lambda_c$. The omission of λ_c from Fig. 7.2 effectively splits the figure into two independent halves, with one half determining the value of α and the other half the values of R_∞, r_p, and r_d.

line	omit	χ^2	dof	$\chi^2_{\lambda_c}$	$\chi^2_{\mu H}$	$\chi^2_{\mu D}$	$\chi^2_{a_e}$	$\chi^2_{a_\mu}$	χ^2_{eH}	χ^2_{eD}
1	*none*	27.5	17	0.18	0.0012	0.000095	0.042	15.7	7.4	4.3
2	λ_c	27.3	16	–	0.0012	0.000095	0	15.7	7.3	4.2
3	μH	25.1	16	0.18	–	0.00043	0.043	15.7	4.8	4.4
4	μD	27.3	16	0.18	0.00076	–	0.042	15.7	7.2	4.2
5	$\mu H, \mu D$	22.8	15	0.19	–	–	0.045	15.7	3.3	3.5
6	a_e	27.3	16	0.000013	0.0012	0.000094	–	15.7	7.3	4.3
7	a_μ	11.8	16	0.18	0.0012	0.000095	0.042	–	7.3	4.3
8	a_e, a_μ	11.6	15	0	0.0012	0.000094	–	–	7.3	4.3
9	$\mu H, \mu D, a_\mu$	7.1	14	0.19	–	–	0.044	–	3.3	3.5
10	eH	20.0	9	0.18	0	0	0.042	15.7	–	4.1
11	eD	23.1	9	0.18	0.00062	0	0.042	15.7	7.2	–
12	eH, eD	15.7	1	0	0	0	0	15.7	–	–
13	$eD, \mu D$	23.1	8	0.18	0.00062	–	0.042	15.7	7.2	–

Table 7.5: Contributions to χ^2 for global fits with different observables omitted. *dof* stands for the number of degrees of freedom. Standard Model physics is assumed. The a_μ sector, when it appears in the global fits, contains only one experimental observable while contributing 15.7 units of chi-squared. All other sectors across all fits have well-controlled contributions to χ^2.

That the Line 1 and Line 2 fitted values for α and R_∞ agree as closely as they do is largely coincidental.

- The fits of Lines 3-5 omit, respectively, μH, μD, and both μH and μD. Lines 3 and 4 report 'small' values for r_p and r_d, while Line 5 reports significantly larger values. The explanation is as follows. r_p and R_∞ are approximately degenerate in the eH sector of the fit; r_d and R_∞, in the eD sector of the fit. See e.g. Fig. B.1 and surrounding discussion. Hence when the μH and μD data are omitted from the fit, as in Line 5, r_p, r_d, and R_∞ float together, up or down, to best-fit values within a relatively thin ellipsoid in (r_p, r_d, R_∞)-space that is determined by the degeneracies. It just happens that r_p, r_d, and R_∞ float together within the ellipsoid to 'large' rather than 'small' values (due to the peculiarities of the data in the eH, eD, and λ_c sectors). When the ultra-precise μH (μD) datum is included in the fit, as in Line 3 (Line 4), it pins r_p (r_d) at a 'small' value. The approximate degeneracy between r_p, r_d, and R_∞ then ensures that r_d (r_p) and R_∞ take 'small' values too.

- The fits of Lines 6-8 omit, respectively, a_e, a_μ, and both a_e and a_μ. In the Line 8 fit omitting both a_e and a_μ, α is fixed trivially by the λ_c datum through the definition of the Rydberg constant, $R_\infty = \alpha^2/2\lambda_c$. As with the Line 2 fit, the close agreement of the Line 8 value for α with the Line 1 value is largely coincidental. The Line 7 fit omitting a_μ reinforces the idea that there is only one experimental anomaly (muon $g-2$). The Line 7 fit is under excellent control across all sectors of chi-squared and favors small radius values for r_p and r_d, consistent with the predictions of muonic spectroscopy. The Line 6 fit omitting a_e finds a value for α which represents a compromise between the competing demands of the a_μ and λ_c sectors, with the a_μ sector favoring a large value for α and the λ_c sector a small value.

- The Line 9 fit omits, respectively, the μH, μD, and a_μ data. The Line 9 fit is designed to be a reasonable facsimile of the final adjustments of C10 and C14, both of which omit all muonic data. The Line 9 values for the fundamental constants are all within one sigma of the corresponding C14 recommended values.

- The fits of Lines 10-12 omit, respectively, the eH data, the eD data, and the eH and eD data. The Line 12 fit omitting both the eH and eD data reports a null value for R_∞[6] and favors the smaller muonic radius values for r_p and r_d. The Lines 10-11 fits also report small values for r_p and r_d, as well as a small value for R_∞. The small values for r_p and r_d in the Lines 10-12 fits are due, respectively, to the inclusion of the μH and μD data in the fit, while the small value for R_∞ in the Lines 10-11 fits is due to the approximate degeneracy between r_p, r_d, and R_∞ in the spectroscopy sectors of the fit. That degeneracy is discussed above with respect to the Lines 3-5 fits.

The results of Tables 7.4 and 7.5 reaffirm the conclusions we drew from the fit

[6]The μH and μD sectors have no explicit R_∞-dependence.

to the reference scheme (Tables 7.2 and 7.3). For a global fit assuming Standard Model physics, the muon $g-2$ anomaly exists independent of the choice of data, while the proton size puzzle exists only for certain choices of data and, in particular, disappears when muonic hydrogen spectroscopy data is included in the fit.

Line 1 versus Line 9

In this section, we take a closer look at the mechanics of the Line 1 and Line 9 fits of Tables 7.4 and 7.5, particularly, as they relate to the proton size puzzle. The Line 1 fit is a fit to the reference scheme and includes all relevant experimental data. The Line 9 fit is a reasonable facsimile of the C14 fit and excludes all (of the putatively anomalous) muonic data— namely, a_μ, μH, and μD.

The Line 1 fit, since it includes all relevant data, can be regarded as a truly 'global' fit, providing global values for r_p, r_d, α, and R_∞. Whether or not those global values can be deemed reliable depends on the extent to which the global fit and its constituent parts (χ^2_{eH}, etc.) are under control. Table 7.5 shows the chi-squared contributions across all the sectors of the Line 1 fit. Except for the a_μ sector (where the muon $g-2$ anomaly holds sway), the fit is under excellent control and hence represents a self-consistent solution to the proton size puzzle, with $r_p = 0.84088(26)$ fm. This value of r_p works not only in the μH sector, where $\chi^2_{\mu H} = 0.0012$ (1 data point), but also in the eH sector, where $\chi^2_{eH} = 7.4$ (8 data points).

In fact the evidence for a proton size puzzle is confined to the Line 9 fit omitting muonic data. The Line 9 fit finds $r_p = 0.883(19)$ fm. Since the muonic data was omitted from the Line 9 fit, $r_p = 0.883(19)$ fm is nominally an 'electronic' radius value. A 'muonic' radius value can be obtained by solving $\Delta E^{theory}_{LS}(\mu H) = \Delta E^{exp}_{LS}(\mu H; r_p, \alpha)$ for r_p, with α fixed at the C14 reference value. The resulting r_p value is 0.84087(26) fm, and the discrepancy between the electronic and muonic ra-

dius values— which is 2.2σ, in units of the electronic radius value's uncertainty[7]— defines the proton size puzzle.

The problem with taking such a discrepancy at face value is that it neglects 1) the interdependencies of the values of r_p, r_d, α, and R_∞ and 2) the sensitivity of the fit results to the choice of data. A shift in the value of one constant can be compensated (or nearly) by a shift in the value of one or more of the other constants. We refer to this kind of compensating mechanism as an approximate degeneracy. For the Line 9 fit, one approximate degeneracy exists in the eH sector of the fit, between r_p and R_∞, and another exists in the eD sector of the fit, between r_d and R_∞. Hence, even though the Line 9 fit favors 'large' values of r_p, r_d, and R_∞, due to the approximate degeneracies, those large values of r_p, r_d, and R_∞ can be traded for 'small' values at the cost of only a few units of chi-squared. See App. C for a more in-depth discussion of the approximate degeneracies.

When the μH and μD data are included in the fit, as in Line 1, the ultra-precise μH and μD data (respectively) pin r_p and r_d at 'small' values. R_∞ is pushed to a small value as well due to the approximate degeneracies in the eH and eD sectors. I.e., R_∞ can be moved down more cheaply than r_p and r_d can be moved up. The upshot is: the Line 9 fit favors large values of (r_p, r_d, R_∞) but exists as a point in an ellipsoid over which chi-squared varies by no more than a few units and which extends to 'small' values of (r_p, r_d, R_∞). The μH and μD data of the Line 1 fit then confine the region of best-fit to a cross-sectional slice of the ellipsoid near $r_p \approx 0.84\ fm$ and $r_d \approx 2.12\ fm$. The correlation matrix for the Line 9 fit is shown in Table 7.6. r_p, r_d, and R_∞ are all mutually positively-correlated, with the smallest correlation between them larger than 0.82. The μH and μD data break up these correlations by slicing into the best-fit ellipsoid, and the largest correlation in the Line 1 correlation matrix is smaller than 0.01.

[7]The uncertainty of the C14 recommended value for r_p is roughly a quarter the size of the uncertainty of r_p from the Line 9 fit, due to the inclusion of the $1S2S$ transition in the C14 fit. See Appendix B for related discussion.

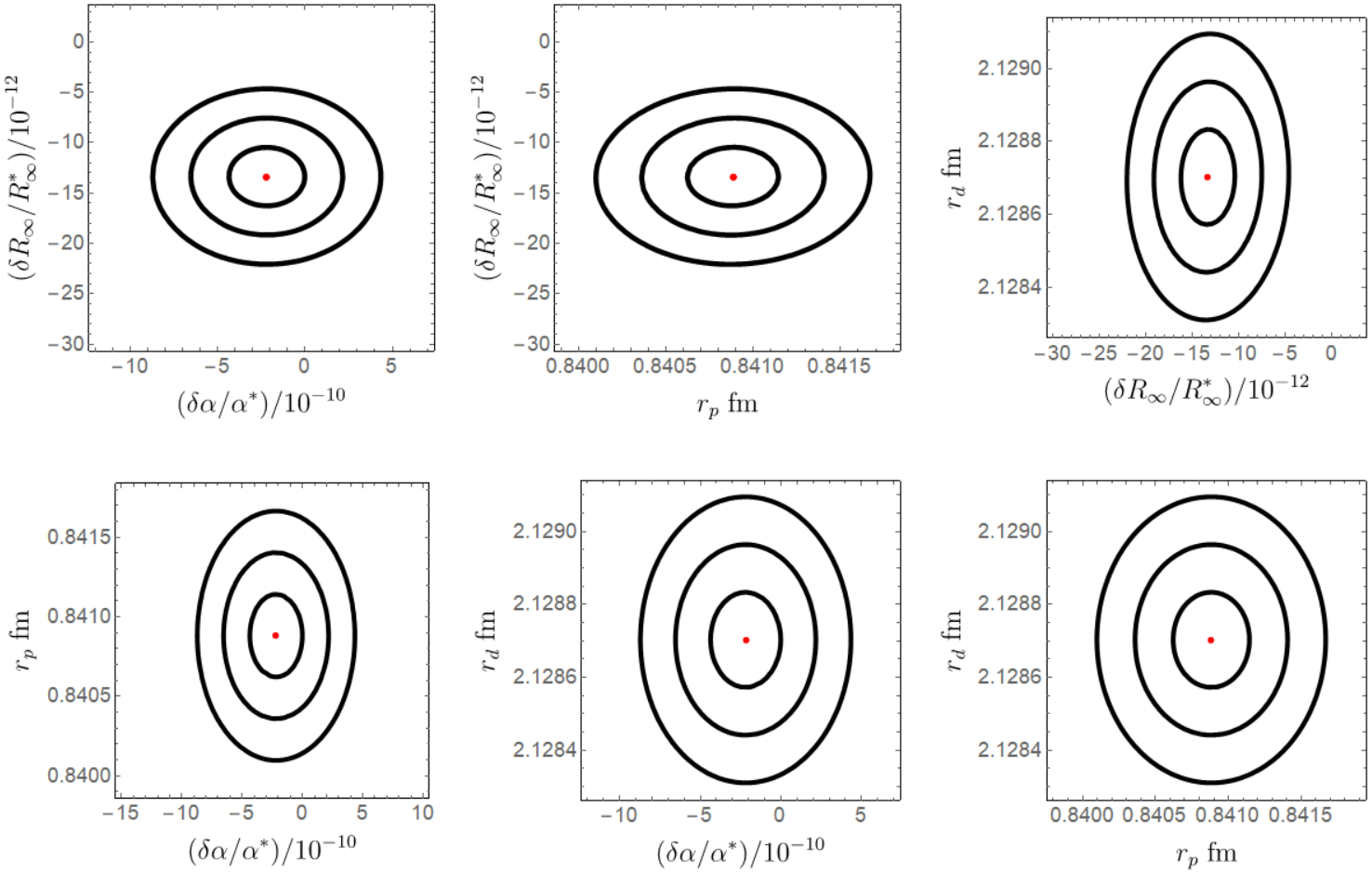

Figure 7.4: 1, 2, and 3σ chi-squared contours for the full global fit in fit-parameter space. In each subplot the fit parameters not shown are fixed at the best fit values of Line 1, Table 7.4.

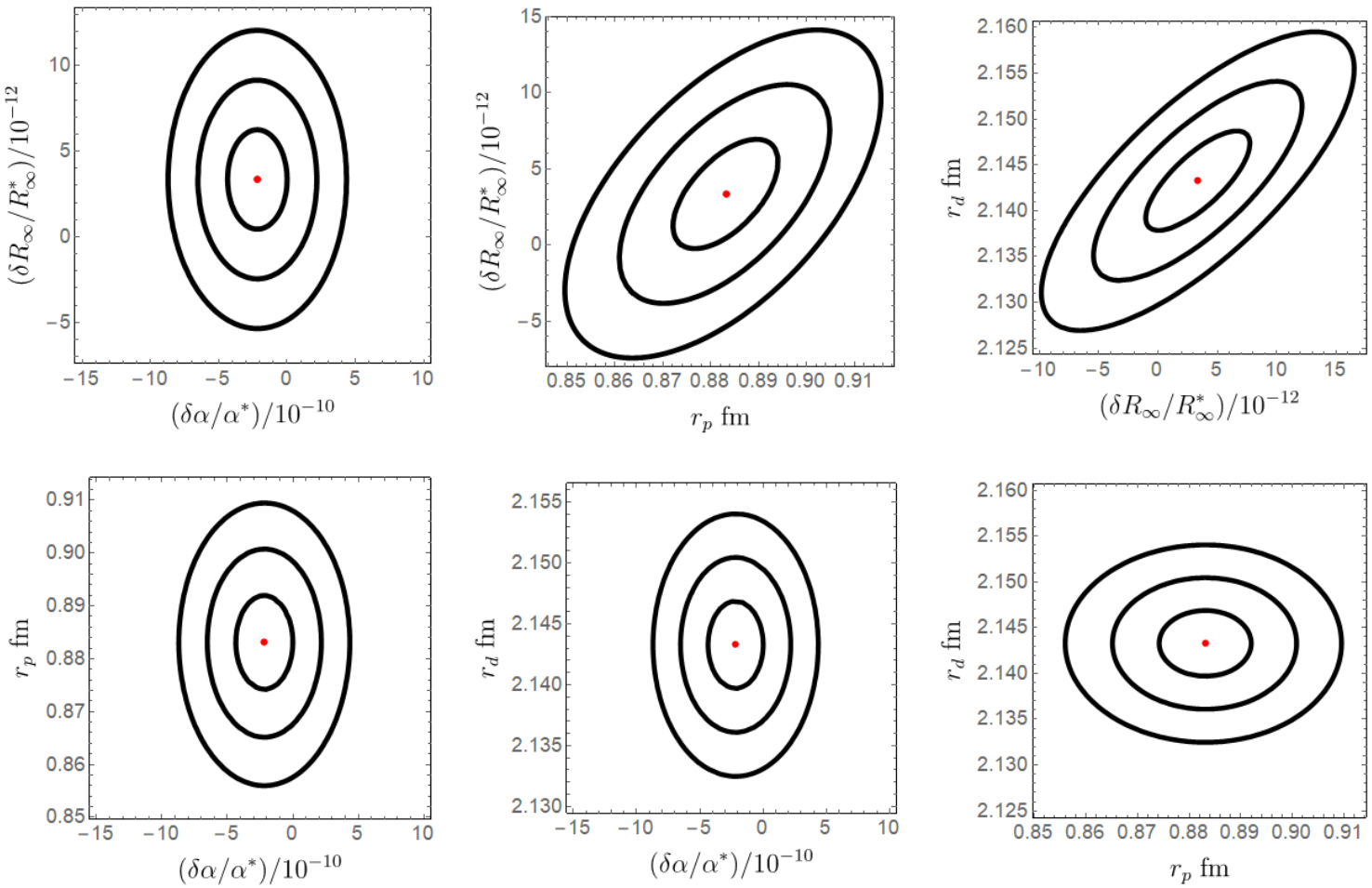

Figure 7.5: 1, 2, and 3σ chi-squared contours for the global fit omitting all muonic data in fit-parameter space. In each subplot the fit parameters not shown are fixed at the best fit values of Line 9, Table 7.4. An approximate degeneracy between R_∞ and r_p and R_∞ and r_d can be seen in the top middle and top right subplots, respectively. The degeneracy is discussed in Fig. **??**.

The effects of μH and μD

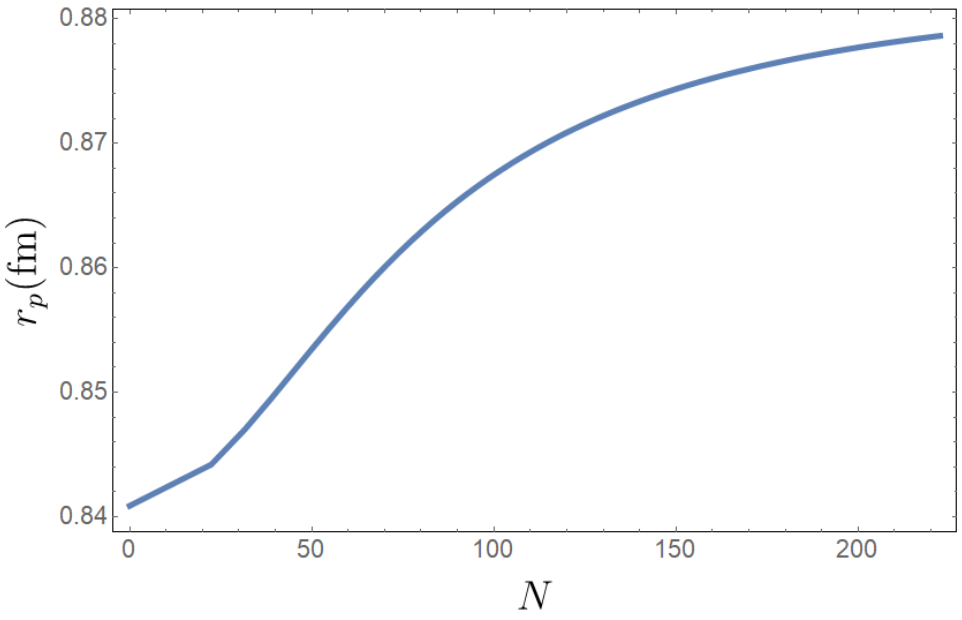

Figure 7.6: The change in the fitted value of r_p from adjusting the experimental error of the μH datum $\Delta E_{LS}(\mu H) \to N\sigma$, where σ is the experimental uncertainty. As N is increased r_p moves from .84 fm, the value favored by the μH datum, to .88 fm, the value favored by the eH sector. The global fit here is the same as Line 1, Table 7.4 omitting muonic deuterium.

$$\begin{bmatrix} R_\infty & \alpha & r_p & r_d \\ 1.00 & 0.00356 & 0.888 & 0.927 \\ 0.00356 & 1.00 & 0.00382 & 0.00395 \\ 0.888 & 0.00382 & 1.00 & 0.822 \\ 0.927 & 0.00395 & 0.822 & 1.00 \end{bmatrix}$$

Table 7.6: The correlation matrix of the fit of Line 9, Table 7.4 omitting all muon data.

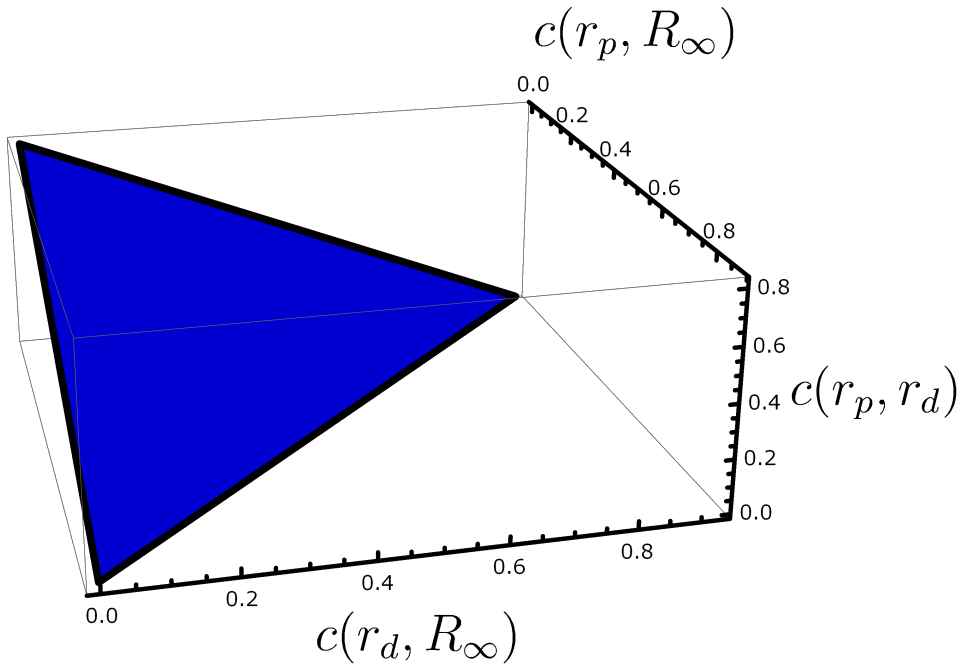

Figure 7.7: The non-trivial correlations of Line 5, Table 7.4, between $r_p - R_\infty$, $r_d - R_\infty$, and $r_p - r_d$. Non-trivial correlations emerge only after removing the μH, μD data from the fit, and are discussed in the text.

3 A global fit to a theory alternative

We explore the effects of adding a no-name vector boson to the global fit as a means of resolving the muon $(g-2)$ anomaly. The no-name X_V is assumed to couple with strength λ to Standard Model leptons through the vector portal, $\mathcal{L} \supset g(X_V)_\mu \bar{\psi}\gamma_\mu\psi$ (see Ch. 6), and contributes to the moments sectors according to Eq. 6.6 and to the spectroscopy sectors according to Eq. 6.12.

We briefly review the relevant phenomenology. Let the coupling of X_V to electrons, muons, and protons be denoted by g_e, g_μ, and g_p, respectively. The matrix element that gives the leading contribution of X_V to a_e (a_μ) is proportional to g_e^2 (g_μ^2). The matrix element that gives the leading contribution of X_V to eH (μH) is proportional to $g_e \cdot g_p$ ($g_\mu \cdot g_p$). X_V does not contribute to the Compton sector of the fit.

Kinetic mixing models, which are the simplest topdown motivation for a vector portal interaction (see App. I), allow g_e, g_μ, and g_p to take any sign. We follow suit and allow $sign(g_\ell \cdot g_p)$ to be either positive or negative for $\ell = e,\ \mu$.

For simplicity, we assume $|g_e| = |g_\mu| = |g_p|$ and take $g_k = \epsilon_k \cdot e$, with subscript k running over e, μ , and p. This identification allows the various leading contributions of X_V to be recast in terms of a mass m_X and a coupling $\alpha_X = \frac{g_k \cdot g_{k'}}{4\pi} = \epsilon_k \cdot \epsilon_{k'} \cdot \alpha$, where α_X is strictly positive in the moments sectors of the fit but can take either sign in the spectroscopy sectors[8].

Within the global fits, α_X has been further recast for convenience in terms of the parameter $\xi = \alpha_X / m_X^2$. This identification allows the explicit m_X-dependence to be removed from the spectroscopy and a_e sectors of the fit. See Eqs. 6.12 and 6.7, respectively. Note: Eq. 6.7 is valid only for $m_X >> m_e$.

3.1 $m_X = 50\, MeV$

We start by adding an $m_X = 50\ MeV$ no-name vector boson to the global fit and reproduce the results of Sec. 2. The results are shown in Tables 7.7 and 7.8. The fits of Tables 7.7 and 7.8, apart from including the effects of the no-name, are identical to the fits of Tables 7.4 and 7.5.

For the Table 7.7 fits omitting a_μ, the no-name is not needed. Consider Line 9, the fit omitting μH, μD, and a_μ. The parameter ξ floats to a value whose error bars cover 0. Additionally, the Birge ratios R_B for the Table 7.8 fits omitting a_μ are considerably less than 1, indicative of overfitting.

For the Table 7.8 fits containing a_μ, the Birge ratios are all close to 1 and the sector-wise values of χ^2 are under control across all sectors of the fit. Each of the Table 7.8 fits containing a_μ represents a candidate solution to the muon experimental anomalies, valid in its own domain.

[8] Additionally, we assume $sign(g_e) = sign(g_\mu)$ and $sign(g_p) = sign(g_d)$.

line	omit	$(\delta R_\infty/R^*_\infty)/10^{-12}$	$(\delta\alpha/\alpha^*)/10^{-10}$	r_p fm	r_d fm	ξ MeV$^{-2}/10^{-11}$
1	*none*	−12.5(2.9)	−5.1(2.3)	0.84115(27)	2.12879(13)	1.52(39)
2	λ_c	−12.4(2.9)	−6.5(2.6)	0.84117(27)	2.12879(13)	1.59(40)
3	μH	−9.4(3.6)	−5.1(2.3)	0.858(11)	2.12879(13)	1.51(39)
4	μD	−14.1(4.4)	−5.1(2.3)	0.84115(27)	2.1261(055)	1.52(39)
5	$\mu H, \mu D$	2.4(9.6)	−5.1(2.3)	0.879(19)	2.1415(96)	1.50(39)
6	a_e	−12.5(2.9)	−0.1(5.0)	0.84117(27)	2.12879(13)	1.59(40)
7	a_μ	−13.6(3.2)	−1.5(4.9)	0.84082(49)	2.12868(19)	−0.3(2.3)
8	a_e, a_μ	4.0(9.0)	0.0(5.0)	0.8463(26)	2.13054(90)	30(15)
9	$\mu H, \mu D, a_\mu$	2.5(9.6)	0.0(5.0)	0.883(20)	2.1428(97)	−1.1(2.3)
10	eH	−11.1(3.9)	−5.1(2.3)	0.84114(27)	2.12879(13)	1.50(39)
11	eD	−14.3(4.4)	−5.1(2.3)	0.84115(27)	2.12879(13)	1.52(39)
12	eH, eD	−1300(1100)	−6.5(2.6)	0.84115(27)	2.12879(13)	1.57(40)
13	$eD, \mu D$	−14.3(4.4)	−5.1(2.3)	0.84115(27)	–	1.51(40)

Table 7.7: Fitted values of R_∞, α, r_p, r_d for global fits with different observables omitted. A no-name boson (Ch. 6) with mass $m_\chi = 50MeV$ and coupling $\alpha_X = \xi m_X^2$ has been introduced.

line	omit	χ^2	dof	R_B	$\Delta\chi^2$	$\chi^2_{\lambda_c}$	$\chi^2_{\mu H}$	$\chi^2_{\mu D}$	$\chi^2_{a_e}$	$\chi^2_{a_\mu}$	χ^2_{eH}	χ^2_{eD}
1	*none*	12.5	15	.91(10)	15.0	1.0	0.0011	0.000096	0.24	0.019	7.0	3.3
2	λ_c	11.2	14	.89(10)	16.1	–	0.0011	0.000096	0	0.0030	6.9	3.3
3	μH	10.2	14	.85(10)	14.9	1.0	–	0.00038	0.24	0.026	4.7	3.4
4	μD	12.3	14	.94(10)	15.0	1.0	0.00068	–	0.24	0.019	6.8	3.2
5	$\mu H, \mu D$	8.2	13	.79(11)	14.6	1.0	–	–	0.24	0.037	3.3	3.0
6	a_e	11.2	14	.89(10)	16.1	0	0.0011	0.000095	–	0.0030	6.9	3.3
7	a_μ	11.8	14	.92(10)	0.017	0.093	0.0012	0.000095	0.022	–	7.4	3.3
8	a_e, a_μ	7.0	13	.73(11)	4.6	0	0.000053	0.000088	–	–	3.5	3.0
9	$\mu H, \mu D, a_\mu$	6.9	13	.73(11)	0.23	0	–	–	0	–	3.3	3.0
10	eH	5.4	7	.88(17)	14.7	1.0	0	0	0.24	0.035	–	3.2
11	eD	8.1	7	1.08(17)	15.0	1.0	0.00056	0	0.24	0.020	6.8	–
12	eH, eD	0	0	–	15.7	0	0	0	0	0	–	–
13	$eD, \mu D$	8.1	6	1.16(18)	15.0	1.0	0.00069	–	0.24	0.020	6.8	–

Table 7.8: Contributions to χ^2 for global fits with different observables omitted. A no-name boson (Ch. 6) with mass $m_\chi = 50MeV$ and coupling α_X has been introduced. The a_μ sector now has well-controlled χ^2 across all fits. $\Delta\chi^2$ gives the improvement in χ^2 due to the model variation over the corresponding Standard Model fit of Table 7.5. $R_B = \sqrt{\chi^2/dof}$ is the Birge ratio. Overfitting is discussed in the text.

3.2 The general m_X-dependence

Table 7.9 shows the results of refitting Line 1 of Table 7.7 for different values of m_X. The improvement in χ^2 due to the inclusion of the no-name in the fit is 6.6 units for $m_X = 15\ MeV$, increasing to about 15 units for $m_X \approx 50\ MeV$ and remaining at about 15 units for values of m_X out to 1 GeV and beyond. The global fits with

$m_X \gtrsim 30\ MeV$ find $\chi^2_{a_\mu} < 4$ (i.e. $|a_\mu^{exp} - a_\mu^{th}(\alpha)| < 2\sigma$) with chi-squared in all other sectors well-controlled.

Figure 7.8 shows the region in the $m_X - \epsilon^2 = \alpha_X/\alpha$ plane favored by the Table 7.9 analysis. The red band represents the fitted value of α_X for given m_X, plus or minus 2σ. The region of the red band to the right of $m_X \gtrsim 30\ MeV$ defines a global candidate solution region over which the muon experimental anomalies can be said to be solved (up to exclusion limits). The solid black lines define a piecemeal candidate solution region which solves the muon $(g-2)$ anomaly but not the proton size puzzle via a piecemeal fit holding the values of α, R_∞, r_p, and r_d fixed at C14 recommended values and varying only α_X and m_X. The piecemeal fit is falsely restrictive for $m_X \lesssim 50\ MeV$ and stands as an illustration, alongside the proton size puzzle, of the hazards of drawing conclusions on the basis of piecemeal fits. Fitting or placing limits on model parameters without also refitting the fundamental constants on which they depend is a mistake in principle and, in practice, can lead to misleading results, as in Fig. 7.8.

m_χ MeV	$\Delta\chi^2$	$(\delta R_\infty/R^*_\infty)/10^{-12}$	$(\delta\alpha/\alpha^*)/10^{-10}$	r_p fm	r_d fm	ξ MeV$^{-2}/10^{-11}$
15	6.6	−10.9(3.1)	−10.6(3.9)	0.84157(37)	2.12894(16)	4.3(1.7)
25	12.4	−11.4(3.0)	−8.9(2.9)	0.84147(31)	2.12890(14)	3.45(98)
50	15.0	−12.5(2.9)	−5.1(2.3)	0.84115(27)	2.12879(13)	1.52(39)
100	15.5	−13.0(2.9)	−3.6(2.2)	0.84101(26)	2.12875(13)	0.70(18)
150	15.6	−13.1(2.9)	−3.1(2.2)	0.84097(26)	2.12873(13)	0.49(12)
200	15.6	−13.1(2.9)	−3.0(2.2)	0.84096(26)	2.12873(13)	0.40(10)
300	15.6	−13.2(2.9)	−2.8(2.2)	0.84094(26)	2.12872(13)	0.320(81)

Table 7.9: Fitted values of $\delta R_\infty/R^*_\infty$, $\delta\alpha/\alpha^*$, r_p, r_d, and $\xi = \alpha\chi/m_\chi^2$ for the full global fit with m_χ fixed at different values. R^*_∞, α^* are reference values. Line 3 of this table corresponds to Line 1 of Table 7.7.

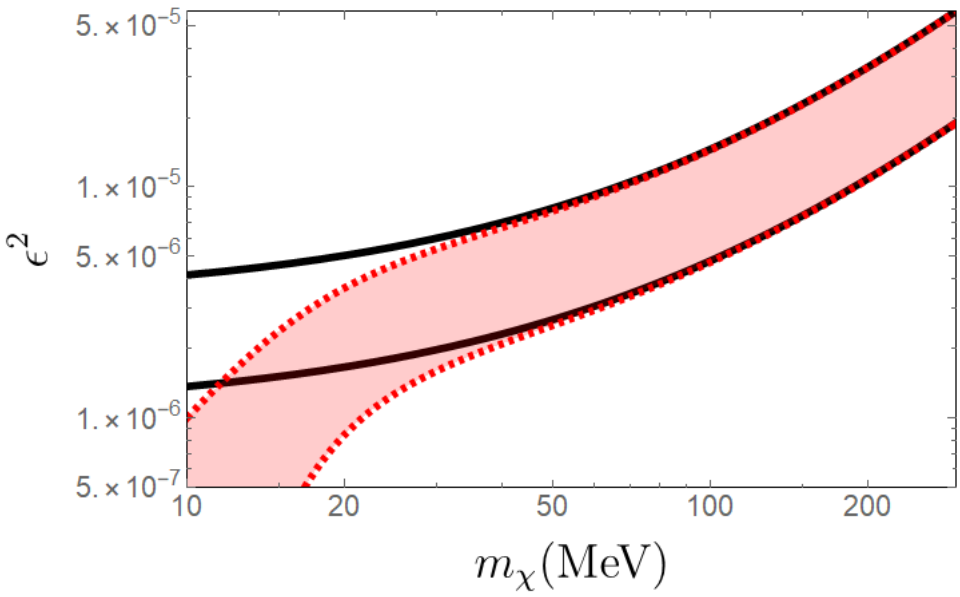

Figure 7.8: Region in the (m_X, α_X) plane favored by the no-name analysis (red). The red band represents the fitted value of α_X for given mass m_X, plus or minus 2σ. Within the red band the improvement $\Delta\chi^2 > 6$ for $m_X > 10MeV$, dropping rapidly to $\Delta\chi^2 > 15$ for $m_X > 50MeV$, and then decreasing monotonically at a much slower rate for larger m_X. No upper limit on m_X can be resolved, The solid black lines define a piecemeal solution region seeking only to solve the muon g-2 anomaly with α, R_∞, r_p, and r_d fixed at C14 recommended values. The region is is falsely restrictive by not implementing a self-consistent global fit.

4 The effect of the Parker datum on the global fit results

Next, we explore the effects of adding the Parker datum [3] to the global fit, with and without a 50 MeV no-name X_V included in the fit.

The Parker datum is discussed in Sec. 1 and implies a value for the fine-structure constant that is 2.4σ larger than the value inferred from the Gabrielse datum [22]:

$$\begin{aligned} Parker: \quad \alpha^2 = \frac{2R_\infty}{c} \cdot \frac{m_{Rb}}{m_e} \cdot \frac{h}{m_{Rb}} \quad &\rightarrow \quad \alpha^{-1}_{Parker} = 137.035999046; \\ Gabrielse: \quad a_e^{exp} = a_e^{th}(\alpha) \quad &\rightarrow \quad \alpha^{-1}_{Gab} = 137.035999084(33); \\ &\alpha_{Parker} > \alpha_{Gab}. \end{aligned} \tag{7.2}$$

4.1 Global fit to the Standard Model

The fits of Tables 7.10 and 7.11 include the Parker datum but are otherwise identical to the fits of Tables 7.4 and 7.5 assuming Standard Model physics.

For the Line 1 fit of Table 7.10, which includes all relevant experimental data, the best-fit value for α floats to a value midway between α_{Gab} and α_{Parker}, leading to a bad fit in the a_e sector (4.9 units of chi-squared for one datum) and the λ_c sector (4.5 units for one datum). $\chi^2_{a_\mu}$ remains approximately 16, as it was for the Line 1 fit of Table 7.5. The net effect of the Parker datum is a layer of complication added to the global fit to the Standard Model: the muon $(g-2)$ anomaly survives unchanged, while the a_e and λ_c sectors of the fit— under good control for the Standard Model fits omitting the Parker datum— are under poor control.

line	omit	$(\delta R_\infty/R^*_\infty)/10^{-12}$	$(\delta\alpha/\alpha^*)/10^{-10}$	r_p fm	r_d fm
1	none	−13.4(2.9)	2.7(1.5)	0.84088(26)	2.12870(13)
2	λ_c	−13.4(2.9)	−2.7(2.4)	0.84088(26)	2.12870(13)
3	μH	−10.2(3.6)	2.7(1.5)	0.858(11)	2.12871(13)
4	a_e	−13.4(2.9)	5.8(1.9)	0.84088(26)	2.12870(13)
5	a_μ	−13.4(2.9)	2.7(1.5)	0.84088(26)	2.12870(13)
6	a_e, a_μ	−13.4(2.9)	5.8(1.9)	0.84088(26)	2.12870(13)
7	$a_\mu, \mu H, \mu D$	3.0(9.5)	2.7(1.5)	0.882(19)	2.1429(96)
8	eH	−12.1(3.9)	2.7(1.5)	0.84087(26)	2.12870(13)
9	eD	−15.3(4.4)	2.7(1.5)	0.84088(26)	2.12870(13)
10	eH, eD	−1700(610)	−2.7(2.4)	0.84087(26)	2.12870(13)

Table 7.10: Fitted values of R_∞, α, r_p, r_d for global fits with different observables omitted. Standard Model physics is assumed. The Table 2.1 reference scheme has been extended to include the Parker datum discussed in Sec. 1.

line	omit	χ^2	$\chi^2_{\lambda_c}$	$\chi^2_{\mu H}$	$\chi^2_{\mu D}$	$\chi^2_{a_e}$	$\chi^2_{a_\mu}$	χ^2_{eH}	χ^2_{eD}
1	none	36.7	4.5	0.0012	0.00010	4.9	15.7	7.3	4.3
2	λ_c	27.3	–	0.0012	0.0000944746	0.0000030	15.7	7.3	4.3
3	μH	34.3	4.5	–	0.00041	4.93624	15.7	4.8	4.4
4	a_e	28.9	1.6	0.00123173	0.000095	–	15.7	7.3	4.3
5	a_μ	21.0	4.5	0.0012	0.00010	4.9	–	7.3	4.3
6	a_e, a_μ	13.2	1.6	0.0012	0.000094	–	–	7.3	4.3
7	$a_\mu, \mu H, \mu D$	16.5	4.6	–	–	5.0	–	3.3	3.5
8	eH	29.2	4.5	0	0.0000059	4.9	15.7	–	4.1
9	eD	32.3	4.5	0.00060	0	4.9	15.7	7.2	–
10	eH, eD	17.3	1.6	0	0	0.0000032	15.7	–	–

Table 7.11: Contributions to χ^2 for global fits with different observables omitted. Standard Model physics is assumed. The Table 2.1 reference scheme has been extended to include the Parker datum discussed in Sec. 1. The muon $(g-2)$ anomaly survives unchanged, while the a_e and λ_c sectors of the fit— under good control for the Standard Model fits omitting the Parker datum (Table 7.5)— are now under poor control.

4.2 Global fit to the Standard Model plus X_V

The addition of a no-name X_V to the global fits of Tables 7.10 and 7.10 has the effect of increasing the tension between the piecemeal values of α_{Parker} and α_{Gab}. X_V contributes a positive quantity Δa_e to a_e(theory), according to Eq. 6.6. With the value of $a_e(exp)$ held fixed, the result of adding a term $\Delta a_e > 0$ to a_e(theory) is a decrease in the value of α inferred from the Gabrielse measurement.[9] Hence, since X_V does not affect the value of α inferred from the Compton sector of the fit (i.e. the value of α inferred from the Parker measurement), the addition of X_V to the global fits of Tables 7.10 and 7.11 increases the tension between the piecemeal values of α_{Parker} and α_{Gab}.

The results of adding a $50 - MeV$ X_V to the fits of Tables 7.10 and 7.11 are shown in Tables 7.12 and 7.13. We focus on the Line 1 results. α floats to a value between α_{Gab} and α_{Parker} but closer to α_{Gab}, and ξ floats to a value such that $\chi^2_{a_\mu} \sim 1$, $\chi^2_{a_e} \sim 8$, and $\chi^2_{\lambda_c} \sim 6.6$. The overall reduction in chi-squared between the Line 1 fit of Table 7.11 and the Line 1 fit of Table 7.13, which is due entirely to the

[9] $a_e^{exp} = a_e^{th}(\alpha) + \Delta a_e(\alpha_X, m_X)$.

inclusion of the no-name in the latter fit, is 9 units. The contribution of X_V to the Line1, Table 7.13 fit absorbs only part of the muon $(g-2)$ anomaly's 16 units of chi-squared and pushes the remainder into the already-discrepant a_e and λ_c sectors of the fit.

Tables 7.13 and 7.12 militate against a $50-MeV$ no-name as a self-consistent candidate solution to the muon $(g-2)$ anomaly. However the Parker datum does not change our earlier conclusions about the proton size puzzle. Chi-squared in the spectroscopy sectors of Tables 7.12 and 7.13 (as well as Tables 7.10 and 7.11) is under good control, and $r_p \sim 0.84\ fm$.

In the remainder of this chapter, we will make small variations to the analyses of Tables 7.12 and 7.13, of the kind enabled by `CONSTANT FINDER`. The goal is to recover a self-consistent global candidate solution to the muon experimental anomalies that accounts for the Parker datum.

line	omit	$(\delta R_\infty/R^*_\infty)/10^{-12}$	$(\delta\alpha/\alpha^*)/10^{-10}$	r_p fm	r_d fm	ξ MeV$^{-2}/10^{-11}$
1	none	−12.8(2.9)	1.7(1.5)	0.84109(27)	2.12877(13)	1.16(38)
2	λ_c	−12.4(2.9)	−6.3(2.6)	0.84117(27)	2.12880(13)	1.59(39)
3	μH	−9.6(3.6)	1.7(1.5)	0.859(11)	2.12878(13)	1.15(38)
4	μD	−14.2(4.4)	1.7(1.5)	0.84109(27)	2.1264(55)	1.16(38)
5	$\mu H, \mu D$	2.8(9.5)	1.8(1.5)	0.880(19)	2.1423(96)	1.14(38)
6	a_e	−12.5(2.9)	5.8(1.9)	0.84117(27)	2.12880(13)	1.59(39)
7	a_μ	−15.3(3.0)	5.6(1.9)	0.84027(35)	2.12850(15)	−3.4(1.3)
8	a_e, a_μ	4.7(8.9)	5.9(1.9)	0.8465(26)	2.13061(90)	32(15)
9	$\mu H, a_\mu$	3.4(9.5)	5.9(1.9)	0.887(19)	2.1451(96)	−3.8(1.3)
10	eH	−11.4(3.9)	1.7(1.5)	0.84108(27)	2.12877(13)	1.14(38)
11	eD	−14.6(4.4)	1.7(1.5)	0.84109(27)	2.12877(13)	1.16(38)
12	eH, eD	−2440(640)	−6.3(2.6)	0.84116(27)	2.12880(13)	1.57(40)
13	$eD, \mu D$	−14.6(4.4)	1.7(1.5)	0.84109(27)	–	1.16(0.38)

Table 7.12: Fitted values of R_∞, α, r_p, r_d for global fits with different observables omitted. A no-name boson (Ch. 6) with mass $m_\chi = 50MeV$ and coupling α_X has been introduced, and the Table 2.1 reference scheme has been extended to include the Parker datum.

line	omit	χ^2	$\Delta\chi^2$	$\chi^2_{\lambda_c}$	$\chi^2_{\mu H}$	$\chi^2_{\mu D}$	$\chi^2_{a_e}$	$\chi^2_{a_\mu}$	χ^2_{eH}	χ^2_{eD}
1	none	27.4	9.3	6.6	0.0011	0.00010	8.5	1.1	7.0	4.2
2	λ_c	11.2	16.1	–	0.0011	0.000094	0.0	0.0030	6.9	4.2
3	μH	25.2	9.1	6.6	–	0.00037	8.5	1.1	4.7	4.3
4	μD	27.3	9.3	6.6	0.00067	–	8.5	1.1	6.9	4.2
5	$\mu H, \mu D$	23.2	8.9	6.6	–	–	8.5	1.2	3.3	3.6
6	a_e	12.8	16.1	1.6	0.0011	0.000094	–	0.0030	6.9	4.2
7	a_μ	14.3	6.7	1.6	0.0015	0.000096	0.029	–	8.3	4.3
8	a_e, a_μ	8.7	4.6	1.6	0.000053	0.000088	–	–	3.5	3.6
9	μ_H, a_μ	8.5	8.0	1.6	–	–	0	–	3.3	3.5
10	eH	20.3	9.0	6.6	0	0.0000048	8.4	1.2	–	4.1
11	eD	23.0	9.3	6.6	0.00055	0	8.4	1.1	6.9	–
12	eH, eD	1.6	15.7	1.6	0	0	0	0	–	–
13	$eD, \mu D$	23.0	9.3	6.6	0.00061	–	8.4	1.1	6.9	–

Table 7.13: Contributions to χ^2 for global fits with different observables omitted. A no-name boson (Ch. 6) with mass $m_\chi = 50MeV$ and coupling α_X has been introduced, and the Table 2.1 reference scheme has been extended to include the Parker datum. In the Line 1 fit, the no-name absorbs only part of the muon $(g-2)$ anomaly's 16 units of chi-squared and pushes the remainder into the already-discrepant a_e and λ_c sectors of the fit.

4.3 Global fit to the Standard Model plus X_V plus Δa_e

We explore the possibility that the experimental value for the electron anomalous moment contains an unaccounted-for systematic bias of size $\sim few \times u(a_e^{exp}) \sim 7 \times 10^{-13}$.

A plausibility argument for such a bias is laid out in Sec. 4. Relativistic corrections to the axial motion of the electron in the Penning trap could be responsible for an unaccounted-for systematic bias in the measured value of a_e of the size discussed. Such a bias, when accounted for, would increase the value of α_{Gab} and bring it in line with α_{Parker}.

The fits of Tables 7.14 and 7.15 use the Table 2.1 value for a_e^{exp} shifted by $\Delta a_e = 7 \times 10^{-13}$ but are otherwise identical to the fits of Tables 7.12 and 7.13. Each of the fits of Table 7.15 is well-controlled across all sectors of chi-squared, with the fits containing a_μ representing viable candidate solutions to the muon experimental

anomalies, valid in their own domains.[10]

Figure 7.9 shows χ^2 (solid line), $\chi^2_{\lambda_c}$ (dashed), and $\chi^2_{a_e}$ (dot-dashed) as a function of the size of the bias correction added to $a_e(exp)$.

line	omit	$(\delta R_\infty/R^*_\infty)/10^{-12}$	$(\delta\alpha/\alpha^*)/10^{-10}$	r_p fm	r_d fm	ξ MeV$^{-2}/10^{-11}$
1	none	−12.6(2.9)	3.8(1.5)	0.84113(27)	2.12879(13)	1.38(38)
2	λ_c	−12.5(2.9)	−0.3(2.6)	0.84117(27)	2.12880(13)	1.60(40)
3	μH	−9.5(3.6)	3.8(1.5)	0.858(11)	2.12879(13)	1.37(38)
4	μD	−14.0(4.4)	3.8(1.5)	0.84113(27)	2.1265(55)	1.38(38)
5	$\mu H, \mu D$	3.1(9.5)	3.8(1.5)	0.881(19)	2.1424(96)	1.35(38)
6	a_e	−12.5(2.9)	5.8(1.9)	0.84117(27)	2.12880(13)	1.59(39)
7	a_μ	−13.9(3.0)	5.6(1.9)	0.84074(35)	2.12865(15)	−0.8(1.3)
8	a_e, a_μ	4.7(8.9)	5.9(1.9)	0.8465(26)	2.13061(90)	32(15)
9	$\mu H, a_\mu$	3.4(9.5)	5.9(1.9)	0.884(19)	2.1439(96)	−1.1(1.3)
10	eH	−11.3(3.9)	3.8(1.5)	0.84112(27)	2.12879(13)	1.36(38)
11	eD	−14.4(4.4)	3.8(1.5)	0.84113(27)	2.12879(13)	1.37(38)
12	eH, eD	−1230(640)	−0.2(2.6)	0.84116(27)	2.12880(13)	1.57(40)
13	$eD, \mu D$	−14.4(4.4)	3.8(1.5)	0.84113(27)	–	1.37(38)

Table 7.14: Fitted values of R_∞, α, r_p, r_d for global fits with different observables omitted. A no-name boson (Ch. 6) with mass $m_\chi = 50MeV$ and coupling α_X has been introduced, the Table 2.1 reference scheme has been extended to include the Parker datum, and a speculative (but well-motivated) systematic bias correction has been added to the Table 2.1 value of a_e^{exp}.

[10]The fits of Table 7.14 omitting a_μ can be regarded as viable candidate solutions to the muon experimental anomalies, too, under appropriate assumptions— e.g. that the BNL measurement of a_μ is in error and should not be included in the fit.

line	omit	χ^2	$\Delta\chi^2$	$\chi^2_{\lambda_c}$	$\chi^2_{\mu H}$	$\chi^2_{\mu D}$	$\chi^2_{a_e}$	$\chi^2_{a_\mu}$	χ^2_{eH}	χ^2_{eD}
1	none	16.5	20.2	2.9	0.0011	0.000099	2.1	0.25	7.0	4.2
2	λ_c	11.2	16.1	–	0.0011	0.000094	0.0	0.0030	6.9	4.2
3	μH	14.3	20.0	2.9	–	0.00037	2.1	0.27	4.7	4.3
4	μD	16.3	20.2	2.9	0.00068	–	2.1	0.25	6.8	4.2
5	$\mu H, \mu D$	12.2	19.9	2.9	–	–	2.2	0.31	3.3	3.5
6	a_e	12.8	16.1	1.6	0.0011	0.000094	–	0.0030	6.9	4.2
7	a_μ	13.5	7.5	1.6	0.0013	0.000095	0.025	–	7.6	4.3
8	a_e, a_μ	8.7	4.6	1.6	0.000053	0.000088	–	–	3.5	3.6
9	$\mu H, a_\mu$	8.5	8.0	1.6	–	–	0.0	–	3.3	3.5
10	eH	9.4	19.9	2.9	0.0	0.0000068	2.1	0.30	–	4.1
11	eD	12.1	20.2	2.9	0.00055	0.0	2.1	0.25	6.8	–
12	eH, eD	1.6	15.7	1.6	0.0	0.0	0.0	0.0	–	–
13	$eD, \mu D$	12.1	20.2	2.9	0.00055	–	2.1	0.25	6.8	–

Table 7.15: Contributions to χ^2 for global fits with different observables omitted. A no-name boson (Ch. 6) with mass $m_\chi = 50MeV$ and coupling α_X has been introduced, the Table 2.1 reference scheme has been extended to include the Parker datum, and a speculative (but well-motivated) systematic bias correction has been added to the Table 2.1 value of a_e^{exp}. The a_μ sector now has well-controlled χ^2 across all fits. $\Delta\chi^2$ gives the improvement in χ^2 due to the model variation over the corresponding Standard Model fit of Table 7.11.

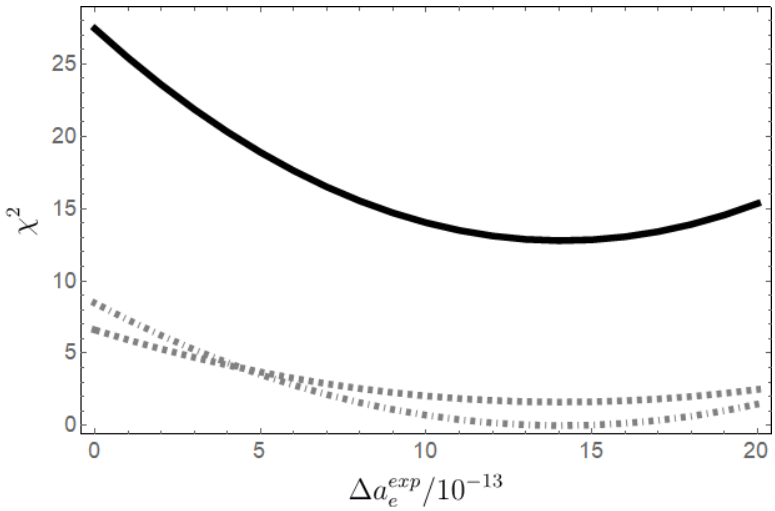

Figure 7.9: χ^2 (solid line), $\chi^2_{\lambda_c}$ (dashed), and $\chi^2_{a_e}$ (dot-dashed) for a variation on the global fit of Line 1, Table 7.15, which has been modified to be a function of Δa_e^{exp}, the bias correction discussed in the text. The Line 1, Table 7.15 fit assumes a bias correction of size 7×10^{-13}.

5 Additional theory alternatives

We explore the effects of adding generic scalar and pseudoscalar particles to the global fit, as we did with the no-name X_V. We denote the generic scalar by X_S and the generic pseudoscalar by X_P. X_S and X_P are discussed in detail in Ch. 6. X_S contributes to the moments sectors of the global fit according to Eq. 6.6 and to the spectroscopy sectors according to Eq. 6.12, while X_P contributes only to the moments sectors of the fit (see Eq. 6.6).

5.1 Global fit to the Standard Model plus lepton-universal $X_V/X_S/X_P$

Line 1 of Tables 7.16 and 7.17 corresponds to Line 1 of Tables 7.12 and 7.13, in which a no-name X_V was added to the fit to the reference scheme modified to include the Parker datum. The fits of Lines 2 and 3 correspond to fits in which X_V was traded for X_S and X_P, respectively. Neither X_S nor X_P is able to reduce the size of the muon $(g-2)$ anomaly. $\chi^2_{a_\mu} = 15.7$ takes the same value as it did before any new physics terms were added to the fit (Line 1, Table 7.13). X_S (X_P) are not able to improve the fit in the a_μ sector because the contribution to the electron anomalous moment due to X_S (X_P) is an order of magnitude larger than the contribution due to X_V for the same ξ. For a fit including $X_{S/P}$, shifting ξ away from zero would create a worse fit in the a_e sector, which is already under strain due to the upward pressure on the fitted value of α applied by the Parker datum. The result is that ξ gets stuck at zero, and the muon $(g-2)$ anomaly remains intact.

line	alternative	$(\delta R_\infty/R^*_\infty)/10^{-12}$	$(\delta\alpha/\alpha^*)/10^{-10}$	r_p fm	r_d fm	ξ MeV$^{-2}/10^{-11}$
1	X_V	−12.8(2.9)	1.7(1.5)	0.84109(27)	2.12877(13)	1.16(38)
2	X_S	−13.4(2.9)	2.9(1.8)	0.84088(26)	2.12870(13)	0.000(94)
3	X_P	−13.4(2.9)	2.9(1.8)	0.84088(26)	2.12870(13)	0.000(94)

Table 7.16: Fitted values of R_∞, α, r_p, r_d for global fits that include the effects of different theory alternatives. An $m_{Xi} = 50MeV$ vector (X_V), scalar (X_S), and pseudoscalar (X_P) have been added to the fits of Line 1, Line 2, and Line 3, respectively, and the Table 2.1 reference scheme has been extended to include the Parker datum. The fits assume $X_{V/S/P}$ couple with equal strength to muons and electrons.

line	alternative	χ^2	$\Delta\chi^2$	$\chi^2_{\lambda_c}$	$\chi^2_{\mu H}$	$\chi^2_{\mu D}$	$\chi^2_{a_e}$	$\chi^2_{a_\mu}$	χ^2_{eH}	χ^2_{eD}
1	X_V	27.4	9.3	6.6	0.0	0.0	8.5	1.1	7.0	4.2
2	X_S	36.7	0.0	4.1	0.0	0.0	5.4	15.7	7.3	4.3
3	X_P	36.7	0.0	4.1	0.0	0.0	5.4	15.7	7.4	4.3

Table 7.17: Contributions to χ^2 for global fits that include the effects of different theory alternatives. An $m_{Xi} = 50MeV$ vector (X_V), scalar (X_S), and pseudoscalar (X_P) have been added to the fits of Line 1, Line 2, and Line 3, respectively, and the Table 2.1 reference scheme has been extended to include the Parker datum. The fits assume $X_{V/S/P}$ couple with equal strength to muons and electrons. X_V absorbs part of the muon $(g-2)$ anomaly and pushes the remainder into the a_e and λ_c sectors of the fit, as discussed in sec:smplusxv. X_S and X_P are not able to improve the fit in the a_μ. See text for discussion.

5.2 Global fit to the Standard Model plus lepton-universality-violating $X_V/X_S/X_P$

We repeat the fits of the previous section but relax the assumption of lepton universality by assuming any new physics couples only to muons. The three fits of Table 7.18 yield substantively the same results. ξ is zero in the a_e sector and comes in to repair the muon $(g-2)$ anomaly in the a_μ sector. The sign difference between ξ on Line 1 and ξ on Line 2 can be traced to the relative minus sign between the Yukawa potential for a vector and the Yukawa potential for a scalar (see Eq. 6.10). Recall that ξ must be positive in the moments sectors but can, in general, take either sign in the spectroscopy sectors. For the Line 3 fit including X_P, ξ does not contribute to the spectroscopy sectors (see Sec. 2) and so takes a positive sign where it enters the fit, in the a_μ sector.

The fits of Tables 7.18 and 7.19 are able to solve the muon $(g-2)$ anomaly but leave the 2.4σ discrepancy between the values of α_{Parker} and α_{Gab} intact. That discrepancy, however, is not inconsistent with the year over year fluctuations observed in historical determinations of the value of α, which are shown in Fig. 1.2. The fits of Tables 7.18 and 7.19, then, represent viable candidate solutions to the muon experimental anomalies, up to complications stemming from the tension be-

tween the piecemeal values of α that can be inferred from the Parker and Gabrielse measurements.

line	alternative	$(\delta R_\infty/R^*_\infty)/10^{-12}$	$(\delta\alpha/\alpha^*)/10^{-10}$	r_p fm	r_d fm	ξ MeV$^{-2}/10^{-11}$
1	X_V	−13.3(2.9)	2.7(1.5)	0.84117(27)	2.12880(13)	1.58(40)
2	X_S	−13.4(2.9)	2.7(1.5)	0.84103(27)	2.12875(13)	−0.79(20)
3	X_P	−13.4(2.9)	2.7(1.5)	0.84088(26)	2.12870(13)	1.60(40)

Table 7.18: Fitted values of R_∞, α, r_p, r_d for global fits that include the effects of different theory alternatives. A $m_\chi = 50MeV$ vector (X_V), scalar (X_S), and pseudoscalar (X_P) have been added to the fits of Line 1, Line 2, and Line 3, respectively, and the Table 2.1 reference scheme has been extended to include the Parker datum. The fits assume $X_{V/S/P}$ couple only to muons.

line	alternative	χ^2	$\Delta\chi^2$	$\chi^2_{\lambda_c}$	$\chi^2_{\mu H}$	$\chi^2_{\mu D}$	$\chi^2_{a_e}$	$\chi^2_{a_\mu}$	χ^2_{eH}	χ^2_{eD}
1	X_V	21.0	15.7	4.5	0.0	0.0	4.9	0.0	7.3	4.3
2	X_S	21.0	15.7	4.5	0.0	0.0	4.9	0.0	7.3	4.3
3	X_P	21.0	15.7	4.5	0.0	0.0	4.9	0.0	7.3	4.3

Table 7.19: Contributions to χ^2 for global fits that include the effects of different theory alternatives. An $m_{Xi} = 50MeV$ vector (X_V), scalar (X_S), and pseudoscalar (X_P) have been added to the fits of Line 1, Line 2, and Line 3, respectively, and the Table 2.1 reference scheme has been extended to include the Parker datum. The fits assume $X_{V/S/P}$ couple only to muons. All three fits are able to solve the muon $(g-2)$ anomaly but leave the 2.4σ discrepancy between the values of α_{Parker} and α_{Gab} intact. See text for discussion.

Chapter 8

The CONSTANT FINDER website

CONSTANT FINDER enables users to fit the fundamental constants according to a scheme of their choosing. This chapter functions as a user guide for the site.

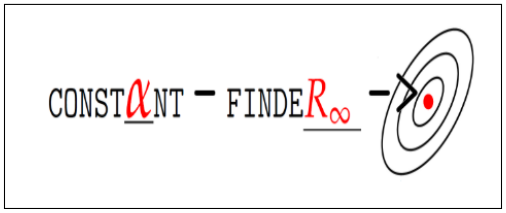

Figure 8.1: CONSTANT FINDER logo.

1 Overview of the site

The site homepage consists of a set of collapsible menus, organized under a sticky header, which remains visible at the top of the page on scrolling. The header, shown in Fig. 8.2, contains links to the auxilliary pages of the site. The auxilliary pages contain information on the data available on the site (via the 'Data Tables' link in the header), how to use the site ('FAQ'), previous implementations[1] of site code ('Downloads'), and known problems with the site ('Bug Reports'). The data available on the site is shown in Table 8.3.

[1]The implementations are contained in downloadable Mathematica notebooks.

Figure 8.2: `CONSTANT FINDER` site header.

The collapsible menus are where users specify the scheme to be fit. The menus, labeled respectively 'Fit-type', 'Input Data', and 'Theory Alternatives', are described in detail below (Secs. 2-4). Once a scheme is chosen, a global fit can be initiated in the 'Global Fit Results' section, below the collapsible menus. The 'Global Fit Results' section is discussed in Sec. 5.

Experimental datum [units]	Experimental value	σ_{expt}
$\nu_H(2S1/2-8S1/2)$ [Hz]	$7.70649350012000 \times 10^{14}$	8600
$\nu_H(2S1/2-8D3/2)$ [Hz]	$7.70649504450000 \times 10^{14}$	8300
$\nu_H(2S1/2-8D5/2)$ [Hz]	$7.70649561584200 \times 10^{14}$	6400
$\nu_H(2S1/2-12D3/2)$ [Hz]	$7.99191710472700 \times 10^{14}$	9400
$\nu_H(2S1/2-12D5/2)$ [Hz]	$7.99191727403700 \times 10^{14}$	7000
$\nu_H(2P1/2-2S1/2)$ [Hz]	1057845000	9000
$\nu_H(2S1/2-2P3/2)$ [Hz]	9911200000	12000
$\nu_H(2P1/2-2S1/2)$ [Hz]	1057862000	20000
$\nu_H(1S1/2-2S1/2)$ [Hz]	$2.466061413187035 \times 10^{15}$	10
$\nu_H(1S1/2-2S1/2)$ [Hz]	$2.466061413187018 \times 10^{15}$	11
$\nu_H(1S1/2-3S1/2)$ [Hz]	$2.922743278678 \times 10^{15}$	130000
$\nu_H(2S1/2-4S1/2)-1/4\nu_H(1S1/2-2S1/2)$ [Hz]	4797338000	10000
$\nu_H(2S1/2-4D5/2)-1/4\nu_H(1S1/2-2S1/2)$ [Hz]	6490144000	24000
$\nu_H(2S1/2-4P1/2)-1/4\nu_H(1S1/2-2S1/2)$ [Hz]	4664269000	15000
$\nu_H(2S1/2-4P3/2)-1/4\nu_H(1S1/2-2S1/2)$ [Hz]	6035373000	10000
$\nu_H(2S1/2-6S1/2)-1/4\nu_H(1S1/2-3S1/2)$ [Hz]	4197604000	21000
$\nu_H(2S1/2-6D5/2)-1/4\nu_H(1S1/2-3S1/2)$ [Hz]	4699099000	10000
$\nu_D(2S1/2-8S1/2)$ [Hz]	$7.708590412457 \times 10^{14}$	6900
$\nu_D(2S1/2-8D3/2)$ [Hz]	$7.708591957018 \times 10^{14}$	6300
$\nu_D(2S1/2-8D5/2)$ [Hz]	$7.708592528495 \times 10^{14}$	5900
$\nu_D(2S1/2-12D3/2)$ [Hz]	$7.99409168038 \times 10^{14}$	8600
$\nu_D(2S1/2-12D5/2)$ [Hz]	$7.994091849668 \times 10^{14}$	6800
$\nu_D(2P1/2-2S1/2)$ [Hz]	1059280000	60000
$\nu_D(2S1/2-2P3/2)$ [Hz]	9912610000	300000
$\nu_D(2P1/2-2S1/2)$ [Hz]	1059280000	60000
$\nu_D(1S1/2-2S1/2)$ [Hz]	$2.4667324085 \times 10^{15}$	700000
$\nu_D(1S1/2-2S1/2)$ [Hz]	$2.466732407521474 \times 10^{15}$	160
$\nu_D(2S1/2-4S1/2)-1/4\nu_D(1S1/2-2S1/2)$ [Hz]	4797338000	10000
$\nu_D(2S1/2-4D5/2)-1/4\nu_D(1S1/2-2S1/2)$ [Hz]	6490144000	24000
a_e	0.00115965218072	2.8×10^{-13}
a_μ	0.00116592089	6.3×10^{-10}
$\Delta E_{LS}(\mu H)$ [meV]	202.3706	0.0023
$\Delta E_{LS}(\mu D)$ [meV]	202.8785	20.0034
λ_e [m]/10^{-12}	2.4263102367	1.1×10^{-9}

Figure 8.3: Input data available on the `CONSTANT FINDER` site. Additional input data can be added by hand. See Fig. 8.7.

2 The Fit-Type menu

The fit-type menu is shown in Fig. 8.4. The available fit-types are chi-squared (Eq. 2.6), chi-squared with pull (Eq. 2.9), and chi-squared marginalized over nuisance parameters (Eq. 2.10). An option to fit chi-squared including correlations between input data (Eq. 2.11) is not available at the time of writing.

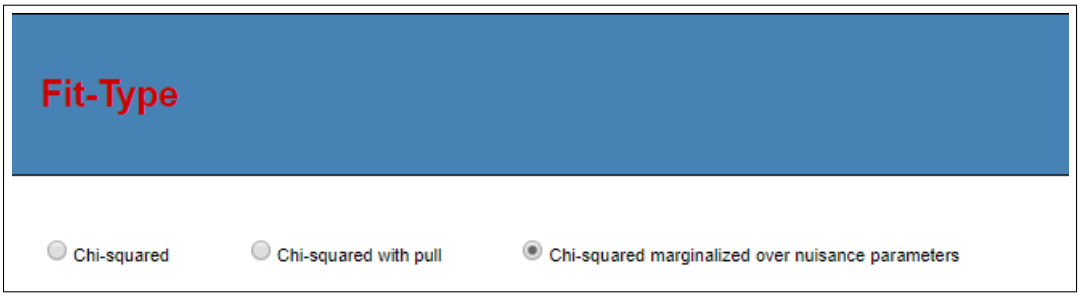

Figure 8.4: 'Fit-type' menu.

3 The Input Data menu

The input data menu opens onto a set of collapsible submenus, which are labeled:

- Fixed parameters; Electronic hydrogen, eH; Electronic deuterium, eD; Muonic hydrogen, μH; Muonic deuterium, μD; Electron anomalous magnetic moment, a_e; Muon anomalous magnetic moment, a_μ; Compton wavelength, λ_e; and Additional input data.

The fixed parameters submenu (Fig. 8.5) enables the fixed parameters of the Standard Model theory entering the global fit to be changed by hand. Descriptions are provided for fixed parameters whose meanings are not obvious to non-experts. The descriptions can be accessed through links marked [INFO].

The remaining submenus— save for the submenu labeled 'Additional Input Data'— are labeled according to the sectors of the global fit. The electronic deuterium submenu is shown in Fig. 8.5 and lists the eD data available on the site.

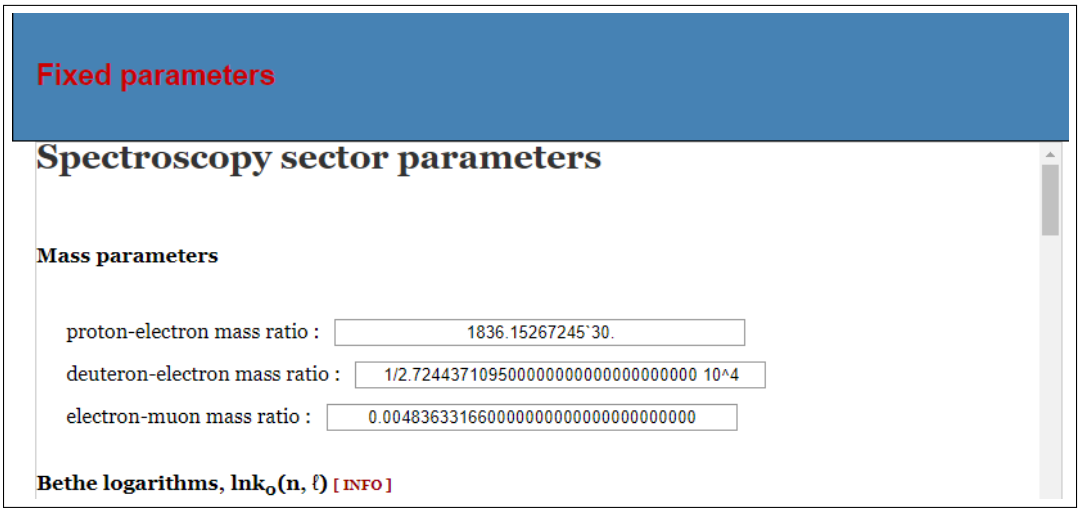

Figure 8.5: 'Fixed parameters' sub-menu of the 'input data' menu. The sub-menu enables the fixed parameters of the Standard Model theory entering the global fit to be changed by hand. Descriptions of the fixed parameters can be accessed through a set of links marked [INFO].

Within the submenu for each sector, the experimental value, experimental uncertainty, and theory (or nuisance parameter[2]) uncertainty for the data in that sector can be changed by hand. Check boxes to the left of each datum control which data are to be included in the global fit.

The default values for all the experimental values and experimental uncertainties contained in the 'Input Data' submenus are given in Table 8.3, the default values for the theory uncertainties are set to zero, and the default values for the nuisance parameter uncertainties are set to the value of the corresponding experimental uncertainty.

Additional input data can be specified via the 'Additional Input Data' submenu. Selecting the 'New' button creates an instance of a fillable form, where information about the new datum can be entered. The fillable form is shown in Fig. 8.7. The form requires the *input datum type* to be specified, in addition to the datum's experimental value, experimental uncertainty, and theory/nuisance parameter uncertainty.

[2]Theory uncertainties must be specified for fit-type chi-squared with pull; nuisance parameter uncertainties, for fit-type chi-squared marginalized over nuisance parameters.

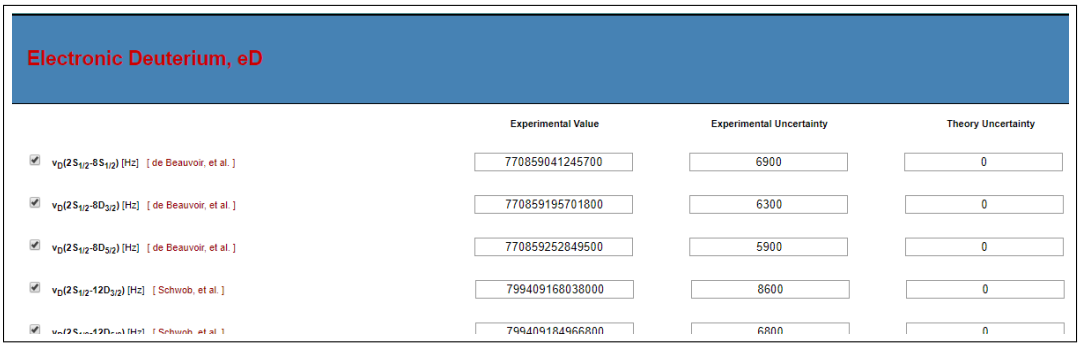

Figure 8.6: 'Electronic deuterium' sub-menu of the 'input data' menu. Editable check boxes determine which data is to be included in the global fit. Each global fit sector has its own sub-menu. The global fit sector sub-menus enable the experimental values, experimental uncertainties, and theory (or nuisance parameter) uncertainties of the selected data to be edited. The default values for the experimental values and experimental uncertainties are given in Table 8.1, the default values for the theory uncertainties are set to zero, and the default values for the nuisance parameter uncertainties are set to the value of the corresponding experimental uncertainty.

A new input datum of type eH, eD, μH, or μD requires the input of additional information.

For a new input datum of type eH or eD, the quantum numbers for the relevant transition must be specified, where the transition is assumed to be of the form

$$\Delta f = (f_{n2,\ell 2,j2} - f_{n1,\ell 1,j1}) - c \cdot (f_{n4,\ell 4,j4} - f_{n3,\ell 3,j3})\ [Hz]. \tag{8.1}$$

The $1S_{1/2}$–$2S_{1/2}$ transition, for example, would have quantum numbers $(n1, \ell 1, j1) = (1, 0, 1/2)$ and $(n2, \ell 2, j2) = (2, 0, 1/2)$, with the parameter c set to zero. (Note the absence of hyperfine splitting quantum numbers from Eq. 8.1. The input datum matched to Δf must be a hyperfine centroid frequency.)

For a new input datum of type μH or μD, a theory expression for the transition must be entered by hand. The hyperfine splitting corrections necessary for computing arbitrary μH and μD transitions are not included in the `CONSTANT FINDER` algorithm. The fundamental constants within the μH or μD theory expressions

should be parameterized as

$$\alpha := aCOD \cdot (1 + 10^{-10} dalp); \quad r_p := rr; \quad r_d = rrD. \tag{8.2}$$

Figure 8.7 cuts off above where the additional fillable blanks required for the input of new spectroscopy data appear. Up to ten additional input data may be added to a given global fit.

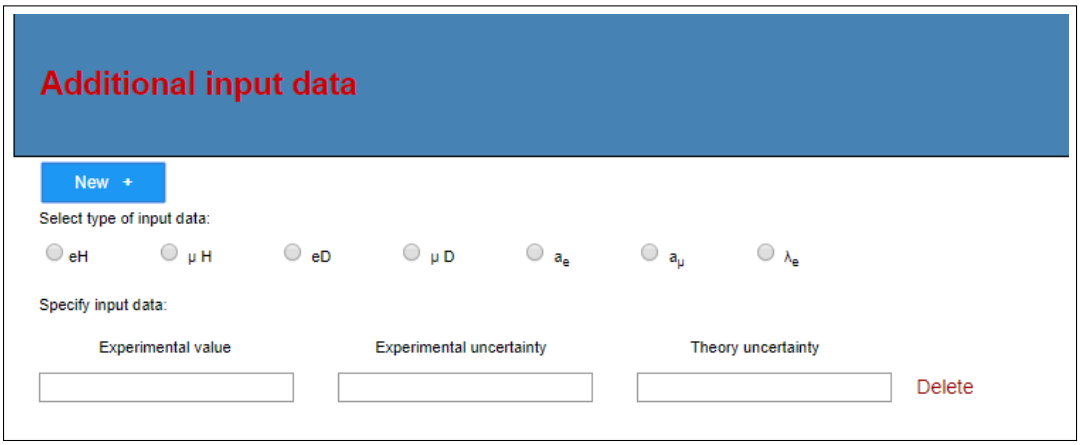

Figure 8.7: 'Additional input data' sub-menu of the 'input data' menu. The sub-menu enables up to ten additional data points to be added to the fit.

4 The Theory Alternatives menu

The theory alternatives menu is shown in Fig. 8.8. The menu consists of three radio buttons. The radio button for theory alternative 'None' specifies a fit to Standard Model theory. The radio button for theory alternative '"No-name" vector boson" specifies a fit to Standard Model theory plus terms added to the moments and spectroscopy sectors modeling the effects of a no-name vector boson. The phenomenology of the no-name boson is discussed in Ch. 6, as well as in Ref. [62]. A mass m_X for the no-name must be specified prior to the global fit, with m_X set to 50 MeV by default. Finally, the radio button for theory alternative 'Other' specifies

a fit to Standard Model theory plus a user-specified theory alternative.

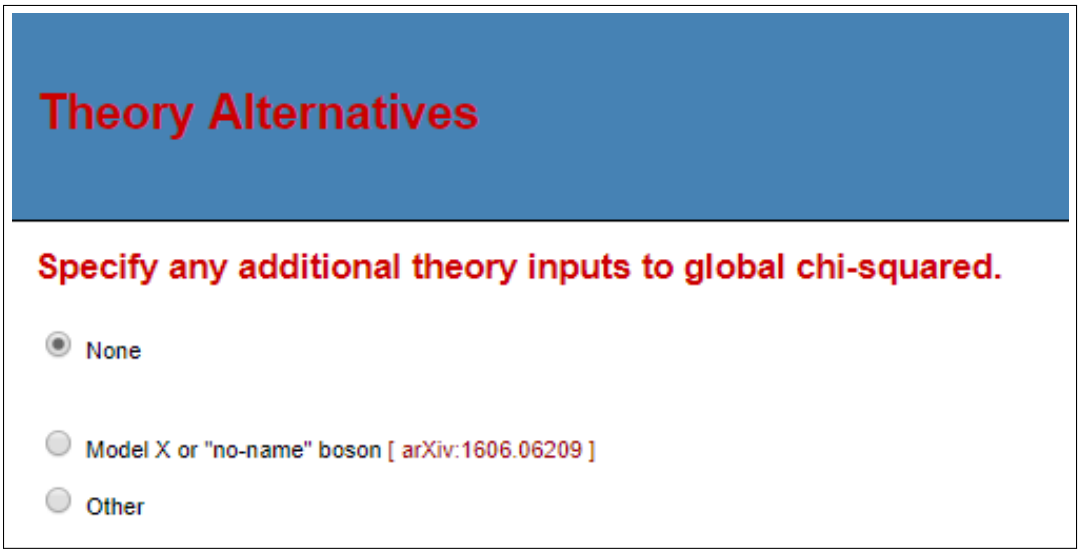

Figure 8.8: 'Theory alternatives' menu. Radio buttons ('None', 'No-name boson', 'Other') determine the theory alternatives to be included in the global fit.

Selecting theory alternative 'Other' creates a 7×3 table of fillable blanks. Each row in the table parameterizes the contribution of the user-specified theory alternative to a given sector. The first blank of each row is for the sector-wise theory expression for the theory alternative, the second blank is for the free parameters of the theory expression (i.e. the parameters to be fit), and the third blank is for the fixed parameters of the theory expression. The blanks for specifying a new contribution to eH theory are shown in Fig. 8.8.

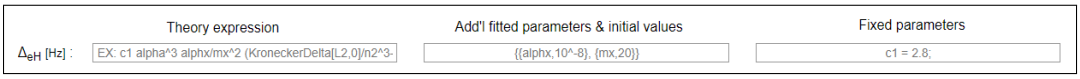

Figure 8.9: Input blanks for a theory alternative of type 'Other'. Each global fit sector has a set of three blanks. The blanks enable the theory expression parameterizing the theory alternative in that sector to be fully specified. The first blank is for the theory expression itself, the second is for the free parameters of the theory expression, and the third is for the fixed parameters of the theory expression. The blanks for the eH sector are shown.

5 The Global Fit Results section

The global fit results section contains two buttons: an 'Evaluate' button and a 'Generate' button. The buttons are shown in Fig. 8.10. The 'Evaluate' button prints the results of a given fit under the global fit results section. See Fig. 8.11 for example fit results. The 'Generate' button exports the fit results to a Mathematica notebook. The Mathematica notebook includes results analogous to those of Fig. 8.11, as well as an analytic expression for the chi-squared function used in the fit. The chi-squared expression allows for analyses along the lines of the analyses of Ch. 7.

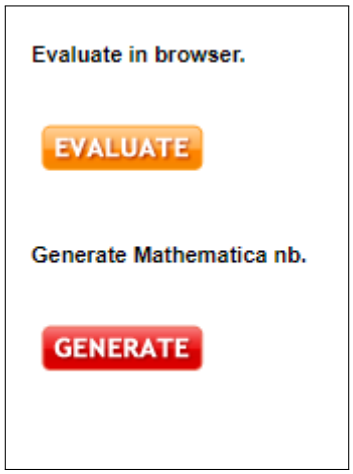

Figure 8.10: Buttons to initiate a global fit. Global fit results can be printed in the browser window ('Evaluate') or exported to a Mathematica notebook file ('Generate').

Fitted values:

dalp	−0.0735618 ± 0.02198
rr	0.840881 ± 0.000261597
rrD	2.12647 ± 0.00547901

Chi-squared:

Sector	Chi-squared
eH	7.1949
eD	4.2455
muH	0.000754973
ae	0.197676
amu	15.6748
Compton	0.0000143215
total	27.3137
dof	16

Covariance matrix:

	dalp	rr	rrD
dalp	0.000483122	1.42619×10^{-7}	0.0000903491
rr	1.42619×10^{-7}	6.84332×10^{-8}	2.66713×10^{-8}
rrD	0.0000903491	2.66713×10^{-8}	0.0000300196

Contour plots:

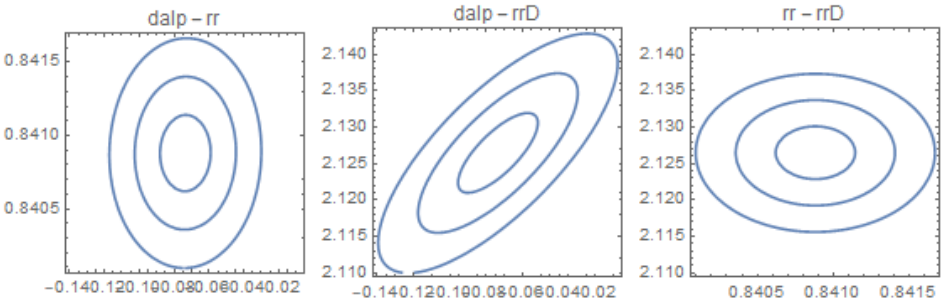

Powered by WOLFRAM WEB MATHEMATICA

Figure 8.11: Example global fit results obtained via the 'Evaluate' button.

Chapter 9

Concluding remarks

Our initial interest in the fundamental constants came out of an interest in the muon experimental anomalies. So, let us take a moment to summarize the status of the muon experimental anomalies in view of the global fits of Ch. 7.

- *The proton size puzzle is not robust.* A global fit to world data resolves the proton size puzzle in favor of the muonic radius and shifts the value of the Rydberg constant by 4σ relative to its C14 recommended value. These results are supported by recent work by Pohl, et al. [56] and Gao, et al. [74]. References [56] and [74] both report a radius value consistent with the muonic radius value, while Ref. [56] also reports a Rydberg value consistent with the shifted Rydberg value from the global fit to world data. (The radius and Rydberg values of Ref. [56] are based on a measurement of the $2S - 4P$ transition in electronic hydrogen. The radius value of Ref. [74] is based on electron scattering data.)

- *The muon $g - 2$ anomaly is robust.* The 4σ discrepancy between theory and experiment persists[1] for any global fit to Standard Model physics. The upcoming measurement of a_μ at Fermilab should help determine whether the muon

[1] The discrepancy is as small as 2.1σ for the largest estimates of the hadronic vacuum polarization and hadronic light-by-light contributions to $a_\mu(theory)$.

$g-2$ anomaly is a signal of new physics or the result of an unaccounted-for systematic effect in the Brookhaven measurement.

- *The discrepancy between the Gabrielse and Parker determinations of the fine-structure constant is robust.* The Gabrielse and Parker measurements are the only data points in the global fit that meaningfully determine the value of the fine-structure constant. The global fit thus trivially reproduces the 2.4σ piecemeal discrepancy first reported by Parker, et al. A systematic effect, such as the one discussed in Sec. 4, may be responsible for the discrepancy. Future determinations of α via atomic interferometry and quantum Hall experiments should provide needed context. The magnitude of the discrepancy is in line with the year-to-year fluctuations of the value of α (Fig. 1.2).

- *The simplest new physics explanations are not by themselves able to resolve all three of the anomalies above at the same time.* Such a conclusion however should be reevaluated as new information comes to light.

The experimental anomalies above are slowly being chased down by new experiments. In a few years, the anomalies may not exist. However, as the precision of precision QED experiments increases, new anomalies are inevitable. In the face of a new anomaly, a self-consistent global fit is needed, first, to determine whether the anomaly is robust and, second— in the event of a robust anomaly— to evaluate theory alternatives. Even in the absence of anomalies, QED theory should be checked against other well-motivated hypotheses as a means of orienting new physics searches. In any eventuality, a self-consistent mechanism for fitting the fundamental constants is needed.

The need for self-consistent global fits is of course not limited to the Rydberg sector. Many subfields of physics are entering a 'precision era', even cosmology, where 95% of what is known is unknown. `CONSTANT FINDER` and the global fits of Ch. 7 could be expanded to include many other constants. The Standard Model

Lagrangian has 26 free parameters; the final adjustment of C14 fits 75 physical constants. In principle, everything from the strong-CP problem to CPT violation to the time-evolution of the fundamental constants could be investigated under the `CONSTANT FINDER` umbrella.

In closing, we note: piecemeal approaches in precision QED have led to a considerable amount of preventable dysfunction. We estimate more than 1,000 man-years have been wasted on the proton size puzzle to-date. A candidate solution to the muon $g-2$ anomaly was also prematurely ruled out on the basis of piecemeal arguments (see Sec. 3.2). We advocate generally for a community-wide embrace of self-consistent global approaches to fitting the constants of nature. Orderly progress within the increasing number of 'high-precision' subfields of physics depends on it.

Appendix A

The decision to fix not fit m_μ

The muon mass m_μ enters the global fits of Ch. 7 through the mass-dependent QED corrections of the electron and muon anomalous moments (Sec. 5.1), the Brookhaven measurement of the muon anomalous moment (Sec. 6), and the muonic hydrogen Lamb shift (Sec. 6). In all four places, the muon-mass dependence is negligible.

- *The m_μ-dependence of the mass-dependent QED contributions to a_e:* The total of all the mass-dependent QED contributions to the electron anomalous moment is $\Delta a_e = 2.7475719(13) \times 10^{-12}$, while $a_e(exp) = 1159652180.72(28) \times 10^{-12}$. Δa_e would need to move by $\gtrsim 10,000$ standard deviations to have a large enough effect on $a_e(theory)$ to perceptibly change the prediction for α that comes out of setting $a_e(theory)$ equal to $a_e(exp)$.

- *The m_μ-dependence of the mass-dependent QED contributions to a_μ:* The total of all the mass-dependent QED contributions to the muon anomalous moment is $\Delta a_\mu = 0.049 \times 10^{-11}$, while $a_\mu(exp) = 116592089(63) \times 10^{-11}$. Δa_μ would need to move by $\gtrsim 20$ standard deviations to have a large enough effect on $a_\mu(theory)$ to perceptibly change the prediction for α that comes out of setting $a_\mu(theory)$ equal to $a_\mu(exp)$.

- *The m_μ-dependence of the Brookhaven measurement of a_μ:* The Brookhaven

value for $a_\mu(exp)$ was obtained from Eq. 3.53, which is reprinted here for convenience:

$$\omega_a = a_\mu \frac{eB}{m_\mu} \quad \rightarrow \quad a_\mu = \frac{2m_\mu \mu_p}{e}\frac{\omega_a}{\omega_p} = (1+a_\mu)\frac{\mu_p}{\mu_\mu}\frac{\omega_a}{\omega_p} \quad \rightarrow \quad a_\mu = \frac{R}{\lambda - R}, \tag{A.1}$$

where $\mu_\mu = (1+a_\mu)\frac{e}{2m_\mu}$, $\mu_p = (1+a_p)\frac{e}{2m_p}$, $\lambda = \frac{\mu_\mu}{\mu_p}$, and $R = \omega_a/\omega_p$.

The parameter λ depends implicitly on a_μ. Pushing all of the a_μ-dependence to one side of the rightmost equation of Eq. 3.53 finds

$$a_\mu = \frac{(1+a_p)m_\mu R}{m_p} \quad \rightarrow \quad \frac{\delta a_\mu}{a_\mu} = \frac{\delta m_\mu}{m_\mu}. \tag{A.2}$$

A one-standard-deviation shift in the muon mass corresponds to $\delta m_\mu/m_\mu \sim 2.5 \times 10^{-8}$. A relative shift in the muon mass of 2.5 parts in 10^8 would shift $\delta a_\mu/a_\mu$ by the same amount, which is about 20 times smaller than the relative precision of $a_\mu(exp)$, $\sim 5.4 \times 10^{-7}$.

- *The m_μ-dependence of the muonic hydrogen Lamb shift:* Updating Eq. 4.86 for a shift in the muon mass finds

$$E(2S_{1/2}^{F=1} - 2P_{3/2}^{F=2}) \simeq 209.9779(49)(\frac{\mu}{\mu^\bullet}) - 5.2262(\frac{\mu}{\mu^\bullet})^3 r_p^2 + 0.0347 r_p^3 \; meV, \tag{A.3}$$

where $\mu^\bullet$ and μ represent the reduced mass of μH before and after the shift in m_μ.

For $\mu = \mu^\bullet + \delta\mu$:

$$(\frac{\mu}{\mu^\bullet}) \approx (1 + \frac{\delta m_\mu}{m_\mu}); \quad (\frac{\mu}{\mu^\bullet})^3 \approx (1 + 3\frac{\delta m_\mu}{m_\mu}). \tag{A.4}$$

The approximations of Eq. A.4 are good to about 20% and come out of the identity $\delta\mu/\mu = \mu/m_\mu(\delta m_\mu/m_\mu)$.

A one-standard-deviation shift in the muon mass would shift the first term of

Eq. A.3 by about 5×10^{-6} meV and the second term by substantially less. The muon mass would need to move by about 30 standard deviations to have a perceptible effect on Eq. A.3.

Appendix B

The $1S2S$ transition

The most precise measurement of the $1S2S$ transition frequency in electronic hydrogen has a vanishingly small uncertainty of 10 Hz [53]. The $1S2S$ measurement is 640 times more precise than the most precise measurement of Table 2.1. Perhaps more astonishing still: $\bar{\sigma}^2/\sigma_{1S2S}^2 \approx 512,000$, where $\bar{\sigma}$ is the mean value of the experimental uncertainties of Table 2.1.

Inclusion of the $1S2S$ in the global fit swamps the fit, creating a de facto constraint:

$$\Delta f_{1S2S}^{exp} - \Delta f_{1S2S}^{th} \sim 0, \tag{B.1}$$

where Δf_{1S2S} denotes the $1S2S$ transition frequency.

Rewriting Δf^{th} as $R_\infty c \cdot \Delta \hat{f}^{th}(r_p, \alpha^\bullet)$— with α fixed for simplicity at the C10 reference value— and then solving Eq. B.1 for r_p, we find

$$r_p \approx 0.877 + 1.05 \times 10^9 \cdot \frac{\delta R_\infty}{R_\infty^\bullet}, \tag{B.2}$$

where $R_\infty^\bullet$ is the C10 reference value. Equation B.2 defines a degeneracy curve in the $r_p - R_\infty$ plane. The CODATA reference values for r_p and R_∞ are consigned by the sheer weight of the $1S2S$ to lie on the curve.

Equations B.1-B.2 allow us to determine approximate uncertainties for R_∞ and

r_p as well, which are in (exact) agreement with those of C10:

$$\delta R_\infty = \sqrt{(\frac{1}{2}\frac{\partial^2\chi^2}{\partial R_\infty^2})^{-1}} = \sqrt{(\sum_j \frac{c^2\Delta\hat{f}_j^2}{\sigma_j^2})^{-1}}$$
$$\approx \sqrt{(\frac{c^2\Delta\hat{f}_{1S2S}^2}{\sigma_{1S2S}^2})^{-1}} \approx 5\times10^{-12}\cdot R_\infty^\bullet; \tag{B.3}$$

$$\delta r_p \approx 1.05\times10^9\cdot\frac{R_\infty}{R_\infty^\bullet} \approx .005\ fm.$$

Chi-squared minimization makes clear the reality of the degeneracy curve. Figure B.1 shows chi-squared contours for a fit to the electronic hydrogen data of Table 2.1 with and without the $1S2S$ transition. Including the $1S2S$ transition in the fit produces chi-squared contours too thin to be resolved. The 1σ contour is shown in the figure. It lies exactly on top of the degeneracy curve of Eq. B.2. The uncertainties for r_p and R_∞ obtained from the 1σ contour are identical to those of C10. The penalty for moving off of the degeneracy curve is severe: $\Delta\chi^2$ is of order 10,000 at the left edge of the error bar marking off the 1σ uncertainty of the C10 reference value for r_p. Removing the $1S2S$ transition from the fit produces the 1, 2, and 3-σ chi-squared contours shown in blue, which are comparatively robust. Consequently we have chosen to omit the $1S2S$ transition from the reference set of Table 2.1.

The C10 and C14 adjustments however include the $1S2S$. As discussed in Sec. 3, the CODATA adjustments introduce additive corrections to the theory expressions describing the electronic hydrogen transition frequencies to fatten out the degeneracy curve created by the $1S2S$. The additive corrections are equivalent to the nuisance parameters of Eq. 2.9. According to C98, they "represent [C98's] lack of knowledge of those expressions [...]. The initial estimate of each [additive correction] is zero but with an appropriate standard uncertainty." In C98 the standard uncertainty for the $1S2S$ additive correction was 90 kHz. In C10, due to advances

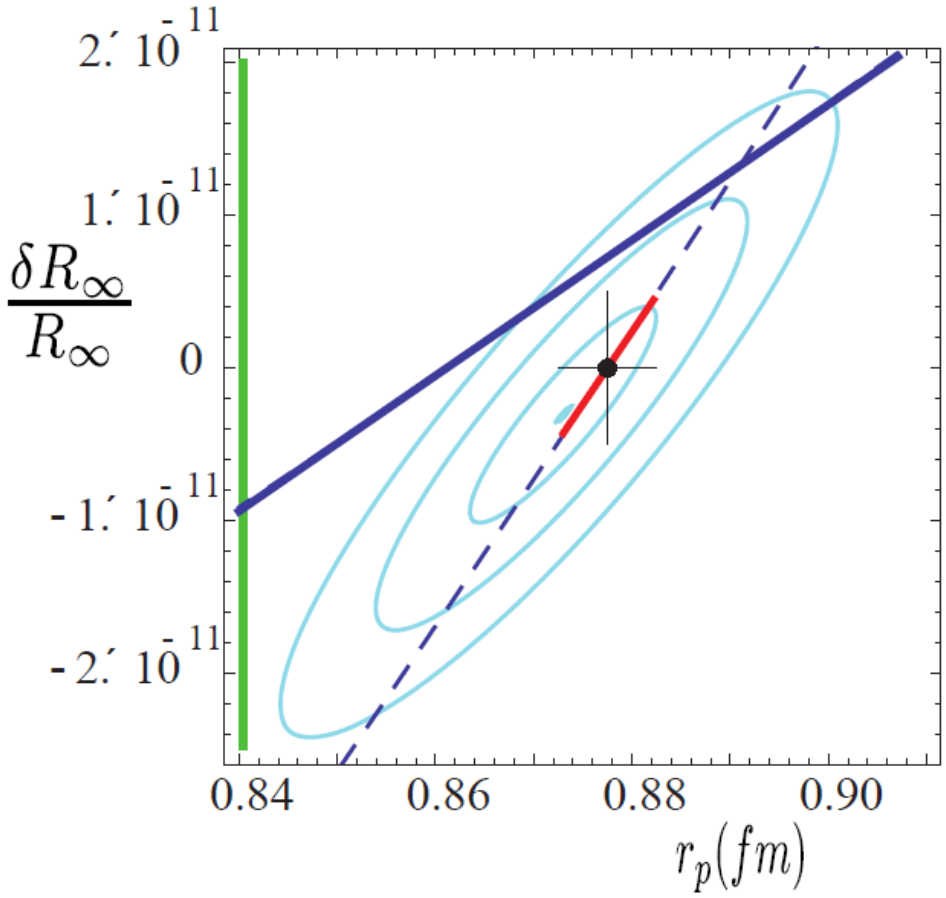

Figure B.1: Contours of χ^2 in the (r_p, $\delta R_\infty/R_\infty$) plane for a fit omitting the $1S2S$ transition. The contours show 1, 2, and 3 σ Gaussian confidence levels corresponding to $\Delta\chi^2$ = 1, 4, and 9. The muonic value r_p = 0.841 fm is at the left edge of the plot, close to the 3σ contour. Including the $1S2S$ transition produces a 1σ contour represented by the red line segment but too thin to be resolved at the scale of the figure. The dashed line is the degeneracy curve predicted by the $1S2S$ transition. Least-squares analysis dominated by this single datum predicts r_p and R_∞ fall on the line, regardless of other data or theory. The point and its error bars are the C10 reference values [5]. See discussion in the text. The second-most precise transition produces a different degeneracy curve (solid blue line), which intersects the 2σ region of the χ^2 contours.

in theory calculations, which are reported in C02, C06, and C10, the uncertainty of the $1S2S$ additive correction was 2.5 kHz.

Our reasons for omitting the $1S2S$ from the global fits of Ch. 7 (rather than mimicking the CODATA procedure) are twofold. First, omitting the $1S2S$ allows us to use an unadorned chi-squared function (Eq. 2.6) to fit the fundamental constants: no additive corrections, no correlations. Outputs follow inputs with a minimum of complication in between. Second, and here we quote liberally from Stump, et al. [75]: "A chi-squared distribution with many degrees of freedom is a very narrow distribution, sharply peaked at $\chi^2 = N$. Therefore small inaccuracies in the values of the [estimated uncertainties] σ_i and [estimated correlations] β_{ij} may translate into a larger error in the confidence levels computed from the chi-squared distribution."

Appendix C

The approximate degeneracies of the eH and eD sectors

We begin by writing the frequency ν_N of electronic hydrogen state $N = |n\ell j>$ as

$$\nu_N = R_\infty \cdot c \cdot (-\frac{1}{n^2} + ... + \hat{\nu}_N^0(FNS) + ...), \tag{C.1}$$

where the first term on the right-hand side is the Schrodinger energy (divided by h) and the second term

$$R_\infty \cdot c \cdot \hat{\nu}_N^0(FNS) = \frac{2\pi}{3h} \cdot \alpha \cdot r_p^2 \cdot |\psi(0)|^2 \sim R_\infty \cdot \frac{r_p^2}{n^2} \cdot \delta_{\ell,0} \tag{C.2}$$

is the leading finite nuclear size (FNS) contribution to ν_N.

Seven of the eight eH transitions of Table 2.1 are of the form $\nu_{nX} - \nu_{2S}$, where $X = S$, P, D and $n > 2$.[1]

For those transitions, the leading FNS contribution is negative:

$$R_\infty \cdot c \cdot (\hat{\nu}_{nX}^0(FNS) - \hat{\nu}_{2S}^0(FNS)) \sim (\frac{1}{n^2} - \frac{1}{2^2}) < 0, \tag{C.3}$$

[1] $\nu_{2S} - \nu_{2P}$ is the lone exception.

which implies that an increase in the value of r_p will decrease the value of $\nu_{nX} - \nu_{2S}$. On the other hand, inspection of Eq. C.1 finds that an increase in the value of R_∞ will increase the value of $\nu_{nX} - \nu_{2S}$.

Hence, for each transition of the form $\nu_{nX} - \nu_{2S}$, there is a degeneracy curve in the (r_p, R_∞)-plane along which the value of $\nu_{nX} - \nu_{2S}$ remains constant.

The approximate degeneracy between r_p and R_∞ in the eH sector (Sec. **??**), then, arises from the collective contribution of all of the degeneracy curves of the Table 2.1 eH data.

A parallel argument explains the approximate degeneracy between r_d and R_∞ that arises in the eD sector.

Appendix D

The SO(4) symmetry of hydrogen

The rotational invariance of the Schrodinger-Coulomb equation under $SO(3)$ implies the $(2\ell+1)$ states of differing m belonging to a given ℓ have the same energy. The spectrum of the Schrodinger-Coulomb equation must have an additional, 'accidental' degeneracy with respect to ℓ since the energy levels of the hydrogen atom depend only on n.[1] As we will see, the accidental degeneracy is in fact dynamically generated and often called a *dynamical* degeneracy as a result.

The dynamical degeneracy is related to the Runge-Lenz vector $\mathcal{L}$ of Newtonian mechanics, which we briefly review here. Consider a planet moving subject to the gravitational potential of the Sun. The Runge-Lenz vector $\vec{\mathcal{L}} = \frac{1}{m}\vec{L} \times \vec{p} + \kappa\frac{\vec{r}}{r}$ is conserved— i.e., $\dot{\vec{\mathcal{L}}} = 0$, where m is the mass of the planet and κ is the numerator GM of the Newtonian gravitational potential, with G the gravitational constant and M the mass of the Sun.

The orbital angular momentum vector $\vec{L}$ is perpendicular to $\vec{r}$ and $\vec{p}$ so that

[1] The hydrogen energy levels are n^2-degenerate:

$$\sum_{\ell=0}^{n-1}(2\ell+1) = n + 2\sum_{\ell=1}^{n-1}\ell = n + 2\frac{(n-1)n}{2} = n^2. \tag{D.1}$$

the planet's motion is confined to a plane. $\vec{L}$ is also perpendicular to $\vec{\mathcal{L}}$. Hence $\vec{\mathcal{L}}$ is confined to the plane of motion. When $\vec{r}$ is perpendicular to $\vec{p}$, which occurs at aphelion and perihelion, $\vec{\mathcal{L}}$ points in the direction of $\vec{r}$, which we can take to be in the direction of the perihelion. Since $\dot{\vec{\mathcal{L}}} = 0$, the perihelion doesn't precess, and the planet's orbit closes. The upshot is: orbits in a $1/r$-potential close due to the existence of a conserved vector.

The quantum mechanical analogue of the planet-Sun system above, with the planet replaced by an electron and the Sun replaced by a proton, superficially resembles a hydrogen atom. The analogy seems clumsy on its face. However we can take it seriously since the Hamiltonian governing the planet's motion reduces to the Schrodinger-Coulomb Hamiltonian once appropriate extensions to quantum mechanics are made. We develop the quantum analogue below, starting with our insistence that the canonical commutation relations hold:

$$\begin{aligned} [r_i, p_j] &= i\delta_{ij}; \\ [L_i, r_j] &= i\epsilon_{ijk} r_k; \\ [L_i, p_j] &= i\epsilon_{ijk} p_k; \\ [L_i, L_j] &= i\epsilon_{ijk} L_k. \end{aligned} \tag{D.2}$$

Equation D.2 is equivalent to the statement, "$\vec{r}$, $\vec{p}$, and $\vec{L}$ transform as vectors." Since $\vec{\mathcal{L}}$ is a vector, the commutation relation $[L_i, \mathcal{L}_j] = i\epsilon_{ijk}\mathcal{L}_k$ should also hold.

Upon symmetrization, the Runge-Lenz vector becomes

$$\vec{\mathcal{L}} = \frac{1}{2m}(\vec{L} \times \vec{p} - \vec{p} \times \vec{L}) + \kappa \frac{\vec{r}}{r}.$$

The condition $\dot{\vec{\mathcal{L}}} = 0$ becomes

$$[H, \vec{\mathcal{L}}] = \dot{\vec{\mathcal{L}}} = 0,$$

where $H = \frac{\vec{p}^2}{2m} - \frac{\kappa}{r}$, with κ now identified with the fine-structure constant α.

Finally, a tedious calculation finds

$$\begin{aligned}[\mathcal{L}_i, \mathcal{L}_j] &= i\epsilon_{ijk}(\frac{-2H}{m})L_k \\ &\rightarrow [M_i, M_j] = i\epsilon_{ijk}L_k,\end{aligned} \tag{D.3}$$

where $\vec{M} = \sqrt{\frac{-m}{2H}}\vec{\mathcal{L}}$ and $\sqrt{\frac{-m}{2H}}$ is real for bound states ($E < 0$; $H|E>= E|E>$). Since $\vec{M}$ is a vector, the commutation relation $[L_i, M_j] = i\epsilon_{ijk}M_k$ holds. This commutation relation along with those of Eqs. D.2 and D.3 specifies an $SO(4)$ Lie algebra:

$$\begin{aligned}[L_i, L_j] &= i\epsilon_{ijk}L_k; \\ [L_i, M_j] &= i\epsilon_{ijk}M_k; \\ [M_i, M_j] &= i\epsilon_{ijk}L_k.\end{aligned} \tag{D.4}$$

The $SO(4)$ Lie algebra breaks apart into two $SU(2)$'s with the substitution of $A_i^{\pm} = \frac{1}{2}(L_i \pm M_i)$ into Eq. D.4:

$$\begin{aligned}[A_i^{\pm}, A_j^{\pm}] &= i\epsilon_{ijk}A_k^{\pm}; \\ [A_i^{\pm}, A_j^{\mp}] &= 0.\end{aligned} \tag{D.5}$$

The irreducible representations (irreps) of $SO(4)$ are specified by (a_+, a_-), where $a_+ = 0, 1/2, 1, 3/2, ...$ and $a_- = 0, 1/2, 1, 3/2, ...$ The states $|b_+, b_- >$ in a given irrep are enumerated by $b_{\pm} = -a_{\pm}, -a_{\pm} + 1, ..., a_{\pm}$, such that the dimensionality of the irrep is $(2a_+ + 1)(2a_- + 1)$.

$\vec{L}$ and $\vec{M}$ are orthogonal, just as $\vec{L}$ and $\vec{\mathcal{L}}$ were orthogonal for the classical system. The relation $0 = \vec{L} \cdot \vec{M} = \vec{A}_+^2 - \vec{A}_-^2$ implies the only irreps allowed are $(a_+, a_-) \rightarrow (a, a)$, where $a = a_- = a_+$.

Computation of $\vec{A}_+^2 + \vec{A}_-^2$ finds

$$\vec{A}_+^2 + \vec{A}_-^2 = \frac{1}{2}(\vec{L}^2 + \vec{M}^2) = -\frac{1}{2}(1 + \frac{m}{2E}\kappa^2). \tag{D.6}$$

Evaluation of the left-hand side of Eq. D.6 on a state $|b_+, b_- >$ in the irrep (a, a) gives

$$(\vec{A}_+^2 + \vec{A}_-^2)|b_+, b_- >= 2a(a+1)|b_+, b_- > . \tag{D.7}$$

The bound-state energy, obtained from Eqs. D.6 and D.7, is thus

$$E = -\frac{m\kappa^2}{2}\frac{1}{(2a+1)^2} \equiv -\frac{m\alpha^2}{2n^2}. \tag{D.8}$$

The definition of n ($\equiv 2a+1$) in Eq. D.8 requires n to be a positive integer for $a = 0, 1/2, 3/2, ...$ The n^2-degeneracy of the hydrogen atom is identifiable as the dimension of the irrep (a, a), consistent with the result of Footnote 1. To be clear: the payoff here is not Eq. D.8. The payoff is in understanding the dynamical origin of the accidental-seeming degeneracy of the Schrodinger spectrum with respect to ℓ.

Appendix E

The Dirac spectrum

Consider u_N with insertions of the parity operator $\mathbb{P}$ as follows:

$$u_N(\vec{x}) =< 0|\psi(\vec{x})|N >=< 0|\mathbb{P}^{-1}\mathbb{P}\psi(\vec{x})\mathbb{P}^{-1}\mathbb{P}|N > .$$

$\psi(\vec{x})$ is the electron or muon field, $|0>$ is the vacuum, $|N>$ is one of a complete set of orthonormal state vectors, and $\mathbb{P} = \mathbb{P}^{-1}$.[1] A parity transformation of the state vector gives $\mathbb{P}|N >= \eta_N|N >$, with $\eta_N = \pm 1$ the intrinsic parity of $|N >$, and a parity transformation of the field gives $\mathbb{P}\psi(\vec{x})\mathbb{P}^{-1} = i\gamma^0\psi(-\vec{x})$.[2] For a parity-symmetric vacuum,

$$u_N(\vec{x}) = i\gamma^0\eta_N u_N(-\vec{x})$$

or equivalently

$$\begin{aligned} f_N(\vec{x}) &= \eta_N f_N(-\vec{x}), \\ g_N(\vec{x}) &= -\eta_N g_N(-\vec{x}). \end{aligned} \tag{E.1}$$

The parity of f_N is the parity of state vector $|N>$.

[1] $\mathbb{P} = \mathbb{P}^{-1}$ follows trivially from the requirement $\mathbb{P}^2 = \mathbb{1}$; performing two consecutive spatial inversions of a vector does not change the orientation of the vector.

[2] $(i\gamma^0\partial_0 - i\vec{\gamma}\cdot\vec{\nabla} - m)\psi(\vec{x}) = 0 \xrightarrow{\mathbb{P}} (i\gamma^0\partial_0 + i\vec{\gamma}\cdot\vec{\nabla} - m)\psi(-\vec{x}) = 0$, whether by taking $\vec{x} \to -\vec{x}$ or by taking $\psi(\vec{x}) \to i\gamma^0\psi(-\vec{x})$.

f_N and g_N can be expanded in spherical harmonics $Y_\ell^m(|\vec{x}|)$, where

$$Y_\ell^m(|\vec{x}|) \sim (d/dx)^{\ell+m}(x^2-1)^\ell e^{im\phi}$$

and $x = cos\theta$. Under a parity transformation, $(\theta, \phi) \to (\pi - \theta, \pi + \phi)$ such that

$$Y_\ell^m \xrightarrow{\mathbb{P}} (-1)^\ell Y_\ell^m. \tag{E.2}$$

According to Eqs. E.1 and E.2, f_N and g_N are required to have values of ℓ that differ by an odd number. Possible values of ℓ are however limited to $j \pm 1/2$.[3] f_N can be taken to have $\ell = j \mp 1/2$, and g_N to have $\ell = j \pm 1/2$. Explicit expansion of f_N and g_N in spherical harmonics finds

$$f_N(\vec{x}) = \begin{pmatrix} CY_\ell^m(\hat{x}) \\ C'Y_\ell^{m'}(\hat{x}) \end{pmatrix} F_N(|\vec{x}|) \qquad g_N(\vec{x}) = (\vec{\sigma}\cdot\hat{x}) \begin{pmatrix} CY_\ell^m(\hat{x}) \\ C'Y_\ell^{m'}(\hat{x}) \end{pmatrix} G_N(|\vec{x}|) \tag{E.3}$$

where C, C' are Clebsch-Gordon coefficients. The factor of $\vec{\sigma}\cdot\hat{x}$ has been introduced to ensure Eq. E.1 is satisfied. Applying $\vec{\sigma}\cdot\hat{x}$ to a wave function preserves its total angular momentum but flips its parity, shifting ℓ by one unit in the process.

Insertion of Eq. E.3 into Eq. 4.5 yields two coupled differential equations in F_N and G_N, which can be solved for E_N, with Eq. 4.6 the result.

[3] $J_z = L_z + S_z \to m_\ell = m_j - m_s$. $m_j^{max} = j$, $m_s = \pm 1/2$, and $0 \le m_\ell \le \ell$. For fixed j, $\ell = j \mp 1/2$. However for $\ell = \ell^{max} = n-1$ only $\ell = j - 1/2$ is allowed since $j + 1/2 \le n$.

Appendix F

The Breit potential

The Dirac Hamiltonian for a lepton of mass m in an electrostatic external field ($A^0 = \phi,\ \vec{A} = 0$) is

$$H = \vec{\alpha} \cdot \vec{p} + \beta m + e\phi, \tag{F.1}$$

where $\vec{\alpha} = \gamma^0 \cdot \vec{\gamma}$, $\beta = \gamma^0$, and $\vec{p}$ is the three-momentum of mass m. The term $\vec{\alpha} \cdot \vec{p}$ is off-diagonal in the Dirac representation, with Eq. F.1 becoming nearly diagonal in the non-relativistic limit. A unitary transformation of $H \to H' = e^{iS} H e^{-iS}$ can be effected to diagonalize Eq. F.1, with the associated four-component lepton wave function transforming along with it: $\psi \to \psi' = e^{iS}\psi$. S is taken to be hermitian. The diagonalization procedure is referred to as a Foldy-Wouthuysen transformation. It separates the Hamiltonian into an upper part acting strictly on a two-component lepton wave function and a lower part acting strictly on a two-component antilepton wave function. In the non-relativistic limit, the lepton and antilepton wave functions reduce to the product of a two-component constant spinor and a one-component Schrodinger wave function, as discussed in Sec. 2.2. The scalar potential in Eq. F.1 decreases the energy of the lepton and increases the energy of the antilepton. The lepton becomes bound; the antilepton gets accelerated.

A time-dependent Hamiltonian will transform according to a time-dependent S :

$$H\psi = i\partial_t(e^{-iS}\psi') \quad \rightarrow \quad i\partial_t\psi' = [e^{iS}(H - i\partial_t)e^{-iS}]\psi' = H'\psi',$$

where $H' = e^{iS}(H - i\partial_t)e^{-iS}$. Application of the Baker-Campbell-Hausdorff lemma to H' gives

$$H' = (H + i[S, H] + \frac{i^2}{2}[S, [S, H]]...) - (\dot{S} + \frac{i}{2}[S, \dot{S}]...), \tag{F.2}$$

with $\dot{S} = \partial_t S$.

H is conventionally separated for bookkeeping purposes into an even (or diagonal) part $\mathcal{E}$ and an odd (off-diagonal) part $\mathcal{O}$.

$$H = \beta m + \mathcal{O} + \mathcal{E} \tag{F.3}$$

where $\mathcal{O} = \vec{\alpha} \cdot \vec{p}$ and $\mathcal{E} = e\phi$.

Insertion of Eq. F.3 into Eq. F.2 gives

$$H' = \beta m + \mathcal{O} + \mathcal{E} + i[S, \beta m] + \mathcal{O}(1/m). \tag{F.4}$$

S is chosen to cancel $\mathcal{O}$, which occurs for $S = -i\beta\mathcal{O}/2m$. H' becomes

$$\begin{aligned} H' = \beta m + \mathcal{E} + i[S, \mathcal{O}] + i[S, \mathcal{E}] + i[S, [S, \beta m]] - \dot{S} + \mathcal{O}(1/m^2) \\ H' = \beta m + \mathcal{E}' + \mathcal{O}' + \mathcal{O}(1/m^2) \end{aligned} \tag{F.5}$$

where the off-diagonal terms in H' have been swept into $\mathcal{O}' = \mathcal{O} + i[S, \mathcal{E}] - \dot{S}$ and the diagonal terms into $\mathcal{E}' = \mathcal{E} + i[S, \mathcal{O}] + i[S, [S, \beta m]]$.

H'' can be found via the same procedure, with $S \rightarrow S' = -i\beta\mathcal{O}'/2m$. H'' gives corrections to the energy up to order $(1/m^2)$. H''' gives corrections up to order $(1/m^3)$, and so on.

The $(1/m^3)$ corrections are the leading relativistic corrections to the energy, as can be seen from the low-momentum expansion of the relativistic energy $E = \sqrt{p^2+m^2} = [m+1/2\cdot p^2/m - 1/8\cdot p^4/m^3 + ...]$. The diagonal order $(1/m^3)$ correction,[1] sandwiched between two-component, non-relativistic lepton wave functions, recovers the $(1/m^3)$ contribution to Eq. 4.7.

Accounting additionally for the finite mass M of the nucleus, assumed here to be spin-1/2, follows a procedure similar to that of Eqs. F.1-F.5. The single-particle wave function is replaced by a two-particle wave function with sixteen components. The corresponding Hamiltonian is 16×16, composed of a sum of outer products of gamma matrices. The Hamiltonian is transformed via a unitary transformation such that, to order $(1/m)$, it rotates the four components of the two-particle wave function that mix the lepton and nucleus wave functions[2] into one another. The transformed Hamiltonian is block diagonal to order $(1/m)$, with a 4×4 block and a 12×12 block. Iterating this procedure to order $(1/m^3)$ gives the desired result. The expectation value of the $\mathcal{O}(1/m^3)$ 4×4 block gives the energy spectrum of Eq. 4.11. Details are in Ref. [76].

A comment about spin: The energy shifts tied to the relative orientation of the spins of the lepton and nucleus are, by convention, split off from the leading relativistic corrections considered here and are dealt with separately as (relativistic) hyperfine splitting corrections (Sec. 5.7). However the two-component spinor contained in the wave function for the spin-1/2 nucleus leads to a contribution to the energy proportional to $\delta_{\ell 0}$, the so-called Darwin-Foldy term. This contribution is absent for spin-0 and spin-1 nuclei.

[1] The off-diagonal order $(1/m^3)$ corrections can be dialed away with S''', leaving diagonal and off-diagonal corrections of order $(1/m^4)$.

[2] as opposed to the anti-lepton and anti-nucleus wave functions or the anti-lepton and nucleus wave functions, for example

Appendix G

The order $(Z\alpha)^5(m/M)$ recoil correction

The leading self-energy correction provides a correction

$$\delta V = -4\pi Z\alpha \, \frac{dF_1(-\vec{q}^2)}{d\vec{q}^2}|_{\vec{q}^2=0} \cdot \delta(\vec{r}) \tag{G.1}$$

to the Coulomb potential. See Sec. 6.2.

By analogy with Eq. 4.57, $-6dF_1(-\vec{q}^2)/d\vec{q}^2|_{\vec{q}^2=0}$ can be thought of as the mean-squared fluctuation of the lepton coordinate due to the lepton self-energy corrections. We denote the mean-squared fluctuation of the lepton coordinate as $< r_\ell^2 >$.

To deal with the two-body nature of the bound-state, $< r_\ell^2 >$ should in all generality be replaced by

$$< (r_\ell - r_N)^2 >=< r_\ell^2 > + < r_N^2 > -2 < r_\ell \, r_N >, \tag{G.2}$$

where $< r_N^2 >$ is the mean-squared fluctuation of the nucleus coordinate.

From Eq. 4.79,

$$< r_\ell^2 >= -6dF_1(-\vec{q}^2)/d\vec{q}^2|_{\vec{q}^2=0} = \frac{2Z\alpha}{\pi m^2}\ln(\frac{m}{\mu}), \tag{G.3}$$

where μ is the scale at which the would-be infrared divergence is cut off. As a first approximation, we set μ equal to the binding energy $m(Z\alpha)^2$.

Following Eq. G.3, we write down analogous expressions for the remaining contributions to $< (r_\ell - r_N)^2 >$:

$$< r_N^2 >= \frac{4Z\alpha}{\pi M^2} \ln(\frac{1}{Z\alpha}); \tag{G.4}$$

$$-2 < r_\ell \, r_N >= -\frac{4Z\alpha}{\pi m M} \ln(\frac{mZ\alpha}{m(Z\alpha)^2}). \tag{G.5}$$

The correlator $< r_\ell \, r_N >$ is assumed to give zero over distances smaller than the scale of the atom $\sim 1/mZ\alpha$. As a consequence, the logarithm in Eq. G.5 is cut off at $mZ\alpha$ rather than m as it was in Eqs. G.3-G.4.

Combining Eq. G.1 with Eqs. G.3-G.5 finds

$$\delta V = \frac{2\pi}{3} Z\alpha < (r_\ell - r_N)^2 > \cdot \delta(\vec{r}), \tag{G.6}$$

where

$$< (r_\ell - r_N)^2 >= \frac{4Z\alpha}{\pi m^2} \ln(\frac{1}{Z\alpha})[1 + (\frac{m}{M})^2 - \frac{m}{M}]. \tag{G.7}$$

The first term of Eq. G.6 gives the leading self-energy correction, the second term gives a recoil correction of order $(Z\alpha)^5(m/M)^2$, and the third term gives a recoil correction of order $(Z\alpha)^5(m/M)$. The $\mathcal{O}((Z\alpha)^5(m/M))$ recoil correction is the leading nontrivial recoil correction. The leading trivial recoil corrections, of order $(Z\alpha)^4$, are implicit in the corrections to the energy generated by the Breit potential (see Sec. 2.4). A more formal treatment of higher-order recoil corrections may be found in Ref. [77].

Appendix H

The BMT equation

Consider a charged particle of mass m with intrinsic spin that is accelerating in the lab frame. We begin by building up the concepts and notation necessary to derive the Bargmann-Michel-Telegdi (BMT) equation, which— in the context of the Brookhaven measurement of muon $(g-2)$— describes the time evolution of the orientation of the particle's spin vector in the particle rest frame metered by a clock in the lab frame.

The angular momentum tensor $J_{\mu\nu}$ is composed of the sum of an orbital angular momentum tensor $L_{\mu\nu} = x_\mu p_\nu - x_\nu p_\mu$ and an intrinsic spin angular momentum tensor $S_{\mu\nu}$, where $L_{\mu\nu}$ represents the part of $J_{\mu\nu}$ that depends on the choice of origin. Total and orbital angular momemuntum three-vectors can be obtained by contracting the spatial components of the relevant angular momentum tensor with $\frac{1}{2}\epsilon_{ijk}$. To define a four-vector S_μ for the spin, it is conventional to introduce the Pauli-Lubanski vector $W_\mu = -\frac{1}{2}\epsilon_{\mu\nu\lambda\rho}J_{\nu\lambda}p_\rho$. W_μ reduces to $(0, m\vec{J}) = (0, m\vec{S})$ in the particle rest frame, suggesting $S_\mu = W^\mu/\sqrt{-W^2}$ as a covariant parameterization of the spin four-vector— which turns out to be correct.

We want to write down an expression for $dS_\alpha/d\tau$, where $\tau = \gamma^{-1}t$ is the proper time, which ensures $dS_\alpha/d\tau$ is covariant, and t is the time as measured in the lab frame. We stipulate that the terms in the expression must be linear in S_α and

contain no higher time-derivatives. The available four-vectors are S_α, $F_{\alpha\beta}$, U_α, and $dU_\alpha/d\tau$, where U_α is the particle four-velocity ($p_\alpha = mU_\alpha$). These considerations lead to a unique expression for $dS_\alpha/d\tau$:

$$\frac{dS_\alpha}{d\tau} = c_1 F_{\alpha\beta} S_\beta + c_2 (U_\beta F_{\beta\gamma} S_\gamma) U_\alpha + c_3 (S_\beta \frac{dU_\beta}{d\tau}) U_\alpha. \tag{H.1}$$

A term $\sim S \cdot U$ is absent from Eq. H.1 since $S \cdot U = 0$— a fact that is easy to see in the particle rest frame, where $U_\alpha = (1, \vec{0})$ and S_α is by inspection purely space-like.

Differentiating $S \cdot U = 0$ with respect to τ finds

$$\frac{dS}{d\tau} \cdot U = -S \frac{dU}{d\tau}, \tag{H.2}$$

which places a constraint on Eq. H.1— namely, Eq. H.1 satisfies Eq. H.2 only if $c_1 = -c_2$ and $c_3 = -1$.

We continue: the covariant form of the Lorentz force equation is

$$dU_\alpha/d\tau = e/m F_{\alpha\beta} U_\beta. \tag{H.3}$$

With Eq. H.3 and the substitutions for c_2 and c_3 necessitated by Eq. H.2, Eq. H.1 becomes

$$\frac{dS_\alpha}{d\tau} = c_1 S_\beta (F_{\alpha\beta} - (U_\gamma F_{\gamma\beta}) U_\alpha) - \frac{e}{m} (S_\beta F_{\beta\gamma} U_\gamma) U_\alpha. \tag{H.4}$$

N.B.: Eqs. H.3-H.4 do not account for the effects of gradient forces.[1]

In the particle rest frame, Eq. H.4 reduces to

$$\frac{dS_j}{d\tau} = c_1 F_{jk} S_k = c_1 (\vec{S} \times \vec{B})_j. \tag{H.5}$$

Equation H.5 describes the precession of the angular momentum vector $\vec{J} = \vec{S}$ in a

[1] We investigated the possibility that gradient forces, which were neglected in the Brookhaven measurement, were responsible for the muon $(g-2)$ anomaly. Possible contributions were too small to be relevant.

magnetic field, i.e., $d\vec{S}/d\tau = \vec{S} \times \vec{\omega}$, where $\vec{\omega}$ is the well-known Larmor frequency, equal to $\frac{ge}{2m}\vec{B} \equiv c_1\vec{B}$.

With c_1 determined, Eq. H.4 becomes

$$\frac{dS_\alpha}{d\tau} = \frac{e}{m}S_\beta[\frac{g}{2}F_{\alpha\beta} + (\frac{g}{2} - 1)(F_{\beta\gamma}U_\gamma)U_\alpha], \tag{H.6}$$

which has the same form as the original BMT equation of B-M-T.

The BMT equation used in the Brookhaven measurement of a_μ is

$$\begin{aligned} d\hat{s}/dt &= \hat{s} \times \vec{\omega}_s, \\ \vec{\omega}_s &= \frac{e}{m}[(a_\mu + \frac{1}{\gamma})\vec{B} - a_\mu(\frac{\gamma}{\gamma+1})(\vec{\beta}\cdot\vec{B})\vec{\beta} + (a_\mu + \frac{1}{\gamma+1})\vec{E}\times\vec{B}], \end{aligned} \tag{H.7}$$

where $a_\mu = \frac{g-2}{2}$, $U_\mu = (\gamma, \gamma\vec{\beta})$, and $\vec{\omega}_s$ is the muon spin-precession frequency.

To see how Eqs. H.6 and H.7 are related, we first note that Eq. H.7 is defined with respect to the precession of the spin vector $\hat{s}$ in the particle rest frame and the time t in the lab frame. Boosting $\vec{S}$ from the lab frame into the particle rest frame finds

$$\hat{s} = \vec{S} - \frac{\gamma}{\gamma+1}\vec{\beta}(\vec{\beta}\cdot\vec{S}). \tag{H.8}$$

Differentiating Eq. H.8 with respect to t yields

$$\frac{d\hat{s}}{dt} = \frac{d\vec{S}}{dt} - \vec{\beta}(\vec{\beta}\cdot\vec{S})\frac{d}{dt}(\frac{\gamma}{\gamma+1}) - \frac{\gamma}{\gamma+1}[\vec{\beta}\frac{d}{dt}(\vec{S}\cdot\vec{\beta}) + (\vec{S}\cdot\vec{\beta})\frac{d\vec{\beta}}{dt}]. \tag{H.9}$$

To bring Eq. H.9 to heel, we make substitutions for $\vec{S}$, $d\vec{S}/dt$, and $d\vec{\beta}/dt$ using the equations of this Appendix. We replace $d\vec{S}/dt$ with the relevant parts of Eq. H.6. We replace $\vec{S}$ with $\hat{s}$ via Eq. H.8. Finally, we replace $d\vec{\beta}/dt$ with $\frac{e}{\gamma m}[\vec{E}+\beta\times\vec{B}-\vec{\beta}(\vec{\beta}\cdot\vec{E})]$, pursuant to Eq. H.3.

After considerable algebra, the result of these substitutions gives an expression of the form $d\hat{s}/dt = \hat{s} \times \vec{\omega}_s$, which is identical to Eq. H.7. The final analysis: the mapping from Eq. H.6 to Eq. H.7 amounts to taking $\vec{S} \to \hat{s}$ and $\tau \to t$.

Parenthetically, the expression for the cyclotron frequency $\vec{\omega}_c$ implied by Eq. 3.50 can be obtained by putting $d\vec{\beta}/dt = \frac{e}{\gamma m}[\vec{E} + \vec{\beta} \times \vec{B} - \vec{\beta}(\vec{\beta} \cdot \vec{E})]$ into the form $\vec{\beta} \times \vec{\omega}_c$, subject to the assumption $\vec{\beta} \cdot \vec{E} = 0$.

Appendix I

Kinetic mixing

The Lagrangian for a basic kinetic mixing model takes the form

$$\mathcal{L} = -\frac{1}{4}F_{\mu\nu}F_{\mu\nu} - \frac{1}{4}F'_{\mu\nu}F'_{\mu\nu} - \frac{\epsilon}{2}F_{\mu\nu}F'_{\mu\nu} + i\bar{\psi}_j[\gamma_\mu(\partial_\mu + ieA_\mu)]\psi_j, \tag{I.1}$$

where A_μ, A'_μ are $U(1)_{em}$, $U(1)_X$ gauge fields, respectively, and $F_{\mu\nu}$, $F'_{\mu\nu}$ are the corresponding field strength tensors. A'_μ is often referred to as a *dark photon.*

We take advantage of the anti-symmetry of $F_{\mu\nu}$ and substitute $F'_{\mu\nu} = 2\partial_\mu A'_\nu + [symmetric]$ into the 'kinetic mixing' term in Eq. I.1 that couples the hidden sector to the Standard Model. The symmetric piece of $F'_{\mu\nu}$ contracted with $F_{\mu\nu}$ gives zero. Integrating what remains by parts yields $\epsilon A'_\nu \partial_\mu F_{\mu\nu}$ plus a surface term. Finally, identifying $\partial_\mu F_{\mu\nu}$ somewhat carelessly as the electromagnetic current j^{em}_ν finds

$$\mathcal{L} = -\frac{1}{4}\tilde{F}_{\mu\nu}\tilde{F}_{\mu\nu} - \frac{1}{4}F'_{\mu\nu}F'_{\mu\nu} + i\bar{\psi}_k[\gamma_\mu(\partial_\mu + ie\tilde{A}_\mu + ie\epsilon A'_\mu)]\psi_k, \tag{I.2}$$

where subscript k indexes the fermion species and the tildes have been added for self-consistency, where $\tilde{A}_\mu = A_\mu - \epsilon A'_\mu$ and $\tilde{F}_{\mu\nu} = \partial_\mu \tilde{A}_\nu - \partial_\nu \tilde{A}_\mu$. Equation I.2 can be obtained more formally by diagonalizing the kinetic terms of Eq. I.1 to $\mathcal{O}(\epsilon^2)$.

The sign of ϵ, while conventionally taken to be positive, is unconstrained in Eq. I.2. Hence A'_μ can mediate a repulsive interaction between lepton and nucleon just

the same as an attractive interaction. The vector portal phenomenology of Ch. 6 is consistent with— but more general than— a Lagrangian of the form of Eq. I.2. Mixing between $\tilde{A}_\mu$ and A'_μ occurs through fermion loops.

Variations on Eq. I.2 exist, many of which assume the hidden sector $U(1)_X$ mixes with the $U(1)_Y$ of the Standard Model. Regardless, a mass term for A'_μ can be obtained via the Higgs mechanism, by adding a Higgs-like particle to the hidden sector. The predicted mass range for A'_μ is model-dependent, with typical masses in the range $MeV - GeV$. The original kinetic mixing model is due to Holdom [78]. A comprehensive review of dark photon phenomenology may be found in [79].

Bibliography

[1] J. C. Martens and J. P. Ralston, "A mechanism for community-wide determination of the fundamental physical constants of qed and the standard model," in *Horizons in World Physics, Volume 298* (A. Reimer, ed.), ch. 4, Hauppauge, NY: Nova Science Publishers, Inc., 2019.

[2] G. W. Bennett *et al.*, "Measurement of the negative muon anomalous magnetic moment to 0.7 ppm," *Phys. Rev. Lett.*, vol. 92, p. 161802, 2004.

[3] R. Parker, C. Yu, W. Zhong, B. Estey, and H. Müller, "Measurement of the fine-structure constant as a test of the standard model," *Science*, vol. 360, pp. 191–195, 04 2018.

[4] A. Beyer *et al.*, "Precision Spectroscopy of Atomic Hydrogen," *J. Phys.: Conf. Ser.*, vol. 467, p. 012003, Dec. 2013.

[5] P. J. Mohr, B. N. Taylor, and D. B. Newell, "CODATA Recommended Values of the Fundamental Physical Constants: 2010," *Rev. Mod. Phys.*, vol. 84, p. 1527, 2012.

[6] G. Newton, D. A. Andrews, and P. J. Unsworth, "A precision determination of the lamb shift in hydrogen," *Philosophical Transactions of the Royal Society of London. Series A, Mathematical and Physical Sciences*, vol. 290, no. 1373, pp. 373–404, 1979.

[7] S. R. Lundeen and F. M. Pipkin, "Separated oscillatory field measurement of the lamb shift in h, n = 2," *Metrologia*, vol. 22, no. 1, p. 9, 1986.

[8] E. W. Hagley and F. M. Pipkin, "Separated oscillatory field measurement of hydrogen $2s_{1/2}$-$2p_{3/2}$ fine structure interval," *Phys. Rev. Lett.*, vol. 72, pp. 1172–1175, Feb 1994.

[9] D. Hanneke, S. Fogwell Hoogerheide, and G. Gabrielse, "Cavity control of a single-electron quantum cyclotron: Measuring the electron magnetic moment," *Phys. Rev. A*, vol. 83, p. 052122, May 2011.

[10] R. Pohl, A. Antognini, F. Amaro, F. Biraben, J. Cardoso, D. Covita, A. Dax, S. Dhawan, M. Diepold, L. Fernandes, A. Giesen, A. Gouvea, T. Graf, T. Haensch, P. Indelicato, L. Julien, C.-Y. Kao, P. Knowles, J. Matias-Lopes, and F. Kottmann, "Laser spectroscopy of muonic hydrogen," vol. 525, pp. 647–651, 09 2013.

[11] R. Pohl *et al.*, "Laser spectroscopy of muonic deuterium," *Science*, vol. 353, no. 6300, pp. 669–673, 2016.

[12] F. Heiße, F. Köhler-Langes, S. Rau, J. Hou, S. Junck, A. Kracke, A. Mooser, W. Quint, S. Ulmer, G. Werth, K. Blaum, and S. Sturm, "High-precision measurement of the proton's atomic mass," *Phys. Rev. Lett.*, vol. 119, p. 033001, Jul 2017.

[13] S. Rau, F. Heiße, F. Köhler-Langes, S. Sasidharan, R. Haas, D. Renisch, C. Düllmann, W. Quint, S. Sturm, and K. Blaum, "Penning trap mass measurements of the deuteron and the hd molecular ion," *Nature*, vol. 585, pp. 43–47, 09 2020.

[14] W. Parker, D. Langenberg, A. Denenstein, and B. Taylor, "Determination of eh, Using Macroscopic Quantum Phase Coherence in Superconductors. 1. Experiment," *Phys. Rev.*, vol. 177, p. 639, 1969.

[15] E. R. Cohen and B. N. Taylor, "The 1973 Least-Squares Adjustment of the Fundamental Constants," *J. Phys. Chem. Ref. Data*, vol. 2, p. 663, 1973.

[16] E. R. Cohen and B. N. Taylor, "The 1986 adjustment of the fundamental physical constants," *Rev. Mod. Phys.*, vol. 59, p. 1121, Oct. 1987.

[17] P. Mohr and B. Taylor, "CODATA recommended values of the fundamental physical constants: 1998," *Rev. Mod. Phys.*, vol. 72, p. 351, 2000.

[18] P. J. Mohr and B. N. Taylor, "CODATA recommended values of the fundamental physical constants: 2002," *Rev. Mod. Phys.*, vol. 77, p. 1, 2005.

[19] P. J. Mohr, B. N. Taylor, and D. B. Newell, "CODATA Recommended Values of the Fundamental Physical Constants: 2006," *Rev. Mod. Phys.*, vol. 80, p. 633, 2008.

[20] P. J. Mohr, D. B. Newell, and B. N. Taylor, "CODATA Recommended Values of the Fundamental Physical Constants: 2014," *ArXiv e-prints*, July 2015.

[21] S. G. Karshenboim, "Precision physics of simple atoms: QED tests, nuclear structure and fundamental constants," *Phys. Rept.*, vol. 422, p. 1, 2005.

[22] D. Hanneke, S. Fogwell, and G. Gabrielse, "New Measurement of the Electron Magnetic Moment and the Fine Structure Constant," *Physical Review Letters*, vol. 100, p. 120801, Mar. 2008.

[23] T. Aoyama, M. Hayakawa, T. Kinoshita, and M. Nio, "Tenth-Order Electron Anomalous Magnetic Moment — Contribution of Diagrams without Closed Lepton Loops," *Phys. Rev.*, vol. D91, no. 3, p. 033006, 2015.

[24] R. Bouchendira, P. Cladé, S. Guellati-Khélifa, F. Nez, and F. Biraben, "State of the art in the determination of the fine structure constant: test of Quantum Electrodynamics and determination of h/m_u," *Annalen Phys.*, vol. 525, no. 7, pp. 484–492, 2013.

[25] T. Aoyama, M. Hayakawa, T. Kinoshita, and M. Nio, "Revised value of the eighth-order contribution to the electrong−2," *Physical Review Letters*, vol. 99, Sep 2007.

[26] C. Patrignani *et al.*, "Review of Particle Physics," *Chin. Phys.*, vol. C40, no. 10, p. 100001, 2016.

[27] R. D. Cousins and V. L. Highland, "Incorporating systematic uncertainties into an upper limit," *Nucl. Instrum. Meth. A*, vol. 320, pp. 331–335, 1992.

[28] D. Erceg-Hurn and V. Mirosevich, "Modern robust statistical methods an easy way to maximize the accuracy and power of your research," *The American psychologist*, vol. 63, pp. 591–601, 11 2008.

[29] F. James, "MINUIT Function Minimization and Error Analysis: Reference Manual Version 94.1," 1994.

[30] E. L. Lehmann, "The fisher, neyman-pearson theories of testing hypotheses: One theory or two?," *Journal of the American Statistical Association*, vol. 88, no. 424, pp. 1242–1249, 1993.

[31] A. E. Kramida, "A critical compilation of experimental data on spectral lines and energy levels of hydrogen, deuterium, and tritium," *At. Data Nucl. Data Tables*, vol. 96, p. 586, Nov. 2010.

[32] P. Zhao, W. Lichten, H. Layer, and J. Bergquist, "New value for the rydberg constant from the hydrogen balmer-β transition," *Phys. Rev. Lett.*, vol. 58, pp. 2506–2506, Jun 1987.

[33] M. Horbatsch and E. A. Hessels, "Evaluation of the strength of electron-proton scattering data for determining the proton charge radius," *Phys. Rev.*, vol. C93, no. 1, p. 015204, 2016.

[34] C. Peng and H. Gao, "Proton Charge Radius (PRad) Experiment at Jefferson Lab," *EPJ Web Conf.*, vol. 113, p. 03007, 2016.

[35] "The MAMI Electron Scattering Program," Johannes Gutenberg Universitat Mainz 2016. [Online] `https://www.jlab.org/conferences/elba/talks/wednesday/morning_session/Schlimme.pdf`.

[36] E. J. Downie, "The MUSE experiment," *EPJ Web Conf.*, vol. 73, p. 07005, 2014.

[37] M. Diepold, "The lamb shift in muonic helium ions," 2015.

[38] B. Franke, J. J. Krauth, A. Antognini, M. Diepold, F. Kottmann, and R. Pohl, "Theory of the n = 2 levels in muonic helium-3 ions," *The European Physical Journal D*, vol. 71, Dec 2017.

[39] M. Diepold, B. Franke, J. J. Krauth, A. Antognini, F. Kottmann, and R. Pohl, "Theory of the lamb shift and fine structure in muonic 4he ions and the muonic 3he– 4he isotope shift," *Annals of Physics*, vol. 396, p. 220–244, Sep 2018.

[40] T. Aoyama, M. Hayakawa, T. Kinoshita, and M. Nio, "Complete Tenth-Order QED Contribution to the Muon g-2," *Phys. Rev. Lett.*, vol. 109, p. 111808, 2012.

[41] J. D. Jackson, *Classical electrodynamics; 2nd ed.* New York, NY: Wiley, 1975.

[42] H. Murayama, "221b lecture notes," 2005.

[43] R. S. Van Dyck, P. B. Schwinberg, and H. G. Dehmelt, "Electron magnetic moment from geonium spectra: Early experiments and background concepts," *Phys. Rev. D*, vol. 34, pp. 722–736, Aug 1986.

[44] B. Odom, "Fully quantum measurement of the electron magnetic moment /," 01 2004.

[45] B. L. Roberts and N. M. . g − 2) collaboration, "Status of the fermilab muon (g − 2) experiment," *Chinese Physics C*, vol. 34, no. 6, p. 741, 2010.

[46] M. E. Peskin and D. V. Schroeder, *An introduction to quantum field theory*. Boulder, CO: Westview, 1995. Includes exercises.

[47] S. Eidelman and F. Jegerlehner, "Hadronic contributions to g-2 of the leptons and to the effective fine structure constant alpha (M(z)**2)," *Z. Phys.*, vol. C67, p. 585, 1995.

[48] F. G. Mariam, W. Beer, P. R. Bolton, P. O. Egan, C. J. Gardner, V. W. Hughes, D. C. Lu, P. A. Souder, H. Orth, J. Vetter, U. Moser, and G. z. Putlitz, "Higher precision measurement of the hfs interval of muonium and of the muon magnetic moment," *Phys. Rev. Lett.*, vol. 49, pp. 993–996, Oct 1982.

[49] W. E. Lamb and R. C. Retherford, "Fine structure of the hydrogen atom. part i," *Phys. Rev.*, vol. 79, pp. 549–572, Aug 1950.

[50] S. Weinberg, *The Quantum Theory of Fields, Volume 1: Foundations*. Cambridge University Press, 2005.

[51] K. Pachucki, "Theory of the Lamb shift in muonic hydrogen," *Phys. Rev. A*, vol. A53, p. 2092, 1996.

[52] R. Barbieri and T. Ericson, "Evidence against the existence of a low mass scalar boson from neutron-nucleus scattering," *Physics Letters B*, vol. 57, no. 3, pp. 270–272, 1975.

[53] A. Matveev, C. G. Parthey, K. Predehl, J. Alnis, A. Beyer, R. Holzwarth, T. Udem, T. Wilken, N. Kolachevsky, M. Abgrall, D. Rovera, C. Salomon, P. Laurent, G. Grosche, O. Terra, T. Legero, H. Schnatz, S. Weyers, B. Altschul, and T. W. Hänsch, "Precision measurement of the hydrogen $1s-2s$ frequency via a 920-km fiber link," *Phys. Rev. Lett.*, vol. 110, p. 230801, Jun 2013.

[54] M. Niering, R. Holzwarth, J. Reichert, P. Pokasov, T. Udem, M. Weitz, T. W. Hänsch, P. Lemonde, G. Santarelli, M. Abgrall, P. Laurent, C. Salomon, and A. Clairon, "Measurement of the Hydrogen 1S- 2S Transition Frequency by Phase Coherent Comparison with a Microwave Cesium Fountain Clock," *Phys. Rev. Lett.*, vol. 84, p. 5496, June 2000.

[55] U. D. Jentschura, S. Kotochigova, E.-O. Le Bigot, P. J. Mohr, and B. N. Taylor, "Precise Calculation of Transition Frequencies of Hydrogen and Deuterium Based on a Least-Squares Analysis," *Phys. Rev. Lett.*, vol. 95, p. 163003, Oct. 2005.

[56] A. Beyer, L. Maisenbacher, A. Matveev, R. Pohl, K. Khabarova, A. Grinin, T. Lamour, D. C. Yost, T. W. Hänsch, N. Kolachevsky, and T. Udem, "The rydberg constant and proton size from atomic hydrogen," *Science*, vol. 358, no. 6359, pp. 79–85, 2017.

[57] K. Pachucki and U. D. Jentschura, "Two-loop bethe-logarithm correction in hydrogenlike atoms," *Physical Review Letters*, vol. 91, Sep 2003.

[58] V. Yerokhin, P. Indelicato, and V. Shabaev, "Two loop selfenergy correction in high Z hydrogen - like ions," *Phys. Rev. Lett.*, vol. 91, p. 073001, 2003.

[59] V. A. Yerokhin, P. Indelicato, and V. M. Shabaev, "Two-loop qed corrections with closed fermion loops," *Phys. Rev. A*, vol. 77, p. 062510, Jun 2008.

[60] R. Faustov, A. Martynenko, G. Martynenko, and V. Sorokin, "Radiative non-recoil nuclear finite size corrections of order $\alpha(Z\alpha)^5$ to the hyperfine splitting of S-states in muonic hydrogen," *Phys. Lett. B*, vol. B733, p. 354, 2014.

[61] A. Antognini, F. Nez, K. Schuhmann, F. D. Amaro, F. Biraben, *et al.*, "Proton Structure from the Measurement of $2S - 2P$ Transition Frequencies of Muonic Hydrogen," *Science*, vol. 339, p. 417, 2013.

[62] J. C. Martens and J. P. Ralston, "The Muon Experimental Anomalies Are Explained by a New Interaction Proportional to Charge," 2016.

[63] M. P. Bradley, J. V. Porto, S. Rainville, J. K. Thompson, and D. E. Pritchard, "Penning trap measurements of the masses of ^{133}cs, $^{87,85}rb$, and ^{23}na with uncertainties ≤ 0.2 ppb," *Phys. Rev. Lett.*, vol. 83, pp. 4510–4513, Nov 1999.

[64] M. Blennow, E. Fernandez-Martinez, A. Olivares-Del Campo, S. Pascoli, S. Rosauro-Alcaraz, and A. V. Titov, "Neutrino portals to dark matter," *The European Physical Journal C*, vol. 79, Jul 2019.

[65] K. Kowalska and E. M. Sessolo, "Expectations for the muon g-2 in simplified models with dark matter," *JHEP*, vol. 09, p. 112, 2017.

[66] L. Calibbi, R. Ziegler, and J. Zupan, "Minimal Models for Dark Matter and the Muon g-2 Anomaly," 2018.

[67] F. S. Queiroz and W. Shepherd, "New Physics Contributions to the Muon Anomalous Magnetic Moment: A Numerical Code," *Phys. Rev.*, vol. D89, no. 9, p. 095024, 2014.

[68] C. Biggio, M. Bordone, L. Di Luzio, and G. Ridolfi, "Massive vectors and loop observables: the $g-2$ case," *JHEP*, vol. 10, p. 002, 2016.

[69] M. Pospelov, "Secluded U(1) below the weak scale," *Phys. Rev.*, vol. D80, p. 095002, 2009.

[70] S. Gninenko and N. Krasnikov, "Probing the muon g $\mu - 2$ anomaly, l $\mu -$ l τ gauge boson and dark matter in dark photon experiments," vol. 783, 06 2018.

[71] S. G. Karshenboim, D. McKeen, and M. Pospelov, "Constraints on muon-specific dark forces," 2014.

[72] D. Tucker-Smith and I. Yavin, "Muonic hydrogen and MeV forces," *Phys. Rev. D*, vol. D83, p. 101702, 2011.

[73] C. E. Carlson and B. C. Rislow, "New Physics and the Proton Radius Problem," *Phys. Rev. D*, vol. D86, p. 035013, 2012.

[74] W. Xiong *et al.*, "A small proton charge radius from an electron–proton scattering experiment," *Nature*, vol. 575, no. 7781, pp. 147–150, 2019.

[75] D. Stump, J. Pumplin, R. Brock, D. Casey, J. Huston, J. Kalk, H. L. Lai, and W. K. Tung, "Uncertainties of predictions from parton distribution functions. I. The Lagrange multiplier method," *Phys. Rev. D*, vol. 65, p. 014012, Jan. 2002.

[76] E. Eriksen, "Foldy-Wouthuysen Transformation. Exact Solution with Generalization to the Two-Particle Problem," *Phys. Rev.*, vol. 111, pp. 1011–1016, 1958.

[77] M. I. Eides, H. Grotch, and V. A. Shelyuto, "Theory of light hydrogen - like atoms," *Phys. Rept.*, vol. 342, p. 63, 2001.

[78] B. Holdom, "Two u(1)'s and charge shifts," *Physics Letters B*, vol. 166, no. 2, pp. 196–198, 1986.

[79] M. Battaglieri, A. Belloni, A. Chou, P. Cushman, B. Echenard, R. Essig, J. Estrada, J. L. Feng, B. Flaugher, P. J. Fox, P. Graham, C. Hall, R. Harnik, J. Hewett, J. Incandela, E. Izaguirre, D. McKinsey, M. Pyle, N. Roe, G. Rybka, P. Sikivie, T. M. P. Tait, N. Toro, R. V. D. Water, N. Weiner, K. Zurek, E. Adelberger, A. Afanasev, D. Alexander, J. Alexander, V. C. Antochi, D. M. Asner, H. Baer, D. Banerjee, E. Baracchini, P. Barbeau, J. Barrow, N. Bastidon, J. Battat, S. Benson, A. Berlin, M. Bird, N. Blinov, K. K. Boddy, M. Bondi, W. M. Bonivento, M. Boulay, J. Boyce, M. Brodeur, L. Broussard, R. Budnik, P. Bunting, M. Caffee, S. S. Caiazza, S. Campbell, T. Cao, G. Carosi, M. Carpinelli, G. Cavoto, A. Celentano, J. H. Chang, S. Chattopadhyay, A. Chavarria, C.-Y. Chen, K. Clark, J. Clarke, O. Colegrove, J. Coleman,

D. Cooke, R. Cooper, M. Crisler, P. Crivelli, F. D'Eramo, D. D'Urso, E. Dahl, W. Dawson, M. D. Napoli, R. D. Vita, P. DeNiverville, S. Derenzo, A. D. Crescenzo, E. D. Marco, K. R. Dienes, M. Diwan, D. H. Dongwi, A. Drlica-Wagner, S. Ellis, A. C. Ezeribe, G. Farrar, F. Ferrer, E. Figueroa-Feliciano, A. Filippi, G. Fiorillo, B. Fornal, A. Freyberger, C. Frugiuele, C. Galbiati, I. Galon, S. Gardner, A. Geraci, G. Gerbier, M. Graham, E. Gschwendtner, C. Hearty, J. Heise, R. Henning, R. J. Hill, D. Hitlin, Y. Hochberg, J. Hogan, M. Holtrop, Z. Hong, T. Hossbach, T. B. Humensky, P. Ilten, K. Irwin, J. Jaros, R. Johnson, M. Jones, Y. Kahn, N. Kalantarians, M. Kaplinghat, R. Khatiwada, S. Knapen, M. Kohl, C. Kouvaris, J. Kozaczuk, G. Krnjaic, V. Kubarovsky, E. Kuflik, A. Kusenko, R. Lang, K. Leach, T. Lin, M. Lisanti, J. Liu, K. Liu, M. Liu, D. Loomba, J. Lykken, K. Mack, J. Mans, H. Maris, T. Markiewicz, L. Marsicano, C. J. Martoff, G. Mazzitelli, C. McCabe, S. D. McDermott, A. McDonald, B. McKinnon, D. Mei, T. Melia, G. A. Miller, K. Miuchi, S. M. P. Nazeer, O. Moreno, V. Morozov, F. Mouton, H. Mueller, A. Murphy, R. Neilson, T. Nelson, C. Neu, Y. Nosochkov, C. O'Hare, N. Oblath, J. Orrell, J. Ouellet, S. Pastore, S. Paul, M. Perelstein, A. Peter, N. Phan, N. Phinney, M. Pivovaroff, A. Pocar, M. Pospelov, J. Pradler, P. Privitera, S. Profumo, M. Raggi, S. Rajendran, N. Randazzo, T. Raubenheimer, C. Regenfus, A. Renshaw, A. Ritz, T. Rizzo, L. Rosenberg, A. Rubbia, B. Rybolt, T. Saab, B. R. Safdi, E. Santopinto, A. Scarff, M. Schneider, P. Schuster, G. Seidel, H. Sekiya, I. Seong, G. Simi, V. Sipala, T. Slatyer, O. Slone, P. F. Smith, J. Smolinsky, D. Snowden-Ifft, M. Solt, A. Sonnenschein, P. Sorensen, N. Spooner, B. Srivastava, I. Stancu, L. Strigari, J. Strube, A. O. Sushkov, M. Szydagis, P. Tanedo, D. Tanner, R. Tayloe, W. Terrano, J. Thaler, B. Thomas, B. Thorpe, T. Thorpe, J. Tiffenberg, N. Tran, M. Trovato, C. Tully, T. Tyson, T. Vachaspati, S. Vahsen, K. van Bibber, J. Vandenbroucke, A. Villano, T. Volansky, G. Wang, T. Ward, W. Wester,

A. Whitbeck, D. A. Williams, M. Wing, L. Winslow, B. Wojtsekhowski, H.-B. Yu, S.-S. Yu, T.-T. Yu, X. Zhang, Y. Zhao, and Y.-M. Zhong, "Us cosmic visions: New ideas in dark matter 2017: Community report," 2017.